University of Southampton Research Repository

University of Southampton

Faculty of Engineering and Physical Sciences

Engineering materials, Mechanical Engineering

Study of Fatigue Crack Initiation and Propagation Mechanisms in a Directionally Solidified Superalloy: Effects of Microstructure, Anisotropy and Oxidation

by

Yuanguo Tan

Thesis for the degree of Doctor of Philosophy

23 September 2023

ORCID: 0009-0003-5077-1938

University of Southampton

Abstract

Faculty of Engineering and Physical Sciences

Engineering Materials

Doctor of Philosophy

Study of Fatigue Crack Initiation and Propagation Mechanisms in a Directionally Solidified Superalloy: Effects of Microstructure, Anisotropy and Oxidation

by

Yuanguo Tan

The Directionally solidified (DS) superalloy CM247LC was first developed by Cannon Muskegon Corporation and is extensively used in turbine blades and vane applications, due to its high strength at elevated temperatures, and excellent resistance to creep comparable with some single crystal (SX) superalloys. Studies on the fatigue behaviour, particularly the interplay between microstructure, oxidation, creep and fatigue at more moderate elevated temperatures (i.e. typical of those seen at stress concentration features like the blade root or at cooling holes) are however relatively few. The thesis provides a deeper understanding of the contribution of these factors to the alloy's failure mechanisms by systematic test design and careful in-situ and post characterization.

Fatigue anisotropy is correlated with the columnar grain elongation direction with the respect to the loading direction and general crack propagation direction. The former relationship induces the anisotropy in the Young's modulus and yield stress, which affects the entire fatigue life, while the later affects the specific fatigue crack initiation and propagation directions. Much shorter fatigue life is found in the specimen (termed as L or LR) with the columnar grains aligned along the loading direction when the applied maximum stress is close to the yield stress. This is attributed to the much lower Young's modulus inducing a higher local plastic strain and hence faster crack initiation. The fatigue short crack propagation behaviours are mainly affected by the relationship between the columnar grain elongation direction and crack propagation direction. The effects of microstructural features on the fatigue short crack initiation and propagation have been assessed by data rich imaging approaches. Short cracks preferentially initiate from carbides or pores, instead of at slip bands, even though the intensity of the localized strain is at similar scale to these features in the early stages of crack initiation. The observation of crack evolution in three dimensions (3D) via X-ray CT further illustrates the fatigue cracks propagate along several slip systems simultaneously instead of a single favoured slip system.

Oxidation preferentially occurs at the stress/strain localisation features such as slip bands and carbides. The detailed oxidation mechanism of the carbides is revealed by 3D reconstruction of the oxidised carbides at different testing times: (Co, Ni) oxides are formed firstly at the interface between carbides and matrix, then protrude beneath these carbides, finally intruding into the bulk, leading to crack formation inside the carbides. Crack initiation from oxidised carbides is widely observed, but their propagation is blocked by the surrounding oxides in fatigue testing with 1-1-1-1 trapezoidal waveform. Thus, the main crack initiation sites transfer from the surface to the subsurface pores.

The phenomenon of oxides prohibiting crack propagation is also shown in the long fatigue crack propagation tests. The degree of crack arrest is linked to testing temperatures and frequencies, as more significant oxidation occurs in the lower frequency and higher temperature tests. Internal (Al, Cr)-rich oxides intrude into the materials, especially ahead of the crack tip, while the external (Co, Ni) oxides fill the crack. Oxidation induced crack closure is thought to be the main factor contributing to observed crack arrests, caused by the thick external oxides. A modified model based on the thickness of the external oxidation layers is proposed to quantitatively evaluate the effective stress intensity, which shows the thicker oxidation layers formed at lower frequencies, causes a dramatic reduction in the crack tip stress intensity and leads to crack arrest.

Further detailed analysis on cracks was performed to assess the steps in the internal (Al, Cr)-rich oxide formation. Al-rich oxides form inside the γ' in the form of nanoparticles, while Cr-rich oxides are formed at the γ channel in the form of stripes. The potential stress-assisted oxidation mechanism is inferred to be: (1) the formation of external oxides depletes γ' of Ni, causing the formation of Al-rich oxides inside the γ' (2) after the γ' is fully oxidized, O diffuses into the γ channel, forming stripe-like Cr-rich oxides; (3) As dense internal oxidation layers are not formed, allowing continuous diffusion of Ni and Co elements, this forms thick external oxidation layers, resulting in oxidation-induced crack closure.

Table of content

Table of content III

List of figures VII

Research Thesis: Declaration of Authorship XVII

Acknowledgements XIX

Abbreviations XXI

Chapter 1 Introduction 1

1.1 Background 1

1.2 Aim and objectives 2

Chapter 2 Literature review 3

2.1 Nickel based (Ni-base) directionally solidified (DS) superalloys 3

2.1.1 Manufacturing process of Ni-base DS superalloys 5

2.1.2 Microstructures of Ni-base DS superalloys 7

2.1.3 Elastic and plastic anisotropy in Ni-base DS superalloys 12

2.1.4 DS CM247LC superalloy 13

2.2 Fatigue behaviours of Ni-base superalloys – findings and challenges 15

2.2.1 Fundamental conceptions of fatigue 15

2.2.2 Fatigue life approach 17

2.2.3 Effects of microstructures on fatigue short crack initiation and propagation behaviours 21

2.2.4 Crack initiation behaviours at the elevated temperatures 27

2.2.5 The crack propagation behaviours at elevated temperatures 32

2.2.6 Effects of anisotropic elastic modulus and yield stress 37

2.2.7 Fatigue behaviour of DS CM247LC superalloy 37

2.3 Summary of literature reviews and challenges 39

Chapter 3 Materials and methodology 43

3.1 Microstructure characterization 43

3.1.1 two-dimensional (2D) materials characterization 43

3.1.2 Three-dimensional (3D) materials characterization [1] 44

3.2 Mechanical tests 45

3.2.1 Tensile tests 45

3.2.2 Tension-tension fatigue tests 46

3.2.3 Three-point bending fatigue tests 49

3.3 Post-test characterization 53

3.3.1 Fractography and three-dimensional reconstruction 53

3.3.2 EBSD analysis 53

3.3.3 Xray computed tomography (Xray-CT) 54

3.3.4 Nanoindentation at the crack tip 56

3.3.6 Focused ion beam (FIB) and scanning transmission electron microscopy (STEM) 57

Chapter 4 The effects of grain orientation on fatigue short crack initiation and propagation 59

4.1 Introduction 59

4.2 Microstructures of DS CM247LC superalloy 61

4.3 Anisotropic mechanical response for DS CM247LC 64

4.4 Comparison of the fatigue short crack growth behaviours 66

4.5 Characterization of the crack initiation and propagation 70

4.6 Discussion 72

4.6.1 The effects of Young's modulus on the fatigue live 72

4.6.2 The effects of anisotropic compatibility of GBs on the fatigue crack initiation 75

4.7 Summary and conclusion 78

Chapter 5 In-depth analysis of microstructure effects on fatigue short crack growth behaviours 81

5.1 Introduction 81

5.2 Fatigue crack initiation and early propagation in the RR sample 83

5.3 Strain localization 87

5.4 In situ SRCT characterization 91

5.5 Discussion 94

5.5.1 Mechanism of crack initiation 94

5.5.2 Comparison of crack growth behaviour in 2D and 3D 98

5.6 Summary and conclusion 99

Chapter 6 Effects of oxidation on fatigue crack initiation behaviours....101

6.1 Introduction....101

6.2 Sustained-load oxidation 101

6.3 High-temperature short crack initiation and propagation 105

6.4 Discussion....110

6.4.1 Stress assisted oxidation mechanism 110

6.4.2 The effects of oxidation on the crack initiation 110

6.5 Summary and conclusion 112

Chapter 7 Effects of oxidation on fatigue crack propagation behaviours 115

7.1 Introduction....115

7.2 High-temperature long fatigue crack growth and fracture surface observation....115

7.3 Interrupted tests and crack tips characterization....119

7.4 Three-dimensional characterization of the crack tip via Xray-CT 123

7.5 Discussion....126

7.5.1 Complete or partial oxidation-induced crack closure ?....127

7.5.2 The effects of COICC 128

7.5.3 The effects of the POICC....130

7.5.4 The effects of the microstructures....134

7.6 Summary and conclusion 135

Chapter 8 Detailed analysis on the oxidation and creep process on the arrested crack....137

8.1 Introduction....137

8.2 Results....137

8.2.1 Strain and mechanical property analysis at the crack tips in the interrupted tests....137

8.2.2 Oxidation mechanism characterization via FIB and STEM....141

8.3 Discussion....145

8.3.1 Crack blunting by creep? 145

8.3.2 The effects of oxidation intrusion 145

8.3.3 The mechanism of internal oxidation 148

8.4 Summary and conclusions 150

Chapter 9 General discussion and Conclusions 151

9.1 General discussion 151

9.2 Overall Summary and Conclusions 153

Chapter 10 Future work 157

10.1 In-situ high-temperature fatigue long crack tests 157

10.2 Crystal plasticity finite element analysis 157

10.3 Further study on the internal oxidation ahead of the crack tip 161

References 163

List of figures

Fig 2.1 The different materials used in a Royal Royce jet engine [9]..3
Fig 2. 2 Blades and the grain structure. (a) Conventional cast blade with equiaxed crystal structure, directionally solidified blade with (b) columnar grains and (c) single crystal blade [9].....................4
Fig 2.3 (a) Equipment for the traditional HRS process, (b) Casting defect map for the traditional directional solidification process showing the narrow operation window for large IGT blade manufacturing [14]..6
Fig 2.4 Equipment of LMC process [14] 7
Fig 2.5 Grain structure of (a) longitudinal section, (b) cross section 1 – 1 and 2 – 2 marked by the dashed line [22]...8
Fig 2.6 The morphology of dendrites along the longitudinal (a) and cross (b) sections [24] 9
Fig 2.7 the morphology of gamma prime: (a) cubic; (b) spherical; (c) irregular shape [37-39].......10
Fig 2.8 The experimental and predicted tension data of DZ125 superalloy at 20 °C (a), 650 °C (b), 760 °C, (c) and 850 °C (d) [52]...13
Fig 2. 9 Depiction of typical dendritic structure within the grains of DS Ni-base superalloys [56].14
Fig 2. 10 Schematic of a typical fatigue cycle under sinusoidal loading [59] 16
Fig 2.11 Schematic representation of the three fundamental crack-opening modes: (a) opening mode, (b) in-plane shear mode, and (c) anti-plane shear mode [60]..17
Fig 2.12 S-N curves of 1045 steel and 2014-T6 aluminium [62] 18
Fig 2.13 Sharp crack in a thin elastic plate [60]..20
Fig 2.14 Schematic representation of the da/dN vs. ΔK in a double-logarithmic plot with the Paris law represented as a straight line [60]...21
Fig 2.15 (a,b) Surface damage morphology after sharp-corner polish and then fatigue; (c) mechanism of PSB extrusion and intrusion [67] 22
Fig 2.16 TEM images showing dislocations in [111]-orientated specimen fatigue tested at room temperature [75]...25
Fig 2.17 Schematic diagram showing the misaligned activated slip systems [95] 26
Fig 2.18 Evolution of cracks from the oxidized grain boundaries at the notch root in the interrupted test at 650 oC a: (a) 9000 cycles, (b) 15000 cycles, (c) 31000 cycles and (d) 36000 cycles; (e) EDS mapping of the region highlighted by the rectangle shown in (d) [109]..29
Fig 2.19 ECCI micrograph next to an oxidized MC carbide (denoted by the dashed red line) during OP-TMF at 850 °C showing high dislocation density within the recrystallized region (denoted by the dashed green line) and within the γ/γ′ microstructure where dissolution of γ′ precipitates occurs [111]...30
Fig 2.20 In-situ SEM images before the final instant fracture, (b) Fracture morphology, (c) Partial enlarged view of fracture morphology for the 120 s of dwell time at 900 °C [113]........................31

Fig 2.21 (a) Area of interest for TEM lamella extraction in the FG LSHR variant tested at 725 °C. The dashed line indicates the extraction position; (b) TEM lamella in the trench before lift-out procedure; (c) bulged oxides and oxide intrusion along grain boundary and the corresponding EDS elemental maps; and (d) close-up of the γ′ depletion zone highlighted in (c) by the rectangle [119] 33

Fig 2.22 (a) Schematic diagram showing the contribution of SAGBO, DE and mechanical damage to FCG at various stages of crack propagation, (b) example of transition of transgranular to intergranular crack propagation in U720Li in the stage I crack propagation [10], (c) and (d) example of transition of predominantly intergranular crack propagation at ΔK of 20 MPa√m to transgranular crack propagation at ΔK of 40 Mpa√m in the CG LSHR alloy variant [10, 119]...... 34

Fig 2.23 (a) Schematic representation of linking and interaction of creep-fatigue damage modes with a normalized hold time at a fixed applied loading level. The number 1 on the vertical axis refers to fully-damage due to creep and fatigue; (b) Effects of creep on FCG in subsolvus heat treated Udimet 720 tested at 700 °C and in RR1000 variants tested at 725 °C with a load ratio of 0.5 in vacuum [82, 130]........ 36

Fig 3.1 (a) Dog-bone specimen dimension (in mm); (b) set-up of the SRCT scanning; (c) tensile specimen dimension (in mm) 46

Fig 3.2(a) Speckle patterns; (b) area of interest for DIC analysis 48

Fig 3.3 Three-point bending specimens and corresponding different types of specimens........ 50

Fig 3.4 Schematic diagram of the long crack tests set-up and the relationship between columnar grains and the loading direction........ 52

Fig 3.5 Schematic diagram showing the extraction of the match stich and set-up of the X-ray CT scanning........ 56

Fig 4.1 Microstructure of CM247LC alloy: (a) Morphology of dendrites at the surface parallel to solidification direction; (b) Morphology of dendrites at the surface perpendicular to solidification direction; (c) morphology of eutectic (γ + γ′) and blocky carbides; (d) morphology of grain boundary and chain-like carbides; (e) and (f) EDX analysis of blocky carbides and chain-like carbides; (g) secondary γ′ and tertiary γ′ 62

Fig 4. 2 SRCT characterization of voids and carbides in CM247LC alloy: (a) pore distribution in 3D; (b) quantified statistical distribution of pore size; (c) pore sphericity; (d) carbide distribution in 3D; (e) quantified statistical distribution of carbide size; (f) projection of voids and carbides to a plane normal to the solidification direction of CM247LC alloy 63

Fig 4.3 The strain-stress curves of (a) L and T specimens subjected to uniaxial tensile testing, (b) LR, RR and RL specimens subjected to cyclic loading, (c) the plastic regime; (d) curves of strain variation against time 65

Fig 4.4 (a) the fatigue life of L, T, LR, RR, RL specimens against applied strain; The replica recording of crack initiation and propagation of LR specimen (b), RL specimen (c); RR specimen (d) at maximum stress of 95% yield stress (for the L-specimen) 67

Fig 4.5 the number of sub-cracks constituting the main crack; (b) cycles of crack initiation and propagation overlayed with applied strain amplitudes; (c) tortuosity of the main cracks; (d) the crack growth rates against ΔK of LR RL and RR specimens 69

Fig 4.6 crack initiation sites of the LR specimen (a) and (b); RL specimen (c) and (d) 70

Fig 4.7 The secondary cracks of LR (a), (b) and RL (c) and (d) specimens 71

Fig 4.8 Top surface of LR specimen at 5000 cycles and RL specimen at 32000 cycles recorded by replicas 74

Fig 4. 9 schematic diagram showing the slip systems in the columnar grains and their relationship to the loading direction, (b) the ideal grains in Euler space and their projections in the IPF X and IPF Z; (c) the m prime with the mis-rotation angle, (d) the magnitude of the residual dislocations (unit: a) at GBs with mis-rotation angle 76

Fig 4.10 IPF maps overlayed with band contrast maps and slip traces of (a) LR specimen, (c) RL specimen, KAM maps of (b) LR specimen and (d) RL specimen 77

Fig 5.1 Morphology of the main crack under OM; (b) replicas of the main crack; (c) Morphology of fracture surface; (d) and (e) initiation sites of the main crack 84

Fig 5.2 (a) and (b) secondary cracks in R1; (c) and (d) slip band cracking and sheared γ′ in R2; (e) and (f) carbides cracking in R3 85

Fig 5.3 (a) and (b) carbides at deflected parts of main crack; (c) propagation of a secondary crack86

Fig 5.4 (a) full-field reference image; (b), (c) and (d) full-field strain maps of ε_{xx}, ε_{yy}, ε_{xy} 89

Fig 5.5 Maximum shear strain distribution at interior of grain (a) at 10,000 cycles; (b) at 15,000 cycles; (c) at 22,700 cycles; (d) SEM image of the carbide after 22,7000 cycles; Maximum shear stress distribution at grain boundary at (a) 10,000 cycles; (b) at 15,000 cycles; (c) at 22,700 cycles; (d) SEM image of the carbide at grain boundary after 22,7000 cycles 90

Fig 5.6 (a) schematic diagram of loading tension-tension test; (b) 3D rendering of the specimen in front view; (c) 3D rendering of the specimen in bottom; (d) carbides distribution around CA; (e) superimposed image of carbides and cracking planes around CA; (f) surface slice of CA; (g) carbides distribution around CB; (h) superimposed image of carbides and cracking planes around CB; (i) surface slice of CB 92

Fig 5.7 CT images of CM247LC crack propagation. (a) cracking planes at 40000 cycles of CA; (b) cracking planes at 52000 cycles of CA; (c) superimposed image of cracking planes at 40000 and 52000 cycles of CA; (d) cracking planes at 40000 cycles of CB; (e) cracking planes at 52000 cycles of CB; (f) superimposed image of cracking planes at 40000 and 52000 cycles of CB 93
Fig 5.8 (a) schematic diagram of main crack at the early stage; (b) at the medium stage; (c) at the last stage 97
Fig 5.9 Facet-like crack section in polycrystal alloys [217]; (b) facet-like crack sections in DS alloys CM247LC; (c) 3D crack morphology in single crystal alloy [51]. 99

Fig 6.1 (a) the oxidized centre regions for samples tested at 650ºC after 2 hours (a), after 16 hours (b); the oxidized carbides after tested for 2 hours (c), for 16 hours (d); the oxidized slip bands tested for 2 hours (e), for 16 hours (f) 102
Fig 6.2 The oxidized carbides and corresponding element distribution maps............................... 103
Fig 6.3 The oxidized slip bands and corresponding element distribution maps............................ 104
Fig 6 4 The SEM image of oxidized carbides after tested for 1 hour (a); the 3D reconstruction of oxidized carbides after 1 hour (b), 2 hours (c), 4 hours (d) 104
Fig 6.5 The 3D reconstruction of the oxidized carbides after testing for 16 hours 105
Fig 6. 6 the crack initiation sites of the LR specimen tested with the frequency of 10 Hz (a), (b); of the RR specimen tested with the frequency of 10 Hz and applied maximum stress of 912 MPa (c) and (d); with applied maximum stress of 1008 MPa... 107
Fig 6. 7 The fracture surface of the RR specimen tested under 1008 MPa, with 1-1-1-1 trapezoidal waveform (a); the crack initiation site (b); the pore inside the crack initiation site (c); the oxides inside the pore.. 108
Fig 6. 8 The top surface of the interrupted LR specimen tested with frequency of 1-1-1-1 (a), the broken carbides and surrounded oxides (b), (c), (d); the broken carbides at the top surface of the LR specimen tested with the frequency of 10 Hz... 109

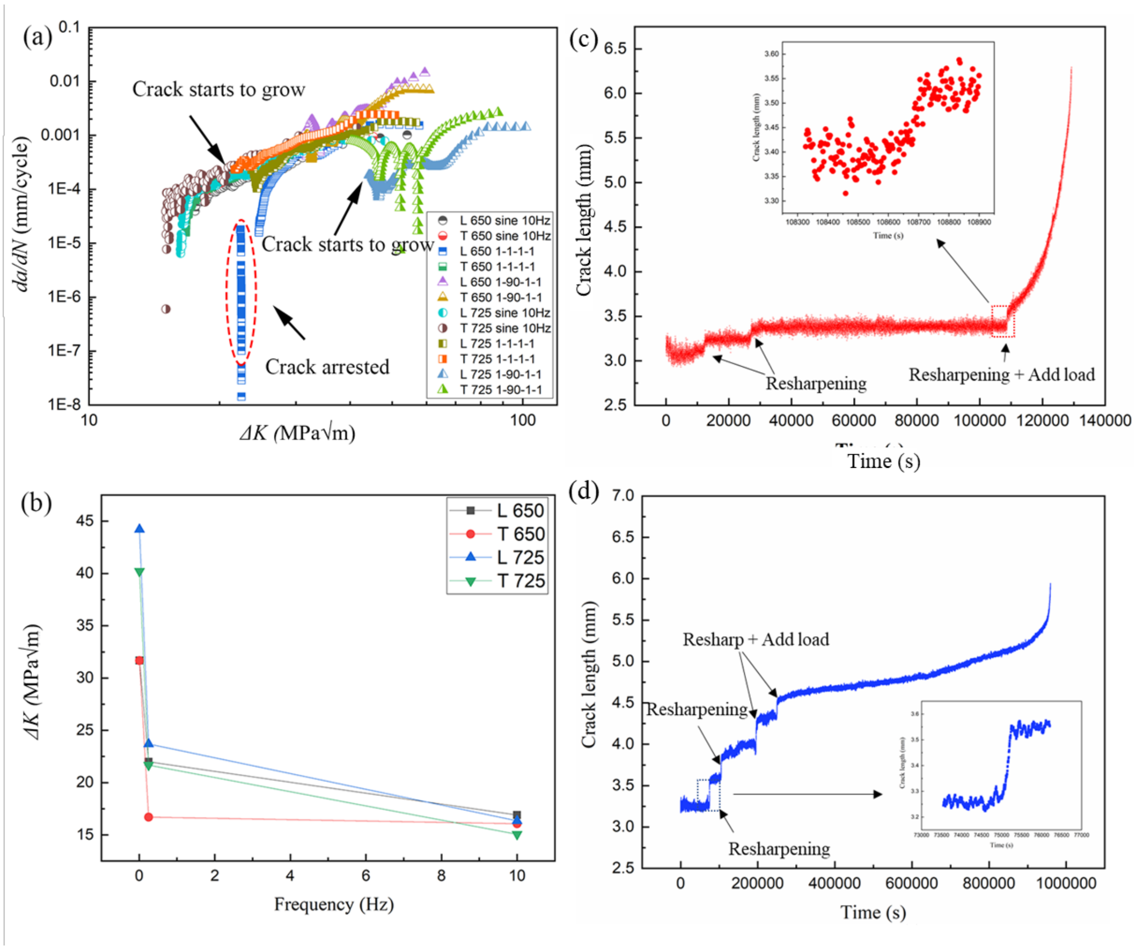

Fig 7.1 (a) Fatigue crack propagation rates of L and T samples tested at various conditions, (b) $\Delta K0$ variation against test frequencies, (c) crack length of L tested at 1-1-1-1 waveform, 725 °C and (d) tested at 1-90-1-1 waveform, 725 °C. 117

Fig 7.2 Optical microscopic (OM) image of T and L samples tested at 1-90-1-1 waveform, 650 °C (a, d), the low-magnification SEM images of the resharpening region for T and L samples (b, e), the high-magnification SEM images of oxidation layers for T and L samples (e, f) 118

Fig 7.3 (a) the OM image of interrupted L sample after tested at 1-1-1-1 waveform, 650 °C for 48 hours, (b) the high magnification SEM image of the crack tip and associated element distribution maps. 120

Fig 7. 4 SEM images of the crack tip of interrupted T sample, tested at 1-90-1-1, 650 °C for 12 hours (a), and the crack wake and associated element distribution maps (b), an EDX line scan perpendicularly across the crack (c)...121

Fig 7. 5 the SEM image of the crack tip for the third interrupted T sample, tested at 1-90-1-1, 650 °C for 96 hours and associated element distribution maps..122

Fig 7. 6 (a) CT 3D rendering of crack profile for the interrupted L sample, tested at 1-1-1-1 650 ˚C for 48 hours, slices corresponding to the line profiles: b (b), c (c), d (d), e (e). 124

Fig 7.7 CT 3D rendering of crack profile for the interrupted T sample, tested at 1-90-1-1 650 ˚C for 96 hours, slices corresponding to the line profiles: b (b), c (c), d (d), e (e). 124

Fig 7.8 crack opening displacement plots across the crack face for interrupted L sample, tested at 1-1-1-1 650 ˚C for 48 hours (a) and T sample, tested at 1-90-1-1 650 ˚C for 96 hours (b), COD line profile plots as measured across the white dotted lines for L (c) and T (d) 126

Fig 7.9 Schematic diagram of fatigue crack opening at maximum load (a) and minimum load (b) without oxidation, maximum load (c) and minimum load (d) with oxidation.............................. 128

Fig 7.10 the SEM images from the crack tip to the crack wake of the interrupted L sample, tested at 1-1-1-1 650 ˚C for 48 hours: (a), (b), (c); COD measured by X-ray CT and SEM-EDX for the test of 1-90-1-1 (d) and 1-1-1-1 (e); $\Delta Keff$ calculated based on Suresh's model (f); Schematic diagram of the model to estimate the CTOD (g); $\Delta Keff$ calculated based on Louat's model 133

Fig 7. 11 the precrack path revealed in X-ray CT 2D tomographs of L, tested at 1-1-1-1, 650 ˚C, (a) and (b); of T tested at 1-90-1-1, 650 ˚C (c) and (d) 135

Fig 8.1 T Specimen tested at 650 ºC for 12 hours: (a) Overlaid IPF (x) map and SEM image of the crack, (b) a higher SEM image of the crack tip, (c) KAM of the crack, (d) total GND energy map of the crack and crack tip 138

Fig 8. 2 (a) the SEM image of the crack tip after the nano-indentation test, (b) hardness map, (c) reduced elastic modulus map, (d) load-displacement curves of internal oxides and matrix, (e) load-displacement curves of external oxides 140

Fig 8.3 (a) the SEM image showing the coated regions of interests, (b) cross-section of the crack wake, (c) cross-section of the crack tip from left view, (d) cross-section of the crack tip from the right view... 142

Fig 8.4 Dark (a) and bright (b) views of the crack wake cross-section and associated element distribution maps, (c) a high-resolution image of the sheared γ′ and associated element distribution maps from the red rectangle ROI identified in (b). 143

Fig 8.5 (a) an overview of the cross-section of the crack tip (RO1-2 right view from Fig 8.3 (a)) high-resolution images of the Cr-rich oxides (red box) (b) and Al-rich oxides (blue box) (c). A higher magnification image of the oxidized region and matrix and associated element distribution maps (d), a higher magnifciation image of the secondary crack and associated element distribution map (e)... 144

Fig 8.6 the TEM foil of the crack tip at low magnification (a), at high magnification (b)............. 145

Fig 8. 7 the schematic diagram of crack opening without oxides (a), with external oxides (b), with internal oxides (c). 146

Fig 8. 8 the schematic diagram of internal oxidation process: (a) partially oxidized γ′, (b) fully oxidized γ′ and partially oxidized γ, (c) fully oxidized γ 149

Fig 10. 1 Virtual L (a) and T (b) samples with ratio of 1:2 159

Fig 10. 2 Tensile properties of L and T specimen from experiments and CPFEA 160

Fig 10.3 (a) strain-stress curve of L specimen via coarse and fine mesh; strain-stress curve of L specimen (b) and T specimen (c) with aspect ratio of 1:2, 1:3, 1:4 160

Fig 10.4 Deformation virtual samples at 0.5%, 1% and 1.5% axial strain coloured by elastic strain, $\epsilon 33$ 161

List of tables

Table 2.1 The composition of some DS superalloys (in wt.%) [15, 16] 5

Table 3.1 Composition of CM247LC alloy (in wt. %)... 43
Table 3.2 Imaging parameters in JEOL SEM JSM 7200F 43
Table 3.3 Parameters of the SRCT scans conducted in Spring-8 45
Table 3.4 Imaging parameters in JEOL SEM JSM7200F 48
Table 3.5 Parameters for DIC analysis... 49
Table 3.6 parameters of the Xray CT scans 55

Table 4.1 The fatigue lifetime variations of the tested specimens 66
Table 4.2 the calculated $\Delta Ee +$ 73

Table 6.1 The fatigue tests results of LR and RR specimens.. 106

Table 10.1 Single crystal elastic constants for DS CM247LC superalloys................................... 159
Table 10.2 Plastic parameters used for DS CM247LC superalloys 159

Research Thesis: Declaration of Authorship

Print name: Yuanguo Tan

Title of thesis: Study of Fatigue Crack Initiation and Propagation Mechanisms in a Directionally Solidified Superalloy: Effects of Microstructures, Anisotropy and Oxidation

I declare that this thesis and the work presented in it are my own and has been generated by me as the result of my own original research.

I confirm that:

1. This work was done wholly or mainly while in candidature for a research degree at this University;
2. Where any part of this thesis has previously been submitted for a degree or any other qualification at this University or any other institution, this has been clearly stated;
3. Where I have consulted the published work of others, this is always clearly attributed;
4. Where I have quoted from the work of others, the source is always given. With the exception of such quotations, this thesis is entirely my own work;
5. I have acknowledged all main sources of help;
6. Where the thesis is based on work done by myself jointly with others, I have made clear exactly what was done by others and what I have contributed myself;
7. Parts of this work have been published as:

Yuanguo Tan, N. Gao, P.A. Reed The anisotropic fatigue short crack initiation and propagation behaviours of a directionally solidified (DS) superalloy CM247LC at room temperature, Fatigue & Fracture of Engineering Materials & Structures. DOI: 10.22541/au.168216306.62559044/v1

Yuanguo Tan, Nong Gao, Philippa Reed, Oxidation induced crack closure in a nickel base superalloy: A novel phenomenon and mechanism assessed via combination of 2D and 3D characterization, Materials Science and Engineering: A, Volume 861, 2022, 144311, ISSN 0921-5093, https://doi.org/10.1016/j.msea.2022.144311.

Yuanguo Tan, D.J. Bull, R. Jiang, A. Evangelou, S. Chaudhuri, S. Octaviani, F. Pierron, N. Gao, H. Toda, I. Sinclair, P.A.S. Reed, Data rich imaging approaches assessing fatigue crack initiation and early propagation in a DS superalloy at room temperature, Materials Science and Engineering: A 805 (2021) 14059, https://doi.org/10.1016/j.msea.2020.140592.

Yuanguo Tan, Ian Griffiths, Gareth Hughes, Neil Young, Nong Gao, Philippa Reed. The oxidation mechanisms for the oxidation induced crack closure in a directionally solidified superalloy, in preparation.

Signature: .... Date: ....

Acknowledgements

Time flies, and the four-year journey of pursuing a PhD has quickly come to an end. At the moment, I would like to express my appreciation for the people guiding me, supporting me and kindly criticising me.

First, my supervisors Professor Philippa Reed and Dr Nong Gao. Thanks for offering me the opportunity for being a member of their lovely research group. Over the past four years, they have put tremendous efforts to guide me how to conduct scientific research properly, inspire me to think of the research critically and taught me necessary research skills. I feel so lucky working with them.

Second, I would like to thank Dr. Diego Martínez de Luca who always solves mess for me when conducting the high-temperature fatigue tests. A strong friendship is built during the process. I also greatly indebted to the past and present members of the research group for their help, both in the research and daily life. In no order, they are Alvaro, Anqi, Ara, Ben, Corentin, Deepak, Ellis, Joe, Luke, Kieran, Mike, Songsong, Talha, Yeajin, Yousif.

I also would like to appreciate Dr Andrew Hamilton and Dr John Walker for their feedback from my 9-month and confirmation progression reviews; Aga Murch, Dr Andy Robinson, Dr Shuncai Wang from University of Southampton, Dr Neil Young, Dr Gareth Hughes, and Dr Ian Griffiths form University of Oxford for their technical support for the experiments. I also note that as part of our COVID mitigation approach to the PhD, in my first year I collated existing data from previous projects to develop further analysis, these are all acknowledged in our co-authored publications, but I would also like to thank Sari Octaviani, Dr Daniel Bull, Dr Dichu Xu and Prof. Rong Jiang for their experimental data and analysis which forms part of my thesis.

Finally, I want to express my gratitude to my family members, particularly My wife, Dr Weiwei Zhang, parents and grandparents, who always unconditionally support me. 爱你们!

Abbreviations

2D	Two dimensional
3D	Three dimensional
AOIs	Areas of interest
APT	Atom probe tomography
ASSEDD	Accumulated shear-strain energy dissipation density
BSE	Backscatter electron
CFI	Creep-fatigue interaction
COD	Crack opening displacement
COICC	Complete oxidation induced crack closure
CPFEA	Crystal plastic finite element analysis
CT	Computed tomography
DCPD	Direction current potential drop
DE	Dynamic embrittlement
DIC	Digital image correlation
DS	Directionally solidified
DVC	Digital volume correlation
EBSD	Electron backscatter diffraction
EDM	Electron discharge machining
EDX	Energy dispersive X-Ray
FCP	Fatigue crack propagation
FIB	Focussed ion beam

FIP	Fatigue indicator parameter
GB	Grain boundary
GND	Geometrically necessary dislocation
HCF	High cycle fatigue
HRS	High rate solidification
IOS	International Organization for Standardization
KAM	Kernel average misorientation
LCF	Low cycle fatigue
LEFM	Linear elastic fracture mechanism
LMC	Liquid metal cooling
NDT	Non-destructive testing
OICC	Oxidation induced crack closure
OM	Optical microscope
PBB	Plain bend bar
PSB	Persistent slip band
POICC	Partial oxidation induced crack closure
ROIs	Region of interests
SAGBO	Stress assisted grain boundary oxidation
SEM	Scanning electron microscope
SF	Schmid factor
SIMS	Secondary ion mass spectrometry
SNBP	Single notch plain bend bar
SRCT	Synchrotron radiation computed tomography

STEM	Scanning transmission electron microscope
SX	Single crystal
TB	Twin boundary
TCP	Topologically closed-packed
TMF	Thermal-mechanical fatigue
ZNSSD	Zero-normalized sum of squared differences

Chapter 1 Introduction

1.1 Background

Gas turbine engines operate under extreme conditions as super-heated pressurized gases flow over the blades. Nickel-based superalloys are selected for blade components due to their good combination of toughness, strength, oxidation resistance and creep resistance. It is found that the engine working efficiency is closely associated with the gas operation temperature, particularly increasing with the combustion temperature. Thus, turbine producers are continuously trying to develop improved superalloys that can be used at higher temperatures. This has motivated the development of the directional solidification technique.

Directionally solidified (DS) and single crystal (SX) superalloys have been replacing conventionally cast polycrystalline superalloys in many gas turbine engine components. The directional solidification technique reduces the number of grain boundaries transverse to the loading axis, considerably enhancing the creep strength in the longitudinal (L) direction (where the columnar grains are aligned with the load axis) and resulting in elastic and plastic anisotropy between both the L and T (transverse direction, where the columnar grains are perpendicular to the load axis). CM247LC superalloy is the latest development of these first-generation DS superalloys, and shows good performance under extreme temperatures and complex stress states [1-3]. This alloy shows the best creep resistance among all the first generation directionally solidified superalloys and is comparable with Rene N5 single crystal superalloys. As a result, CM247LC is widely used in turbine blade components. However, the blade material not only suffers damage from static loading (tensile or creep), it also experiences fatigue damage from the cyclic centrifugal stresses caused by any accelerating and decelerating rotation of the turbine engine. The alternating load at high temperature (usually over 650 °C) coupled with the aggressive environment usually causes combined damage arising from fatigue, creep and oxidation of the blades during the course of service. This accelerates material failure causing shorter fatigue lives and faster crack propagation rates [4, 5].

To optimize the overall fatigue-creep-oxidation performance, significant efforts have been made to assess the effects of the microstructure and service condition as well as loading modes on the fatigue behaviour of the alloys. A series of investigations have been conducted studying the low cyclic fatigue (LCF) and thermal-mechanical fatigue (TMF) behaviours, and developing fatigue-life prediction modelling In CM247LC [2, 3], there are however at least two critical issues that need to be further studied. Firstly, the microstructure effects coupled with the elastic and plastic anisotropy in the L and T directions have not been fully understood. It is widely accepted that the crack initiation and early propagation behaviour is sensitive to the microstructure that induces strain localization at room temperature [6-8]. However, in the DS alloys, the situation becomes more complex, as there exists elastic and plastic anisotropy in the L and T direction, which could be coupled with microstructure features to influence the crack growth behaviours'. Secondly, the contribution of microstructure, anisotropy, oxidation and creep to the fatigue crack initiation and propagation processes in this DS alloy at these moderate elevated temperatures has not been systematically assessed. The DS alloy will experience creep-oxidation-fatigue damage during the course of service, so establishing the contribution of each factor is important in improving the fatigue performance of this and analogous DS superalloys as well as further developing appropriate materials optimization approaches in terms of alloying design and processing techniques to improve high temperature blade performance.

1.2 Aim and objectives

The main aim of this study is to understand the fatigue crack initiation and propagation mechanisms in the DS CM247LC superalloy. To achieve this, the following broad objectives have been set:

1. To characterize the microstructure of DS CM247LC superalloy and assess the effects of microstructure as well as mechanical property anisotropy on short crack initiation and propagation at room temperature.
2. To investigate the role of oxygen in crack initiation and propagation over a range of temperatures, from which, the interlinks between oxidation, microstructure and anisotropy are revealed.
3. To systematically establish the effects of microstructure, anisotropy, oxidation and creep on crack growth behaviour by introducing different frequency and dwell times during fatigue crack growth.

Chapter 2 Literature review

2.1 Nickel based (Ni-base) directionally solidified (DS) superalloys

Superalloys are generally based on an austenitic metallic material, based on nickel, cobalt, and iron. They are widely used in aero-engine and power generation turbomachinery due to their high strength at elevated temperature, excellent fatigue and creep resistance and good corrosion resistance. These properties are required as they experience extremes of temperature and complex loading conditions in service. Based on the composition of the matrix, superalloys can be divided into Ni-based, Co-based and Fe-based superalloys, among which Ni-based superalloys possess better chemical composition and phase stability as well as higher strength at elevated temperature. Thus this class of alloy is mostly used as aero-engine components shown in Fig. 2.1 [9].

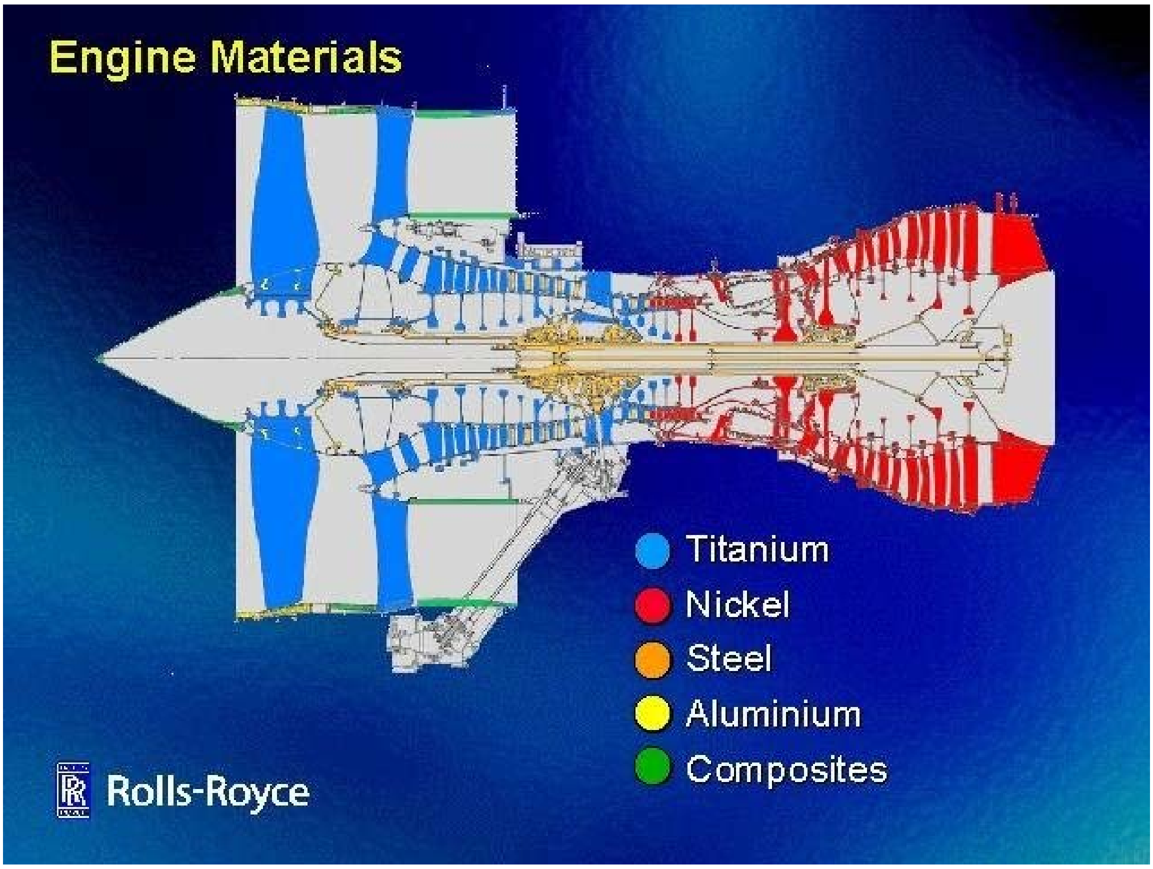

Fig 2.1 The different materials used in a Royal Royce jet engine [9]

Ni-based superalloys can be further divided into three categories: wrought, powder metallurgy and cast, according to their manufacturing process. Generally, wrought and powder metallurgy alloys are used in disc components, as these alloys possess finer grains and generally superior fatigue resistance. Cast superalloys possess excellent strength and creep resistance at elevated temperatures, and hence are usually used in blade components, serving at higher temperatures [10]. With the development of directional solidification techniques, conventional cast superalloys are gradually being replaced by directionally solidified (DS) columnar and single crystal (SX) superalloys [11]. Superalloys manufactured by directional solidification possess fewer grain boundaries (GBs) transverse to the primary loading axis (Fig. 2.2 [9]), giving an improved creep resistance in the longitudinal (L) orientation and resulting in the highly anisotropic property. Moreover, the high yield stress in the L orientation (<001> solidification direction) enhances the low cycle fatigue (LCF) resistance in displacement-control conditions [3, 12-14]. As a result, DS and SX superalloys have increasingly been used for advanced turbine blade components in recent years.

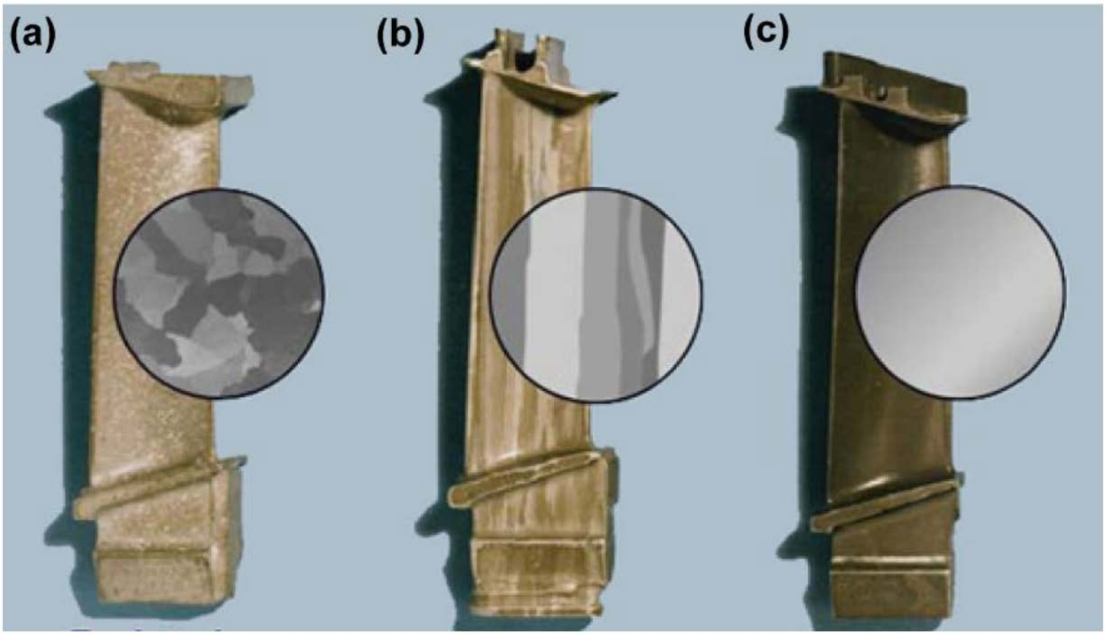

Fig 2. 2 Blades and the grain structure. (a) Conventional cast blade with equiaxed crystal structure, directionally solidified blade with (b) columnar grains and (c) single crystal blade [9]

The composition of some DS superalloys are listed in the Table 1.1. The number of alloying elements exceeds 10, consequently leading to the complex microstructures of the superalloys. Reported in [10], the elements play different roles in the materials according to their position within the periodic table. Elements with similar atomic radius to nickel (Ni), such as cobalt (Co), chromium (Cr), ruthenium (Ru), molybdenum (Mo), rhenium (Re) and tungsten (W) tend to partition to the austenitic γ, stabilizing and solution strengthening the matrix. In comparison, the elements with obviously greater radius, including aluminium (Al), titanium (Ti), niobium (Nb) and tantalum (Ta) preferentially form the significant strengthening phases $Ni_3(Al, Ta, Ti)$, known as γ'. Other trace elements, like carbide (C), boron (B) and zirconium (Zr) promote the formation of carbides and borides at the grain boundaries (GB) and inter-dendritic regions. Compared with other DS superalloys, the most notable compositional features of CM247LC (the target material in the current work) is it has the highest content of W and lowest content of C. The role of these two elements in the material is further described in the following section introducing the superalloy DS CM247LC.

Table 2.1 The composition of some DS superalloys (in wt.%) [15, 16]

Alloy	Cr	Co	Mo	W	Al	Ti	Ta	Nb	Re	Hf	C	B	Zr	Ni
CM247LC	8.0	9.0	0.5	10.0	5.6	0.7	3.2	-	-	1.4	-	-	-	Bal.
CM186LC	6.0	9.0	0.5	8.0	5.7	0.7	3.0	-	3.0	1.4	-	-	-	Bal.
CMSX-4	6.5	9.0	0.6	6.0	5.6	1.0	6.5	-	3.0	0.1	-	-	-	Bal.
MAR M002	8.2	10.0	-	10.0	5.5	1.5	2.5	-	-	1.5	0.2	-	-	Bal.
PWA 1426	6.5	12.0	2.0	6.0	6.0	-	4.0	-	3.0	1.5	0.1	-	-	Bal.
Rene′80H	14.0	9.0	4.0	4.0	3.0	4.7	-	-	-	0.8	0.2	-	-	Bal.
Rene′142	6.8	12.0	2.0	5.0	6.2	-	6.0	-	3.0	1.5	0.1	-	-	Bal.
GTD 111M	14.0	9.5	1.6	3.8	3.0	4.9	2.8	-	-	1.5	0.1	-	-	Bal.

2.1.1 Manufacturing process of Ni-base DS superalloys

2.1.2.1 High-rate solidification (HRS, Bridgman Method) process

High rate solidification (HRS) is the most widely used directional solidification technique in industry, and a large number of turbine blades and guide vanes are produced by this technique [14].

The HRS process is shown in Fig. 2.3 (a) [14]. The ceramic shell is set on a cooling-chill copper plate, surrounded by a graphite heater. At the bottom of the heater, there is an insulation baffle and a water-cooled jacket. The insulation baffle inhibits the heat radiation from the graphite heater. The rod lifter at the bottom drags the ceramic shell down together with the copper plate, causing heat flow from the melted alloy diffusing to the cooling-chill copper plate in the early stages of directional solidification. During solidification, the heat flow is dissipated to the water-cooled jacket through heat radiation, and a high temperature gradient is formed at the solid-liquid interface, hence guaranteeing the melted alloy will nucleate and grow along one direction (the <001> direction).

However, with the increase of casting scale, as larger and larger turbine blades are manufactured, the temperature gradient at the solid/liquid interface is decreased even during the process of HRS, leading to a large number of defects in the casting. Researchers found changing process parameters such as drag rates, furnace temperature, had little effect on limiting defect formation [17, 18]. This is because the larger-scale casting has a higher level of heat exchange with the air, decreasing the temperature gradient at the solid/liquid interface. Fig. 2.3 (b) [14] shows that in the HRS process, the process window is very narrow (the grey ellipse in Fig. 2.3 (b) [14]), where the formation of defects is largely eliminated. For large-scale castings, especially turbine blades, the process window is further narrowed, due to the lower temperature gradient achieved at the solid/liquid interface and the stricter requirement on limiting defect volume fraction, size and morphology.

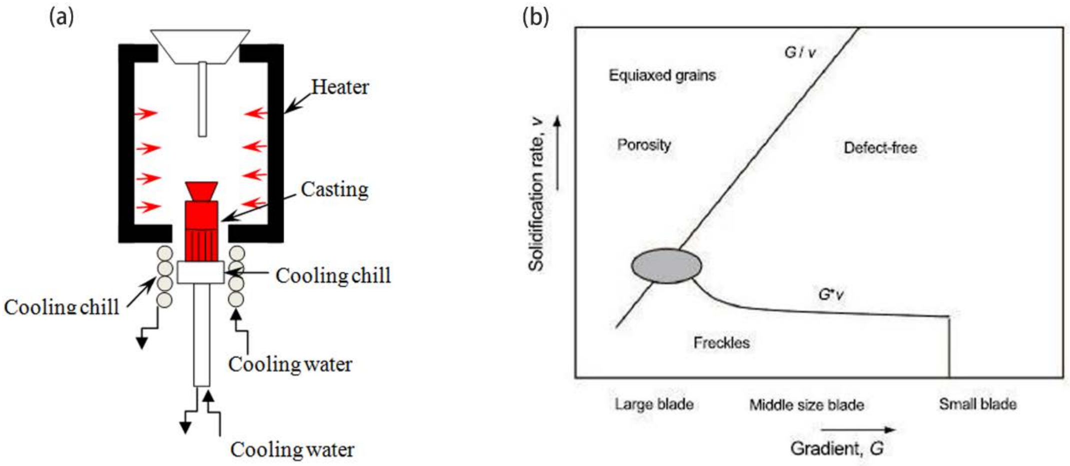

Fig 2.3 (a) Equipment for the traditional HRS process, (b) Casting defect map for the traditional directional solidification process showing the narrow operation window for large IGT blade manufacturing [14]

2.1.2.2 Liquid metal cooling (LMC) process

To successfully produce large-scale and high-quality blades, some newly developed directional solidification techniques have emerged. Liquid metal cooling (LMC) is one of these new high-rate solidification processes [19, 20]. The process adopts liquid Al or Sn as the cooling medium, which enhances convective heat transfer and minimizes heat radiation. These metals are characterized by a low melting point, high thermal conductivity, high evaporation in a vacuum temperature, the lack of toxicity, and low price [21]. The melt is continuously stirred and maintained at a constant temperature. The approach is shown in Fig. 2.4 [14]. During the solidification process, the ceramic shell and cooling chill plate are moved with set speed from the heating furnace to the tank with a low-melting-point liquid metal. This technique reduces the heat radiation via air and hence increases the temperature gradient at the solid/liquid interface. DS superalloys produced by this technique contain far fewer defects and are not limited by the scale of the component. In addition, the directional solidification process facilitates a higher cooling rate, subsequently obtaining a finer dendritic structure in the superalloy.

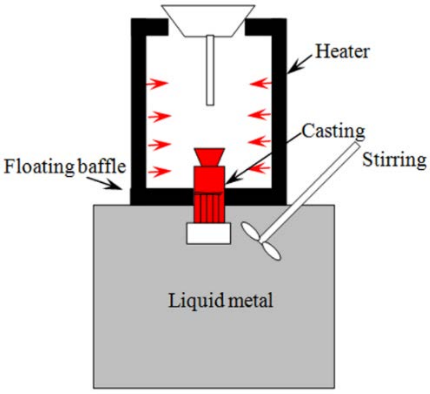

Fig 2.4 Equipment of LMC process [14]

2.1.2 Microstructures of Ni-base DS superalloys

2.1.2.1 Columnar grains

As mentioned in the manufacturing process, the perpendicular temperature gradient from heating furnace to the cooling tank causes the growth of columnar grains. The morphologies of the columnar grains are shown in Fig. 2.5 [22] showing the view of longitudinal and transverse cross-sections. The <001> crystallographic orientation is the most favourable grain growth direction aligned with temperature gradient in the cubic-structure alloys [23], and the other slower orientation is overgrown by the <001> orientation. Thus, all the grain elongation direction of the columnar grains are <001>. The grain orientation of the secondary direction (transverse to the growth direction) is random due to the temperature gradient being nondirectional.

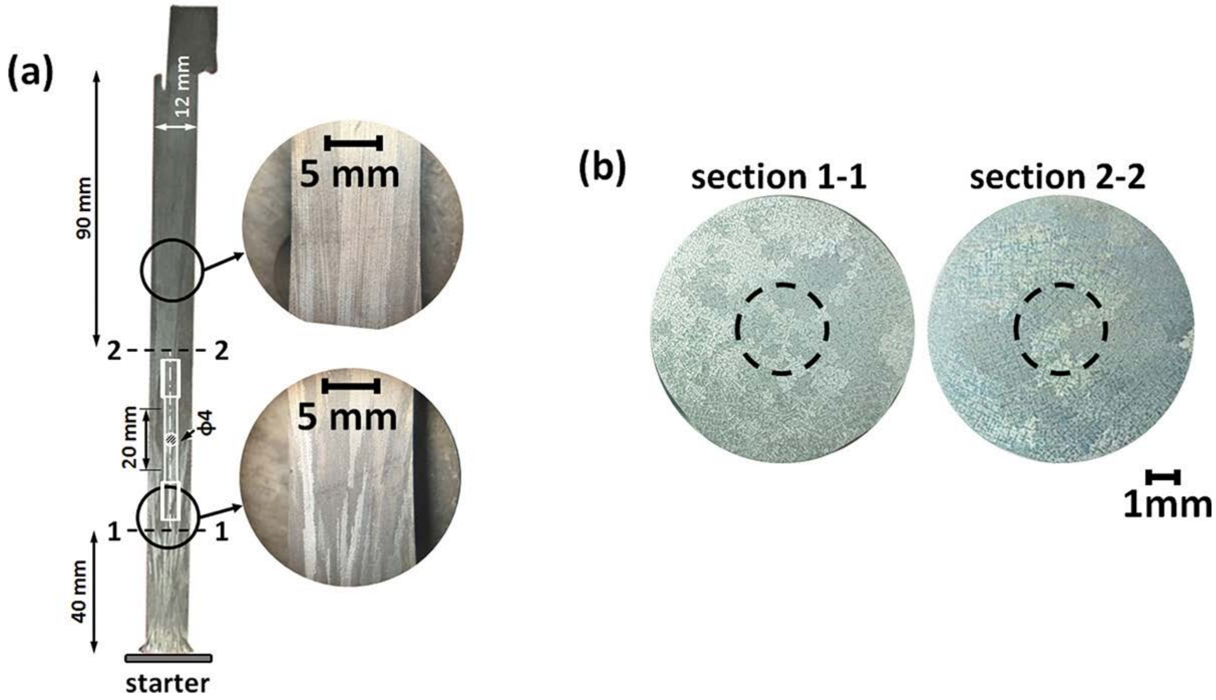

Fig 2.5 Grain structure of (a) longitudinal section, (b) cross section 1 – 1 and 2 – 2 marked by the dashed line [22]

The dendritic structures formed in the columnar grains shown in Fig. 2.6 [24]. The dendrites are white in colour, while the inter-dendritic regions are dark in colour due to the elemental segregation of Nb, Ta, W and Mo as well as some potential secondary precipitates, such as Laves phase, Delta phase and μ phase [25, 26]. In the longitudinal section, the primary dendrites are generally aligned with the solidification direction. However, it can be seen that some of the dendrites deviate from the solidification direction by a few degrees [27, 28]. This deviation could be caused by many factors, one of which is the theoretical temperature gradient is not achieved in the manufacturing process. Another reason is correlated to the competing mechanisms of grain growth. Gandin et. al [29] found the deviation of crystallographic orientation is at a minimum for the grains near the surface of the chill, but reaches 0.21 rad (12 degree) at the position 2 mm away from the surface.

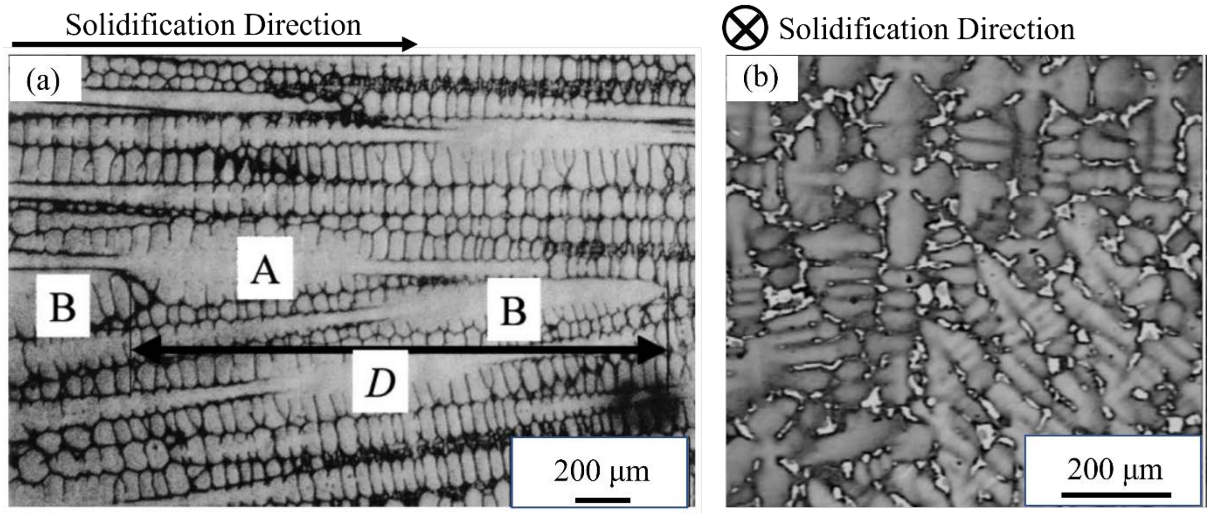

Fig 2.6 The morphology of dendrites along the longitudinal (a) and cross (b) sections [24]

2.1.2.2 Precipitates

Precipitates are largely formed and distributed at the interior of the grains or grain boundaries, dendrites or inter-dendritic regions, due to the large amounts of elements added to the DS superalloys. The effects of these precipitates are complicated, and for instance, whilst γ′ is known for strengthening the materials, some other minor precipitates, particularly at the grain boundaries, act as crack initiation sites during deformation processes [30, 31]. Herein, the roles of some common and important precipitates are introduced.

(I) Gamma prime (γ′): γ′ is the main strengthening phase in DS superalloys [32]. The structure of γ′ can be defined as Ni_3Al, although in some alloys [25], elements titanium (Ti) and niobium (Nb) can partly replace the Al in the crystal structure, forming $Ni_3(Al, Ti, Nb)$. Other elements such as tantalum (Ta), hafnium (Hf) can also substitute into the γ′ and strengthen the phase further. The crystal structure of the phase is an ordered face centred cubic structure ($L1_2$) with a lattice constant, between 0.352 and 0.360 nm [10]. The morphologies of the precipitates are strongly dependent on the lattice misfit (δ) between γ′ and γ matrix. According to Nathal [33, 34], when the absolute value of δ is in the range of 0.1% to 0.5%, cubic γ′ will form (Fig. 2.7 (a)). On the other hand, when δ is below 0.1% or above 0.5%, spherical or irregular-shaped γ′ will be formed respectively shown in Fig. 2.7 (b) and (c). The optimal morphology of the precipitates is cuboidal, as the elastic strain field is formed at the interface, blocking dislocation motion and enhancing the strength. The ideal size of the precipitates in these blade materials appears to be around 500 nm [33, 35], which could provide high yield stress as well as extended creep rupture life. The volume fraction of γ′ is expected to be around 60% to 70% in DS superalloy, and with a further increase of γ′ volume fraction, the overall plasticity will decrease due to the reduction of γ channel width. The phase is designed to be homogeneously distributed in the material. However, influenced by the solidification sequence and element segregation, the γ′ at the dendrites have a more irregular shape and larger size [36]. Thus, solution and precipitation hardening heat treatment are largely studied and designed to reduce the heterogeneous distribution of the γ′.

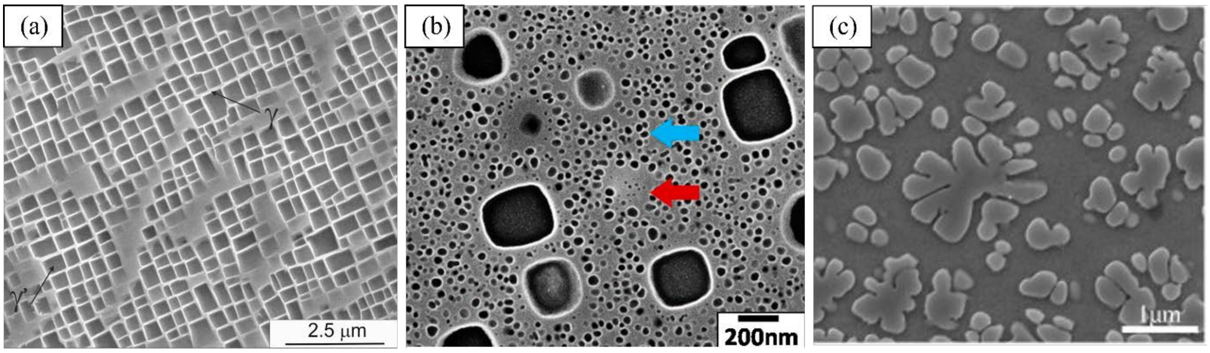

Fig 2.7 the morphology of gamma prime: (a) cubic; (b) spherical; (c) irregular shape [37-39]

(II) Carbides: carbides are another common and important precipitate in DS superalloys. Generally, three types of carbides are most likely to form during the solidification or heat treatment process: MC, M_6C and $M_{23}C_6$ [40]. MC-type carbides usually have a face-centred cubic structure with high density and strength. The lattice constant is in the range of 0.418 ~ 0.468 nm. M refers to a range of possible metal elements, including Hf, Zr, Ta, Nb, Ti, V, and a certain amount of W and Mo. MC type carbides are primary carbides precipitated during the solidification process, and their morphology depends on the cooling rate. Normally, a higher cooling rate (around 50 μm/s) results in script-like morphology, in comparison, a lower cooling rate (at 0.5 μm/s) leading to blocky MC carbides in a DS superalloy [27]. Wasson *et al.* [41] compared the effects of MC carbide morphology on mechanical properties of a SX superalloy (CMSX-4), and they found that the formation of script-like carbides acted as crack initiation sites and decreased the high cycle fatigue (HCF) life at 850 °C, while blocky carbides resulted in longer fatigue lifetime. Therefore, blocky MC carbides are preferred than script-morphology MC carbides. During heat treatment or service life, primary MC-type carbides could be transformed to secondary M_6C and $M_{23}C_6$-type carbides (both with complicated face centred structures), which depends on the temperature and amount of W, Mo, Cr [9]. M_6C type carbides tend to form in the alloys with a high content of W, Mo at the temperature range from 850° C to 1210 °C. $M_{23}C_6$ type carbides form at a lower temperature range from 650 °C to 1050 °C, when superalloys contain a high content of Cr. Both M_6C and $M_{23}C_6$ type carbides tend to be precipitated at grain boundaries in the form of blocky shapes. The opinions regarding the effects of M_6C and $M_{23}C_6$ are somewhat mixed, but the general view is that carbide particles precipitated at GBs (in a fine distribution) are beneficial through preventing crack initiation in creep tests [10, 42].

(III) Other: Topologically closed-packed (TCP) phases are minor phases that form in DS superalloys [10, 43]. During the solidification and heat treatment process, some solution strengthening elements such as Cr, Mo, W, Ru tend to segregate together and form TCP phases. Common TCP phases include: Laves phase, μ phase, σ phase, etc. Although the proportion of these phases is small, their influence on mechanical properties is significant. These phases usually have plate-like or needle-like structures and exhibit undesirable, brittle characteristics, hereby serving as crack initiation sites. In addition, most of the TCPs deplete strengthening elements from the microstructure, decreasing the strength of the superalloys.

2.1.2.3 Pores

Defects like freckles, block structures and pores are always produced in the casting process of the DS superalloys [44], among these, pores have been widely studied, having significant detrimental effects on mechanical properties, particularly resistance to fatigue. As reported in [45], porosity is mainly formed during the solidification and heat treatment processes. Pores produced during solidification are irregular in shape, located at inter-dendritic regions. They are formed due to the overlapping of inter-dendrites preventing the flowing of melt. The potential explanation of pore formation in the heat treatment process is the well-known Kirkendall mechanism [46]. The diffusion rate of elements with higher atomic number such as Cr, Co, W, is lower than of elements such as Al and Ti, leading to the formation of vacancies, finally agglomerating into pores. Due to this element segregation, for instance, the Cr, Co and W tend to diffuse from dendrites to the inter-dendritic region, while Al and Ti diffuse in the opposite direction, pores are again mainly formed at the inter-dendritic regions. Many studies have revealed that pores generally act as stress concentration and fatigue crack initiation sites, and their effects are closely correlated to their size, shape and locations [47-50]. However, most of these research studies have been limited to evaluating the role of pores in two dimensions (from surface or fractography observations), which might introduce errors in understanding the interlinking between pores and fatigue crack initiation processes. Jiang et. al [51] proposed to correlate the three-dimensional tomography of pores to the strain field. They found that the highest strain localization site (causing crack initiation) was not at the surface plane of the pore but at the ridge in depth.

2.1.3 Elastic and plastic anisotropy in Ni-base DS superalloys

DS superalloys possess elastic and plastic anisotropy between their longitudinal (along the columnar grain elongation direction, termed as L) and transverse (perpendicular to the columnar grain elongation direction, termed as T) directions. The alloys are approximately isotropic in the transverse direction (T), as the grains are randomly distributed in this direction, (although it should be noted they are still relatively large grains, typically several hundred micro-meters). Shi et al. [52] conducted a detailed analysis on the elastic and plastic anisotropy of a DS superalloy – DZ125. Their results showed that materials tested along the L direction possess lower elastic modulus but higher yield stress than materials in the T direction at temperatures ranging from 20 °C to 850 °C (as shown in Fig. 2.8 [52]).

The difference in elastic modulus is thought to be attributed to the anisotropy of the GBs [69]. When the loading is applied in the T direction, the grain boundaries between the columnar grains will experience strain mismatch and deform which produces boundary dislocations. The introduction of boundary dislocations causes further local lattice distortion around the dislocation lines, and thus the deformation energy required increases accordingly. Compared to the L direction which only has a few grain boundaries parallel to that loading direction, the stress needed for a given strain along the T direction is therefore bigger. Therefore, the measured elastic modulus in the T direction is higher than in the L direction. Moreover, due to the absence of many grain boundaries in the L direction, the ability to resist localised fracture is improved (GBs always act as crack initiation sites due to the localized stress at their vicinity), which might be the reason that the yield stress of the L direction is higher than T direction [52]. In another study, they proposed that the discrepancy in yield strength is attributed instead to the crystal orientation [53]. In the L <100> direction, there are 8 equally loaded slip systems (more than any other crystal directions), which enhances the resistance to plastic deformation. The mechanism for the elastic and plastic anisotropy is still under investigation, but the effects of anisotropy on DS superalloys fatigue performance have been confirmed in many research studies [2, 3].

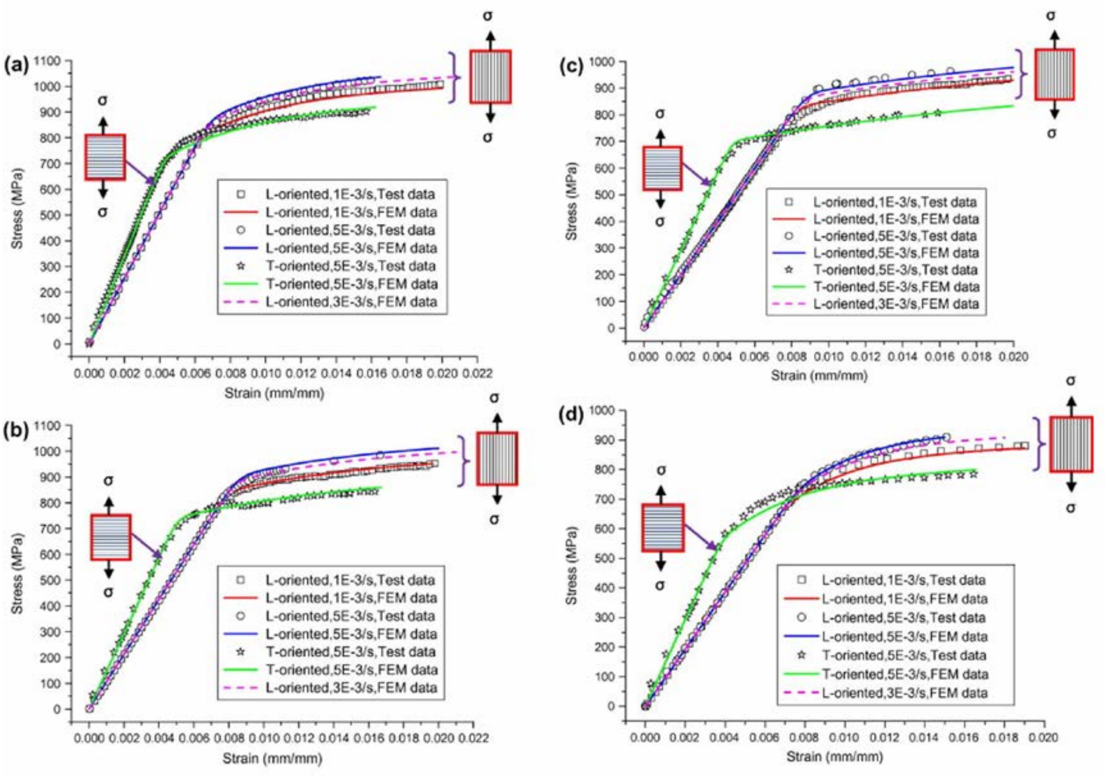

Fig 2.8 The experimental and predicted tension data of DZ125 superalloy at 20 °C (a), 650 °C (b), 760 °C, (c) and 850 °C (d) [52]

2.1.4 DS CM247LC superalloy

DS CM247LC superalloy was first developed by Cannon-Muskegon Corporation and is extensively used in turbine blades and vane applications. The alloy is developed from the parent alloy MAR-M 247LC. The chemical composition change from Mar-M247LC to CM247LC is detailed in the study by Erikson [54]. This showed that the reduction in C considerably improved DS grain boundary cracking when compared with the parent alloy. This change was offset by tailoring the W and Mo content. The improved cracking resistance resulted from the additional reduction in composition of elements such as B, Si, and Zr, without compromising strength. The addition of Cr and Al enhances corrosion resistance. Moreover, the alloy has a relatively low Hf ingot content (1.4%), which allows for a very clean casting. This is in contrast to similar DS alloys with higher (>1.5%) Hf content which exhibits a greater number of inclusions due to high rates of reactivity with some ceramics used in the casting process [55]. The average composition of DS CM247LC alloy and other similar Ni-based superalloys are shown in Table 2.1.

The standard heat treatment regime for the alloy is a solutioning heat treatment at 1220 °C, 1232 °C, 1246 °C and 1260 °C and a two-step aging process at 1080 °C and 870 °C with air cooling following each heating step. The solutioning heat treatment provides an increased volume fraction of fine γ′ particles and has the effect of homogenizing the as-cast structure. The two-step aging is a precipitation hardening process, modifying the size and morphology of γ′ phase [2].

Like most other Ni-based superalloys, the DS CM247LC alloy is a dual phase intermetallic, mainly consisting of γ matrix and γ′ strengthening precipitations. The primary component of the γ phase is Ni, yielding significant strength and corrosive resistance at high temperatures. The γ′ is the main strengthening phase of the alloys, which provides high yield and tensile stress at operating temperatures [35]. The γ′ of DS CM247LC alloy is approximately 500 nm in cuboidal shape. The volume fraction of the phase is nearly 60%, which is relatively standard among turbine blade Ni-base superalloys. While a high volume fraction of γ′ is desirable for high yield and tensile strengths at operating temperatures, the creep strength of pure γ′ is poor [3]. Additionally, with increasing volume fraction, finer γ′ particles can also be found. These are not stable for long at high temperatures (982°C and above) and have a tendency to dissolve into the matrix at these temperatures [2].

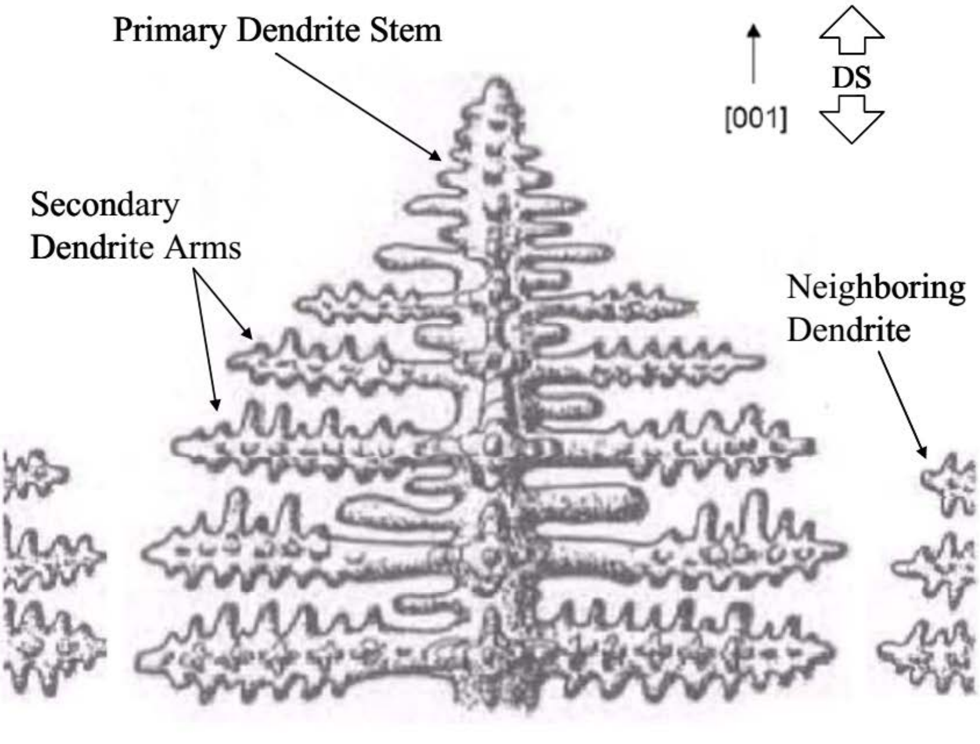

Fig 2. 9 Depiction of typical dendritic structure within the grains of DS Ni-base superalloys [56]

MC-type and $M_{23}C_6$-type carbides are precipitated in the alloy. Primary MC-type carbides are precipitated in script-like or blocky shape during the solidification process, distributed in the inter-dendritic region and GBs, while $M_{23}C_6$-type carbides are mainly precipitated in dot-like shapes during the heat treatment process at GBs. The existence of M_6C-type carbides of the alloy is debatable, as Robert et al. [2] found they could be precipitated along with $M_{23}C_6$-type at GBs, while Jeong et al. [57] found this type of carbide is only formed in long-term thermal exposure at least over 1000 h. In addition, according to Jeong's investigation [57], TCP phases were not formed in the alloy even with the thermal exposure time exceeding 10000 h.

The large columnar grains that form in the alloy, with a diameter around 500 μm, are a result of the slow cooling process during solidification. The dendritic structure which forms within grains during solidification is illustrated in Figure 2.9 [56]. The collective columnar structure of the primary dendrites is thought to serve as a fracture toughening mechanism, which temporarily arrests propagating cracks or prevents crack coalescence [2].

2.2 Fatigue behaviours of Ni-base superalloys – findings and challenges

2.2.1 Fundamental conceptions of fatigue

Fatigue is referred to as a failure mode of materials that occurs under cyclic loading. In 1964, materials fatigue was defined as the mechanical property variation in metals under alternating strain or stress by the International Organization for Standardization (IOS). This definition is also applicable to non-metallic materials. Most machinery parts and engineering structures in transportation, aviation and power industries serve under alternating loading, and fatigue damage can be an important failure mode [58, 59]. Approximately 90% of the failures reported in non-static industrial components are caused by fatigue. Superalloys serving as engine components in aircraft or power generation plants work under extremes of temperature and cyclic loading conditions. Understanding and predicting the fatigue performance of materials is clearly important, in light of the benefits to safety, performance and subsequently the economy.

Generally four important parameters are employed to describe the fatigue cyclic loading [59]. These parameters are defined as follows, taking a simple case of a sinusoidal load, as shown in Figure 2.10 [59].

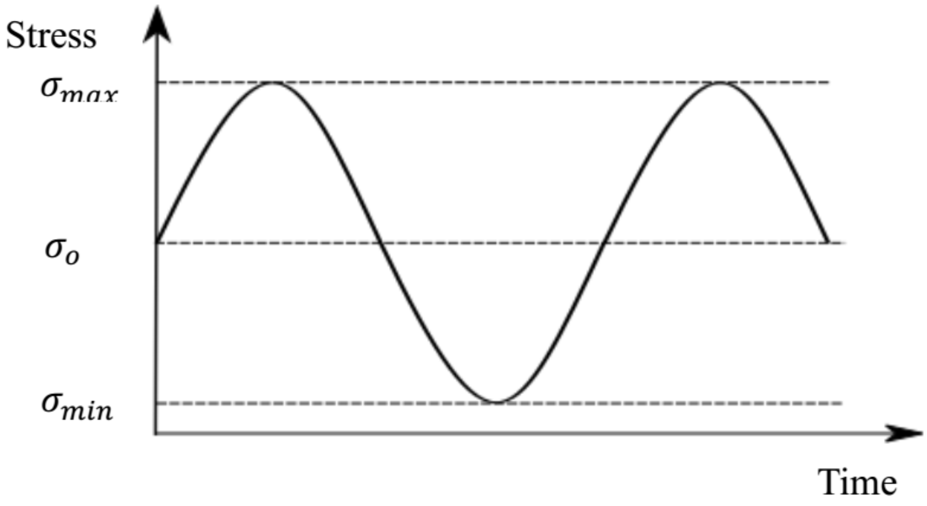

Fig 2. 10 Schematic of a typical fatigue cycle under sinusoidal loading [59]

Mean stress: $\sigma_0 = \frac{\sigma_{max} + \sigma_{min}}{2}$ (2.1-a)

Mean strain: $\varepsilon_0 = \frac{\varepsilon_{max} + \varepsilon_{min}}{2}$ (2.1-b)

Stress amplitude: $\sigma_a = \frac{\sigma_{max} - \sigma_{min}}{2}$ (2.2-a)

Strain amplitude: $\varepsilon_a = \frac{\varepsilon_{max} - \varepsilon_{min}}{2}$ (2.2-b)

Stress range: $\Delta\sigma = \sigma_{max} - \sigma_{min}$ (2.3-a)

Strain range: $\Delta\varepsilon = \varepsilon_{max} - \varepsilon_{min}$ (2.3-b)

Load (stress) ratios: $R = \frac{\sigma_{max}}{\sigma_{min}}$ (2.4-a)

Strain ratio: $R = \frac{\varepsilon_{max}}{\varepsilon_{min}}$ (2.4-b)

Three fracture loading modes are defined for the fatigue process, as shown in Fig. 2.11 [60]. Mode I is the opening mode where the applied loads are perpendicular to the crack faces and the crack faces separate in a direction normal to the plane of the cracks. Mode II is called the in-plane shear mode, where the loads are applied along the planes of the crack and the crack faces are sheared in a direction normal to the crack front. Mode III is the tearing or anti-plane shear mode, where the loads are again applied in the plane of the crack but the crack faces are sheared parallel to the crack front.

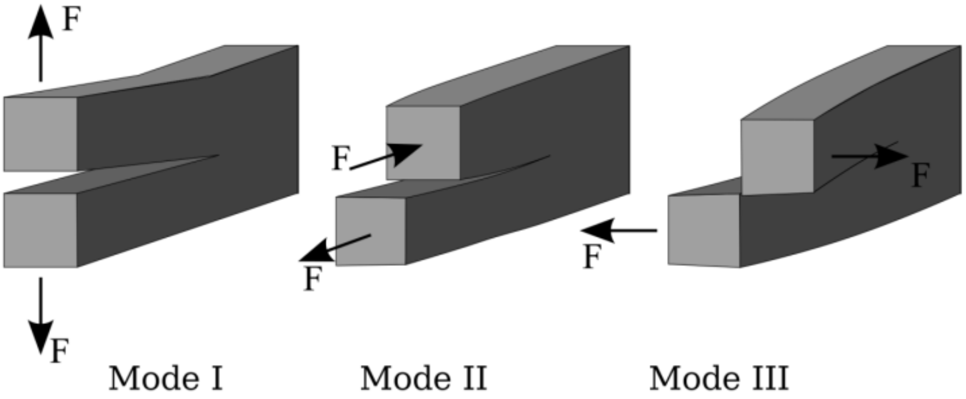

Fig 2.11 Schematic representation of the three fundamental crack-opening modes: (a) opening mode, (b) in-plane shear mode, and (c) anti-plane shear mode [60]

2.2.2 Fatigue life approach

2.2.2.1 Total life approach

The S-N curve is the earliest approach taken to describe the relationship between life time and applied stress or strain amplitude [61]. One typical S-N curve is shown in Fig. 2.12 [62]. The fatigue life limit is defined in terms of the stress amplitude, where the fatigue life is infinite (or exceeds 10^7 cycles, which is termed the endurance limit). This stress-life approach is used more for high-cycle-fatigue (HCF) conditions, where the strain amplitude is very low and elastic deformation controls the fatigue damage. In low-cycle fatigue (LCF) conditions, where a relatively large strain amplitude is applied, the cyclic plastic deformation is the main parameter controlling the damage mechanism and the strain-life curve is found to be more applicable.

In 1910, Basquin [63] found the relationship between stress amplitude and fatigue life (S-N curve) could be linearized under full log coordinates. Thus, the exponential description of fatigue lifetime is established following equation 2.5:

$$\frac{\Delta\sigma}{2} = \sigma_\alpha = \sigma_f'(2N_f)^\beta \tag{2.5}$$

where σ_f' is the fatigue strength coefficient, N_f is the cycle to failure and β is the fatigue strength exponent. Similarly, Coffin and Manson [64, 65] found the exponential relationship between applied strain amplitude and fatigue life, and described it in the following equation 2.6:

$$\frac{\Delta\varepsilon_p}{2} = \varepsilon_\alpha = \varepsilon_f'(2N_f)^c \qquad (2.6)$$

where ε_f' is the fatigue ductility coefficient, and c is the fatigue ductility exponent.

Considering that the total strain amplitude $\Delta\varepsilon$ consists of two parts, the elastic strain $\Delta\varepsilon_e$ and plastic strain $\Delta\varepsilon_p$, a modified total-strain amplitude-fatigue life could be described following equation 2.7:

$$\frac{\Delta\varepsilon}{2} = \frac{\Delta\varepsilon_e}{2} + \frac{\Delta\varepsilon_p}{2} = \frac{\sigma_f'}{E}(2N_f)^\beta + \varepsilon_f'(2N_f)^c \qquad (2.7)$$

The total life approach is more applicable in materials with low levels of minor defects, because with an increase in defect level, the crack propagation becomes very dependent on individual defects. In such a case, the fatigue life will then show a lot of scatter even at the same strain/stress amplitude. Thus this approach is more useful in materials where crack initiation takes up a major part of fatigue life. However, most engineering materials contain flaws, and hence a damage-tolerant life approach is also an important approach to take in lifing.

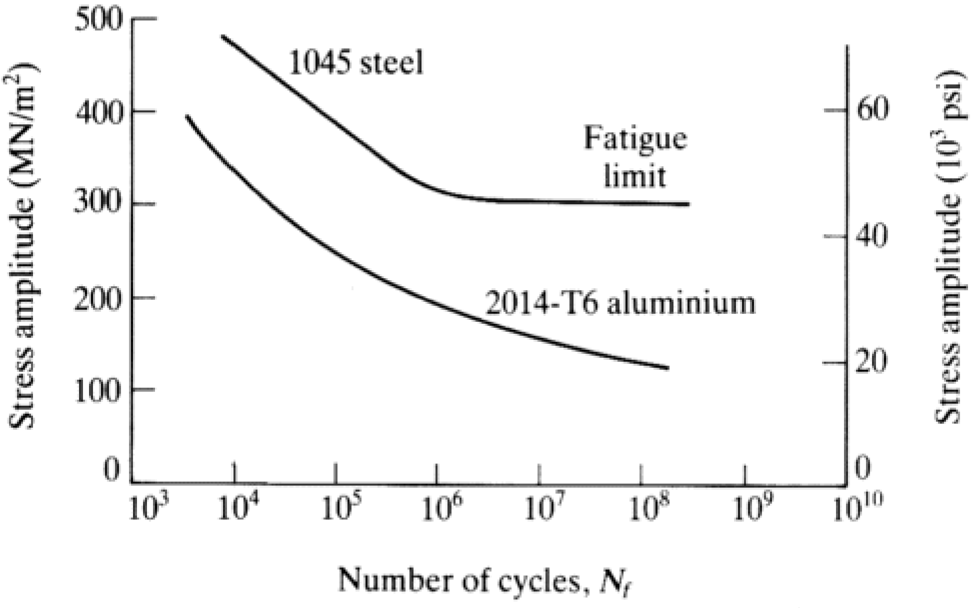

Fig 2.12 S-N curves of 1045 steel and 2014-T6 aluminium [62]

2.2.2.2 Damage-tolerant approach

The damage-tolerant approach is established on the basis that most engineering materials contain potential defects. The initial size of such defects, a_0, could be detected by non-destructive testing (NDT) techniques such as visual, dye-penetrant, X-ray techniques, etc. The safe fatigue life is then defined as the cycles of loading required to grow this defect from the initial size of defect, a_0 propagating to a critical size a_c that causes fast failure or affects compliance beyond design tolerance. Linear elastic fracture mechanics (LEFM) is the most widely-accepted damage-tolerant approach for characterizing the usable fatigue life [59, 60]. The approach aims to relate the crack growth rate to some characteristic driving force.

LEFM is used to characterise the stress field ahead of crack tips in terms of the nominal applied stress, crack length etc. Use of the approach requires that the plastic zone at the crack tip is small compared to the crack length (so that linear elastic continuum approaches apply). As shown in Fig. 2.13 [60], there is a sharp, through thickness crack of length 2a in a thin, infinite plate subjected to mode I loading. The local stress ahead of the crack tip can be expressed in polar coordinates (r, θ):

$$\sigma_{xx} = \frac{K_I}{\sqrt{2\pi r}}[cos\frac{\theta}{2}(1 - sin\frac{\theta}{2}sin\frac{3\theta}{2})] \tag{2.8}$$

$$\sigma_{yy} = \frac{K_I}{\sqrt{2\pi r}}[cos\frac{\theta}{2}(1 + sin\frac{\theta}{2}sin\frac{3\theta}{2})] \tag{2.9}$$

$$\sigma_{xy} = \frac{K_I}{\sqrt{2\pi r}}[cos\frac{\theta}{2}sin\frac{\theta}{2}cos\frac{3\theta}{2})] \tag{2.10}$$

where K_I is the stress intensity factor, defined in terms of the applied stress σ and flaw length a as:

$$K_I = \sigma\sqrt{\pi a}f(\frac{a}{\pi}) \tag{2.11}$$

where $f(\frac{a}{\pi})$ is the compliance function which allows for differing component geometry and shape.

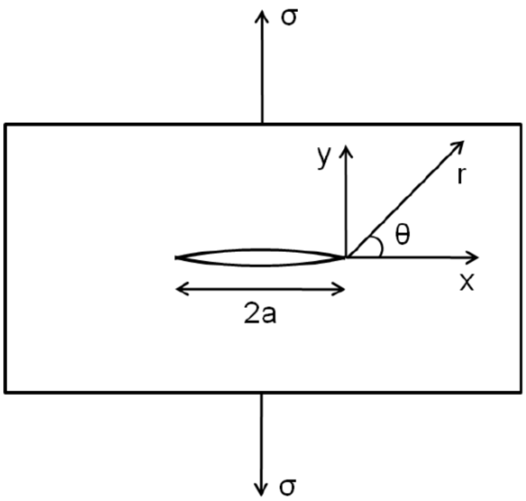

Fig 2.13 Sharp crack in a thin elastic plate [60]

It is worth noting that the stress intensity tends to infinity as r approaches zero according to equation (2.11). However, this is inconsistent with the plastic yielding of materials which will occur and that makes LEFM invalid in describing very near crack-tip stress/strain states, although K will describe the local crack tip stress state further away from the plastically yielded regions. The concept of stress intensity factor is adopted in fatigue theory to describe the relationship between crack growth rate and crack driving force in terms of stress intensity factor range $\varDelta K$. By plotting the fatigue crack growth rate da/dN against $\varDelta K$ in log-log co-ordinates, a sigmoidal curve is obtained which can be divided into three distinct regions, as depicted in Fig. 2.14 [60]

Region A represents the stage of crack initiation and short propagation. Thus, the stress intensity range $\varDelta K$ is low, indicating a small driving force. The minimum driving force required for a detectable (relatively long) crack length is named as $\varDelta K_{th}$. In region B, there is a quasi-linearized relationship between crack growth rate and stress intensity, indicating that the crack growth rate in the region can be described as following the Paris law:

$$\frac{da}{dN} = C\varDelta K^{m} \tag{2.12}$$

where C and m are materials-specific constants determined experimentally. In region C, the crack grows extremely fast. The onset of fast crack growth under static loading is represented by the fracture toughness K_c being reached during cycling for the loading mode in question. In this project, a $\varDelta K$–based approach is adopted to characterize the crack growth behavior, as for the DS superalloy with high yield stress, the crack tip plastic yielding zone is much smaller compared to crack length and uncracked region in the testing carried out.

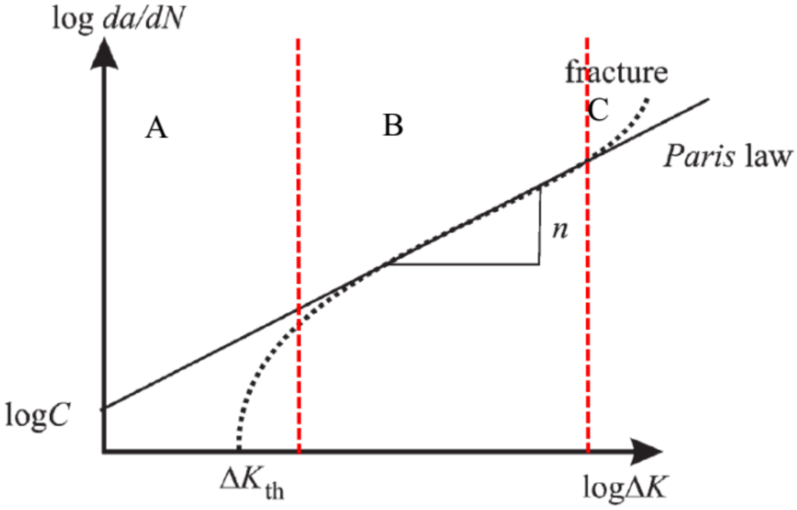

Fig 2.14 Schematic representation of the da/dN vs. ΔK in a double-logarithmic plot with the Paris law represented as a straight line [60]

2.2.3 Effects of microstructures on fatigue short crack initiation and propagation behaviours

Due to the complexity of the microstructural features of Ni-based superalloys, there are many factors interacting and influencing the short fatigue crack growth behaviours, such as slip bands, precipitates, grain boundaries (GBs) and pores. The section provides a general review of the respective effects of these microstructures on the short crack initiation and propagation behaviours.

2.2.3.1 Slip bands

Slip bands play a significant role in crack initiation during cyclic deformation and this was first reported in polycrystalline copper alloy by Ewing and Humfrey et al. [66] in 1903. They summarized the typical crack initiation behaviour within these bands as follows: firstly, heterogeneous deformation occurred within some micro slip-band structures, which is related to dislocation slip along preferential slip systems within grains. Then with the increase in loading cycles, these slip-band structures become wider and clearer under a microscope (or in later studies were observed in SEM) forming extruding or intruding band regions at the surface. In addition, the density of slip bands increases with strain/stress amplitude. Finally, this extrusion or intrusion leads to surface roughening, and hence causes crack initiation. These slip-band structures were named as persistent slip bands (PSB) shown in Fig. 2.15 [67].

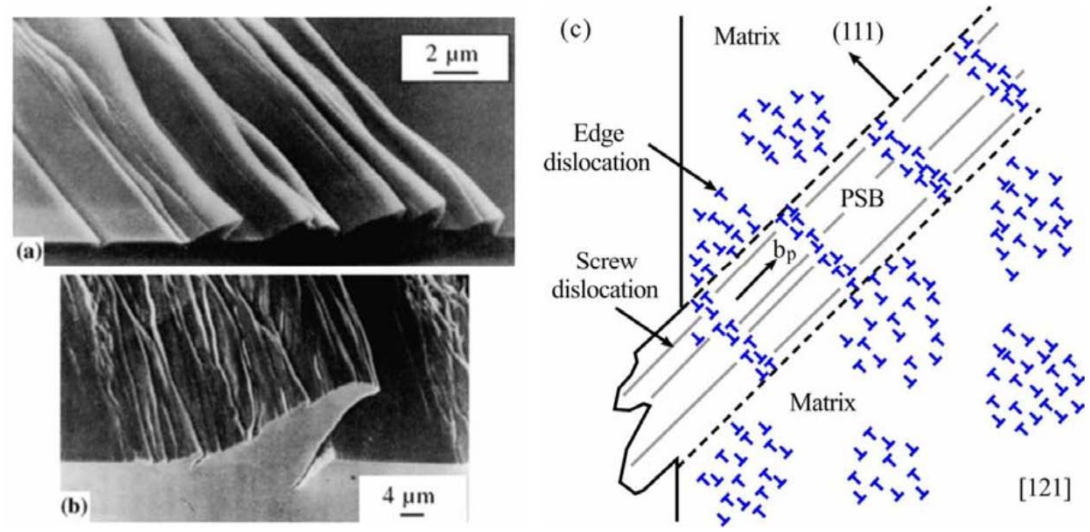

Fig 2.15 (a,b) Surface damage morphology after sharp-corner polish and then fatigue; (c) mechanism of PSB extrusion and intrusion [67]

Slip band cracking under cyclic deformation was also found in nickel based superalloys. Dislocations are believed to move forth and back within these slip bands during cyclic deformation, leading to a dissolution of γ' precipitates, degrading the material's strength. As a consequence, cracking occurs along the slip band. Jiang et al. and Stinville et al. [68, 69] further studied formation of PSBs (or slip bands) using digital image correlation (DIC) coupled with electron backscatter diffraction (EBSD) characterization. They found slip band formation is closely related to the activated slip systems with the highest Schmid factors (Schmid factors are used to determine the resolved shear stress operating on each slip system). However, a few of these cracks might not be initiated from the slip bands with the maximum Schmid factor, due to the coupled effects of other microstructure features. For instance, cracks are observed initiated from the slip bands parallel to the twin boundaries (TBs) instead of the slip bands with the maximum Schmid factor.

The propagation of the fatigue short crack is predominantly controlled by the slip systems in the SX superalloys [70, 71]. The fatigue crack tends to grow along one of the octahedral slip systems, usually with the maximum Schmid factor. Due to the high symmetry of the octahedral slip systems, a secondary slip system with similar Schmid factor might be also activated, when loading in some specific crystallographic orientation [72], such as [001] and [111]. However, the crack might not follow the secondary slip system at the beginning of the propagation, but with crack growth, the stress intensity factor ahead of the crack tip is increased. Some secondary cracks are initiated along the secondary slip systems and coalesce with the primary crack, forming zig-zag cracks. The formation of a secondary crack ahead of the primary crack retards the original crack growth rate, but when the coalescence occurs, the crack length of the original crack will be increased suddenly. This crack propagation behaviour somewhat explains the scattered short crack growth rate. In DS superalloys, relevant research studies are quite few, and the situation should be more complicated, as the crack needs to propagate from one columnar grain to another grain. The crack is not only controlled by the slip system in the first grain, but also affected by the GBs, similar to that observed in the polycrystalline superalloy [73, 74]. Although it should be noted there is crystallographic texture and distinct grain anisotropy, with very large grains, so only a few grain boundaries will be encountered in these systems compared to most polycrystalline systems. The detailed mechanism of crack propagation at the vicinity of GBs is in the section 2.2.3.3 introducing the role of GBs.

2.2.3.2 Precipitates

Introduced in section 2.1.4, the precipitates in CM247LC are γ' and carbides, and hence the roles of the two phases in fatigue performance of the alloy are focussed. γ', known as the main strengthening precipitate in superalloys, is closely associated with slip band cracking. As the dislocations slide along the slip systems, gamma prime precipitates prohibit their movement, and thus the dislocations are piled up at the interface between γ and γ' as shown in Fig 2.16 (a) [75]. In this case, the resistance to forming slip bands and subsequent crack initiation is increased [75]. With the increase of fatigue cycling, dislocations could cut into the γ', forming anti-phase boundary or stacking faults [76, 77], which in turn increase the difficulty for dislocations to move into the precipitates shown in Fig. 2.16 (d) [75]. Therefore, gamma prime generally plays a role in resisting short fatigue crack initiation and propagation. Similar results have been reported in the study of Pang et. al [78]. Careful comparison of the short fatigue crack initiation and propagation behaviours are performed in superalloys U720Li, with different microstructures achieved by appropriate heat treatments. It shows that the fatigue crack growth rates decrease with the increasing size and amounts of secondary and tertiary γ' due to the associated increase in material strength. Care should be taken since the strength of the superalloys could be decreased by further increasing the size of γ', as the interaction between dislocations and γ' changes from cutting (by weakly coupled and strongly coupled dislocations) to bowing [10]. Therefore, the increase in resistance of crack propagation with the size of γ' should be true only over a certain range of γ' size. Studies showing the effects of γ' morphology on fatigue crack initiation and early propagation behaviours are extremely limited. The difficulty lies in adjusting the morphology of the phases without any associated changes in the size and volume fraction, and apparently the latter two factors play a more important role in strengthening the superalloys.

Carbides, due to their brittle nature, have triggered great interest in fatigue research in Ni-base superalloys [79-81]. Similarly to the γ', dislocations pile up at the interface between carbides and matrix, resulting in strain/stress localization [82]. The difference is that the ability to accommodate deformation for the carbides is poor, easily leading to crack initiation. This phenomenon is widely observed in the relevant fatigue research [83-86]. Although dislocation pile-up cracks initiated at carbides are often observed, quantifying the strain/stress concentration is always an issue in previous research. With the development of characterization techniques, such as digital image correlation (DIC) and high-resolution electron backscatter diffraction (HR-EBSD), the strain distribution can be mapped around the carbides [51, 87]. This has shown that the maximum strain is localized at one tip of the blocky carbides, acting as the first crack initiation site in the cyclic process. Therefore, utilizing these kinds of techniques in fatigue research could help to provide a more precise description of the interaction between carbides and fatigue behaviours. Moreover, the carbides tend to be oxidised [88] at the high temperature, and this might have a significant effect on the high-temperature fatigue crack behaviours, which are described in the following section.

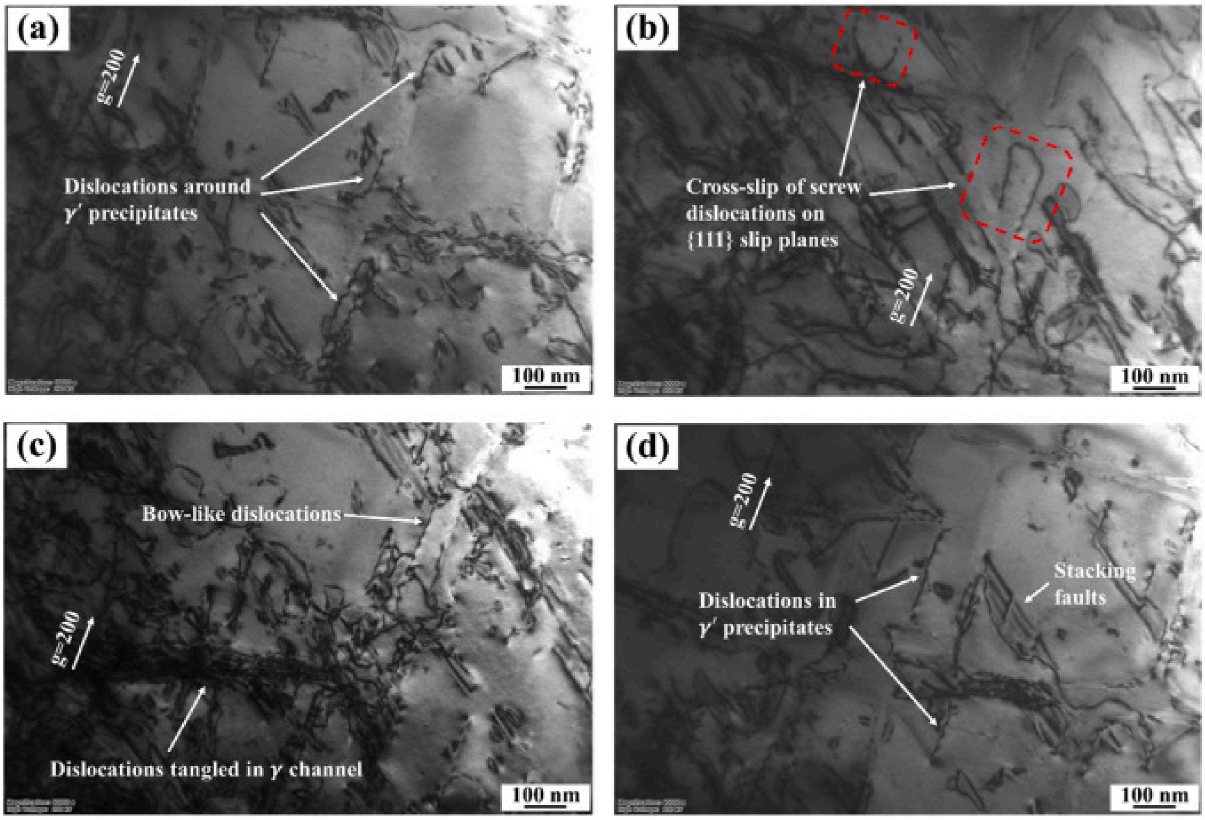

Fig 2.16 TEM images showing dislocations in [111]-orientated specimen fatigue tested at room temperature [75]

2.2.3.3 Grain boundaries

The effects of grain boundaries (GBs) on the fatigue behaviours are mainly studied in the polycrystalline superalloys. Fatigue cracks are often initiated from GBs, due to the anisotropic deformation of the neighbouring grains. However, whether the initiated crack grows transgranularly or intergranularly depends on the testing conditions. In the study of [89, 90], intergranular cracks always occur at elevated temperature, where the oxidation of GBs further decrease their strength or cohesion (seeing the detail in the section 2.2.4.1). In comparison, the fatigue crack at the room temperature is transgranular or mixed [68]. The GBs are generally thought of as the barriers for transgranular crack propagation, as crack deflection always occurs at the vicinity of the GBs, decreasing the fatigue propagation rate. Initially, the retardation effects of GBs were thought to be correlated to the misorientation between the neighbouring grains. In particular, Miao et. al [91] found the fatigue cracks were seen to subsequently grow in a grain cluster within which grains are misoriented by < 20° relative to the initiation grains in Rene 88DT. It should be noted that fatigue cracks tend to grow along slip bands at room temperature, therefore models [92-94] considering the misalignment of the activated slip systems between the neighbouring grains are proposed, rather than simply considering the grains' misorientation. A schematic diagram of model is presented in the Fig. 2.17 [95]. The misalignment can be evaluated using the following equation:

$$m' = cos\kappa \times cos\psi \tag{2.12}$$

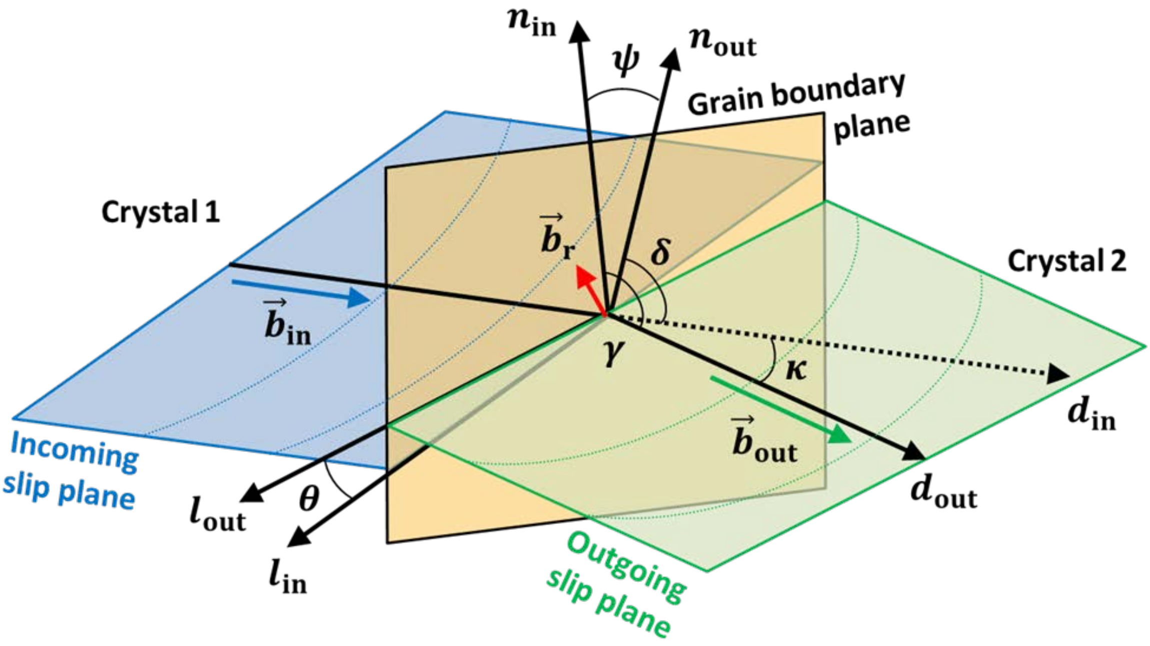

Fig 2.17 Schematic diagram showing the misaligned activated slip systems [95]

m' is the parameter assessing the misalignment, κ is the angle between the normal direction of the slip systems, while ψ is the angle between the activated slip directions. A high value of m' means a low misalignment of the slip systems and so a high possibility for dislocations to transfer across the GBs. The model is initially used to predict the activated slip systems and showed good agreements with experiments [94]. Jiang et. al [96] used the model to predict the short crack propagation behaviours at the vicinity of GBs at room temperature, based on the fact that the short crack always grows along the slip systems. The results showed that the deflection of the crack occurred at the GBs due to the two different slip systems being followed in the neighbouring grains with the minimum m'. With respect to the current study, it is interesting to consider in DS superalloys that when cyclic loading is applied longitudinal or transverse to the columnar grains' long axis, although the grain misorientations are the same, the activated misalignment of the slip systems is different. This might then cause anisotropic fatigue behaviours in the two loading alignments.

2.2.4 Crack initiation behaviours at the elevated temperatures

Fatigue lives of superalloys are dramatically reduced when they serve at elevated temperatures. Many studies [97-99] have shown that oxidation and creep are involved in the fatigue process, particularly in dwell-fatigue conditions (where long dwells are applied at the maximum load in the fatigue cycle), causing faster degradation of the materials. The mechanism of the interaction between fatigue behaviours and environmental effects have triggered widespread research interest. However, due to the complicated chemical composition and microstructures, the interplay among fatigue crack, microstructures and environmental effects are extremely difficult to understand. In these cases, the recently developed robust characterization techniques (like spherical aberration corrected scanning TEM (Cs-corrected STM), 3D atom probe tomography (3D APT), Nanoscale secondary ion mass spectrometry (Nano SIMS)) are largely used to analyse the underlying micro-mechanism. In the section, the findings about the environmental effects (focussed on oxidation and creep) on crack initiation are introduced, and their effects on the crack propagation mechanism is discussed in the next section.

2.2.4.1 Oxidation induced fatigue crack initiation

Oxygen diffusion is enhanced by both temperatures and mechanical loading. The phenomenon is widely observed in the Ni-base superalloys [100-102]. Evangelou [103] performed three-point bending sustained-loading tests on plain-bend bar (PBB) SX superalloy CMSX-4 at 550 °C which applied a stress (and strain) gradient along the bar, allowing the effect of varying stress and strain level to be evaluated in one specimen. This found that the size of external oxides forming on the surface and the γ' depleted zone (due to internal oxidation) at the plastically strained centre of the PBB was greater than that in the outer regions experiencing merely elastic strain. In RR1000 [104], similar results are observed that the oxidation-linked microstructure damage becomes more significant under tensile stress when temperatures increased from 700 °C to 800 °C. The enhanced oxygen diffusion accelerates the oxidation process of microstructures such as GBs, carbides and slip bands, causing the degradation of these features, and hence leading to crack initiation.

Generally, two mechanisms are proposed to explain the degradation of GBs caused by oxygen at elevated temperatures under mechanical loading. Both acknowledge that the GBs are the preferential diffusion path for oxygen, due to the existence of a large number of vacancies on the GBs. The difference is that the subsequent fatigue cracking behaviour is considered to be caused by (1) the formation of brittle oxides or (2) the decohesion of GBs due to the intrusion of oxygen ions or in the form of clusters of oxygen ions. The former mechanism is termed as stress assisted grain boundary oxidation (SAGBO) [105, 106] while the second is termed dynamic embrittlement (DE) [107, 108]. Actually, the dispute mainly exists for the crack propagation process, as both mechanisms are observed in superalloys, but for the crack initiation process, few studies support the DE mechanism. In comparison, crack initiation from external oxides is observed in [109] in interrupted high-temperature fatigue short crack tests (shown in Fig. 2. 18 [109]). In a stress-assisted oxidation process, both external and internal oxidation layers are formed. Due to the composition difference of superalloys, and the sequence of oxidation, the composition of these oxidation layers is different. For the N18 superalloy used in [109], the external layers consist of Cr-rich and Co-rich oxides, and due to the different volume expansion between the two types of oxides and the matrix, additional stress is introduced [110], causing easier crack initiation at the GBs.

Carbides are another microstructural features that the oxygen attacks at elevated temperatures, and the oxidized carbides may act as fatigue crack initiation sites. The cracking mechanism is initially thought similar to that of oxidized GBs, the volume expansion of oxidized carbides introduces a locally higher stress, therefore cracks initiate at this porous and brittle phase. Nevertheless, a different micro-mechanism is proposed recently characterized by 3D tomography data. Kontis et. al [111] propose the oxidized carbides soften the materials around the phase, which leads to the crack initiation during thermal-mechanical fatigue tests at 850 ºC.

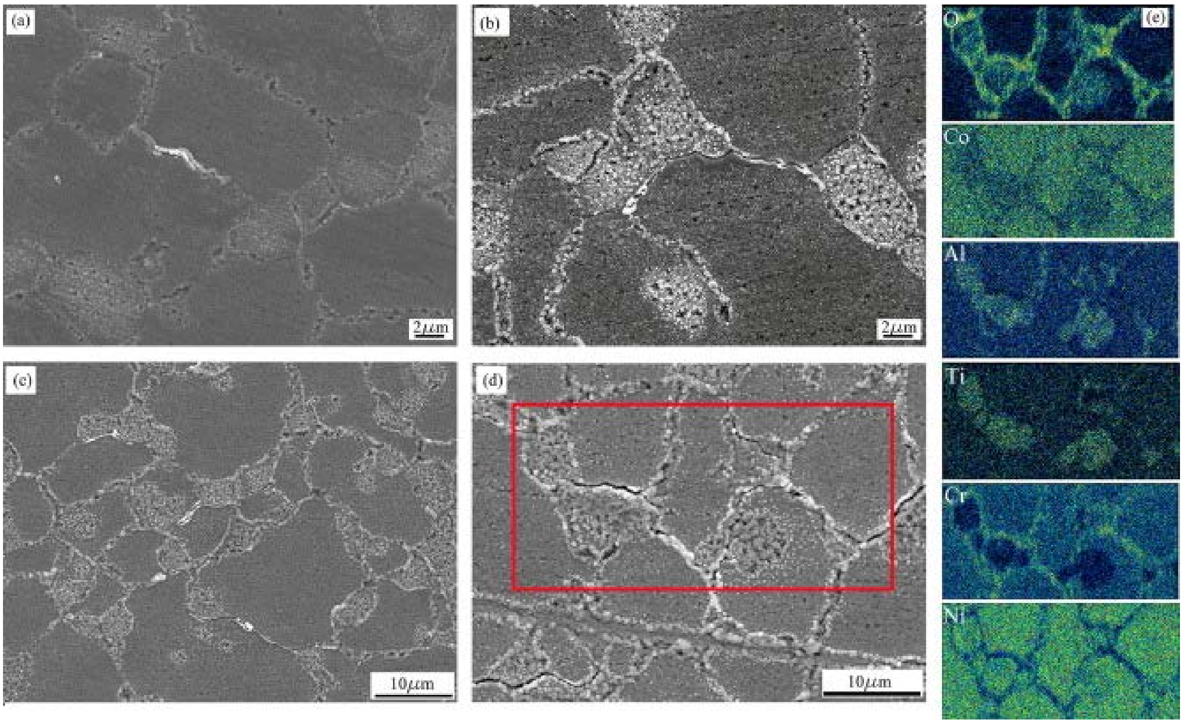

Fig 2.18 Evolution of cracks from the oxidized grain boundaries at the notch root in the interrupted test at 650 oC a: (a) 9000 cycles, (b) 15000 cycles, (c) 31000 cycles and (d) 36000 cycles; (e) EDS mapping of the region highlighted by the rectangle shown in (d) [109]

The softening mechanisms is proposed as follows: high densities of dislocations are formed in the adjacent matrix of the carbides due to the volume expansion and cyclic loading. They provide a fast element diffusion path, known as 'pipe' diffusion, which accelerates the dissolution of γ' and leads to recrystallization. Finally, the fatigue crack potentially initiates from the carbides and into the adjacent matrix. The observed γ' depletion crystallization zone is shown in the Fig. 2.19 [111].

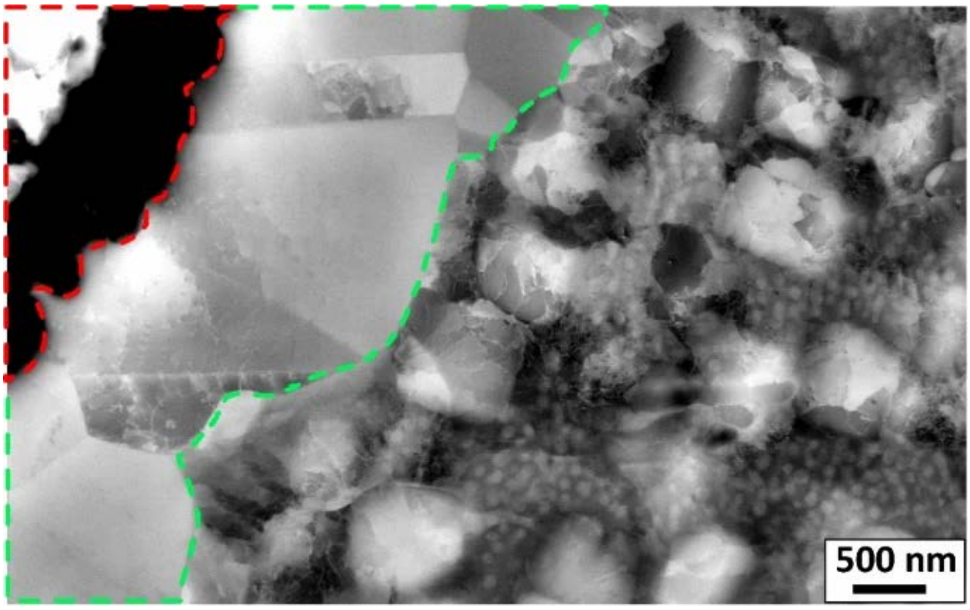

Fig 2.19 ECCI micrograph next to an oxidized MC carbide (denoted by the dashed red line) during OP-TMF at 850 °C showing high dislocation density within the recrystallized region (denoted by the dashed green line) and within the γ/γ′ microstructure where dissolution of γ′ precipitates occurs [111]

Slip bands, the preferential fatigue crack initiation sites, are also preferential sites for oxidation. As discussed above in section 2.2.3.1 surface roughening is achieved by forming slip steps, and once oxides are formed at the freshly exposed slip steps, reverse slip will be more difficult on the slip plane upon load reversal. In this case, the surface roughening process is enhanced, potentially leading to an earlier fatigue crack initiation. The study of Peng et. al [112] confirmed this process, as they found crack initiation from the oxides formed on slip bands. Moreover, the oxygen could be quickly transferred to the matrix beneath the slip bands, causing further degradation. So far, studies on the oxidation of slip bands are very few. It is proposed that the activation of cross slip reduces the density of slip bands at elevated temperatures, which makes slip band cracking not the predominant cracking mode.

2.2.4.2 The effects of creep on crack initiation

The interaction between creep and fatigue are extremely complex as the creep process itself is complicated, containing lots of interplay between dislocations and microstructure features. Here, just a brief introduction is made to the findings on fatigue-creep damage. This is for two reasons: (1) the current research is performed at 650 °C and 725 °C, where the creep process is relatively limited for the DS superalloy studied. (2) fatigue-creep damage is intensively studied, but only a few studies focus on the crack initiation behaviours.

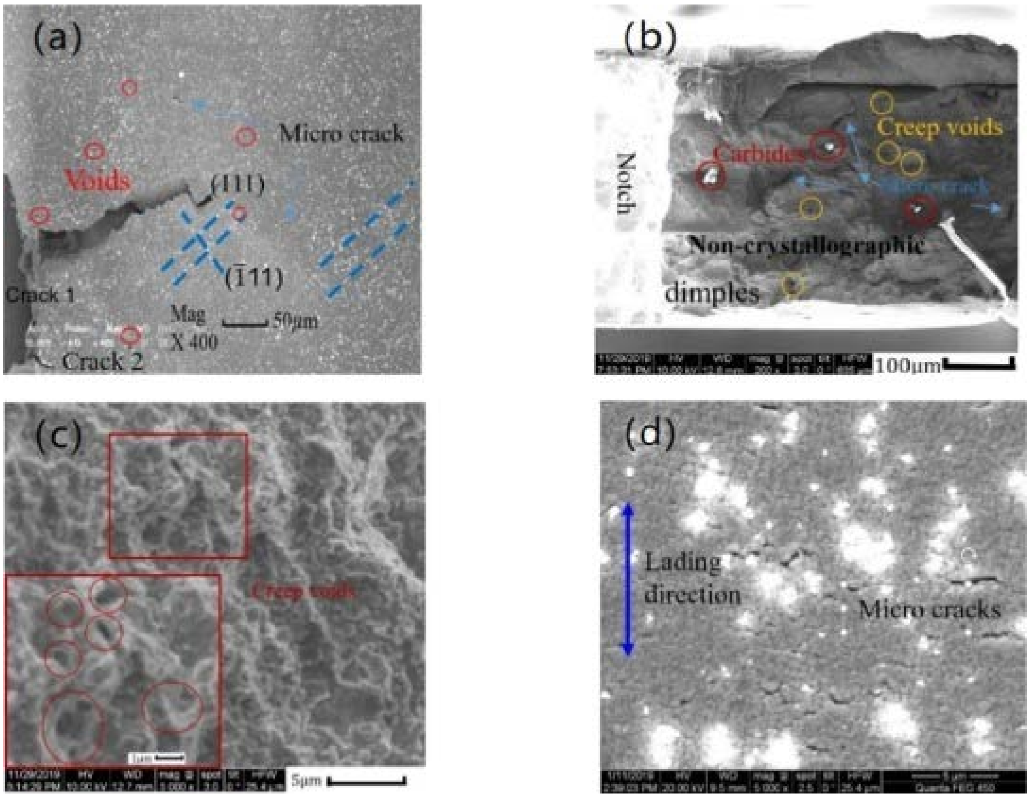

Fig 2.20 In-situ SEM images before the final instant fracture, (b) Fracture morphology, (c) Partial enlarged view of fracture morphology for the 120 s of dwell time at 900 °C [113]

The introduction of significant dwell time (at maximum load) within fatigue loading largely reduces the fatigue cycles to failure observed in both polycrystalline and SX superalloys. The crack initiation mechanism transfers from predominantly slip-band cracking to grain boundary cracking in polycrystalline superalloys [114, 115] and creep voids and subsequent cracking in SX superalloys due to the absence of GBs. The underlying mechanism is that the introduction of dwell time enhances the inelastic strain accumulation achieved by dislocation movement, leading to the formation of micro voids. In polycrystalline superalloys, two main types of voids are found (i) round, or spherical voids also known as r-type voids and (ii) cylindrical voids (w-type voids). These voids grow and coalesce at the GBs, resulting in micro-cracks under applied tensile stress. Therefore, the typical intergranular crack is observed and become the predominant cracking modes with the increase of the dwell time. In SX superalloys, micro cracks are purely formed by the coalescence of the voids, supported by two pieces of evidence in the research of Wang et. al [113]. The first one is the appearance of plastic dimples and creep voids on the fracture surface after a fatigue test with a dwell time of 120 s at 900 ºC. The other is the in-situ observation of a micro crack from voids using SEM in the same study shown in the Fig. 2.20 [113].

2.2.5 The crack propagation behaviours at elevated temperatures

2.2.5.1 Effects of oxidation

It is found that the fatigue propagation rates of polycrystalline superalloys are sharply increased at elevated temperature and when tested in air, compared to the fatigue lives at room temperature or in vacuum. This indicates that the reduction in life is associated with oxygen-related damage mechanisms. The two basic mechanisms explaining this oxygen-related damage: SAGBO and DE have been introduced in the section 2.2.4.1, where their roles in the crack initiation were discussed. Herein, their effects on the fatigue crack propagation process will be introduced [116-120].

In SAGBO damage, the grain boundary oxidation process degrades the material's resistance to fatigue crack propagation and results in intergranular cracking along the oxidized grain boundaries. Usually typical oxidation layers can be observed around the crack shown in Fig. 2.21 [119]. The oxides formed consist of external NiO/CoO layer and internal Cr_2O_3/TiO_2/Al_2O_3 layer. Particularly, internal oxides formed ahead of the intergranular crack tip not only lead to weakening of the grain boundaries, but also act as stress concentrators.

However, in some polycrystalline superalloys like IN718, no evident oxides are formed in the crack wake, though intergranular cracks and a much faster FCG rate are found in the long crack fatigue tests. McMahon [120] suggested that enhanced crack propagation should be interpreted as occurring by dynamic embrittlement (DE). The dynamic embrittlement (DE) mechanism is associated with a reduction in cohesion strength of GBs at a small scale (normally tens of nanometres) due to oxygen segregation, which in turn accelerates the crack propagation rate. Other evidence supporting this hypothesis is that it has been found that the intergranular FCG at high temperature is much faster than the oxidation rate in some alloys. In this case, DE was a more likely mechanism responsible for the enhanced FCG, as oxygen has a rapid diffusion rate along GBs in the plastic zone ahead of the crack tip.

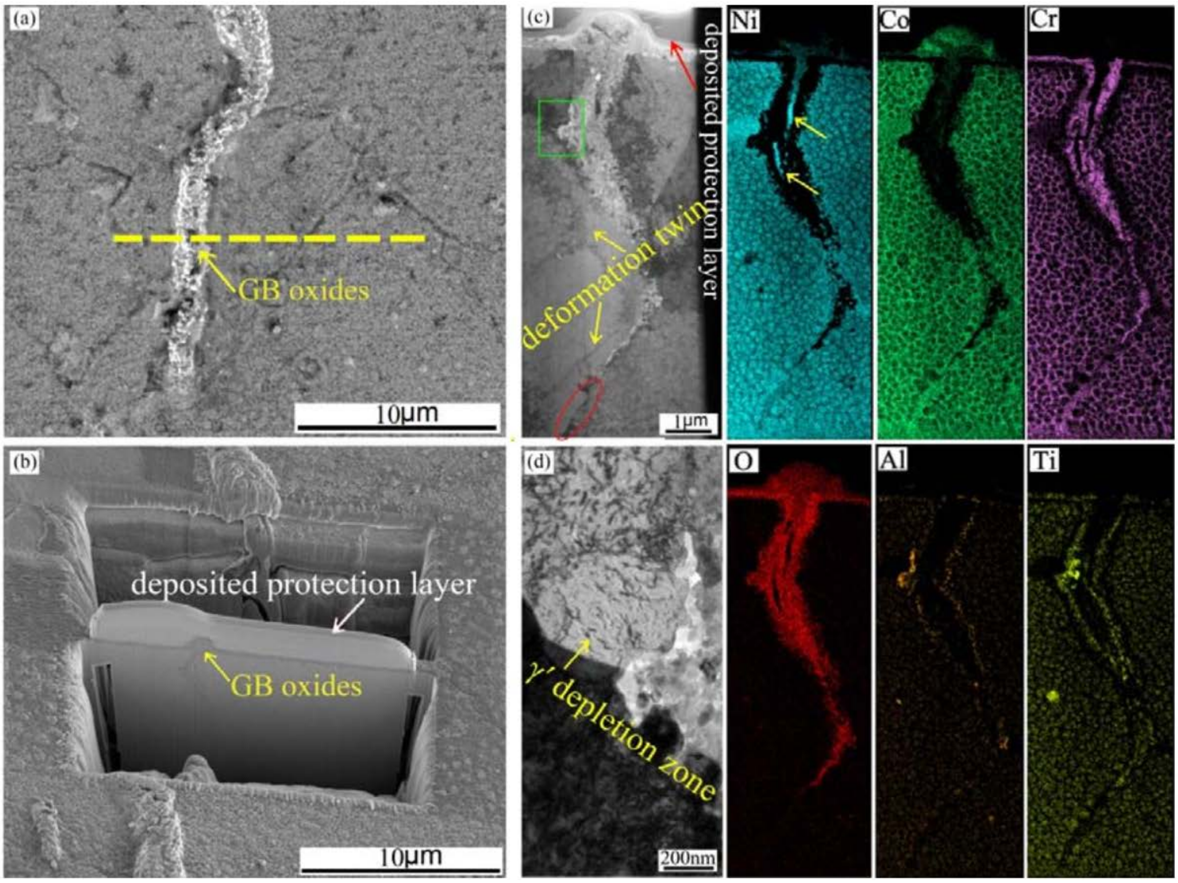

Fig 2.21 (a) Area of interest for TEM lamella extraction in the FG LSHR variant tested at 725 °C. The dashed line indicates the extraction position; (b) TEM lamella in the trench before lift-out procedure; (c) bulged oxides and oxide intrusion along grain boundary and the corresponding EDS elemental maps; and (d) close-up of the γ′ depletion zone highlighted in (c) by the rectangle [119]

In a recent study conducted by Jiang et. al [117, 119], they found either SAGBO and DE damage could exist in the same fatigue process. The dominant damage (SAGBO or DE) is dependent on the crack propagation rate shown in Fig. 2.22 [10, 119]. In the early crack propagation regimes (slow crack growth rate), crack tip oxidation makes a dominant contribution to these processes. As the crack propagation rate increases, the contribution of oxidation diminishes, and the mechanism for oxygen enhanced fatigue crack propagation may be overtaken by dynamic embrittlement. With further increase of fatigue crack propagation rate, the mechanical damage may outstrip the oxygen-related damage, resulting in a transition from intergranular to transgranular crack propagation. Most of the investigation above was carried on polycrystalline superalloys, which possess a large amount of GBs.

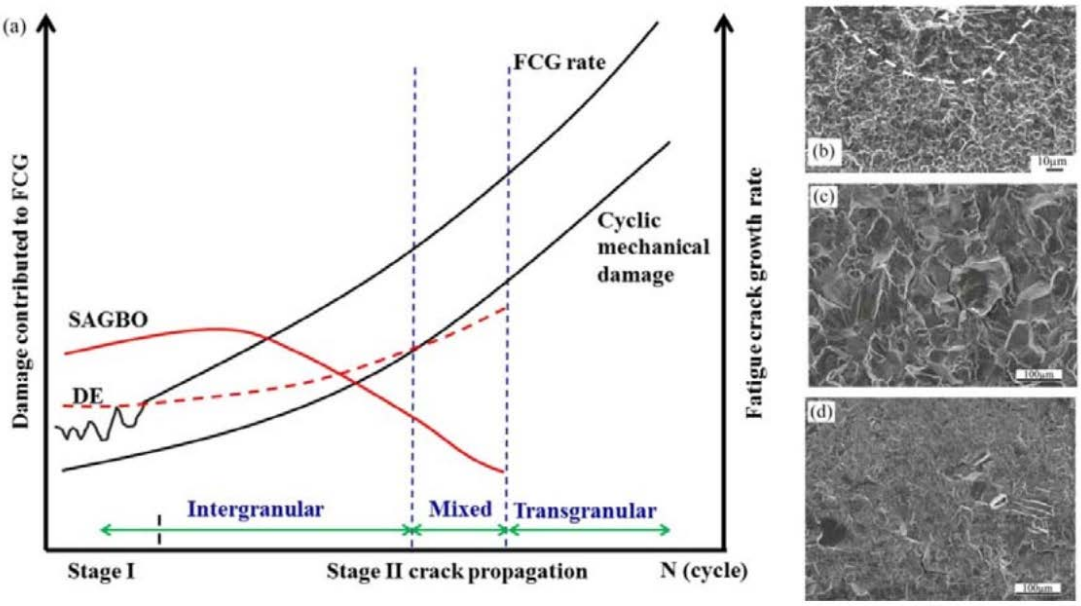

Fig 2.22 (a) Schematic diagram showing the contribution of SAGBO, DE and mechanical damage to FCG at various stages of crack propagation, (b) example of transition of transgranular to intergranular crack propagation in U720Li in the stage I crack propagation [10], (c) and (d) example of transition of predominantly intergranular crack propagation at Δ K of 20 MPa √ m to transgranular crack propagation at Δ K of 40 Mpa √ m in the CG LSHR alloy variant [10, 119]

In addition to the prevalent SAGBO and DE mechanisms, another oxygen-related fatigue mechanism is sometimes considered for single crystal (SX) superalloys: oxidation induced crack closure (OICC). This was initially proposed between the 1970s and 1980s [121-124], as the near-threshold crack growth was found to be greatly decelerated in the air/moisture conditions, compared to vacuum conditions. Oxides with comparable thickness to crack opening displacement (COD) were thought to form within cracks, wedging cracks open, hence reducing the effective stress intensity range factor (ΔK_{eff}) and crack propagation rate. Further studies found that OICC process might be also related to test frequencies, as the crack propagation threshold is increased at lower frequency tests in single crystal (SX) superalloys [125]. More interestingly, the OICC process is thought to compete with DE process in a fatigue study of CMSX-6 and SRR99 SX superalloys tested at intermediate temperatures (500 °C) [125]. A two-way slope of the $da/dN - \Delta K$ curve is found, as the OICC is inferred to occur in the low-ΔK regime, while DE happened in the high-ΔK regime. Although an OICC process may be of significance due to its potential benefit in improving crack propagation resistance, detailed knowledge of this mechanism is very limited. Suresh and Louat et. al [121, 126] proposed two models to quantitively assess

OICC in the 1990s, considering the geometry relationship between the fatigue crack and oxides. Suresh's model could correlate the crack closure effects with the oxides' thickness and position within the crack wake. Nevertheless, they used oxides measured from the fracture surface to validate the model. This might cause an overestimation of the crack closure effects, as the oxides' thicknesses are formed both in the near-threshold regime and non-near-threshold regime. Henceforth, no more models were developed, partly due to the difficulty in validating the OICC models by using experimental data. Therefore, characterizing the OICC process appropriately is a considerable challenge, which may only occur in the near-threshold regime for fatigue tests (when a load shedding routine is typically followed to determine the crack growth threshold value).

2.2.5.2 Effects of creep

Creep has similar effects in promoting intergranular crack growth as the oxygen-related damage in fatigue tests for polycrystalline superalloys. Although their mechanisms are different, where intergranular crack propagation is mainly attributed to the GBs sliding in creep-fatigue interaction tests (CFI), it is very difficult to distinguish creep damage from oxygen-related damage based on the fractography (as both present as intergranular cracking modes). Therefore, to further clarify the effects of creep damage on the fatigue crack propagation rate, conducting the tests in a vacuum environment is desirable. Many fatigue crack propagation tests [127-129] have shown that the effects of creep are correlated to the dwell time, the applied maximum load and the microstructure features such as the grain size and precipitates/secondary phases at the GBs. The schematic diagram in Fig. 2.23 (a) [82, 130] shows the effects of dwell time on the crack growth mode in terms of fatigue-creep coupling damage [130]. Fatigue crack propagation evolves from transgranular to intergranular cracking with an increase of dwell time. At the same time, the fatigue crack propagation rate (FCP) also increases as shown in the Fig, 2.24 (b) [82, 130], changing from cycle-dependent to time-dependent. The phenomenon of creep free and saturation crack propagation are found in most of the superalloys, where the crack propagation rate (in cycles) does not change when the holding time is low or above the threshold value [82, 128]. Moreover, the creep damage seems more obvious at low or medium ΔK, and diminishes at high ΔK as shown in the Fig. 2.23 (b) [82, 130]. It is inferred that this is associated with the fast FCP rate at the high ΔK, resulting in limited time for creep damage to occur at the crack tip. However, an interesting finding is that in RR1000, the creep effects are more significant at high ΔK level [128]. They performed tests on specimens with different amounts of sigma phases on the GBs. It was found that grain boundary sigma-phase precipitation can promote formation of cavities and enhance intergranular FCP modes, especially at high ΔK levels. Hence, the creep effects on FCP is influenced by the dwell time, stress level at the crack tip as well as the local microstructures.

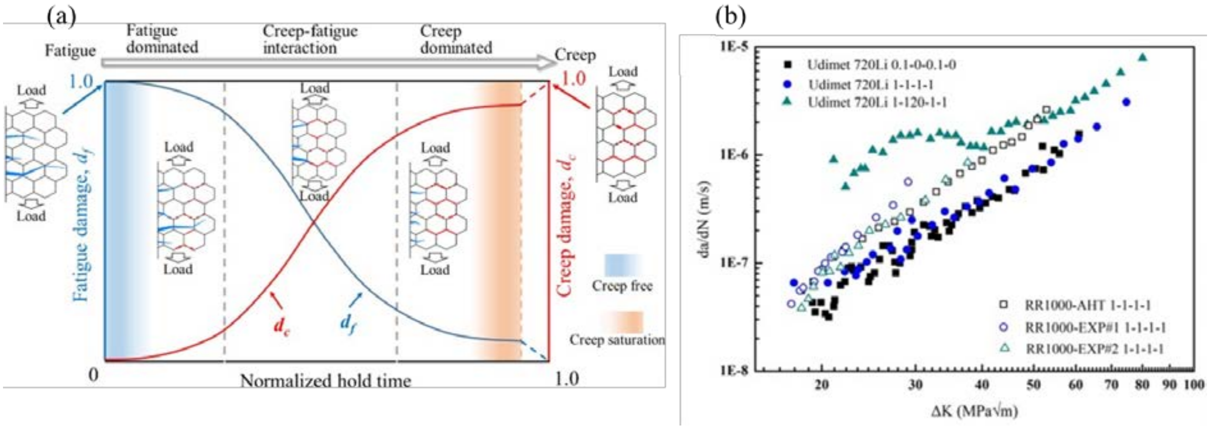

Fig 2.23 (a) Schematic representation of linking and interaction of creep-fatigue damage modes with a normalized hold time at a fixed applied loading level. The number 1 on the vertical axis refers to fully-damage due to creep and fatigue; (b) Effects of creep on FCG in subsolvus heat treated Udimet 720 tested at 700 °C and in RR1000 variants tested at 725 °C with a load ratio of 0.5 in vacuum [82, 130]

In the DS superalloys, the transition from transgranular crack propagation to the mixed mode of transgranular and intergranular cracking are largely found with the increase of dwell time in DZ445 and DZ125 superalloy in the temperatures range of 850 ºC to 980 ºC [131-133]. Nevertheless, fully intergranular crack propagation is not observed, even though the dwell time reached 8 min. This is attributed to the large radius of the columnar grains which will cause significant crack deflection once the cracks propagate along the GBs (and may be associated with significant shielding so the crack will be arrested). A very interesting finding is that the fatigue life is increased with the further introduction of dwell time (over 3 min), observed in DZ445 [131, 132]. In the paper, this abnormal phenomenon is inferred to be correlated to a mixture of creep and plastic deformation, as the authors observed large amounts of stacking faults evidencing the extent of plastic deformation. However, the underlying mechanism is not revealed – that is once the plastic deformation occurs, what is the effect on the fatigue propagation behaviours and how to explain the decreased crack propagation rate in the tests? The crack-tip blunting mechanism in [134] might be used to explain the phenomenon. Due to the long dwell at the maximum load, significant plastic deformation occurred at both the crack tip and wake, resulting in tresidual strain/stress in the loading reversal process. In this case, the effective stress intensity range factor (ΔK) is decreased, corresponding to the decreased crack FCP rate. The mechanism is also termed as plasticity–induced crack closure, which will occur when the fatigue specimen is overloaded, causing severe plastic deformation around the crack tip. The decrease of FCP rate at long dwell time is likely to be associated with this range of evolving shielding mechanisms (including the role of crack path).

2.2.6 Effects of anisotropic elastic modulus and yield stress

With the developing knowledge of the elastic and plastic anisotropy of the DS and SX alloys, the effects of the anisotropy on the materials' more complex creep and fatigue behaviours have incurred significant research interest, because these are closely associated with the service life of the DS and SC superalloys. Reed et. al [135, 136] designed a series of tests to study the orientation effects (with respect to loading and crack propagation direction) on long fatigue crack propagation behaviour. They found that the fatigue propagation behaviour is not only affected by the crystal orientation aligned with the loading direction, but also influenced by the 'secondary crystal orientation', which is perpendicular to the loading direction but parallel to (and defining) the overall crack growth direction. Cervellon et. al [137] also noticed the effects of anisotropy induced by grain orientation. They carefully compared the high-cycle fatigue behaviours of a SX superalloy with [001], [011] and [111] orientation aligned with the loading direction, under different maximum stress. It was found that [001]-orientation sample only shows a longer fatigue life at very low (elastic) stress levels (around 250 MPa). The same results have been found in the work of Yu et. al [138] where the [111] loading direction exhibits the highest fatigue strength. This was mainly attributed to the different movement modes of dislocations which cut through γ and γ' for the [001] and [011] directions, forming superlattice stacking faults for the [111] direction. All these results indicate that significant effects have been induced by the material anisotropy on the fatigue resistance of DS and SX superalloys. These effects should clearly be considered when manufacturing blades with DS or SX superalloys.

2.2.7 Fatigue behaviour of DS CM247LC superalloy

Since the DS CM247LC superalloys are widely used in industry, some studies have been carried out to assess the fatigue behaviours in the short fatigue crack [139], low cycle fatigue (LCF) [140] and thermal mechanical fatigue (TMF) tests [141, 142]. The short fatigue crack test was conducted at 600 °C with a frequency of 10 Hz and R-ratio of zero, and acetyl cellulose film was employed to replicate the surface crack propagation processes. Only the L specimen with columnar grains' long axis aligned with the loading direction is studied. The fatigue cracks were found to grow along the crystallographic planes, and propagation rates were decreased when encountering GBs or when secondary slip systems are activated. According to the literature review, oxygen- and creep-related damage will not occur in such a test. The LCF and TMF tests (both in phase (IP) and out of phase (OP)) compared the fatigue behaviours between L and T samples in the temperature range of 500 °C to 950 °C, and it was reported that the fatigue life of the L specimen is much longer than that of the T specimen. Particularly, the cycles to crack initiation for the L specimen is more than seven times as long as the T case. This is mainly due to the higher yield stress coupled with lower elastic modulus in the L-loading direction which resulted in a reduction of the induced inelastic strain range. In terms of microstructures, some small cracks are found along the inter-dendritic regions in the L specimen, while intergranular cracks are observed in the T sample. The faster crack initiation behaviours might also be correlated to the different cracking mechanisms caused by the relationship between microstructures and loading directions. However, there is still a lack of unambiguous evidence supporting this. Oxygen – related damage is found in the OP tests that cracks grow in the oxide films forming in the inter-dendritic interface for the L specimen and at GBs for the T specimen at the surface. Creep – related degradation is also found in the L and T specimens in both IP and OP tests, as the rafting of γ' is observed, parallel to the loading direction for in the OP test, transverse to the loading direction in the IP test. Another interesting finding is that when a stress concentration is introduced by machining a notch, the cycles of crack initiation for the L specimen is largely reduced and eventually shorter than that for the T specimen when the stress concentration factor k_t is over 2 in the LCF tests. This indicates that the crack initiation behaviours are closely associated with the anisotropic mechanical properties (the difference in elastic modulus and yield stress) and potentially microstructures.

Although these tests reveal quite important fatigue behaviours of the DS CM247LC, the detailed crack initiation and propagation behaviours are not well studied, which is necessary in revealing the underlying mechanism of the fatigue behaviours, such as the interplay among the fatigue crack, microstructures, oxidation and creep. For instance, the cycles to the crack initiation are determined by the drop of stress in the strain-controlled LCF and TMP tests. However, the method is not validated by interrupting the test and measuring the cracks, once the stress drop is observed. There is a possibility that a relatively large crack has already been formed when the stress drop occurs. In addition, the crack propagation behaviours are analysed solely based on the fractography. Due to the lack of FCP rate data, oxygen-related and creep-related effects on the FCP is difficult to quantitatively evaluate. Therefore, systematic work with careful consideration in test design, combined with some quantitative characterization is needed to provide a deeper understanding of the fatigue behaviours of the material.

2.3 Summary of literature reviews and challenges

- Ni-based DS superalloys are widely used in aero-engine and power generation turbomachinery due to their excellent mechanical properties coupled with good oxidation/corrosion resistance. The directional solidification process effectively reduces the number of transverse grain boundaries and hence improves the tensile and creep stress.
- Complicated microstructures are formed in the Ni-base DS superalloys due to incorporating tens of alloying elements. The microstructural features comprise the general straight GBs, primary dendrites, inter-dendritic regions, precipitates such as γ′ and carbides, defects like pores. These microstructures play important roles in determining the material's mechanical properties, as some (γ′) strengthen the materials by prohibiting the dislocation movements, while some (pores) worsen the materials due to accelerating the degradation under stress states or elevated temperatures. Most (carbides, dendrites) have somewhat ambiguous effects on the mechanical properties, dependent both on the external service conditions and intrinsic parameters (e.g. the size, morphologies and distributions of the carbides).
- DS CM247LC is a typical dual-phase intermetallic, with γ matrix and γ′ precipitates. The γ′ is ~ 500 nm in cuboidal shape, accounting for 60 % volume fraction. MC-type and $M_{23}C_6$-type carbides are the minor precipitates of the material, distributed at the inter-dendritic region and GBs. The columnar grains are parallel to the solidification direction, with the diameter typically in the range of 800 - 1200 μm.
- The total-life approach or damage-tolerance approach is employed in the fatigue design of engineering components. The total-life approach is useful for selecting materials containing very limited defects, where the resistance to crack initiation is important. The

damage-tolerant approach is adopted to deal with the materials containing potential defects, where resistance to crack propagation is important.

- Fatigue short crack initiation processes are sensitive to the local microstructures at the room temperature. The preferential crack initiation sites are always associated with these microstructural features, such as slip bands, carbides, GBs and pores, resulting in strain/stress localization. However, the mechanisms inducing crack initiation are different, as the slip bands lead to the strain/stress concentration by roughening the surface. Carbides and pores cause the strain/stress concentration by prohibiting the dislocation movement, while crack initiation at GBs is caused by the anisotropic plastic deformation behaviours of the neighbouring grains.
- Fatigue short crack propagation is dominantly transgranular cracking following the most favoured slip system. The slip system is mostly the one with the maximum Schmid factor, but it changes at the vicinity of GBs to the pair potentially with the highest m' influenced by the GBs.
- Fatigue crack initiation and propagation behaviours are the synergistic result of microstructure, temperature, environment as well as elastic and plastic anisotropy in combination with loading mode. These factors are coupled together to produce fatigue, creep and oxygen-related damage to the alloys. Identifying the specific contribution of each factor is both challenging but necessary.
- The fatigue knowledge of DS CM247LC superalloys has been limited so far largely to determining their LCF and TMF behaviour. The fatigue lives of L and T specimens exhibit a large gap, indicating the strong effects of the mechanical and microstructural anisotropy on the fatigue behaviours. However, the detailed crack initiation and propagation behaviour understanding is lacking, as well as the characterization of the interplay among fatigue crack, microstructures, oxidation and creep.
- Based on the literature review, it is clear that the fatigue behaviour of DS superalloys is still not fully understood yet which is critically important for their future applications. Therefore, there are two main aims of this project. Firstly, a comprehensive study will be conducted on the micro-mechanism of short crack initiation and early propagation behaviour regarding the effects of grain orientation and microstructure features in the DS CM247LC superalloy. Secondly, a series of long crack tests are designed to

investigate the contribution of grain orientation, temperature, dwell time and oxygen to crack propagation behaviour.

Chapter 3 Materials and methodology

3.1 Microstructure characterization

The CM247LC DS superalloy used in the present work was provided by GE Power. The composition (in wt.%) of the alloy (supplied by the company) is listed in Table 3.1. This DS alloy was provided in the form of a block with the longest dimension in the solidified direction (<100> direction). Subsequently, the block was solution heat-treated at 1221 °C, 1232 °C, 1246 °C, respectively, followed by dual aging heat treatments at 1080 °C and 870 °C.

Table 3.1 Composition of CM247LC alloy (in wt. %)

Cr	Co	Al	Ti	W	Mo	Ta	Hf	C	Zr	B	Ni
8.25	9.23	5.31	0.75	9.50	0.51	3.20	1.46	0.75	<0.02	<0.02	Bal

3.1.1 two-dimensional (2D) materials characterization

Metallographic samples for optical and SEM microscopy were prepared using standard techniques. Rectangular samples with dimensions of 10 mm × 10 mm × 10 mm were cut from the heat-treated samples. Both surfaces parallel and perpendicular to the <100> solidification direction were ground on 120, 800, 1200, 4000 grit abrasive papers sequentially, followed by polished on Struers DP-Mol cloth with 3 μm and 1 μm Diamond suspensions, and finally etched in Kalling's reagent (40 g $CuCl_2$ + 80 ml HCl + 40 ml CH_3OH) for 10 – 20 s, to reveal the morphology of dendrites, grain boundaries and precipitates. Electro-etching was conducted in a solution of 10% orthophosphoric acid and 90% H_2O at a voltage of 2 V for 25 s to reveal secondary and tertiary γ'. The microstructural features were observed by an Olympus BH2 OM and a JEOL JSM 7200F field emission gun (FEG) SEM (imaging parameters are shown in Table 3.2). The element analysis was performed using Energy Dispersive X-ray Spectrometer (EDX) attached to the SEM.

Table 3.2 Imaging parameters in JEOL SEM JSM 7200F

Imaging mode	Acceleration voltage	Probe current	Imaging time	Working distance
SEI	15 kV	8 mA	20 s	9.9 mm

Electron Backscatter Diffraction (EBSD) was used to investigate the crystalline orientations. To prepare the EBSD sample, two polishing methods are employed. The first one is chemical-mechanical polishing, using alumina suspension (OPA, 0.3 μm), and colloidal silica suspension (OPUS, 0.04 μm) for the final polishing stage. However, the mechanical polishing always introduces scratches, affecting the precision of the analysis. Therefore, electro-polishing is also adopted. Specimens, after being ground on the 4000 grit paper, were electropolished for 10 s with a solution of 10 ml perchloric acid and 90 ml ethanol and voltage of 15 V for 15 s, using Kristall 620 automatic electrolytic polisher. EBSD measurements were also performed on the same SEM machine with Oxford Instrument C-NANO EBSD detector. The unified acquisition parameters were applied: 20 kV acceleration voltage, 14 mA current and 5 μm step size. All the EBSD data are processed by Aztec Crystal commercial software and Matlab-based open-source toolbox MTEX [143].

3.1.2 Three-dimensional (3D) materials characterization [1]

The three-dimensional characterization of the microstructural features was conducted using synchrotron radiation computed tomography (SRCT), Spring-8, Japan[1]. The tiny dog-bone specimen with dimensions is shown in Fig 3.1 (a). The narrowest cross section in the middle is designed to be only 0.9 mm × 0.9 mm, due to the high attenuation of the synchrotron radiation through the Ni-based superalloys. The columnar grains and primary dendrites are aligned with the elongation direction of the specimen. The set-up of the scanning is shown in the Fig 3.1 (b). The parameters of the scan settings used at Spring-8 are listed in Table 3.3. Carbide and void information were segmented using a global threshold approach in ImageJ software. The threshold value was determined by following an ISO 50% approach taking the middle value between the mean greyscale value representing carbides/voids, and the mean greyscale value of the material. The BoneJ analyse particles plugin tool for ImageJ was used to quantify the size and distribution of carbides and voids in the material. Segmented features were imported into VG Studio MAX software for 3D rendering and visualisation.

---

[1] This data was previously collected by Dr Dan Bull and made available for this project, this is acknowledged in a joint publication on this data where he is a co-author and is hereby acknowledged with thanks in this dissertation.

Table 3.3 Parameters of the SRCT scans conducted in Spring-8

Parameters	Spring-8 SRCT
Energy	53 kV
Voxel resolution	0.5 µm
Scan time	1.2h
Field of view	~1.0 × 1.0 ×1.0 mm3
Number of projections	1800
Exposure time	2 s
Dectector bining	× 1

3.2 Mechanical tests

3.2.1 Tensile tests

Tensile tests were conducted at room temperature for two types of specimens, one with columnar grains parallel to the loading axis (named as L), and the other with columnar grains perpendicular to the loading axis (named as T). The dimension of the tensile specimen is shown Fig. 3.1 (c). The specimen has a gauge cross-section of 4 × 4 mm^2, with a gauge length of 40 mm. A Vishay EA-15-125BZ-350/E strain gauge was attached to the specimen surface (within the gauge centre) with a ground finish produced by 1200 grit abrasive paper. The test was conducted on an electro-mechanical testing machine (Instron Electropuls E1000) with a constant strain rate of 1.0×10^{-4}/s, which is widely used in comparable tensile tests for single crystal or directionally solidified nickel-based superalloys [144, 145].

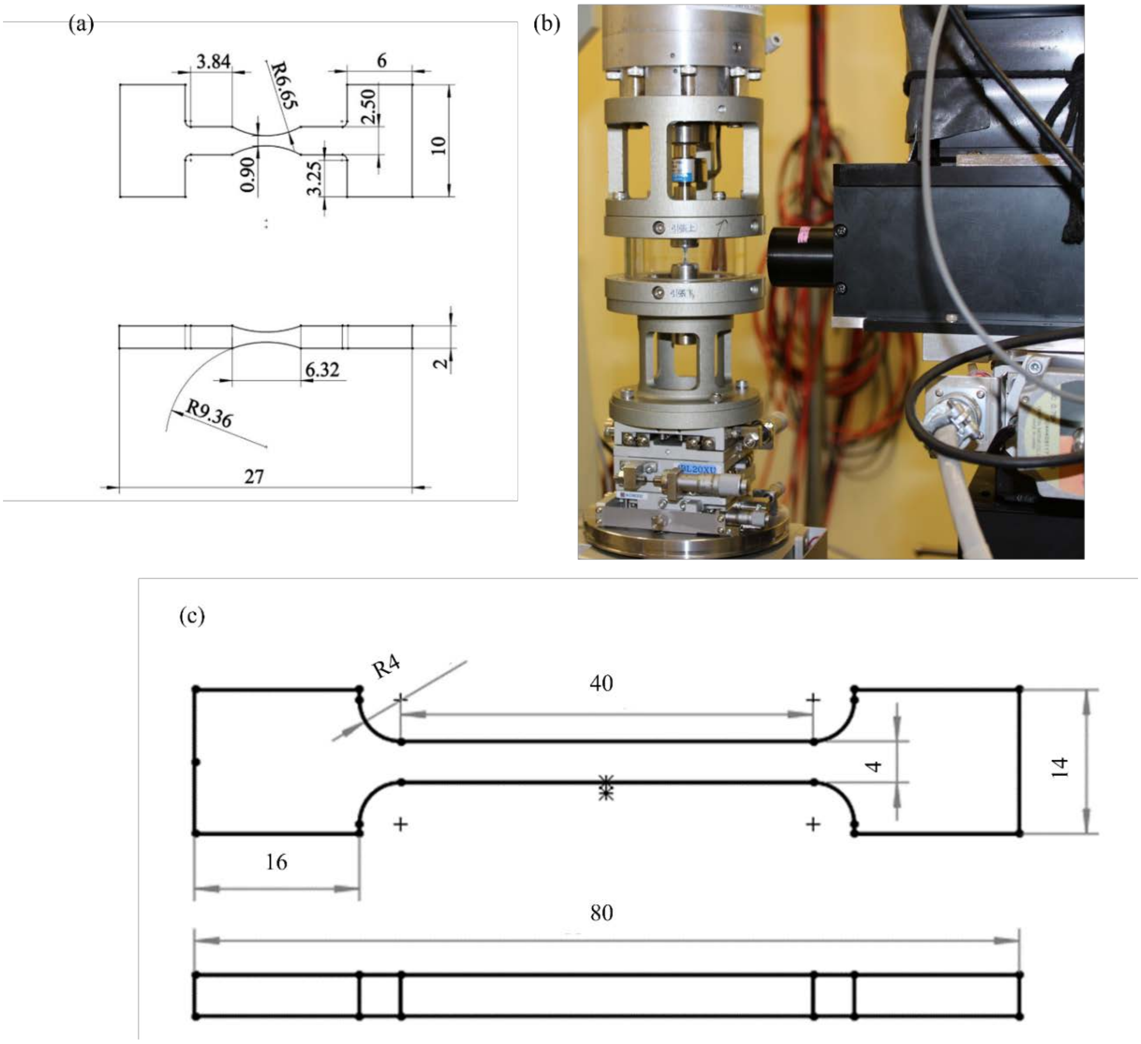

Fig 3.1 (a) Dog-bone specimen dimension (in mm); (b) set-up of the SRCT scanning; (c) tensile specimen dimension (in mm)

3.2.2 Tension-tension fatigue tests

Both in-situ and ex-situ tension-tension fatigue tests were performed using the dog-bone specimens shown in the Fig 3.1 (a). The interaction between crack growth behaviours and microstructural features are observed in three dimensions by using the SRCT for the in-situ tests. The strain localization in the process of crack initiation and early propagation were analysed by using the DIC technique for the ex-situ fatigue tests.

3.2.2.1 In-situ fatigue tests using synchrotron radiation computed tomography (SRCT) [2]

The specimen with primary dendrites perpendicular to the loading direction was pre-cycled up to 40,000 cycles on an Instron Electropuls universal test machine, using a sinusoidal waveform at 20 Hz with an applied peak load 85% yield stress (274 N) and R ratio of 0.1. Then further in-situ interrupted cyclic tests were conducted by adding 5k, 7k, 8k, 10k, and 12k cycles sequentially to the pre-cycled specimen using the same loading conditions. The specimen was CT scanned with an applied tensile load of 85% (274 N) of yield stress at each cycling interval to facilitate the detectability of the cracks by holding the cracks open. The parameters of the scan are the same with the scan for characterizing the microstructures. Cracks were segmented from CT volumes using the seeded region growth tool in VG Studio MAX software. These were performed at 40k and 52k cycles to compare differences in crack growth and crack morphology[2].

3.2.2.2 ex-situ fatigue tests [3, 4]

Tension-tension fatigue tests were performed for dog-bone specimens (both L and T samples) on an Instron Electropuls testing machine with a 20 Hz sine waveform and a load ratio of 0.1 at room temperature. The applied loads were chosen to produce a maximum nominal stress of 85% of yield stress of the L specimen at the narrowest cross-section of the gauge. Dog-bone specimens (for DIC analysis) were ground with 4000 grit and etched in Kalling's solution to reveal the γ' as speckle patterns for subsequent SEM-DIC (shown in Fig. 3.2 (a) with subsets indicated)[3]. Reference images were taken at the gauge section by SEM under secondary electron imaging (SEI) mode and stitched together via Image J before fatigue testing commenced. The imaging parameters are shown in Table 3.4, following guidelines proposed by the literature [68]. Loading direction is perpendicular to the primary dendrite direction of the specimens. The tests were interrupted at 10000, 15000 and 22700 cycles to obtain SEM images at the deformed gauge section.

---

[2] Tensile tests were performed by Prof. Rong Jiang.

[3] SEM-DIC work was carried out by Sari Octaviani. Both Rong Jiang and Sari Octaviani are also gratefully acknowledged as co-authors on the published work discussing these results, and is hereby acknowledged in this dissertation

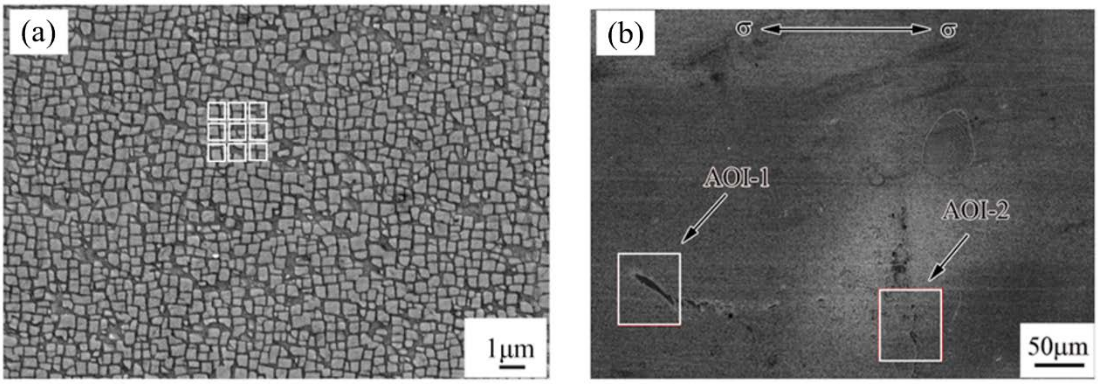

Fig 3.2(a) Speckle patterns; (b) area of interest for DIC analysis

Table 3.4 Imaging parameters in JEOL SEM JSM7200F

Imaging mode	Acceleration voltage	Probe current	Imaging time	Working distance	Strain field	Pixel size
SEI	15 keV	13 mA	80 s	9.9 mm	600 × 600 μm^2	38 nm/pixel

DIC analysis of the strain localization in the gauge section of the dog-bone specimens was conducted via MatchID commercial software [146]. A subset of 21 × 21 pixels (0.798 µm × 0.798 µm) and a step size of 7 pixels were used. This is a compromise between larger step sizes which are computationally efficient and smaller ones which capture the local strain peaks more accurately. The zero-normalized sum of squared differences (ZNSSD) criterion, which accounts for offset and scaling in intensity variations of the investigated images, was adopted to perform the correlation in order to exclude the effects of contrast difference in the SEM images taken at different observation times. Deformed images were interpolated using bicubic splines to obtain subpixel accuracies in the displacement calculation. Quadratic shape functions were used to expand the displacement field in the subset. This is a better choice than linear shape functions, as demonstrated in [147] and leads to enhanced spatial resolution. Once the displacement field was calculated, the Logarithmic Euler-Almansi strain fields were derived by performing a local bilinear polynomial fit in MatchID using a window of 3 x 3 data points (or a 'strain window' of 3). The smallest possible strain window was selected here to enhance spatial resolution at the cost of strain resolution [68]. Due to the ex-situ nature of SEM-DIC, a noise sensitivity study was performed and the details of the noise assessment can be found in a previous publication [68].

A full-field strain map was measured in a region containing two columnar grains shown in Fig. 3.2 (b). Strain components were calculated and transformed into local coordinates associated with the maximum shear strain in the left columnar grain. Two AOIs were selected from the stitched image for further analysis, shown in Fig. 3.2 (b). AOI-1 is a carbide within grains, while AOI-2 is a carbide at a grain boundary. To simplify the comparison of strain bands of different orientations, maximum shear strains in each DIC characterization were calculated using following equation. This is the radius of Mohr's circle and is independent of the coordinate system

$$\varepsilon_{xy}^{max} = \sqrt{(\frac{\varepsilon_{xx} - \varepsilon_{yy}}{2})^2 + \varepsilon_{xy}^2} \tag{3.1}$$

Table 3.5 Parameters for DIC analysis

DIC software	MatchID
Correlation alogorithm	ZNSSD
Interpolation	Bicubic spline
Shape functions	Quadratic
Pre-smoothing	Gaussian 5
Subset	21 pixels
Step size	7 pixels
Strain window	3 data points
Virtual strain gauge size	35 pixels

3.2.3 Three-point bending fatigue tests

3.2.3.1 Three-point bending strain gauge tests

Three-point bending fatigue tests were carried out for plain bend bars (PBB) with dimensions of 55 mm × 10 mm × 10 mm (as shown in Fig. 3.3) using an Instron 8501 hydraulic testing machine. One roller was placed at the bottom centre of the PPB, while the other two were respectively placed at the ends of the top surface with 20 mm to the centre line. Three types of specimens were evaluated: (1) termed as LR with columnar grains parallel to the loading direction and perpendicular to the normal direction of the PBB top surface; (2) termed as RL with columnar grains aligned perpendicular to the loading direction but parallel to the normal direction of the PBB top surface; (3) is RR with columnar grains both perpendicular to the loading and normal directions of the PBB top surface. The schematic diagram in Fig. 3.3 shows the relationship among the loading direction, grain elongation direction and top surface normal direction for these three loading orientations. To assess the cyclic response of the three different specimen orientations, a strain gauge EA-

13-120LZ was placed at the centre area of the top surfaces for exemplar LR, RL and RR specimens. Each specimen was cyclically loaded for 50 cycles at 95% of their yield stress at the top centre surface with an R of 0.1 and 1 Hz sine waveform, and then the load was increased to produce 105% of the yield stress for another 50 cycles. Finally, the load of the RL and RR specimens was increased to produce the maximum stress equal to 105 % of LR-specimen yield stress for the last 50 cycles.

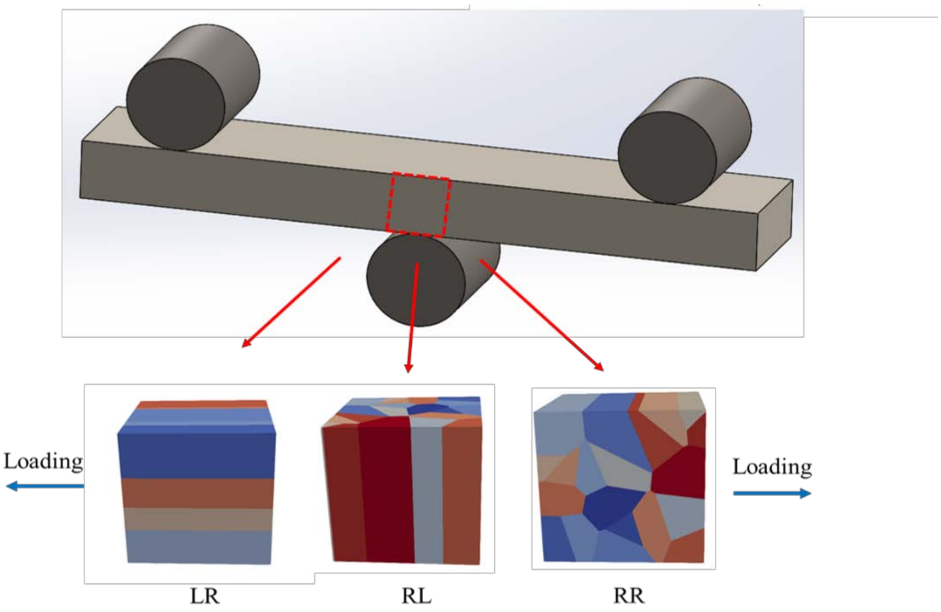

Fig 3.3 Three-point bending specimens and corresponding different types of specimens

3.2.3.2 Fatigue short crack tests

Fatigue short crack tests were performed at both the room and elevated temperatures (650 °C) using the PBB with the same dimensions in the Fig 3.3. For the room temperature tests, specimens of three types are tested on an Instron 8501 hydraulic testing machine with a 20 Hz sine waveform and a load ratio (R) of 0.1. The load was applied to produce a maximum total stress equal to 90% and 95% of the yield stress of the L tensile test specimen on the top central surface, calculated using simple elastic beam theory. To monitor the crack initiation and propagation behaviour, replicas were firstly made at the top surface at intervals of every 5000 cycles until crack initiation, then at intervals of every 1000 cycles to observe the crack propagation. These replicas were then observed under optical microscope with magnification of 20 × (the minimum crack could be observed is around 20 μm). For the high temperature tests, the specimens are tested at 650 °C with thermocouples spot welded on the front surface to monitor the temperatures. The maximum applied stress was 912 MPa and 1008 MPa, with R of 0.1 and frequency of 10 Hz sine and 1-1-1-1 trapezoidal waveforms.

The 1 s segments represent loading, dwell at maximum load, unloading and dwell at minimum load times.

3.2.3.3 Three-point bending sustained loading tests

Sustained-loading tests were performed at the elevated temperature of 650 ºC using the same set-up shown in Fig 3.3. RL specimens are tested to assess the stress-assisted oxidation behaviour and its interaction with the microstructural features. Four PBBs are loaded with the maximum stress of 912 MPa at the centre of the specimens for 1, 4, 8, 16 hours.

3.2.3.4 High-temperature fatigue long crack tests

High temperature long fatigue crack tests were conducted on single edge notch bend bars (SENB) using Instron 8501 servo-hydraulic testing machine. the set-up of the tests is shown in Fig. 3.4. A notch with a depth of 2.5 mm was machined by electrostatic discharge machining at the middle of the bend bar, acting as the stress concentrator to initiate the crack during the fatigue tests. The crack length was monitored via the direct current potential drop (DCPD) method. Current was provided via the wires spot welded at the end of the specimen. The potential drop caused by the crack growth could be obtained from the wires spot welded across the notch, while two more wires were placed away from the notch to normalize the data against temperature and current variations. The fatigue crack length could be derived from the potential drop using the secant method, and a calibration check was made by post-test crack measurement by comparing the calibrated crack length with beachmarks on the surface. Four high intensity quartz lamps were used to heat the specimen. The temperature was monitored and controlled to an indicated ± 1 °C by a Eurotherm 815 thermal controller and R-type (platinum + 13% rhodium/platinum) thermal couples spot welded to the front side surface of the specimen. Two types of samples are designed for the tests, where columnar grains aligned with loading direction are termed as L sample and perpendicular to loading direction termed as T sample, as shown in Fig. 3.4. Both L and T samples were tested under 650 °C and 725 °C, in air condition, 0.1 load ratio, with 10 Hz sine waveform and 1 s – 1 s/90 s – 1 s – 1 s trapezoidal waveforms. 1 s – 1 s/90 s – 1 s – 1 s trapezoidal loading waveforms denotes 1 s segments for loading, 1 s/90 s for dwelling at the maximum load, 1 s for unloading, and 1 s for dwelling at the minimum load. The temperatures of 650 °C and 725 °C were chosen to represent typical service temperatures in the turbine blade root region and at cooling holes, where stress concentration features exist and fatigue is more of a service consideration.

Pre-cracking was conducted prior to the long fatigue crack tests, using a load shedding method with a sine waveform with frequency of 10 Hz, a stress ratio of 0.1, and an initial ΔK of 20 MPa√m after samples were stabilized at test temperature for 10 minutes. The ΔK was stepped down in 10% increments after the crack had grown through four monotonic plastic zone sizes until $\Delta K \approx$15 MPa√m was achieved, which ensured that crack growth out would occur from a microscopically sharp crack away from any residual effects induced in the machining of the notch. Then the loading waveform was changed to a trapezoidal waveform (depending on the test frequency) with an initial ΔK of 15 MPa√m under constant load range (and increased ΔK levels) until specimen failure occurred.

Cracks completely arrested occurred in specific test conditions (which are detailed in results), and two methods were adopted to re-start the crack growth. One is increasing the stress intensity factor range by 10% via increasing the load range. The other one is a burst of high-frequency testing at the same load range, hence resharpening the crack tip, e.g. changing the test frequency to 10 Hz sinewave form and ensuring the crack grows until ΔK has increased by10% due to crack growth, then transferring back to the test frequency. However, in some cases, the two methods had to be combined together, because neither increasing stress intensity factor range or high-frequency resharpening of the crack tip alone could re-start the crack growth.

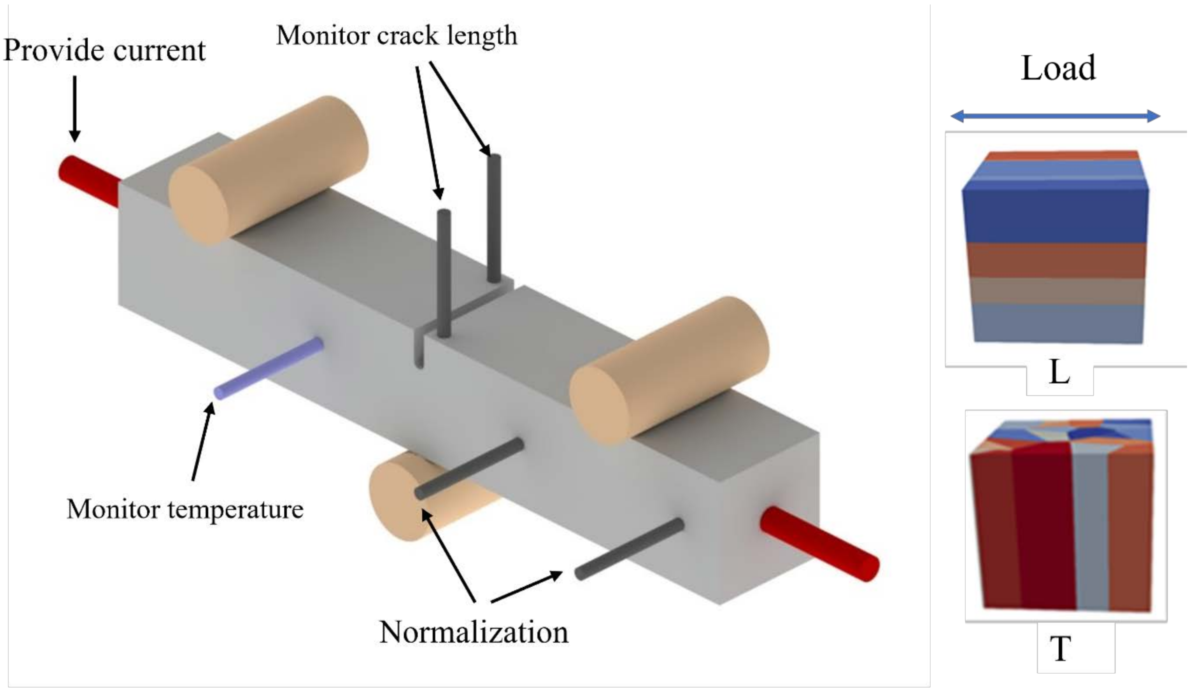

Fig 3.4 Schematic diagram of the long crack tests set-up and the relationship between columnar grains and the loading direction

3.3 Post-test characterization

3.3.1 Fractography and three-dimensional reconstruction

Fracture surfaces obtained from fatigue tests were firstly observed using a wild M420 macroscope to obtain the entire fracture surface. For the regions of interest, they were observed at the higher magnification on a JSM 6500F FEG-SEM, and JSM 7200 FEG-SEM at an accelerating voltage of 15 kV and working distance of 10 mm. The SEM images of some microstructural features were taken by tilting the specimen stage along the Y axis to ± 5 degree in the 7200 FEG-SEM. Then the three-dimensional surfaces of these features were reconstructed from the tilted SEM images automatically using the commercial software Alicona MeX.

3.3.2 EBSD analysis

To analyse the effects of crystal orientation on the fatigue behaviour of the materials, the Schmid factor (SF), slip trace and compatibility factor of GBs (m') were calculated based on the crystal orientations and the loading directions. A rotation matrix is induced to connect the crystal coordinates and sample coordinates:

$$\boldsymbol{g} = \begin{bmatrix} \boldsymbol{cos\varphi_1 cos\varphi_2 - sin\varphi_1 sin\varphi_2 cos\phi} & \boldsymbol{sin\varphi_1 cos\varphi_2 + cos\varphi_1 sin\varphi_2 cos\phi} & \boldsymbol{sin\varphi_2 sin\phi} \\ \boldsymbol{-cos\varphi_1 sin\varphi_2 - sin\varphi_1 cos\varphi_2 cos\phi} & \boldsymbol{-sin\varphi_1 sin\varphi_2 + cos\varphi_1 cos\varphi_2 cos\phi} & \boldsymbol{cos\varphi_2 sin\phi} \\ \boldsymbol{sin\varphi_1 sin\phi} & \boldsymbol{-cos\varphi_1 sin\phi} & \boldsymbol{cos\phi} \end{bmatrix} \quad (3.2)$$

The loading direction from sample coordinates can be transferred to crystal coordinates by the following equation:

$$L_{crystal} = g \times L_{sample} \quad (3.3)$$

where $L_{crystal}$ denotes the loading direction in crystal coordinate, and L_{sample} denotes the loading direction in sample direction. The Schmid factor (SF) for the {111} slip family thereby can be calculated using the following equation:

$$SF = \left|(L_{crystal} \cdot n^s)(L_{crystal} \cdot l^s)\right| \quad (3.4)$$

where n^s represents the normal vector of slip plane, l^s represents the vector of slip direction. The possible slip traces at the side surface of the specimen could be identified by calculating the angle (α) between slip traces and loading direction using the following equation:

$$cos\alpha = (n^s \times Z^s) \cdot L_{crystal} \tag{3.5}$$

where Z^s donates the surface normal vector in crystal coordinates. Using the angle α, the slip systems of the crack segments during the fatigue tests could be identified

To compute the m', assuming that the numbers of activated equivalent slip systems of the maximum Schmid factors are i and j in grain 1 and 2 respectively, the potential combinations of the slip systems are $i \times j$. Then the m' matrix with elements of $i \times j$ could be calculated as follows:

$$\begin{bmatrix} m'_{11} & \cdots & m'_{1j} \\ \vdots & \ddots & \vdots \\ m'_{1i} & \cdots & m'_{ij} \end{bmatrix} = dot\left\{\left(\begin{bmatrix} n_1^1 \\ \vdots \\ n_i^1 \end{bmatrix} \times \begin{bmatrix} n_1^2 & \cdots & n_j^2 \end{bmatrix}\right), \left(\begin{bmatrix} d_1^1 \\ \vdots \\ d_i^1 \end{bmatrix} \times \begin{bmatrix} d_1^2 & \cdots & d_j^2 \end{bmatrix}\right)\right\} \tag{3.6}$$

$$m' = max\left(\begin{bmatrix} m'_{11} & \cdots & m'_{1j} \\ \vdots & \ddots & \vdots \\ m'_{1i} & \cdots & m'_{ij} \end{bmatrix}\right) \tag{3.7}$$

The superscript of n_k^h and d_k^h refers to the grain number and subscript refers to the number of the slip system activated. The most likely potential combination of slip systems is considered as the pair with the maximum m', described by equation (3.7).

The total geometry necessary dislocations (GND) energies were calculated using a Matlab open toolbox – MTEX. Firstly, the GND densities were calculated based on the lattice curvature, according to [148]. The energy of the single edge dislocation is assumed to be 1, while the dislocation of the screw dislocation should be 0.7 [149]. Then the total GND energy was obtained by multiplying the GND densities with the single dislocation energy. It should be noted this is a semi-quantitatively measurement for indicating the dislocations localization.

3.3.3 Xray computed tomography (Xray-CT)

X-ray CT was employed to evaluate the 3D morphology of the crack (particularly the crack tip). Due to the high X-ray attenuation of nickel, a 'matchstick' specimen of 0.7 × 0.7 × 10 mm^3 was extracted from the L and T tested coupons interrupted after being tested for

48 and 96 hours under 1-1-1-1 and 1-90-1-1 trapezoidal waveform at 650 °C shown in Fig 3.5. To generate the matchstick, the sample with the dimension of approximately 1.5 × 1.5 × 10 mm^3 was firstly cut off before being carefully ground down to the desired dimensions of 0.7 × 0.7 × 10 mm^3. The sample was scanned via Xradia Versa CT scanner with parameters shown in Table 3.6 The comparatively lower voxel resolution scanning is used for capturing the microstructure features, the whole crack morphology and obtaining the coordinates of the crack tip (region of interest, ROI), while the high voxel resolution (0.6 μm) scanning is for obtaining the detailed morphology of the crack tip and crack opening displacement (COD).

Table 3.6 parameters of the Xray CT scans

Parameters	Overview scanning	High-resolution scanning
Energy	160 keV	160 keV
Voxel resolution	2.035 μm	0.66 μm
Scan time	4 h	62 h
Field of view	~2.04 × 2.04×2.04 mm^3	~0.66 × 0.66×0.66 mm^3
Number of projections	1601	2401
Exposure time	7 s	90 s
Detector binning	1 × 2	1 × 2

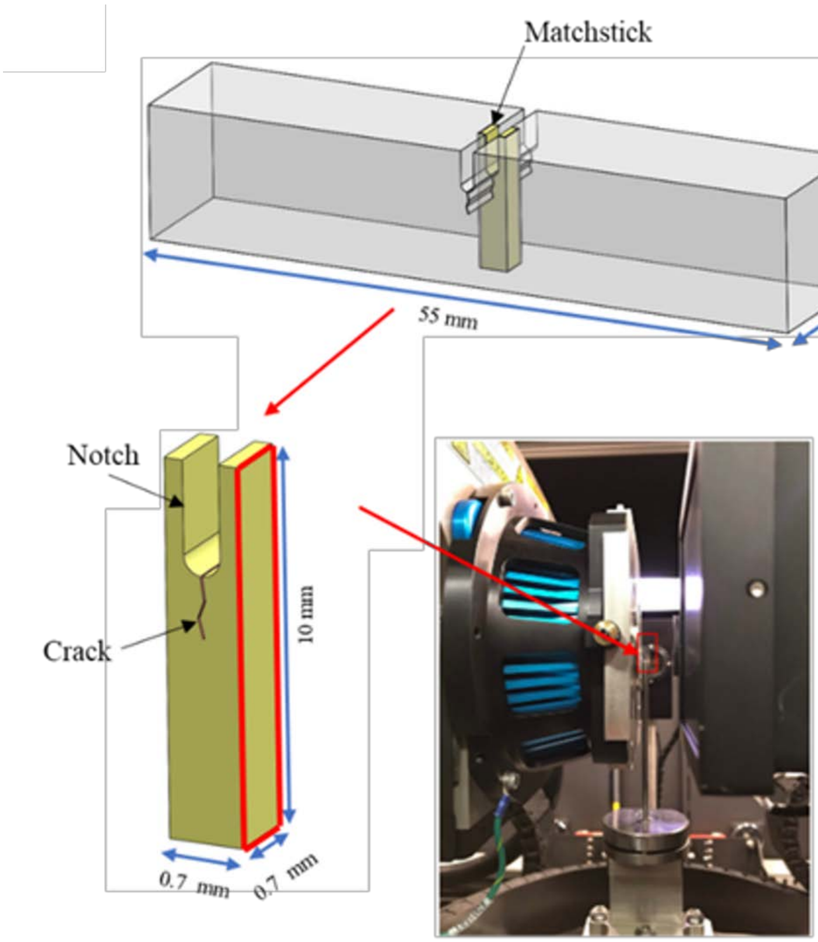

Fig 3.5 Schematic diagram showing the extraction of the match stich and set-up of the X-ray CT scanning

The cracks were segmented out in Avizo commercial software, using the combination of seeded region growing techniques and global thresholding using the ISO 50% techniques [150]. A direction ray casting technique was used to acquire the COD by projecting the number of voxels representing the crack along a line perpendicular to the crack face [151, 152].

3.3.4 Nanoindentation at the crack tip [4]

To probe the local mechanical properties of the oxides at the crack tip, nanoindentation was performed at the interrupted T sample tested after 96 hours under 1-1-1-1 at 650 °C, with mesh grids of 35 × 26, indent spacing of 1 µm and total number of 910 indents. The test was conducted under displacement control, using a MicroMaterials NanoTest Vantage system equipped with a Berkovich indenter at a stabilized chamber temperature of 21°C. The indenter was loaded at a rate of 0.5mN/s until reaching an 80 nm depth after contacting with

---

[4] The nanoindentation tests were performed by Dr Dichu Xu

the sample, then dwelled at this load for 30s and unloaded at a rate of 1mN/s. The depth is chosen to guarantee that the local properties of oxides could be determined reliably. During the testing process, the thermal drift was corrected based on a group of post-indentation data gathered with a dwell period of 60s. The load vs displacement data were also recorded, which were then transferred to load depth curves after being corrected to build the basis for calculating mechanical properties. The hardness and residual elastic modulus were calculated according to Oliver-Pharr method [62].

3.3.6 Focused ion beam (FIB) and scanning transmission electron microscopy (STEM) [5]

A Zeiss Nivsion 40 dual beam FIB-SEM was used to extract the cross-sections at the crack tip and wake of the T sample interrupted after 12 hours. Protective tungsten layers are deposited at the regions of interest (ROIs) to prevent Ga ion or e^- beam damage to the underlying oxide. Then trenches were cut by focusing a 30 kV Ga ion beam with a current of 15 nA at both sides of the ROIs, followed by polishing the exposed surfaces of the cross-section using a rastered 30 kV and 300 pA beam. The J-cutting was conducted to remove materials beneath the ROI, but leave a neck to connect the cross-section of ROI to the matrix materials. A tungsten probe needle was welded to the top side of the cross-section to hold it before the cutting off from the bulk materials. The final step polishing was carried out at 5 kV and 200 pA to thin down the cross-section and give a smooth surface. High-resolution elemental distribution analysis was performed using an analytical STEM JEOL-ARM200F, equipped with an Oxford Instruments silicon drift detector operating at an accelerating voltage of 200 kV.

---

[5] The FIB and STEM work was carried out via a collaboration with the Royce Centre at Oxford, and we acknowledge Dr Neil Young, Dr Gareth Hughes and Dr Ian Griffiths for their work in preparing and analysing these samples with the author

Chapter 4 The effects of grain orientation on fatigue short crack initiation and propagation

4.1 Introduction

Directionally solidified (DS) and single crystal (SX) superalloys have largely replaced polycrystalline superalloys for gas or aircraft turbine blades, serving under high temperatures and complex stress states. Their use in such applications is due to their superior high temperature mechanical properties (i.e. creep) deriving from reducing the grain boundary areas. However, with the associated decrease in the number of grains, the mechanical properties move from isotropy to anisotropy [153-156], which means the relationship between grain orientation and loading direction, plays a much more important role in DS or SX superalloys than in polycrystalline superalloys. As a result, many studies[157-159] have been carried out to understand the role of these anisotropic mechanical properties, in an attempt to explore the optimum relationship between the grain orientation and loading direction to prolong the service life of DS and SX superalloys.

Initially, researchers have mainly focused on the elastic and plastic anisotropy of the DS and SX superalloys, which are the fundamental mechanical properties. It was found that the Young's modulus is the lowest when directionally solidified grains (parallel to <001> direction) are aligned with the loading direction, while it is highest when the loading direction is 45 degree inclined to the <001> grain elongation direction [52, 158, 160]. With the developing knowledge of the elastic and plastic anisotropy of the DS and SX alloys, the effects of the anisotropy on the materials' more complex creep and fatigue behaviours have incurred significant research interest, because these are closely associated with the service life of the DS and SC superalloys. Reed et. al [135, 136] designed a series of tests to study the orientation effects (with respect to loading and crack propagation direction) on long fatigue crack propagation behaviour. They found that the fatigue propagation behaviour is not only affected by the crystal orientation aligned with the loading direction, but also influenced by the 'secondary crystal orientation', which is perpendicular to the loading direction but parallel to (and defining) the overall crack growth direction. Cervellon et. al [137] also noticed the effects of anisotropy induced by grain orientation. They carefully compared the high-cycle fatigue behaviours of a SX superalloy with [001], [011] and [111] orientation aligned with the loading direction, under different maximum stress. It was found that [001]-orientation sample only shows a longer fatigue life at very low (elastic) stress levels (around 250 MPa). The same results have been found in the work of Yu et. al,[138] where the [111] loading direction exhibits the highest fatigue strength. This was mainly attributed to the different movement modes of dislocations which cut through γ and γ′ for the [001] and [011] directions, forming superlattice stacking faults for the [111] direction. Lindström [161] found the anisotropic fatigue behaviours for an additively manufactured superalloy in the low cycle fatigue (LCF) and thermal mechanical fatigue (TMF) tests at elevated temperatures. The fatigue crack initiation life is obviously decreased when loading direction is transverse to the building direction in both LCF and TMF tests. All these results indicate that significant effects have been induced by the material anisotropy on the fatigue resistance of DS and SX superalloys. These effects should clearly be considered when manufacturing blades with DS or SX superalloys.

Although the above results clearly reveal the anisotropic fatigue behaviours, most of them explain the results by primarily considering the different dislocation slip mechanisms. However, this explanation is only based on considering the anisotropic plastic deformation modes, neglecting the potentially more significant effects brought in by the strong elastic anisotropy [162, 163], since most of these materials will in fact operate under conditions where the loading stress is lower than their yield stress. In addition, the studies of fatigue anisotropy are mostly focused on single crystal superalloys where it is easy to control the relationship between loading direction and crystal orientation [164, 165]. For DS superalloys, another very important industrial material system, related research is much less, partly due to the difficulty in aligning a specific crystal orientation to the loading direction. In a DS system, columnar grains grow along [001] direction (the solidification direction) [166, 167], while the direction perpendicular to the solidification direction has a random secondary crystal orientation. The grain sizes are also large, often in the order of millimetres. The anisotropic Young's modulus and yield stress are dependent on the relationship between the grain elongation direction and the loading direction. Therefore, the current work is carefully designed to systematically assess the effects of elastic modulus anisotropy on the fatigue short crack initiation and propagation behaviours in a DS material, in addition to the expected effects of slip system orientation with respect to the loading axis. Some aspects of the work detailed in this chapter have been published in the following paper:

Yuanguo Tan, Sari Octaviani, N. Gao, P.A. Reed, The anisotropic fatigue short crack initiation and propagation behaviours of a directionally solidified (DS) superalloy CM247LC at room temperature, Fatigue & Fracture of Engineering Materials & Structures. DOI: 10.22541/au.168216306.62559044/v1

4.2 Microstructures of DS CM247LC superalloy

Two typical dendrite morphologies were observed at the surfaces parallel and perpendicular to the solidification direction as shown in Fig. 4.1 (a) and (b). Elongated straight columnar grains were observed on the surface parallel to the solidification direction. The radius of the columnar grains is ~ 1.2 mm. Primary dendrites are parallel to the solidification direction, while secondary dendrites are perpendicular to the solidification direction, acting as connecting bridges between primary dendrites. Randomly distributed grains were observed on the surface perpendicular to the solidification direction. Primary dendrite branches were observed in this view, and it was found these branches grew in random different directions (showing the common alignment of the primary growth direction but random secondary arm orientation perpendicular to this as expected in columnar grains produced by directional solidification).

There are two types of carbides in the alloy. One is identified as blocky carbides and the other as chain-like carbides according to their morphology (Fig. 4.1 (c) and (d)). The large blocky carbides mainly precipitated at inter-dendritic regions and partially formed at grain boundaries (GBs), while the small chain-like carbides are formed merely at GBs. Their chemical compositions were determined by SEM-EDS in Fig. 4.1 (e) and (f). Blocky carbides are rich in Hf and the chain-like carbides are rich in W, Co, Cr. Another common phase in Ni-based superalloy, i.e. eutectic ($\gamma + \gamma'$), was found to precipitate at both the inter-dendritic regions and at GBs. The morphology of the secondary γ' was revealed after electro-etching. Cubic secondary γ' with a size of hundreds of nm and tertiary γ' with a size of several nm are shown in Fig. 4.1 (g).

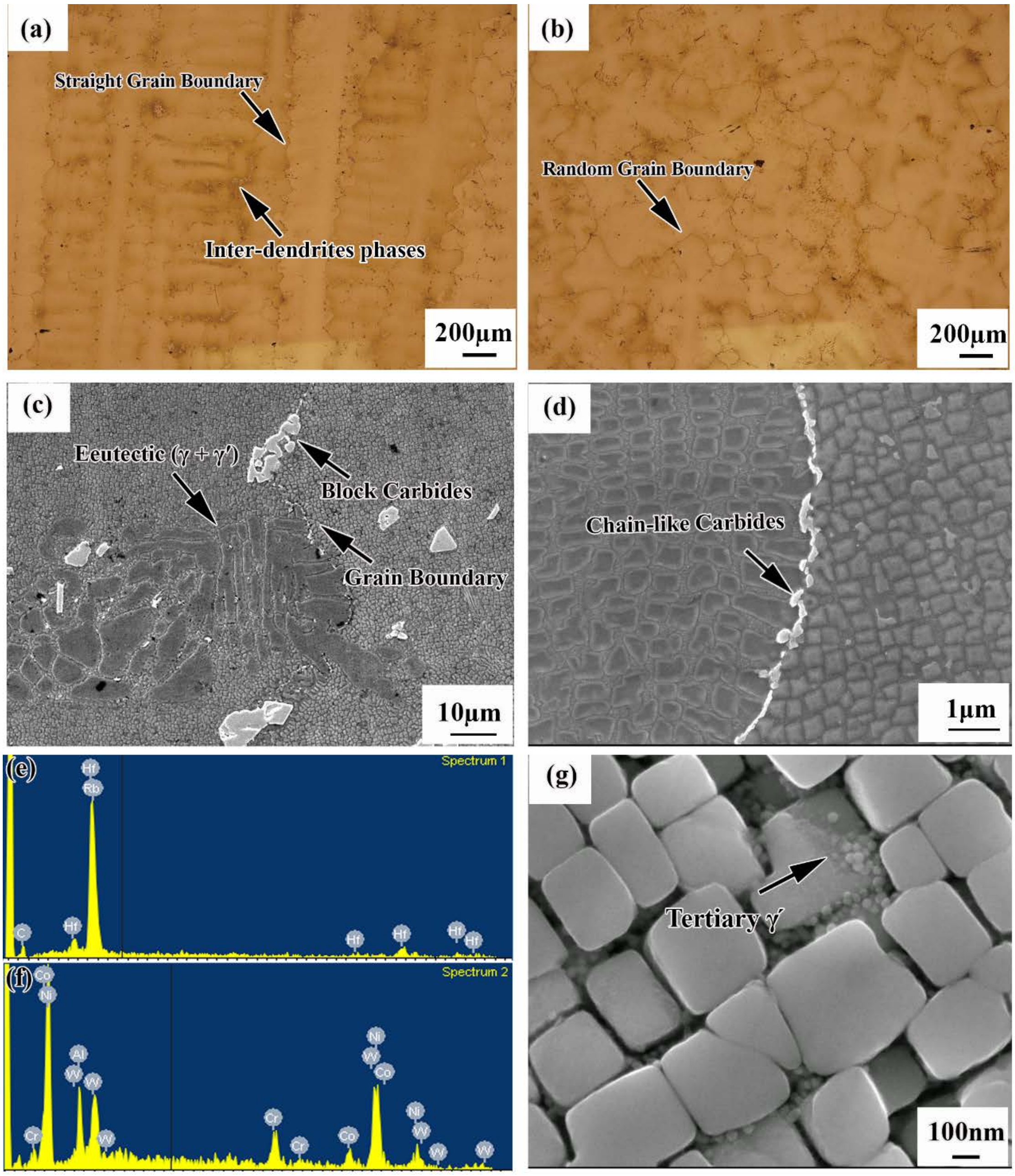

Fig 4.1 Microstructure of CM247LC alloy: (a) Morphology of dendrites at the surface parallel to solidification direction; (b) Morphology of dendrites at the surface perpendicular to solidification direction; (c) morphology of eutectic (γ + γ') and blocky carbides; (d) morphology of grain boundary and chain-like carbides; (e) and (f) EDX analysis of blocky carbides and chain-like carbides; (g) secondary γ' and tertiary γ'

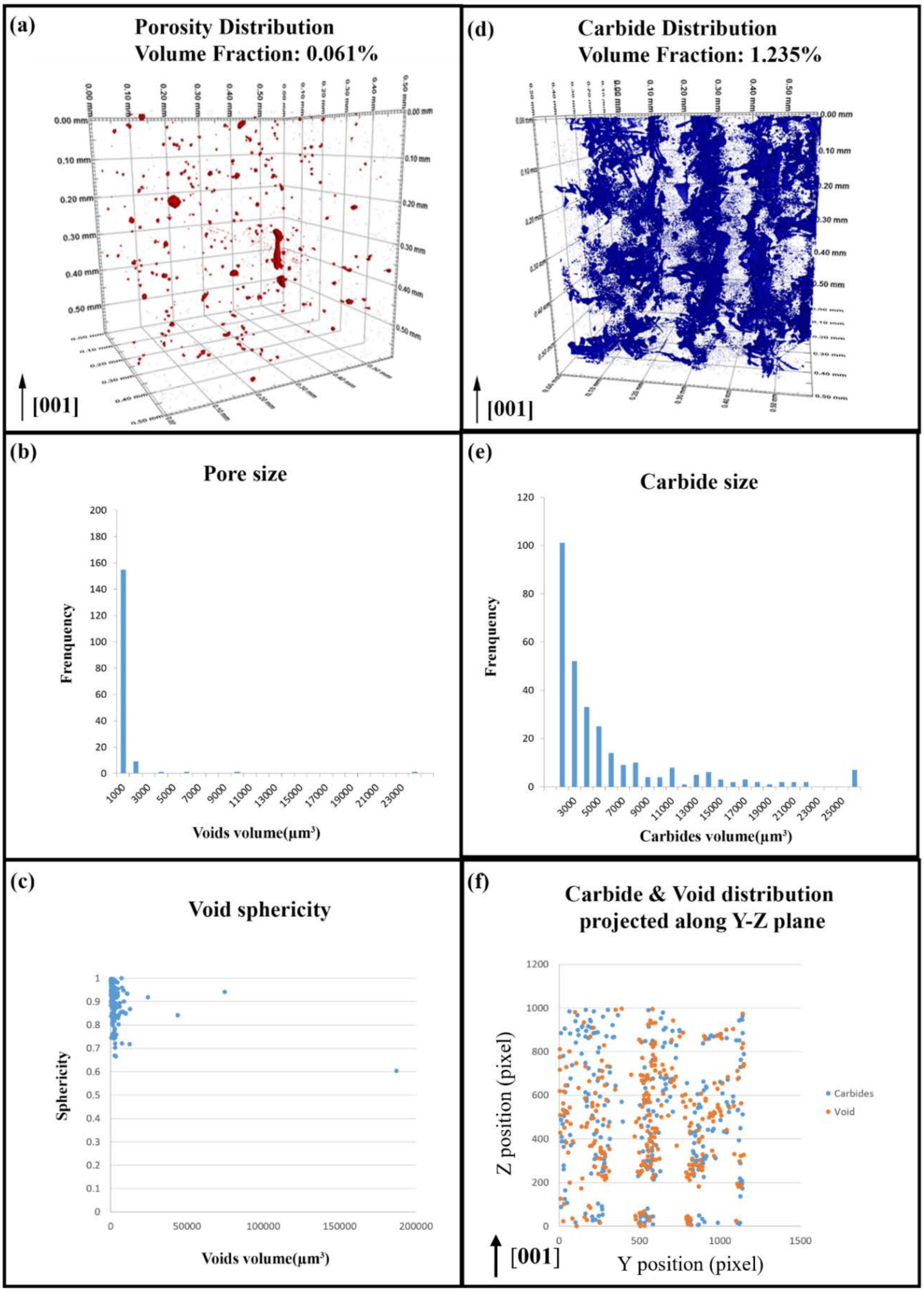

Fig 4. 2 SRCT characterization of voids and carbides in CM247LC alloy: (a) pore distribution in 3D; (b) quantified statistical distribution of pore size; (c) pore sphericity; (d) carbide distribution in 3D; (e) quantified statistical distribution of carbide size; (f) projection of voids and carbides to a plane normal to the solidification direction of CM247LC alloy

The visualized 3D renderings and statistical data obtained from SRCT are presented in Fig. 4.2. The porosity volume fraction is 0.061% in the alloy (Fig. 4.2 (a)), which is far less than that reported for many DS and SX superalloys like MD2 and CMSX-4 [7, 51]. Most pores are smaller than 3000 μm^3 in volume and have a near spherical shape as shown in Fig. 4.2 (b) and (c). In contrast, the volume fraction of carbides is quite high, up to 1.235% (Fig. 4.2 (d)), and the carbide size is more varied, ranging from 1000 to over 25000 μm^3 (Fig. 4.2 (e)). These are distributed at the inter-dendritic regions and often associated with pores as shown in Fig. 4.2 (f), an image of the projection plane normal to the solidification direction. From the 2D observation via OM and SEM, carbides are indeed largely precipitated at the inter-dendritic regions, but pores are seldom observed in those regions due to their low volume fraction. It should be noted that the carbide precipitation along GBs cannot be reflected by the 3D renderings, because the size of the chain-like carbides is lower than the minimum resolution of SRCT and also the narrow gauge of the dog-bone specimen is smaller than the average columnar grain size, meaning that potentially no grain boundary is included in the CT scanning region.

4.3 Anisotropic mechanical response for DS CM247LC

Fig. 4.3 (a) clearly shows the differences in the stress-strain curve for the L and T specimens in the tensile test. The Young's modulus of the L specimen is 150 GPa, clearly lower than that of T specimen at 177 GPa, while the L yield stress is 932 MPa, higher than that of the T sample at 820 MPa. These results are consistent with [168, 169] who also found that in single crystal (SX) Ni base superalloys the [001] direction always exhibited lower Young's modulus but higher yield stress compared with other directions. The mechanical responses to cyclic loading under bend exhibited similar behaviour to the monotonic loading under tension in the elastic regime for the LR, RR and RL specimens in Fig. 4.3 (b). The Young's modulus of the LR specimen (columnar grains aligned with the loading axis) is 138 GPa, lower than that of RR (187 GPa) and RL (175 GPa). It should be noted that although the columnar grains are both perpendicular to the loading direction, Young's modulus are somewhat different for the RR and RL specimens. These results indicate that the anisotropy of mechanical response for three-point bending is not only dependent on the relationship between columnar direction and loading direction, but also is affected by the columnar direction with respect to the normal direction of the top surface.

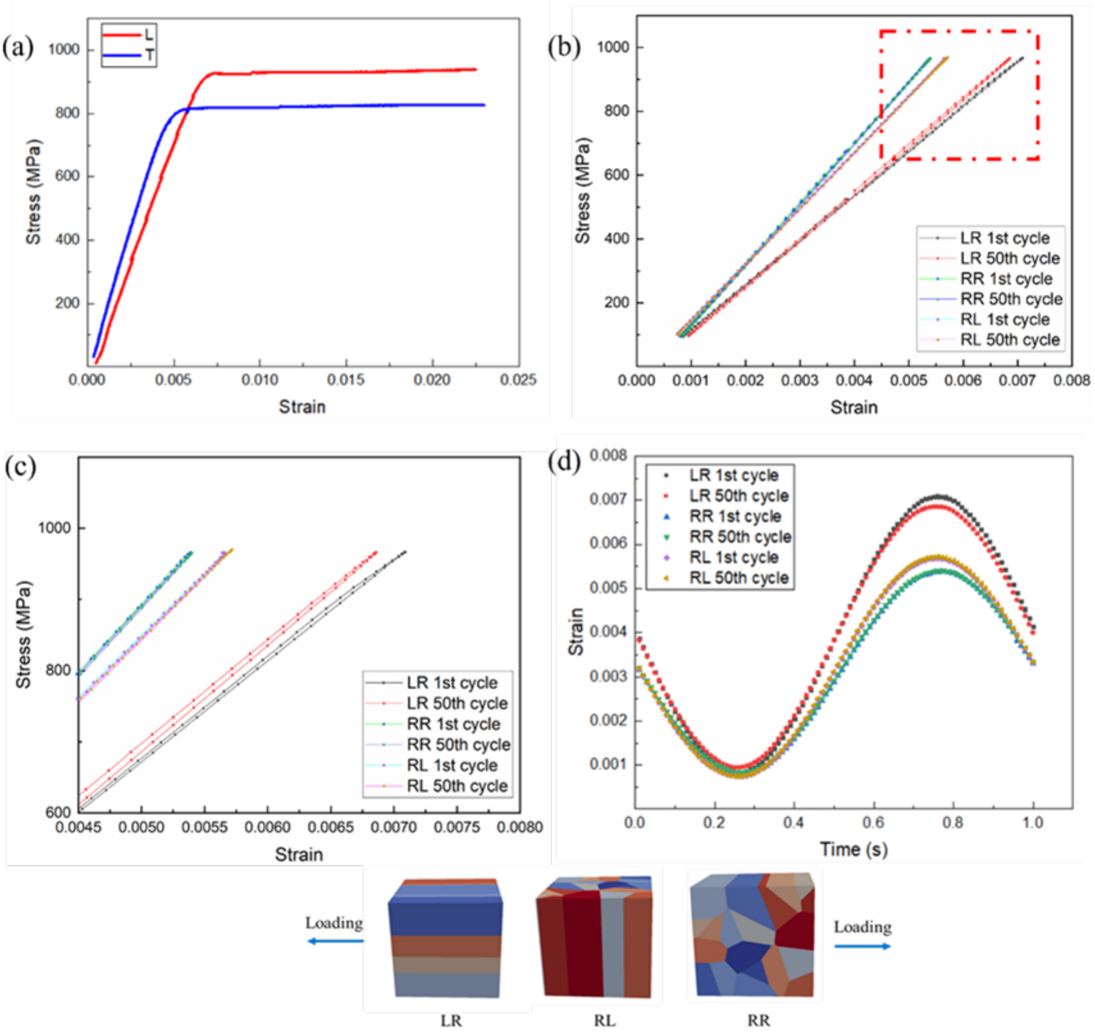

Fig 4.3 The strain-stress curves of (a) L and T specimens subjected to uniaxial tensile testing, (b) LR, RR and RL specimens subjected to cyclic loading, (c) the plastic regime; (d) curves of strain variation against time

Fig. 4.3 (c) presents the elasto-plastic response of the three PBBs subjected to the different levels of cyclic loading, corresponding to the red rectangle in Fig. 4.3 (b). The loading and unloading curves are distinct for the LR sample, showing that the specimen yields (as expected) when subjected to the cyclic loading at a maximum stress 105% of the expected yield stress. In addition, cyclic strain hardening was observed for the LR sample, as the maximum strain decreases from the 1st cycle to the last cycle (50th cycle). It is expected [170] that the piling-up of dislocations will lead to strain hardening, and this also confirms plastic deformation is occurring in the LR specimen. However, plastic deformation does not seem to occur for the RR and RL samples, even though the maximum stress produced by the loading is expected to be 117% of the expected yield stress (i.e. the same applied maximum stress as the LR specimen). This is confirmed by the coincident loading and unloading curves in Fig. 4.3 (c). In addition, the curves of strain variation against time in Fig. 4.3 (d) are identical for the first and last cycle, also indicating minimal plastic deformation for RL and RR specimens under bend loading. Therefore, the plastic deformation behaviours are quite different for T and RR (RL) specimens, when subjected to monotonic (uniaxial) tensile and cyclic bending (where a stress gradient is expected) loads, although the grains are all oriented perpendicular to the loading axis.

4.4 Comparison of the fatigue short crack growth behaviours

All the fatigue tests performed and their corresponding lifetimes are summarized in Table 4.1. The notional maximum strain measured from tensile tests (Fig. 4.3 (a)) and cyclic loading tests (Fig 4.3 (b) and (c)) are plotted against cycles in Fig. 4.4 (a). The large gap of notional maximum strain between L and T or LR and RR (RL) are mainly attributed to the anisotropy in Young's modulus (the material has not yielded according to Fig. 4.3). The increase in notional maximum strain for L and LR specimens is more remarkable than T and RR (RL) specimens with the increase in applied maximum stress. Accordingly, the decrease in fatigue life of L and LR specimens are much more significant, compared with T and RR (RL) specimens. Particularly, when the notional maximum strain is increased to 0.0064 for LR specimen (corresponding to 95% of the L-specimen yield stress), the fatigue lifetime is lower than that of RR and RL specimens. As stated in the introduction section, the SX superalloy with [001] direction shows the longer fatigue life at low applied stress, and with the increase in the applied stress, the [111] direction exhibits a higher fatigue life. The current work is consistent with this research, though the material studied here is a DS system. To consider this in greater depth, the following sections focus on the crack initiation and

Table 4.1 The fatigue lifetime variations of the tested specimens

Maximum stress	L (LR)	T (RR, RL)
792 MPa (tension-tension test)	180041 cycles (L) 152611 cycles (L)	75896 cycles (T) 75554 cycles (T)
838 MPa (three-point bending test)	101352 cycles (LR) 70432 cycles (LR)	66604 cycles (RL) 53894 cycles (RL)
885 MPa (three-point bending test)	50819 cycles (LR) 37500 cycles (LR)	77125 cycles (RL) 78540 cycles (RR)

propagation behaviours of the DS materials at an applied maximum stress of 95% of the L-specimen's measured yield stress.

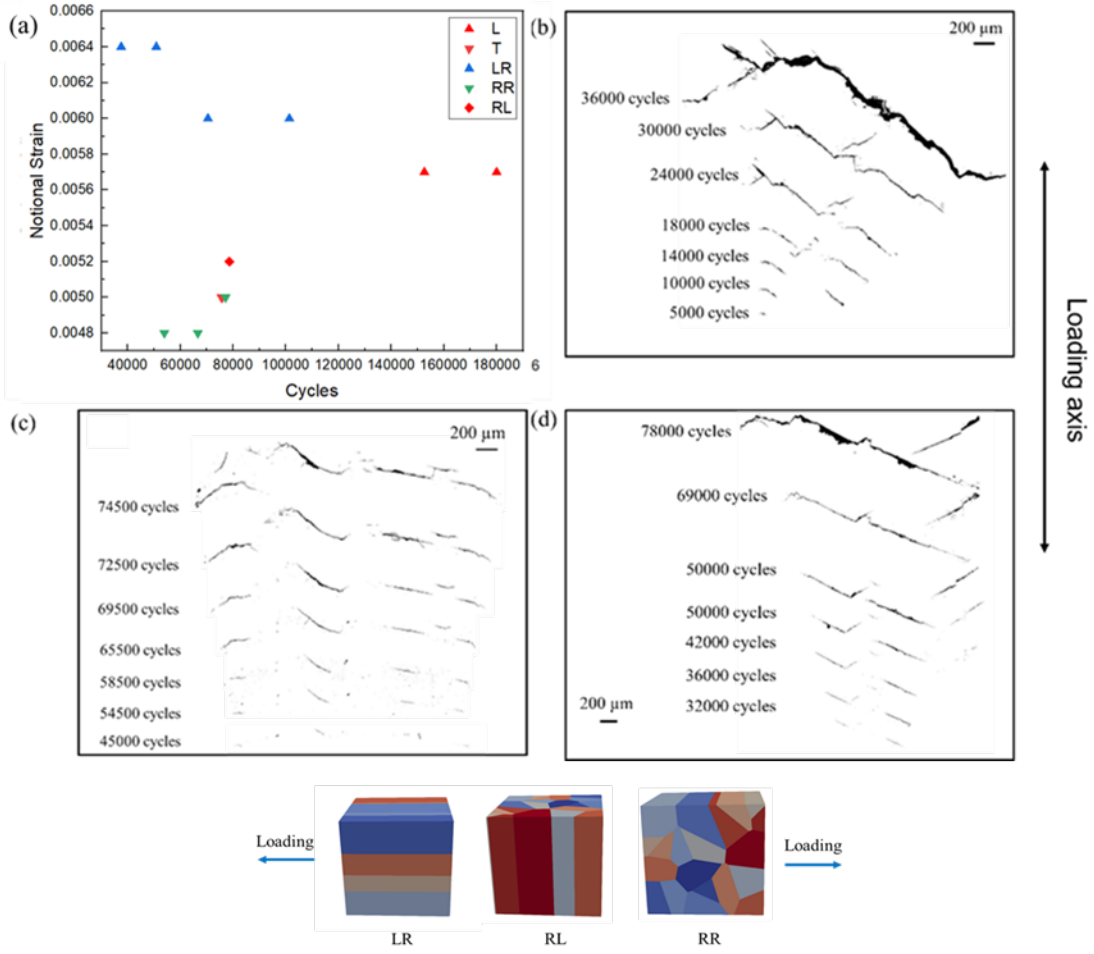

Fig 4.4 (a) the fatigue life of L, T, LR, RR, RL specimens against applied strain; The replica recording of crack initiation and propagation of LR specimen (b), RL specimen (c); RR specimen (d) at maximum stress of 95% yield stress (for the L-specimen).

The primary short crack initiation and propagation behaviours of LR, RL and RR specimens under the maximum stress of 95% L-specimen yield stress, are compared in Fig. 4.4 (b), (c) and (d), recorded by replicas. For LR and RR specimens, the primary (main) cracks originate from 2 small cracks (termed sub-cracks). The two sub-cracks both initially grew straight with the angles approximately close to 40° inclined to the loading direction (following the expected slip systems with maximum resolved shear). Some deflections occurred during the later crack propagation. Finally, the two sub-cracks coalesced to become a longer main crack and propagated until the final failure of the specimen occurred. Completely different crack propagation behaviours occurred in the RL specimen, where the main crack initiated from 5 different sites. These small sub-cracks propagated in different directions, and did not coalesce to a long crack until close to the final failure stage, as recorded in Fig. 4.4 (c). Therefore, the final failure is controlled more by the crack propagation of a single relatively "long" crack for LR and RR specimens, while lifetime was controlled more by the coalescence of several small cracks for the RL specimen. Although the total fatigue life in these tests is not obviously influenced by the grain elongation direction difference with respect to the normal direction of the top surface, in the RL and RR specimens, the propagation behaviour is significantly affected.

Quantitative information on the crack initiation and propagation behaviours has also been obtained from the replicas. The variation in the sub-crack numbers as a function of number of cycles (Fig. 4.5 (a)) clearly shows that the LR sample has earlier crack initiation, compared with RL and RR samples. In addition, the much higher number of sub cracks that evolve in the RL sample during the whole fatigue process, confirms that the final failure is formed predominantly by crack coalescence rather than any substantial period of long crack propagation. The total cycles until first crack initiation and number of cycles after the first crack initiation (i.e. when crack propagation is occurring) until the final failure are compared in Fig. 4.5 (b). For the LR sample, the fatigue life is controlled by the crack propagation, as the cycles for crack initiation is only around one sixth of the crack propagation cycles. In comparison, the cycles needed for crack initiation and propagation are quite equivalent in the RL and RR samples. Strain amplitudes measured from the strain gauge tests for these specimens (when they are subjected to the same applied maximum stress) are also compared in Fig. 4.5 (b). The highest strain amplitude corresponds to the shortest crack initiation and propagation phases, as seen in the LR sample. With the decrease of strain amplitude, the relative number of cycles in crack propagation accordingly increases, which is consistent with the Coffin-Manson relationship. However, an unexpected drop in cycles to crack initiation was found comparing RL to RR specimens, even with the decrease of strain amplitudes. This is mainly attributed to the difference caused by the microstructural features, as the difference of strain amplitudes between the two types of specimens is quite small.

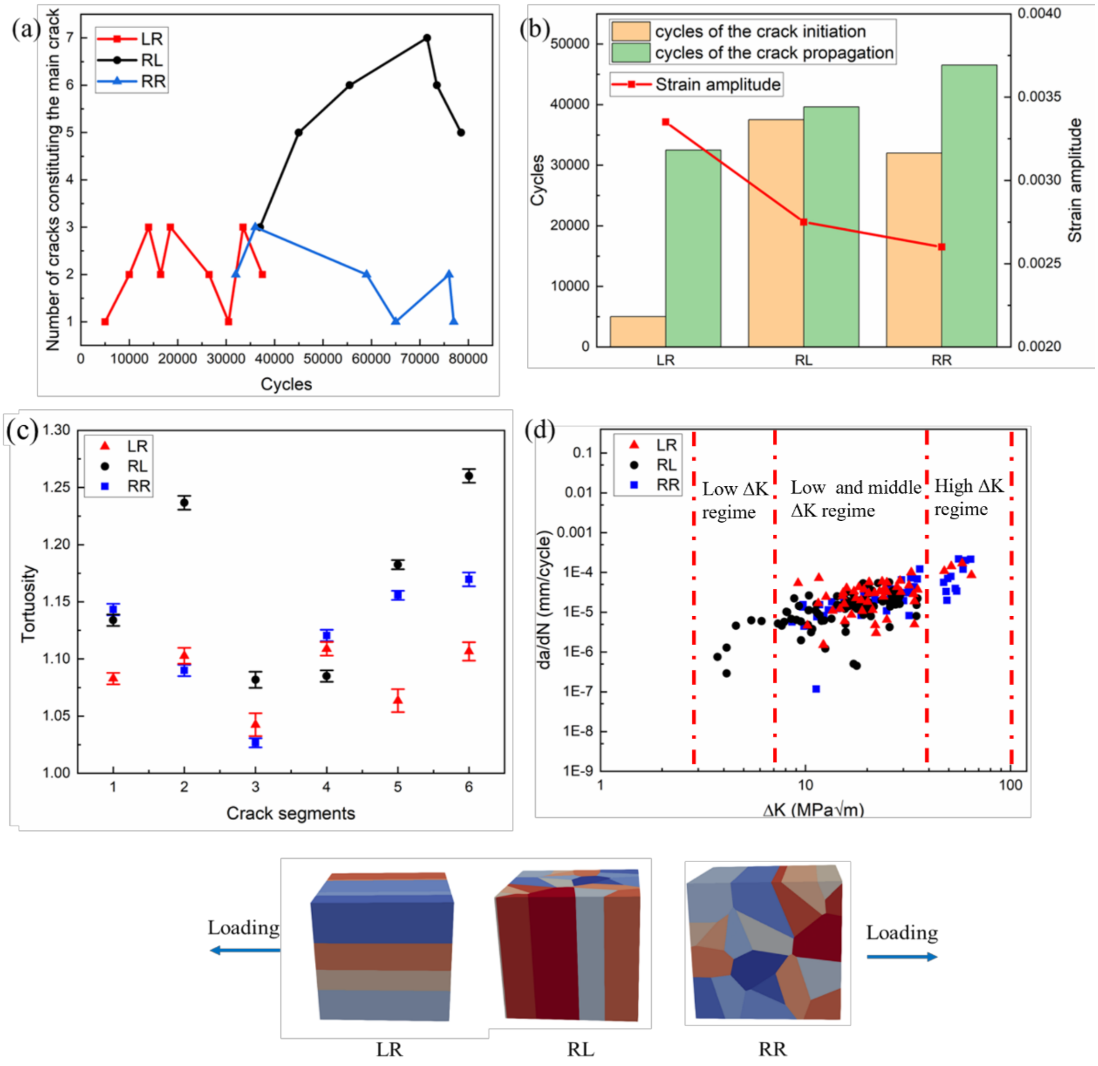

Fig 4.5 the number of sub-cracks constituting the main crack; (b) cycles of crack initiation and propagation overlayed with applied strain amplitudes; (c) tortuosity of the main cracks; (d) the crack growth rates against ΔK of LR RL and RR specimens

Further analysis of crack propagation behaviour is presented in Fig. 4.5 (c) and (d). The whole primary crack (which led to final failure) in these specimens has been considered by being divided into 6 segments, and then the tortuosity of each segment is measured using the distance ratio proposed in [171]. Most of the crack segments in the RL specimen are seen to be more tortuous than those in the LR and RR specimens, indicating greater deflection of cracks. However, the short crack growth rates do not show any noticeable difference between LR, RL and RR specimens in the low and mid ΔK regimes (7 MPa√m to 40 MPa√m) as marked in Fig. 4.5 (d). At high ΔK regime (over 40 MPa√m), the crack growth rates of LR and RR samples are similar, while no crack growth data of the RL sample is recorded, due to the non-formation of a final long crack. At the very low ΔK regime (4 MPa√m to 7

MPa√m), most of the crack growth data is from the RL specimen, attributed to the greater number of crack initiation sites resulting in more records being taken of the early stages of small crack growth.

4.5 Characterization of the crack initiation and propagation

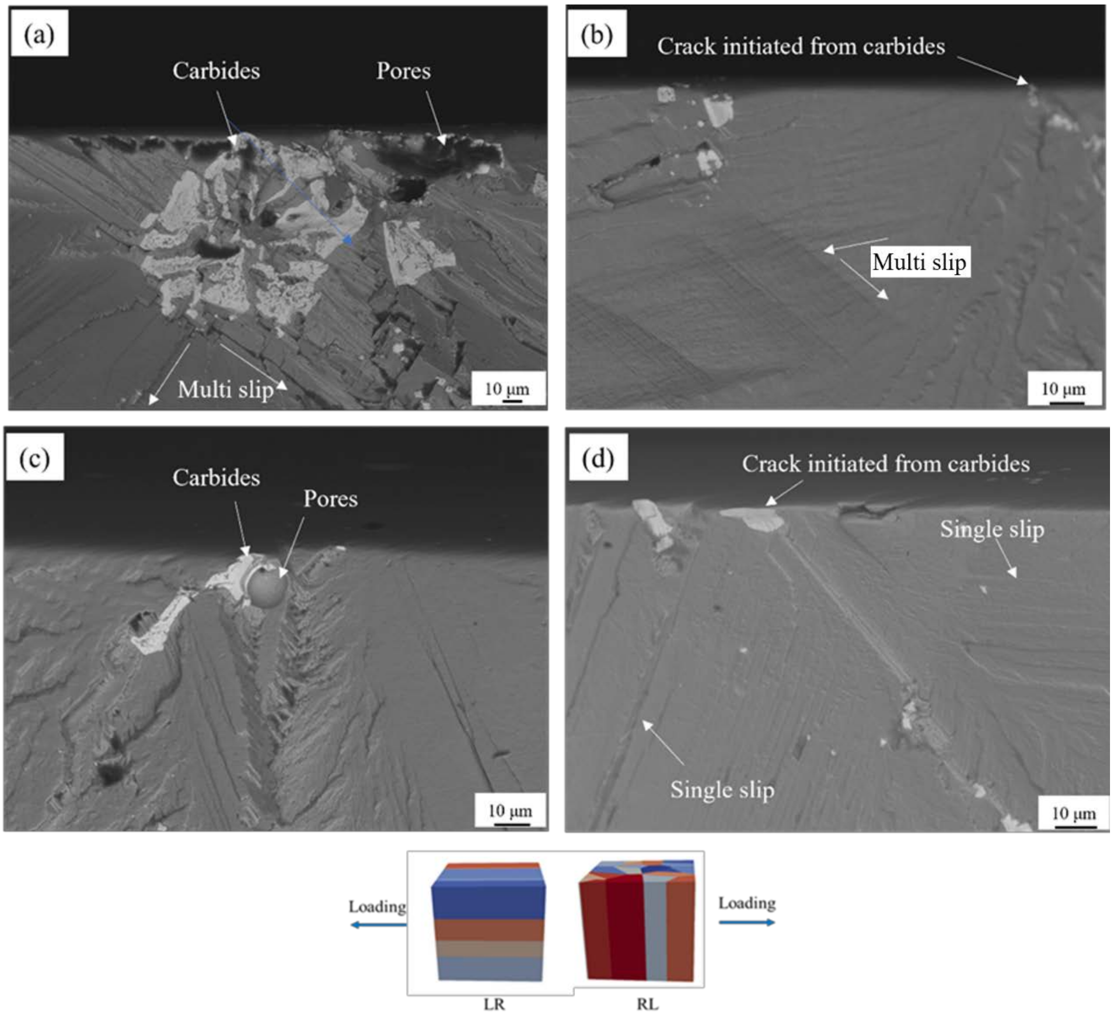

Fig 4.6 crack initiation sites of the LR specimen (a) and (b); RL specimen (c) and (d)

To clearly determine the interactions between these microstructure features and crack initiation behaviours, the fracture surface was carefully examined under SEM, using a Robinson-type backscatter detector (BED-C). Crack initiation sites (recorded by replicas) are mostly located at broken carbides and pores for both LR and RL specimens, presented in Fig. 4.6 (a), (b), (c) and (d). Visible slip bands emanated from these microstructure features, indicating the crack growth following slip systems (i.e. slip band crack growth). Nevertheless, multiple slip systems are activated in the vicinity of crack initiation sites in the LR specimen, while mostly single slip is found in the RL specimen. The results suggest a higher local strain at the crack initiation sites in the LR specimen, consistent with the higher strain amplitude experienced by the sample. The crack initiation sites of the RR specimen are similar to the RL specimen, shown in the next chapter where an in-depth characterization was performed on the specimen [150].

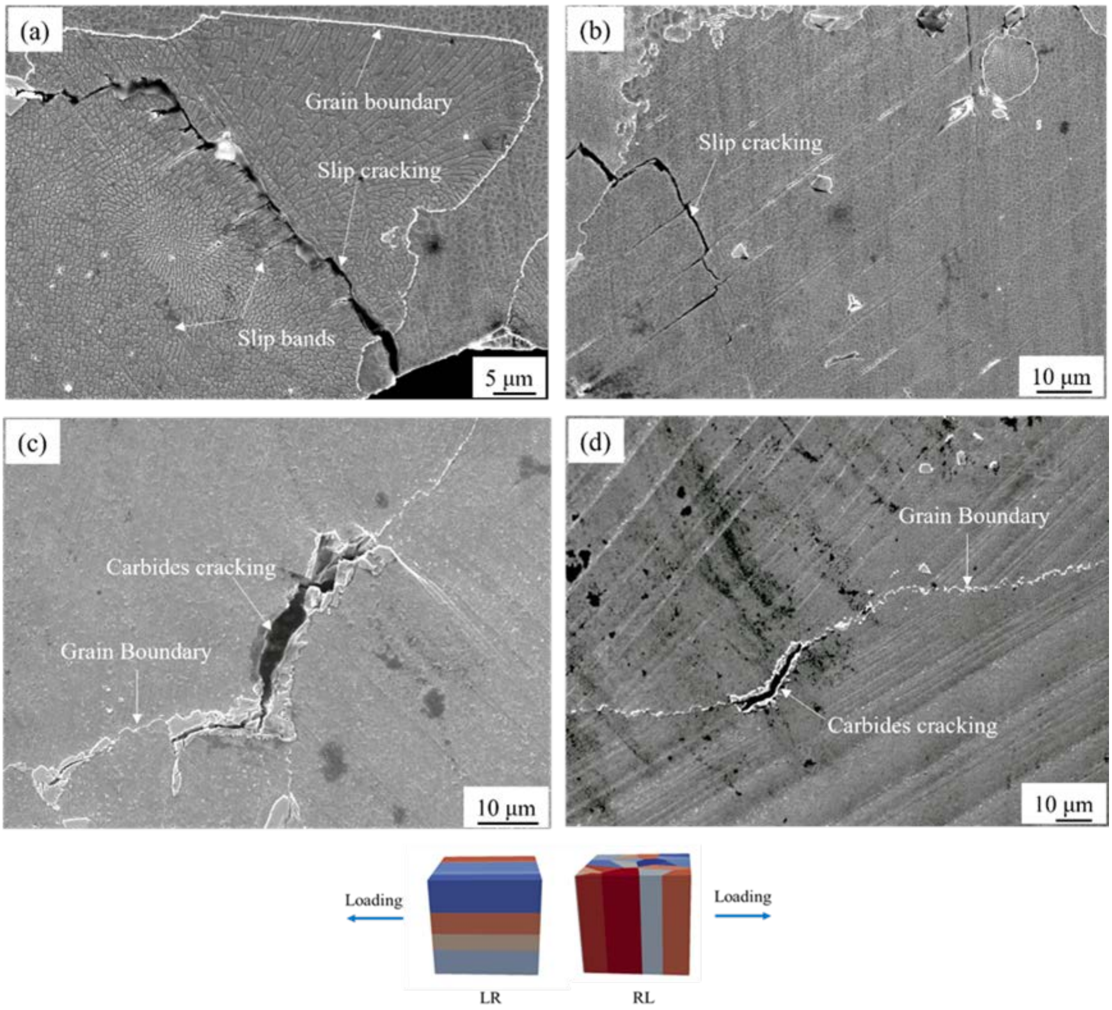

Fig 4.7 The secondary cracks of LR (a), (b) and RL (c) and (d) specimens

The secondary cracks on the top surfaces of the LR and RR specimens are compared in Fig. 4.7. Transgranular slip-band cracking is largely observed in the vicinity of the main crack of the LR sample (Fig. 4.7 (a) and (b)), while more intergranular cracks are initiated from the large carbides at the grain boundaries (GBs) of the RL specimen. For the RR specimen [150], the secondary crack initiation behaviours are closely related to the plastic zone of the main crack. With the increase of the main crack length, the plastic zone of the crack tip is enlarged and the secondary crack initiation sites transfer from large carbides or pores to the slip bands. Therefore, the large amounts of slip-band cracks are potentially due to the larger plastic zone caused by the higher strain amplitude for LR specimen. One long primary crack is not formed during the fatigue life of the RL specimen, resulting in few slip-band cracks and more carbide initiated cracks. It is interesting that although cracks initiate from the large carbides at GBs, the following propagation is not along the GBs for the RL specimen. The same results were found in the RR specimen, attributed to the tiny chain-like carbides at GBs inhibiting crack propagation.

4.6 Discussion

The current work aims to illustrate the effects of anisotropy on the fatigue behaviour of a DS superalloy. According to previous research [172-175], the anisotropic effects are derived from two aspects, of which one is mechanical anisotropy, including Young's modulus [175, 176] and yield stress [177, 178], and the other one is microstructural differences, like textures[179]. The monotonic tensile tests (Fig. 4.3 (a)) and cyclic strain-gauge tests (Fig. 4.3 (b) and (c)) confirm that all the fatigue specimens are under bulk elastic strain, and hence the anisotropic effects brought by gross yield stress differences are not considered here (although local slip band processes will be operating).

4.6.1 The effects of Young's modulus on the fatigue live

A clear trend is presented in the work that specimens with lower Young's modulus (T specimens) exhibit a longer fatigue life when subjected to the lower stress levels (85% and 90% of the L-specimen yield stress). Once the applied maximum stress is increased to 95% of the L-specimen yield stress, the specimen (RR and RL) with the higher Young's modulus shows the longer fatigue life. It seems that the Young's modulus influences the fatigue life through different elastic strains experienced under the same stress amplitude. To quantify the contribution of the Young's modulus to the fatigue live, the positive elastic strain energy density (PESED, ΔE_e^+) is introduced [180, 181]. Researchers proposed different relationships between the ΔE_e^+, Young's modulus and applied stress [182-184]. Herein, the model proposed by Koh[183] is used to assess the effects of Young's modulus:

$$\Delta E_e^+ = \frac{(\sigma_{max} - \sigma_{min})^2}{2E} \tag{4.1}$$

E is the Young's modulus, σ_{max} is the maximum applied stress, while σ_{min} is the minimum applied stress. The calculated ΔE_e^+ is listed in Table 4.2. For specimens (L and LR) with lower Young's modulus, the resultant higher ΔE_e^+ leads to a higher elastic energy accumulation for each fatigue cycle, and finally results in a shorter fatigue life. With the further reduction of the maximum applied stress, the difference of ΔE_e^+ is decreased from 0.49 MJ/m3 to 0.26 MJ/m3 between LR (L) and RL (T). Hence, the effects of Young's modulus are minimized and ΔE_e^+ variation might not be the main factor controlling fatigue life at lower applied stress levels.

Table 4.2 the calculated ΔE_e^+

Maximum stress	L (LR)	T (RR, RL)
792 MPa	1.69 MJ/m^3 (L)	1.43 MJ/m^3 (T)
838 MPa	2.06 MJ/m^3 (LR)	1.52 MJ/m^3 (RL)
885 MPa	2.29 MJ/m^3 (LR)	1.70 MJ/m^3 (RL)

Although the effects of Young's modulus on the whole fatigue life can be understood for LR, RL and RR specimens by considering the PESED model, its specific influence on the crack initiation or propagation behaviours are not described or evaluated in the PESED approach. The replica record of crack growth behaviour shows a strong correlation between the cycles to first crack initiation and the Young's modulus. The subsequent fracture surface characterizations do not show any significant differences in the main crack initiation process. Thus, the crack initiation is mainly influenced by Young's modulus rather than differing microstructures. Another strong evidence supporting the hypothesis is presented in Fig. 4.8. It clearly shows the emergence of slip bands in the vicinity of the main crack at the initial stage of fatigue (5000 cycles) for LR specimen, while few slip bands are observed in the RR specimen even at 32000 cycles. As the microstructural features such as carbides and pores (acting as crack initiation sites) are the same for the two specimens, the localized plastic strain indicated by the slip bands are most likely induced by the higher level of globally applied elastic strain.

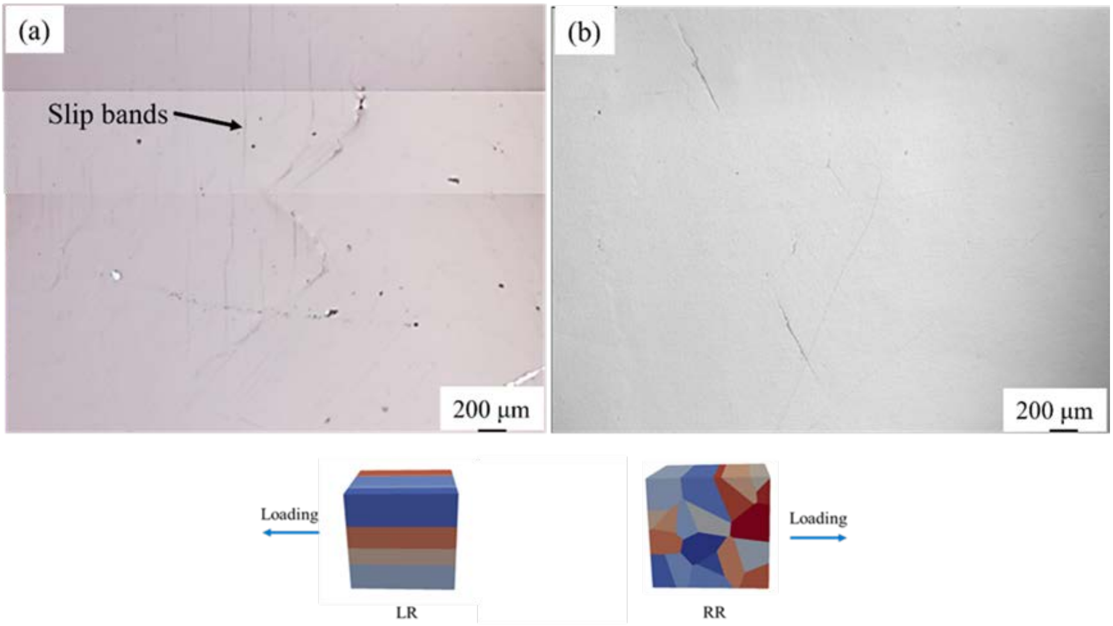

Fig 4.8 Top surface of LR specimen at 5000 cycles and RL specimen at 32000 cycles recorded by replicas

A similar relationship between crack propagation lifetime and Young's modulus is also presented in Fig. 4.5 (b), but the difference of the crack propagation lifetime for these specimens is not as significant as that for crack initiation. Although the crack propagation rates (Fig. 4.5 (d)) do not show apparent differences for these specimens, it should be noted that the data is somewhat scattered and the crack length measurements made manually from replicas might introduce some error. Many models [163, 185-187] are proposed to predict the correlation between crack growth data and Young's modulus, and most of them are based on the following relationship:

$$CTOD = \alpha \frac{K^2}{E\sigma_Y} \tag{4.2}$$

CTOD is the crack tip opening displacement, which acts as the driving force for crack propagation; E is the Young's modulus; $\sigma_Y$is the initial yield stress. In this work, all the specimens are subjected to the same stress. Given that only the driving force for the same length of crack is considered, K would then be the same for LR, RR and RL specimens. The ratio of CTOD of LR, RR and RL are calculated to be 1.19:1:1.07. Based on this hypothesis, the driving force of crack propagation (at any given K-level) for the LR specimen is the highest, which does correlate to the shortest crack propagation lifetime. However, the lowest driving force predicted for the RR specimen does not correspond to the longest crack propagation lifetime. This might be caused by the different crack propagation behaviours, as many cracks propagated simultaneously for the RL specimen, accelerating the total failure process, with coalescence being an important contributor to early failure.

4.6.2 The effects of anisotropic compatibility of GBs on the fatigue crack initiation

As shown in the Fig 4.7, the main difference between the crack initiation behaviours of RL and LR samples are whether the fatigue cracks are initiated from GBs (in RL) or slip bands (LR). The precipitates at the GBs and misorientation between neighbouring grains are the same for both the RL and LR specimens. Therefore, the different crack initiation behaviours are potentially correlated with the crystal orientation with respect to the loading direction. Introduced in the section 2.2.3.3, m' is recognised as the parameter assessing the compatibility of GBs under the loading direction.

To theoretically calculate m' for GBs in DS materials, a series of columnar grains with idealised crystallographic orientation were created using the MATLAB-based open-source software – MTEX [188]. The crystallographic direction [001] is aligned with the long axis of the columnar grains, due to the grains preferentially growing along the [001] direction during solidification [150, 167, 189]. Thus, the misorientation between these columnar grains are derived from relative rotations of the crystals around the [001] axis. In this case, the slip systems of each grain also rotate around the same axis (in the paper, the Z axis is set aligned with the grain growth direction) as shown in Fig. 4.9 (a). Two loading directions are considered in the current work to analyse the anisotropic compatibility of the GBs. One is aligned with the [001] direction, termed as the LR sample, while the other one is perpendicular to the [001] direction (for some grains, the load is along the [010] direction), termed as RL. Due to the symmetrical nature of the FCC crystal, the crystal rotation angle is considered in the range of 0 to 90 degree, with a minimum rotation angle difference of 5 degree (the minimum grain misorientation is set as 5 degree). Since the [001] direction is aligned with the grain growth direction for the idealised grains, the only non-zero Euler angle φ1 represents the rotation angle around the [001] axis shown in Fig. 4.9 (b). The inverse pole figure along the Z and X axis (IPF Z and IPF X) shows a consistent result, that all the grains have a crystal plane normal of [001] along the Z axis, while this varies along the triangle edge from [001] plane normal to [011] plane normal in IPF Y. Therefore, when loading along Z axis (L specimen), eight equivalent slip systems are activated with the same Schmid factor [190]. In comparison, when loading along the Y axis, the number of equal slip systems depends on the rotation angle φ1.The m' is calculated using the equation 3.6 and 3.7.

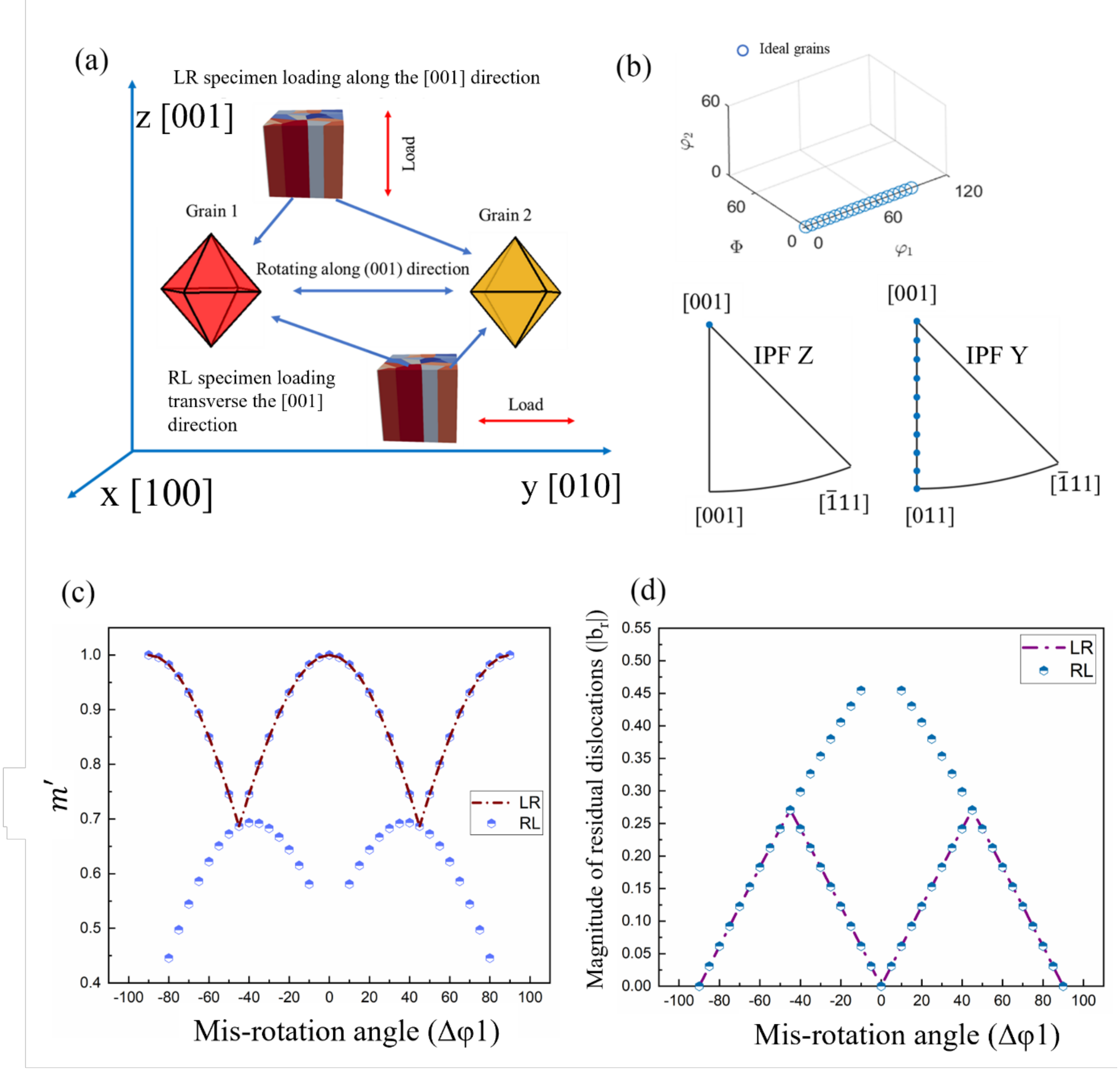

Fig 4. 9 schematic diagram showing the slip systems in the columnar grains and their relationship to the loading direction, (b) the ideal grains in Euler space and their projections in the IPF X and IPF Z; (c) the m prime with the mis-rotation angle, (d) the magnitude of the residual dislocations (unit: a) at GBs with mis-rotation angle

Based on this model, the compatibility of GBs between these idealised columnar grains could be calculated and plotted against the difference in the rotation angle, termed as Δφ1 in Fig. 4.9 (c). For the LR sample, the m' is only a function of Δφ1, reaching a maximum at 90 degree and a minimum at 45 degree. For the T sample, the m' is not only affected by Δφ1, but also the crystallographic orientation with respect to the loading direction. Therefore, for the neighbouring grains with the same Δφ1, the m' might be different. Generally, the compatibility of GBs in LR sample is much better than the RL sample. The magnitude of residual dislocations is calculated following [191, 192], using the pair of slip systems with the maximum m', shown in Fig. 4.9 (d). This shows the consistent result that more residual dislocations are generated at the GBs of the T sample, particularly when $\Delta\varphi1$ is in range of -45 to 45 degree. Therefore, the anisotropic compatibility of GBs is shown for idealised columnar grains of DS materials. The lower m' is potentially the reason for the multiple intergranular cracks in the RL sample.

4.6.3 The effects of crystal orientation on the crack propagation

The results in the Fig. 4.4 and Fig. 4.5 (c) shows the difference of crack propagation behaviours between RL and LR (RR) specimens. Linking to the previous discussion, this should be attributed to the anisotropy of microstructures rather than the global mechanical property differences. To further understand the microstructure effects, EBSD mapping was performed on the regions of the top surface containing the crack initiation sites in Fig. 4.10. The inverse-pole-figure (IPF, projected along the loading direction) coloured map is overlayed with band contrast maps (Fig. 4.10 (a) and (c)) to show the interaction between the grain orientation and the main cracks. The slip traces which the cracks always propagate

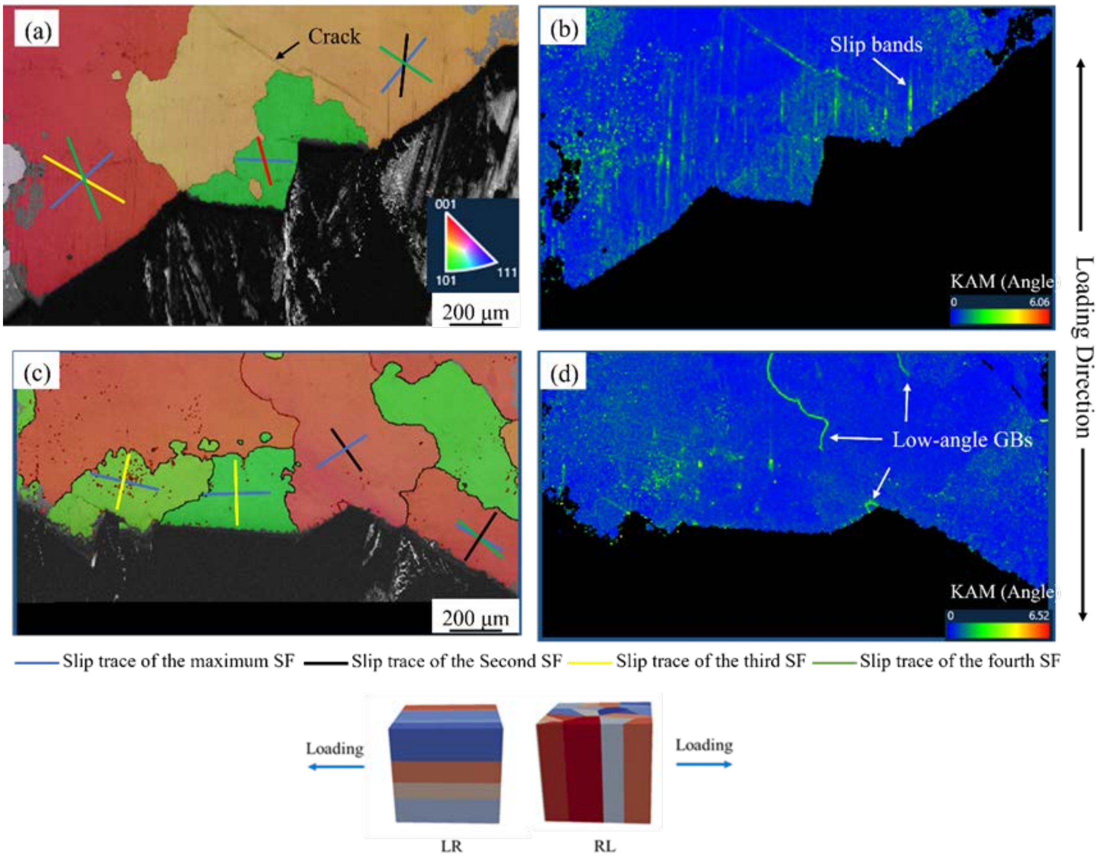

Fig 4.10 IPF maps overlayed with band contrast maps and slip traces of (a) LR specimen, (c) RL specimen, KAM maps of (b) LR specimen and (d) RL specimen

along are also drawn in the grains alongside the main crack. The study of Jiang et. al [73] show that the short fatigue cracks only grow along the slip traces of high Schmid factor (SF) at room temperature. Hence, only the slip traces with top-four SF are picked in Fig. 4.10. The main cracks follow the slip traces of maximum SF for most of the grains in both LR and RL specimens, except in the grains containing crack coalescence. Apparently, the deflections occur when the crack encounters GBs, due to the misalignment of slip systems between neighbouring grains for both LR and RL specimens[193]. Kernel average misorientation (KAM) maps are performed on the same area, which could be used to analyse the localized strain [194] in Fig. 4.10 (b) and (d). The results are consistent with the records of replicas that large amounts of localized strain bands are emerging from the main crack for the LR specimen.

4.7 Summary and conclusion

The current work systematically studies the anisotropic fatigue behaviours of a DS superalloy with grains oriented parallel and transverse to the loading direction. The specimens are subjected to different levels of applied stress below the yielding point. The following conclusions could be drawn from careful analysis.

(1) SRCT can accurately capture the location, size and morphology of blocky carbides and pores in CM247LC alloy. It is found the two microstructural features are mainly congregated in the inter-dendritic region. Chain-like carbides at grain boundaries cannot be characterized in the technique because their size is lower than the SRCT resolution employed here.

(2) The specimens with columnar grains aligned with the loading direction exhibit higher fatigue lives than the specimens with transverse grains when subjected to the lower applied stress (85% of L-specimen yield stress). With an increase in applied stress, the fatigue lives of specimens with parallel grains decrease dramatically, failing at lower lifetimes than specimens with transverse grains.

(3) The shorter fatigue life of the LR specimen is attributed to the lower Young’s modulus. Particularly, when the applied stress is increased to 95% of the yield stress, the higher associated global elastic strain will induce plastic localized strain more easily in the LR specimen, leading to earlier crack initiation at stress concentration features and faster crack propagation rates (when considering effective CTOD at similar K levels).

(4) Crack initiation behaviours are the same for these specimens, as they all initiated from microstructural features such as carbides and pores that act as stress concentration features.

(5) The anisotropic compatibility of the GBs in the DS materials is found. Theoretical calculations are performed, showing the higher compatibility of GBs in the LR sample and lower compatibility of GBs in the RL sample, which potentially cause multiple intergranular crack initiation.

(6) Crack propagation is mainly influenced by the microstructural orientations as it always follows the slip trace with the maximum Schmid factor. However, the low-compatibility or curved grain boundaries in the RR specimen are inferred to provide more crack initiation sites, resulting in the final failure occurring by coalescence of several cracks (giving a shorter lifetime)

Chapter 5 In-depth analysis of microstructure effects on fatigue short crack growth behaviours

5.1 Introduction

The previous chapter revealed that the fatigue crack initiation and early propagation behaviours are correlated to the microstructural features such as carbides and GBs, though it focused on the anisotropic fatigue behaviours induced by the Young's modulus and crystal orientation with the respect to the loading direction. In the current chapter, only RR-type and T-type specimens are used for in-depth analysis of the interaction between fatigue crack growth behaviours and microstructural features. To achieve this, two recently developed techniques – high-resolution DIC and in-situ fatigue tests under SRCT are employed.

Digital image correlation (DIC) is able to provide a full-field strain distribution at a sub-micron scale, by correlating a random speckle pattern in reference and deformed images. Because crack initiation behaviour is closely related to the strain localization/distribution at microstructural features, this technique has been employed widely in studying early crack growth behaviours [68, 73, 195-197]. Stinville et.al [69] found the strain is mainly accumulated within slip bands adjacent and parallel to twin boundaries (TBs) via this technique, confirming TBs enhance the strain localization. Wael et.al [197] studied the plastic strain accumulation and dislocation interaction at GBs via combining a DIC technique with molecular dynamic (MD) simulations. It is revealed that strain localization at the vicinity of GBs is increased with the magnitude of the residual Burgers vectors (|br|) of dislocations. The magnitude of |br| is associated with misalignment of the slip systems in neighbouring grains. Larger misalignment is less favoured in dislocation transmission across GBs, leading to a high magnitude of residual Burgers vector and strain accumulation. Jiang et.al [68] combined DIC with electron backscatter diffraction (EBSD) in their research on a polycrystal superalloy, and developed a new fracture criterion for future crystal plastic finite element (CPFE) models. The transverse strain ε_{yy} measured by DIC and inclination angle θ (between dislocation slip direction and activated slip trace on $\{111\}$ planes) were identified as two indicators determining development of out-of-plane and in-plane cracks. Moreover, DIC measurement was used in characterizing the strain localization process around pores of different size and shape [51]. It was found that larger sized pores with a sharp tip or local 'ridge' could be more effective stress concentrators and cause crack initiation. All these research studies show that DIC is a promising tool for understanding the very localized strain accumulation and crack initiation mechanisms in such systems.

The aforementioned measurements are two-dimensional (2D), providing information only on the surface fatigue crack behaviours. However, in reality cracks initiate and extend in three directions under triaxial stress states [198]. The dimension normal to the surface cannot be captured by surface based 2D characterization tools. As a result, some bias in understanding the fatigue cracking mechanism might be brought in. To overcome the disadvantages of 2D assessment, 3D techniques are employed. Widely used 3D characterizations include metallography serial sectioning, FIB milling and X-ray computed tomography (X-ray CT) [68, 73, 199, 200]. For the destructive methods (metallography serial sectioning/FIB milling) the observed crack growth behaviour is highly dependent on the selected regions/planes of observation. X-ray CT and SRCT are both non-destructive tools and capable of reconstructing the three-dimensional representations of the area of interests (AOIs) at sub-micron scale [199-202]. Meanwhile, the acquisition time of projection images via SRCT is much reduced compared to traditional X-ray computed tomography (CT), facilitating in situ observation of the damage evolution in the bulk. Thus, this technique can provide a relatively unambiguous insight into historically inaccessible cracking processes at the microstructure-length scale [203, 204]. Morgeneyer et.al [198] combined this technique with digital volumetric correlation (DVC) to investigate early formation of slant fracture. The research confirmed that strain localization at the slant bands is present at the onset of slant ductile fracture, and revealed the process of crack formation in 3D. In addition, SRCT can provide detailed quantification of microstructure features, such as the size, location and shape of larger secondary phases, as well as defects and grains. Hassanipour et.al [205] ranked the contribution of microstructural features to crack growth behaviour, by utilizing the quantification offered by SRCT combined with global sensitivity and principal component analysis.

A so-called data-rich image approach is hence employed to provide a well-rounded and deep understanding of fatigue crack initiation and early propagation mechanism in a DS superalloy CM247LC at low temperatures, by combining traditionally well-established and recently emerging characterization techniques. Replica record analysis, Alicona confocal microscope, OM and SEM were utilized to capture the interaction between cracks and GBs, secondary phases and defects. SEM-DIC was employed to further analyze the strain localization process at these microstructure features. SRCT was carried out to provide an in-situ observation of crack evolution at the microstructural scale. This 3D observation is compared to the 2D observations and reveals a better understanding of fatigue cracking mechanisms in this system. Some aspects of the work detailed in this chapter have been published in the following paper and the co-authors are duly acknowledged for their contributions:

Yuanguo Tan, D.J. Bull, R. Jiang, A. Evangelou, S. Chaudhuri, S. Octaviani, F. Pierron, N. Gao, H. Toda, I. Sinclair, P.A.S. Reed, Data rich imaging approaches assessing fatigue crack initiation and early propagation in a DS superalloy at room temperature, Materials Science and Engineering: A 805 (2021) 14059, https://doi.org/10.1016/j.msea.2020.140592.

For the paper, the In-situ fatigue tests were performed by Dr Daniel Bull, and the DIC analysis was performed by Prof. Rong Jiang and Sari Octaviani

5.2 Fatigue crack initiation and early propagation in the RR sample

The morphology of the main crack is presented in Fig. 5.1 (a), which can be divided into three regions according to the crack propagation behaviour. In region 1 (R1), the main crack generally propagated inclined to loading direction, with an angle of nearly 67.5 degree (measured by Image J). This indicates that the main crack in this region is in stage I of the fatigue process, where cracks follow a single slip system in this 2D view. According to the replica record (Fig.5.1 (b)), two sub cracks were initiated from R1, and propagated in the same inclined direction to coalesce as the main crack. A deflected path occurred at the coalescence point of the two cracks and a "lump" in R1 was formed because of the deflected path. In region 2 (R2), the path of the main crack became tortuous, which might be related to the activation of multiple slip systems moving into the stage II crack growth regime. However, little information on the crack propagation behaviour was recorded in this region as it was close to final fracture and the replica record was limited. In region 3 (R3), the main crack was perpendicular to the loading direction and propagated so fast that no crack history was captured by the replica record. A large plastic zone can be observed near to this region, indicating the main crack unstably propagated to fracture. The fracture surface was reconstructed by Alicona and is shown in Fig. 5.1 (c). The inclined and perpendicular crack paths in R1 and R3 were marked by white arrows on the fracture surface. Large amounts of slip steps were observed close to R1, whilst a dendritic fracture surface is observed close to R3 and in fracture surface regions far from R1. Crack initiation sites were identified by combining the replica record observations and associated fracture features. These initiation sites were usually at the origins of slip steps. Cracks were confirmed to initiate from carbides via SEM when observed at a higher magnification (Fig. 5.1 (d) and (e)), and a large number of slip steps were found to emanate from the carbides which extended in different directions.

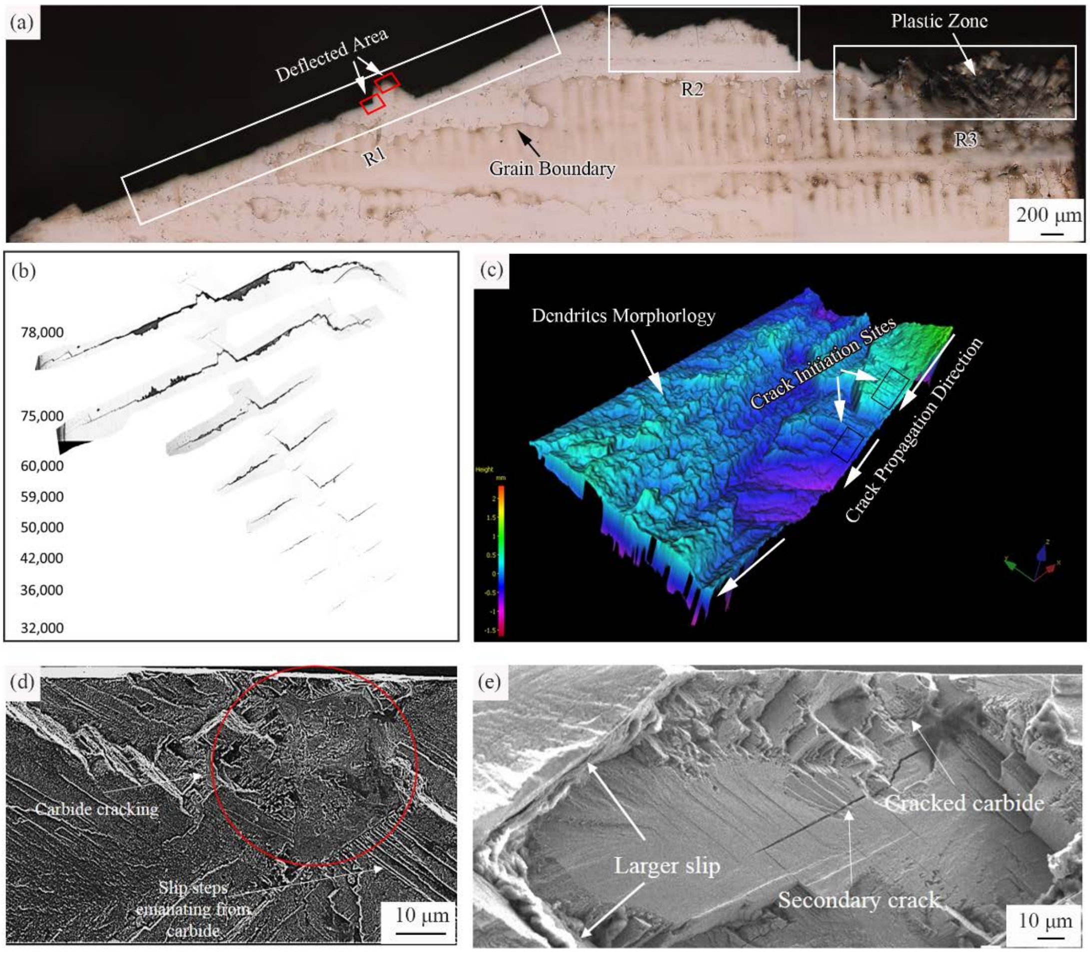

Fig 5.1 Morphology of the main crack under OM; (b) replicas of the main crack; (c) Morphology of fracture surface; (d) and (e) initiation sites of the main crack

Secondary cracks were observed close to R1, R2 and R3 as shown in Fig. 5.2. A handful of micro cracks were found in R1. These secondary cracks mainly initiated at the interior or at the interface of blocky carbides in Fig. 5.2 (a) and (b), although slip band cracking was also observed at the “lump” of R1. To differentiate from secondary cracks in other regions, the cracks seen in R1 are designated as microstructure-induced cracking. In R2, the number of secondary cracks sharply increased, but slip band cracking became the dominant cracking mechanism (Fig. 5.2 (c)). Secondary γ′ was severely sheared by the slip bands in this region (Fig. 5.2 (d)), indicating the decohesion caused by dislocation motion. In R3, carbide cracking was the predominant mode of propagation of secondary cracks. However, in contrast to the cracked carbides in R1, these cracks were more likely to propagate perpendicular to the loading direction within elongated carbides as seen in Fig. 5.2 (e) and (f). Moreover, crack openings in these carbides are large and visible. This type of crack is designated as opening mode carbide cracks in this paper. Cracking mechanisms in R1 are not as clear as those observed in R2 and R3, and were further assessed by DIC in the following section.

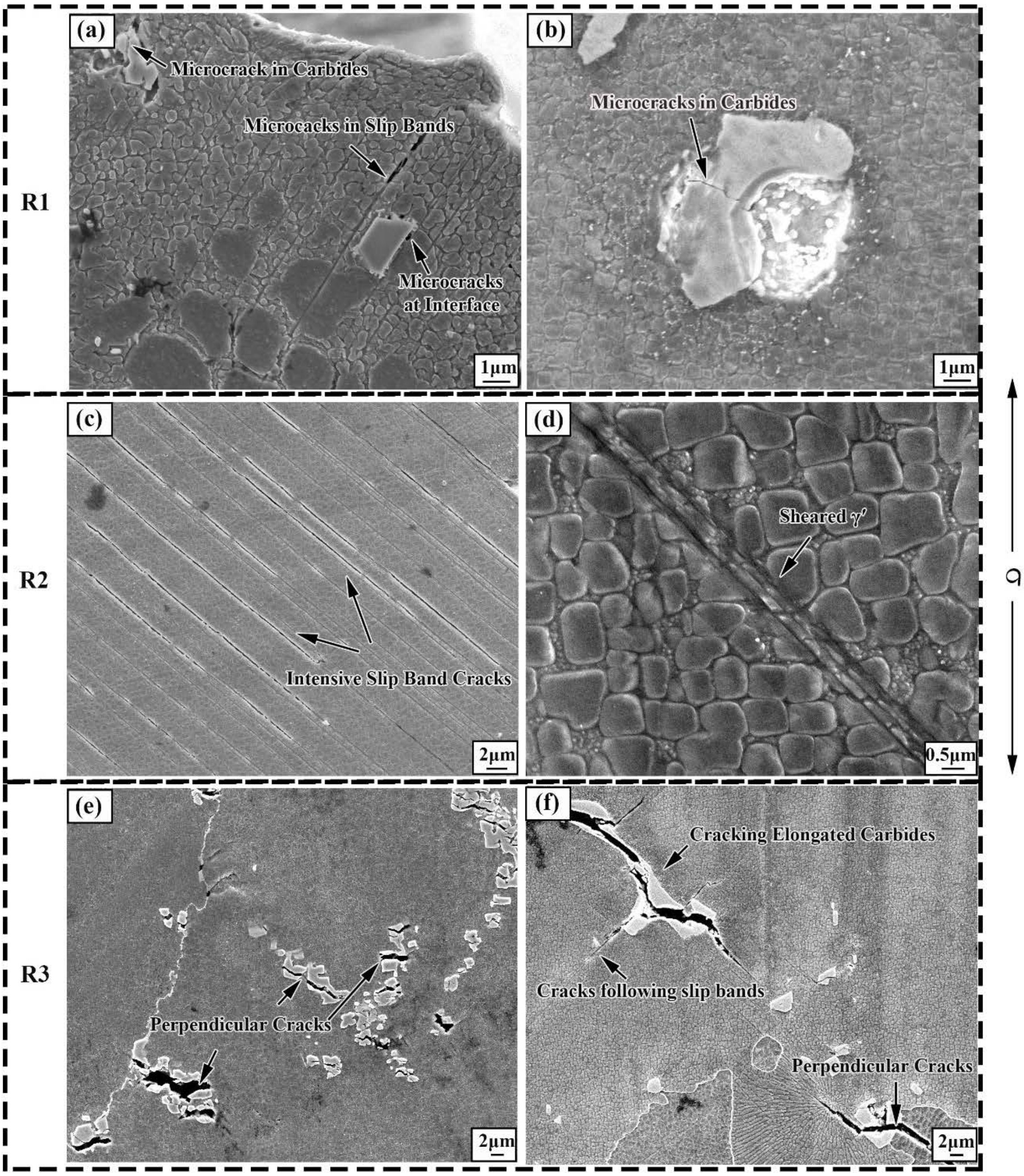

Fig 5.2 (a) and (b) secondary cracks in R1; (c) and (d) slip band cracking and sheared γ′ in R2; (e) and (f) carbides cracking in R3

Slip band cracking was also observed at the "lump" of R1. To differentiate from secondary cracks in other regions, the cracks seen in R1 are designated as microstructure-induced cracking. In R2, the number of secondary cracks sharply increased, but slip band cracking became the dominant cracking mechanism (Fig. 5.2 (c)). Secondary γ′ was severely sheared by the slip bands in this region (Fig. 5.2 (d)), indicating the decohesion caused by dislocation motion. In R3, carbide cracking was the predominant mode of propagation of secondary cracks. However, in contrast to the cracked carbides in R1, these cracks were more likely to propagate perpendicular to the loading direction within elongated carbides as seen in Fig. 5.2 (e) and (f). Moreover, crack openings in these carbides are large and visible. This type of crack is designated as opening mode carbide cracks in this paper. Cracking mechanisms in R1 are not as clear as those observed in R2 and R3 and were further assessed by DIC in the following section.

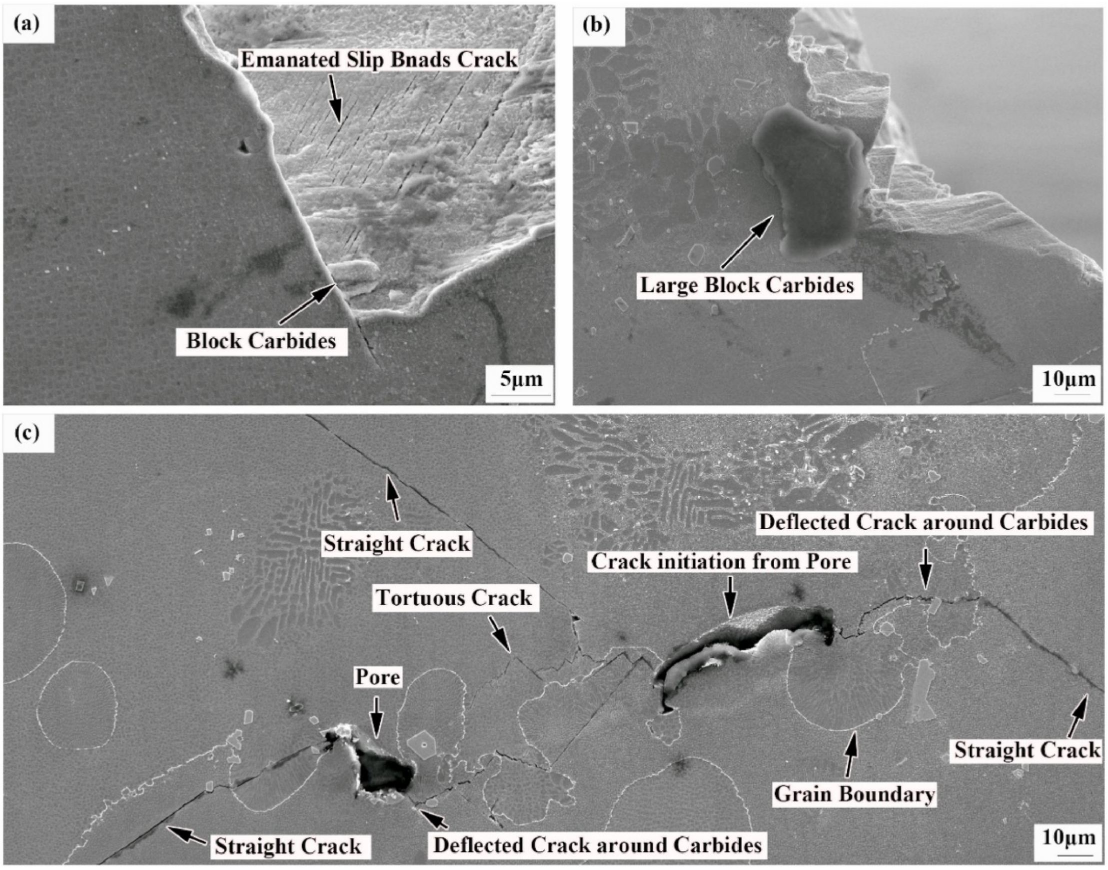

Fig 5.3 (a) and (b) carbides at deflected parts of main crack; (c) propagation of a secondary crack

When assessing effects of microstructure features on early crack propagation, observations were focussed on the deflected areas in R1 marked by red rectangles in Fig. 5.3 (a). This is because once the main crack has passed into stage II (e.g. in R2 and R3) the crack propagation behaviour is relatively uninfluenced by microstructural features. Fig. 5.3 (a) and (b) are SEM images of the deflected parts of the main crack. Carbides blocked crack propagation and led to a deflected or tortuous crack path as shown in the images. It is noteworthy that Fig. 5.3 (a) showed a carbide beneath the surface which impinged on the original crack path and activated more slip systems. This means crack propagation behaviour on the surface is indeed influenced by some microstructure features beneath, which is often not captured by 2D characterization. Several secondary cracks away from R1 were stitched together into Fig. 5.3 (c). These cracks initiated from two pores at GBs, but didn't propagate along GBs, indicating that the chain-like carbides possess good resistance to cracking. After initiation from the pores, cracks generally propagated straight (along slip-bands) within grains. However, the cracks cannot directly traverse the carbide phase, consequently the path bows or is deflected in the vicinity of carbides.

5.3 Strain localization

The early stages of strain localization were analysed via ex-situ SEM-DIC. The analysed region and full-field strain distribution at 10000 cycles are presented in Fig. 5.4. This region contained two columnar grains, located on the left and right parts of the image, respectively in Fig. 5.4 (a). The grain boundary is marked in the image, though it is not very clear at this magnification. Local coordinates shown in Fig. 5.4 (c) were chosen to measure the strain localization in the left grain, as the left grain takes up the majority of the full field of view. Three types of strain were identified and measured as shown in Fig. 5.4 (b), (c) and (d). ε_{xx} refers to strain in the X axis direction named as longitudinal strain, ε_{yy} refers to strain in the Y axis direction named as transverse strain, and ε_{xy} is the shear strain. Strain localization of ε_{xx} was not discerned in Fig. 5.4 (b). In contrast, apparent transverse strain was localized within bands in the ε_{yy} map in the left grain, which is associated with crack opening or extrusion/intrusion of the slip bands. Shear strain ε_{xy} was also localized within the same bands of transverse strain, and the strain is related to dislocation slip driven by pure shear stress as indicated by the sheared γ' precipitates in Fig. 5.2 (d). Transverse and shear strain both traversed the whole grain, but impinged at the carbides and GB. Two AOIs were selected to be further analysed under global coordinates using ε_{xy}^{max}, maximum shear strain as the indicators. One area is in the proximity of an elongated carbide named as AOI-1, whilst the other is a carbide precipitated at a GB, named as AOI-2.

The maximum shear strain localization evolution of AOI-1 and AOI-2 are presented in Fig. 5.5. Similarly straight strain bands were discerned within the grains in Fig. 5.5 (a), and the strain intensity was higher than 0.2 at 10000 cycles. However, ex-situ DIC could only provide semi-quantitative assessments of strain, as significant noise was brought into the characterization by repositioning the specimens during the necessary series of image acquisition processes. Thus, the relative strain intensity of different regions could be compared, but cannot be absolutely measured. The strain intensity increases slightly on further loading to 15000 and 22700 cycles in Fig. 5.5 (b) and (c), but the density of strain bands is obviously increased comparing the strain maps at 10000 cycles and 22700 cycles. Some grey spots appeared within the strain bands at 227000 cycles, possibly due to the extrusion/intrusion of strain bands leading to failure in correlating the speckles of the γ' distribution. Carbides are confirmed to have direct effects on material deformation, as the strain band was clearly blocked by the carbide in AOI-1 in Fig. 5.5 (a). The intersection sites of strain bands and the carbide are indicated in Fig. 5.5 (b), and it is interesting to observe that the crack indeed occurred at the intersection sites as shown in Fig. 5.5 (d). Although intensive strain was localized within bands and intensive intrusion of strain bands was observed in Fig. 5.5 (d), no cracks initiated from these bands, which indicates carbide-induced cracking occurs prior to slip band cracking. In AOI-2, two sets of strain bands impinged on the grain boundaries in Fig. 5.5 (e), (f) and (g). Nevertheless, the strain concentration at the proximity of the GB was not obvious until loading to 22700 cycles. In contrast, early strain localization occurred at the carbides located at the GB in Fig.5.5 (e) and caused the carbide cracking finally seen in Fig. 5.5 (h). The crack path includes the early strain localization site marked in Fig. 5.5 (e). It is noteworthy that the crack became bowed as it encountered the blocky carbide below in Fig. 5.5 (h), which is consistent with the aforementioned observation of secondary crack propagation.

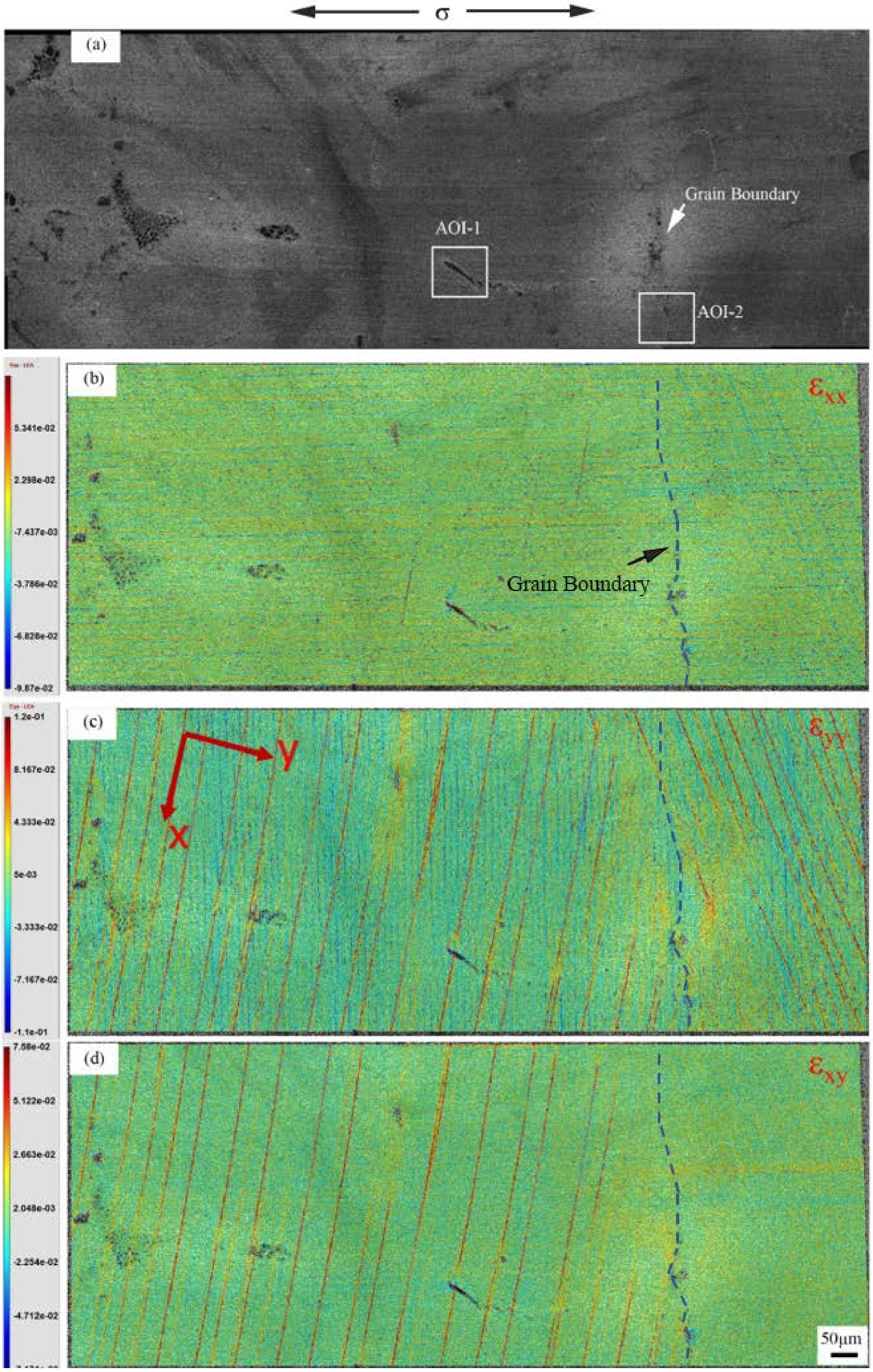

Fig 5.4 (a) full-field reference image; (b), (c) and (d) full-field strain maps of ε_{xx}, ε_{yy}, ε_{xy}

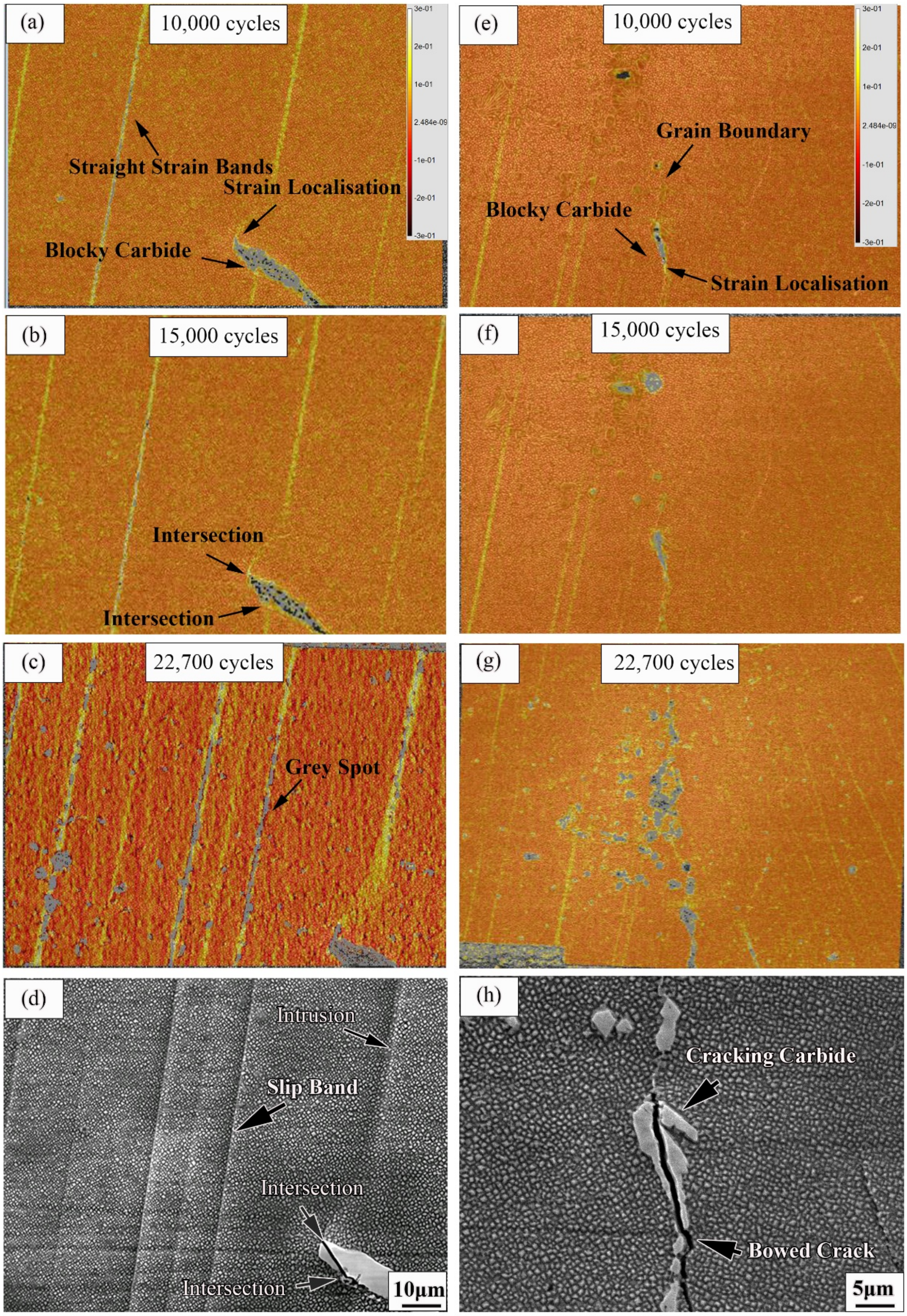

Fig 5.5 Maximum shear strain distribution at interior of grain (a) at 10,000 cycles; (b) at 15,000 cycles; (c) at 22,700 cycles; (d) SEM image of the carbide after 22,7000 cycles; Maximum shear stress distribution at grain boundary at (a) 10,000 cycles; (b) at 15,000 cycles; (c) at 22,700 cycles; (d) SEM image of the carbide at grain boundary after 22,7000 cycles

5.4 In situ SRCT characterization

Two cracks that initiated from pores were selected for CT scanning, one of which was located at the lower parts of the 3D rendering in Fig. 5.6 (b), referred to as crack A (CA), and the upper one was referred to as crack B (CB). From the bottom view of the 3D rendering, the two cracks were located at a nearby side surface. The CB primary growth direction was aligned with the inter-dendritic regions, whilst the CA primary direction lay perpendicular to them. In Fig 5.6 (d), (e), (g) and (h), blue identifies pores, grey identifies carbides, red regions show the crack morphology at 40000 cycles, while the green area shows the crack morphology at 52000 cycles. Carbide distribution in the proximity of CA and CB is presented in Fig. 5.6 (d) and (g) respectively. It is apparent that the density of carbides in the vicinity of CB was much higher than that of CA, with the upper crack being within the inter-dendritic region. Crack morphology segmented by a seeded region growth algorithm was superimposed on the carbide distribution in Fig 5.6 (e) and (h). In the CA, nearby carbides were mainly congregated at one side of the 3D rendering, and cracking planes clearly interacted with these carbides. One cracking plane was parallel and even adjacent to a faceted carbide marked in Fig 5.6 (d) and (e). However, carbides at the far side seemed to have little effect on crack growth from the 3D observation. In the CB, these interactions between carbides and cracks were more obvious, as more cracking planes were induced by the surrounding carbides. One cracking carbide was found in Fig 5.6 (g), and the corresponding cracking plane was marked in Fig 5.6 (h). This is the first report observing a cracking carbide and its associated cracking plane in 3D in a DS system, owing to the high resolution provided by SRCT. The surface slice of the two cracks were shown in Fig 5.6 (f) and (i). Carbides were indeed seen to be congregated at one side of the pore for the CA, which is consistent with the SRCT result. Nonetheless, only one crack was observed on the surface slice, which indicates the inadequacy of 2D observations in accurately characterizing complex crack initiation and growth behaviour. More complicated cracks were observed on the surface slice of the CB, especially, one cracking carbide was captured.

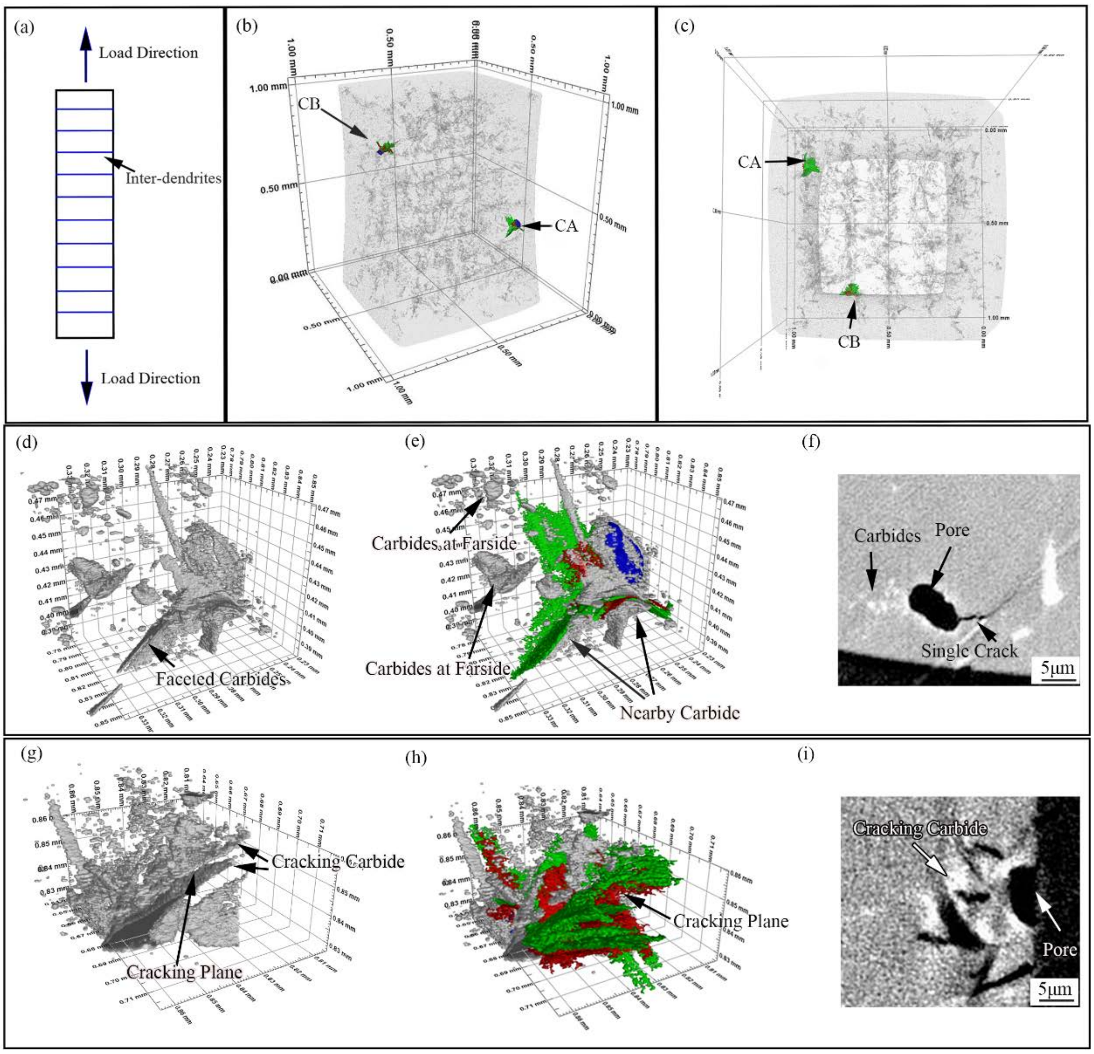

Fig 5.6 (a) schematic diagram of loading tension-tension test; (b) 3D rendering of the specimen in front view; (c) 3D rendering of the specimen in bottom; (d) carbides distribution around CA; (e) superimposed image of carbides and cracking planes around CA; (f) surface slice of CA; (g) carbides distribution around CB; (h) superimposed image of carbides and cracking planes around CB; (i) surface slice of CB

The evolution history of CA and CB are presented in Fig. 5.7, respectively. In CA, four sub cracks are named as CA1, CA2, CA3 and CA4 (Fig. 5.7 (a)). CA1 was initiated from the pore and corresponded to the single crack observed at the surface in Fig. 5.6 (f), whilst other cracking planes CA2, CA3 and CA4 were initiated in the bulk. The four cracking planes propagated in different directions shown in Fig. 5.7 (b) at 52000 cycles. CA1 seems to propagate along a slip system, as nearly no carbides were present in the vicinity of the cracking plane (Fig. 5.6 (e)), while CA2 propagated parallel to a carbide facet shown in Fig. 5.6 (d) and Fig. 5.7 (b). The two cracks both grew substantially as shown in Fig. 5.7 (c).

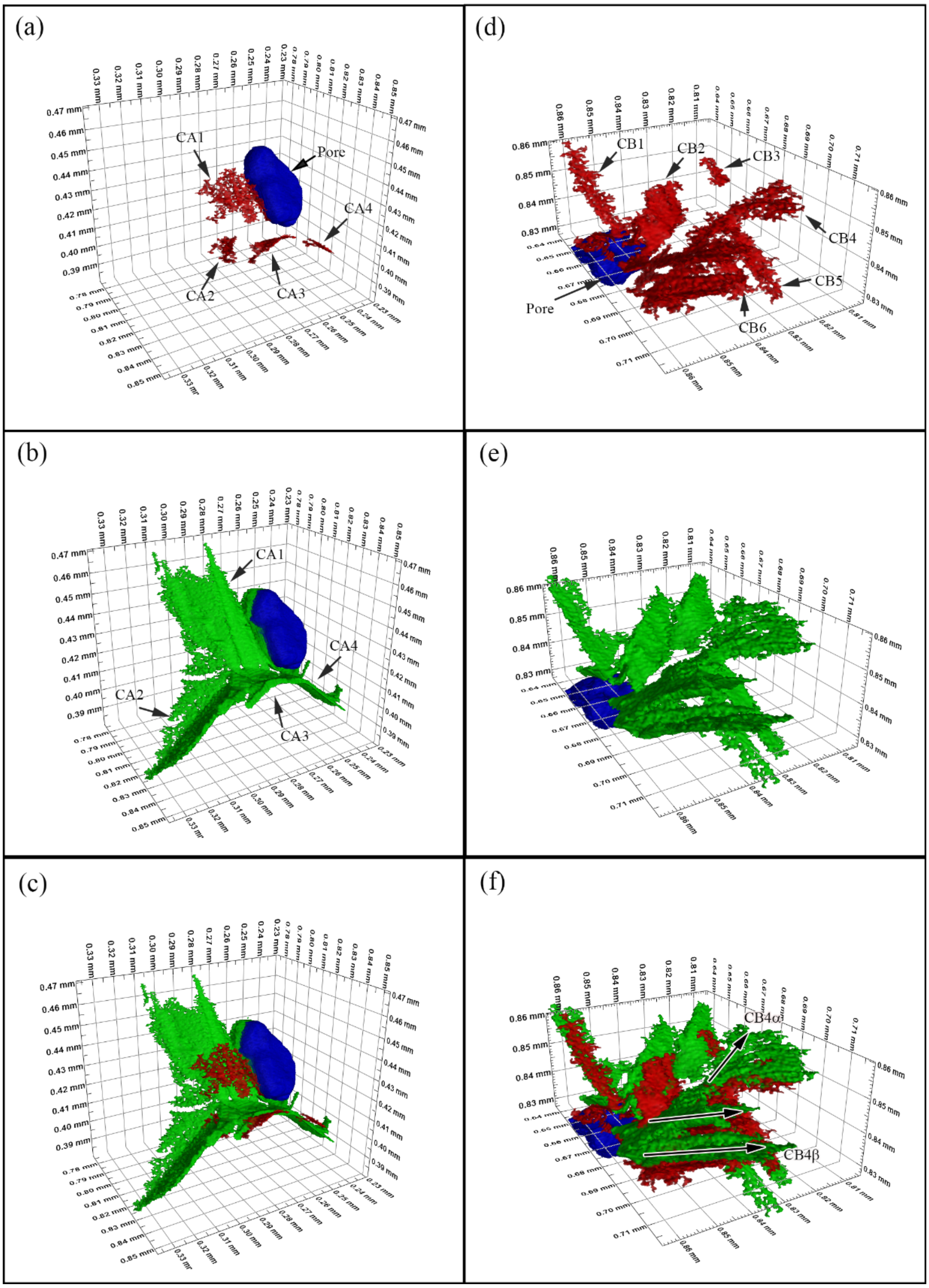

Fig 5.7 CT images of CM247LC crack propagation. (a) cracking planes at 40000 cycles of CA; (b) cracking planes at 52000 cycles of CA; (c) superimposed image of cracking planes at 40000 and 52000 cycles of CA; (d) cracking planes at 40000 cycles of CB; (e) cracking planes at 52000 cycles of CB; (f) superimposed image of cracking planes at 40000 and 52000 cycles of CB

CA3 and CA4 had a very limited growth compared to CA1 and CA2, potentially because carbides were concentrated at regions that blocked CA3 and CA4 propagation. This result confirms the potential of shielding effects of carbides on crack propagation. More sub-cracks were generated in CB, named as CB1 to CB6 respectively in Fig. 5.7 (d). Observation was focussed on CB4, which was initiated from a carbide as noted above. It was found that CB5 and CB6, the two parallel cracking planes, were branches of CB4, indicating that more slip planes were activated after CB4 initiated from the carbide and propagated subsequently. On further loading to 52000 cycles in Fig. 5.7 (e) and (f), CB4 was found to have formed by slipping mainly in two directions. One was along a carbide elongated direction, named as CB4α. The other slip direction was inclined to CB4α, named as CB4β, marked in Fig. 5.7 (e). Thus, influenced by carbides, several cracking planes and extension directions were simultaneously activated, explaining the highly deflected crack path at the vicinity of carbides observed in the SEM.

5.5 Discussion

5.5.1 Mechanism of crack initiation

Three secondary cracking modes were captured in different regions in the alloy DS CM247LC during the fatigue process shown in Fig 5.2, and they were designated as microstructure-induced cracking at early stage (R1), slip band cracking at intermediate stage (R2) and opening mode carbide cracking at the final stage (R3) respectively in this work. These cracking behaviours are normally observed in fatigue and tensile failure in these materials systems, but it is interesting to discern that most of the secondary cracks belonged to only one or two of these modes as reported in other investigations [7, 200, 206-209]. Almost no research reports these three modes of cracks operating simultaneously in one alloy to the best of our knowledge, indicating the complicated cracking mechanisms during fatigue in this DS alloy system.

Microstructure-induced cracking refers to cracks induced by the interaction between dislocation movement and micro-features like defects, secondary phases and GBs. Plastic deformation of metallic materials is linked to activation of slip systems for dislocation motion and formation of slip bands. But the plastic incompatibility between matrix and secondary phases/defects prevents dislocation motion, causing strain/stress localization at the microstructural scale, thereby leading to crack initiation. Obviously, carbide-induced cracking was observed in the early stages of fatigue in the current work. Strain distribution around carbides was captured via DIC in Fig 5.4 (b), (c) and 5.5 (a), (b), (c). The strain was localized at the intersection of the strain bands and carbides, and then a micro crack was formed by bridging the strain accumulated sites as indicated in Fig 5.5 (d). Similar results were presented in another fatigue investigation on alloy CM247LC, which revealed dislocation pile-ups and tangling around carbides [47]. Moreover, this work proposed a similar explanation for carbide induced cracking, i.e. the cracking was caused by bridging between closely strain-located crack initiation sites. However, their experiments could not directly verify this hypothesis, which has now been directly confirmed in this study via the SEM-DIC approach. Pore-induced cracking was also observed, but it did not account for most secondary cracks in the R1 specimen due to the low volume fraction, small size and spherical shape of pores. Consistent with Jiang's elastic-plastic finite element modelling results [51], these large-sized pores with irregular shapes more easily induce strain/stress concentration at their local 'ridges'. GB-induced cracking was not observed in these tests on DS CM247LC. Although some cracks were initiated from pores on GBs, they propagated into the grains rather than along GBs in Fig 5.3 (c) and Fig 5.5 (h), showing the high resistance of the GB to cracking under these test conditions. Strain accumulation close to GBs was not as intensive as strain bands formed within grains, further confirming that slip band-GB impingements were not preferable sites for crack initiation. Similar phenomena are also shown in studies conducted by Stinville et.al and Wael et. al [69, 197]. They showed that a dislocation could fully transmit (i.e. cross slip) or partially transmit through GBs, particularly in the case of grains with low angle GBs and small tilt angle of slip planes in adjacent grains. In addition, small-scale precipitates on GBs enhance the cracking resistance in Chen's investigation [210], and the enhanced cracking resistance is attributed to the small scale (even nano-scale) of GB phases. Because the nano-scale phases not only strengthen the GBs, but also are able to pin dislocations at GBs, hindering GB slip or migration during plastic deformation. Thus, the high cracking resistance of GBs observed in this study is probably attributed to two factors, one of which is the release of strain accumulation related to dislocation transmission, and the other is the sub μm-scale carbides precipitated on the GB shown in Fig 4.1 (d).

Slip band cracking was the dominant source of secondary cracks in R2. The micro cracks initiated within slip bands and coalesced to form straight cracks in Fig 5.2 (c). The cracking mechanism is associated with γ' decohesion in slip bands, caused by repeated dislocation shearing. During fatigue tests, dislocations are forced to move back and forth within the slip bands, shearing γ' and causing severe dissolution and decohesion along the slip band [211-213]. Micro voids hence nucleate and grow in the slip bands to form micro cracks [213]. According to Pang's work, slip band cracking is mostly generated in alloys with a large grain size, which can facilitate the formation of long planar slip lengths [200]. Another feature of slip band cracking is reported in Jiang's investigation, where severely sheared γ′ precipitates within slip bands could be a clear indicator for slip band cracking [51, 68]. Consistent with the aforementioned research, the large columnar grains of CM247LC are prone to slip band cracking, whilst extensive shearing of the γ′ precipitates is also observed (Fig 5.2 (d)). Moreover, slip band cracking lagged behind carbide induced cracking which was characterized by DIC in this work. Strain intensity within slip bands and at intersection of carbides were both over 0.2 (a very high apparent strain intensity) at 22700 cycles in Fig 5.5 (c) and (h). However, cracks were initiated at carbides. Slip bands near the cracking carbides still remained uncracked in Fig 5.5 (d) and (h). The result is in agreement with the three-point bending test. Carbide induced cracking mainly occurred at R1, the early stage, while slip band cracking occurred at R2, the intermediate stage. This delay in slip band cracking, compared to carbide induced cracking, has not been reported and explained previously. It seems then that the formation of long planar slip bands and their cracking might require more cycling (to accumulate damage) than initial dislocation pile-ups at carbides, with the latter providing a more potent initiation mechanism.

Opening mode carbide-cracking occurred at the last stage of fatigue (R3), where cracks inside of carbides propagated nearly perpendicular to the loading direction with a large apparent crack opening displacement. In fact, this phenomenon is often observed in tension tests, where materials experience substantive plastic deformation, not only in fatigue failure (where small scale and progressive cyclic plastic deformation processes build up more gradually and sparsely throughout the material). Lindley et.al [214] proposed that dislocation pile-up mechanisms were unable to explain the result, as dislocation pile-up sites at carbides would be random, so there should be equal possibilities to crack carbides at all angles to any loading direction. Fiber loading mechanisms might be a more appropriate explanation [215]. This assumes that the matrix does not slip only along one specific direction when the macro stress reaches quite a high level, above yield stress. General shear stress exerted on the phase surface by the plastically yielding matrix is balanced by internal tensile stresses in the secondary phase. Thus, the total internal stress of the secondary phase is related to the macro plastic strain of the matrix. As a result, perpendicular cracks within the brittle carbides would preferentially occur (the carbides are directly loaded overall and crack, rather than the local impingement of a slip band causing only a very localized stress on the carbide) [216].

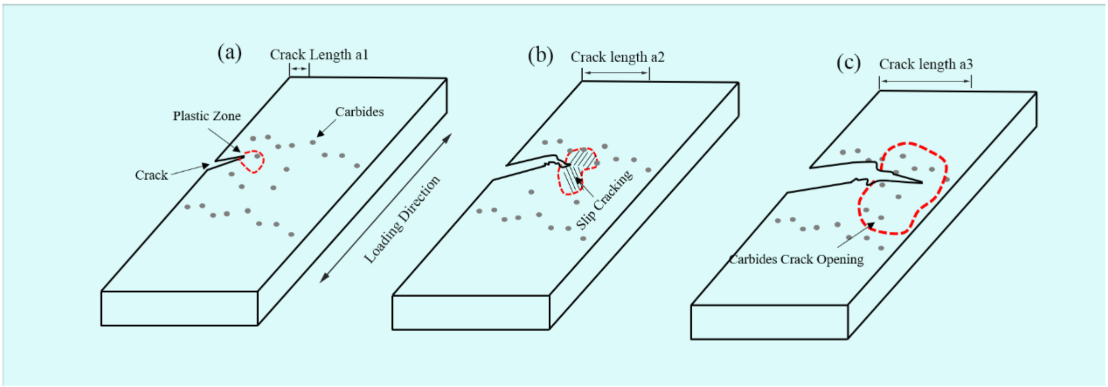

Fig 5.8 (a) schematic diagram of main crack at the early stage; (b) at the medium stage; (c) at the last stage

The different cracking behaviours in DS CM247LC can be inferred to be associated with the growing plastic region at the main crack tip shown in a schematic diagram in Fig. 5.8, based on the cracking mechanism discussed above and crack evolution history. At the early stage of the fatigue process, the main crack was in stage I, propagating along one slip direction inclined to the loading direction, shown in Fig 5.8 (a). The plastic zone of the crack tip is related to crack length according to Von-Mises yield criterion. In R1 (Fig 5.8 (a)), the area of plastic zone is the smallest compared to that formed in R2 and R3 and is not conducive for the formation of long planar slip bands. In this stage, carbide-induced cracking is the dominant crack initiation behaviour in the region. However, only a handful of carbides are included in such a small plastic zone, so the number of cracks observed in R1 are much less than in R2 and R3. With the increase in crack length, the plastic zone extended as shown in Fig 5.8 (b). Meanwhile, the main crack transitioned into stage II of the fatigue process, where multiple slip systems were activated, and thereby the main crack path became tortuous. The enlarged plastic zone facilitated the formation of planar slip, giving rise to (observed) slip band cracking. In this stage, both slip band cracking and carbide induced cracking could notionally occur, but from the observation of R2 in Fig 5.1 (c), slip band cracking became the predominant crack initiation behaviour. This was thought to be caused by two factors. Firstly, the plastic zone of the crack tip was believed to not be large enough to extend into the inter-dendritic region nearby, where carbides were congregated, as shown in Fig 4.1, Fig 4.2 and Fig 5.8 (b). The second reason is that the heterogeneous plastic strain was concentrated within slip bands, as shown in Fig 5.5. Carbides contained in the plastic zone could be located between these strain bands, therefore, strain accumulation around these carbides was insignificant. As a result, less carbide induced cracking was observed than slip band cracking in R2. When the main crack propagated from R2 to R3, it became perpendicular to loading direction. The plastic zone at the crack tip became much larger, causing relatively fast fatigue fracture. The inter-dendritic region was then partially covered by the extended plastic zone, and lots of carbides exhibiting brittle cracking were observed in Fig 5.1 (e) and (f). As discussed above, the increased macro plastic strain gave a rise to the higher internal tension stress within the carbides and caused them to crack perpendicular to the loading direction (opening mode carbide cracking occurred).

5.5.2 Comparison of crack growth behaviour in 2D and 3D

The 3D morphology of early cracking planes and surrounding carbides are presented and described in detail in Fig 5.6 and 5.7. To the best of our knowledge, this is the first time to characterize the interaction between cracks and carbides at a submicron scale in 3D, owing to the high resolution of SRCT and appropriate segmentation strategies [199]. Effects of carbides on inducing cracking and shielding crack propagation were both captured in 3D renderings, as firstly, more cracks were observed initiated at the region with a high density of carbides in Fig 5.6. When the cracking plane extension appeared to be blocked, another propagation direction was activated by the congregated carbides, see Fig 5.7. The results are mostly consistent with the 2D observation, in which cracks were found initiated at strain localisation sites of blocky carbides (Fig 5.5). Otherwise previously straight crack paths were deflected and tortuous in the proximity of carbides, see Fig 5.3. However, the chain-like carbides at grains boundaries could not be captured in SRCT, as these carbides are of the order of ~100s nm, lower than the minimum resolution of SRCT. Also, the narrow field of view and low penetration for nickel base superalloy is another factor limiting characterizing the chain-like carbides, as reported in Marine's research [199].

The crack propagation behaviour within grains in the DS superalloy CM247LC is compared with that in polycrystal and single crystal alloys in Fig 5.9. In the polycrystal alloy, faceted cracks mainly grow on the most favourable plane within grains. These activated crack planes are influenced by the co-effects of resolved shear stress (Schmid factors) and neighbouring grains [68, 73, 217]. Two neighbouring grains of polycrystal alloys are shown in Fig 5.9 (a) extracted from Hassanipour's research [217], named as grain 149 and 160. In grain 149, three slip planes of high shear stress (Schmid factors) might be activated. However, to minimize the mismatch angle of cracking plane in 160, one slip plane is activated eventually [217]. These phenomena have been found in many previous studies on crack growth behaviour in polycrystal alloys [68, 69, 205, 217]. Some of the research is however based on 2D observation, in which it is assumed that the straight crack observed at the surface within grains corresponds to a facet-like crack growing along one slip plane. These straight crack paths are largely affected by crack coalescence between neighbouring grains. In the DS alloy CM247LC, four facet-like cracks were activated within an individual grain (Fig 5.9 (b)), although only one straight crack was observed at the surface (Fig 5.9 (f)). This crack behaviour is more closely to linked to that in the single crystal alloy in Fig 5.9 (c), where two slip planes were activated from a pore [51]. It is reasonable to infer that the simultaneous activation of several cracking planes is attributed to the minimized effects of neighbouring grains. Firstly, in the DS alloys CM247LC, the columnar grains possess fewer surrounding grains, because there are no neighbouring grains along their longitudinal direction. Secondly, the intragranular area is larger than most of polycrystal alloys, as the average width of the columnar grains reached 1.2 mm. In addition, columnar grains have a more uniform elongated direction which is conducive to compatible deformation compared to polycrystal alloys. Therefore, the deformation of intragranular areas is less constrained by neighbouring grains, and more slip systems for crack growth could be activated. However, more characterization work still needs to be done to further verify this hypothesis.

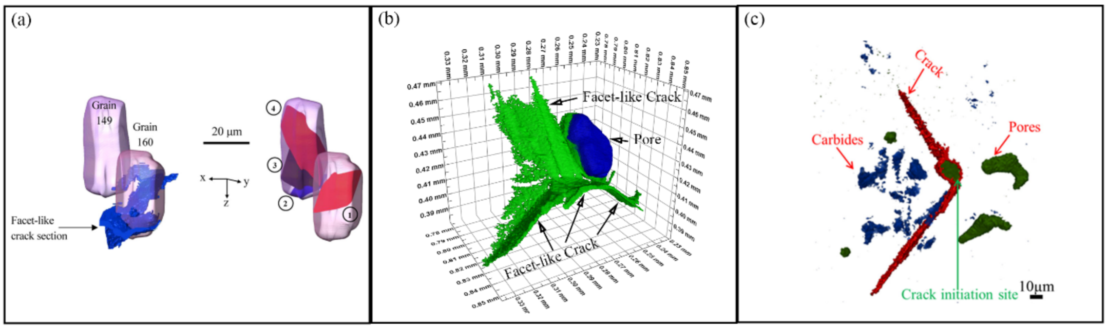

Fig 5.9 Facet-like crack section in polycrystal alloys [217]; (b) facet-like crack sections in DS alloys CM247LC; (c) 3D crack morphology in single crystal alloy [51].

5.6 Summary and conclusion

The effects of microstructural features such as carbides and GBs are carefully investigated using the data-rich imaging approach. The main conclusions to be drawn are:

(1) Three modes of secondary crack behaviours are identified in the proximity of the main crack. It is inferred these crack behaviours are associated with varying plastic zone of the crack tip as it grows. In the early stages of the fatigue process, the plastic zone is relatively small, a few carbides are contained in the plastic zone and become the main

sites inducing secondary crack formation. As the length of main crack increases, the crack tip plastic zone is enlarged, facilitating the formation of more extended slip band cracking. In the final stage, the plastic zone extends into the inter-dendritic region, causing the fibre loading damage of carbides.

(2) The effects of carbides on inducing crack formation and shielding crack propagation are identified by the in-situ 3D observation of cracking planes. Also, it is found several cracking planes are formed simultaneously at the proximity of pores from the 3D analysis, indicating that cracks grow on several slip planes around such stress concentration features rather than along just one favourable slip plane in the early stage of fatigue.

Chapter 6 Effects of oxidation on fatigue crack initiation behaviours

6.1 Introduction

Since the effects of microstructural features on the room temperature fatigue behaviour have been extensively studied in Chapters 4 and 5, the effects of environment and temperature are now focussed upon in the following chapters. Considering turbine blade superalloys operate at high temperatures (typically 650 °C and above), oxidation degradation is unavoidable. As illustrated in the section of literature review, the oxygen attacks microstructural features, such as slip bands, carbides and GBs at high temperatures, which induce earlier crack initiation and accelerate crack propagation. For the DS superalloy, the microstructures are complex, as introduced in the previous chapter, therefore oxidation of carbides, slip bands and GBs are all possible. However, which is the predominant factor inducing earlier crack initiation is still unclear. In this chapter, the sustained-load oxidation tests are carried out to study the stress-assisted oxidation process, especially the oxidation of these microstructures. Then, three-point bending tests are performed at the same temperature and comparable stress levels at different frequencies to understand the effects of these oxidised microstructural features on fatigue crack initiation and early crack growth behaviour. The test frequencies used here are 10 Hz sine-wave and 1-1-1-1 trapezoidal waveforms, thus creep effects should be minimized, as the time holding at the maximum stress is short for the temperatures studied here.

6.2 Sustained-load oxidation

The centre of the bend bar surfaces were examined under the SEM after stress-assisted oxidation for 2 and 16 hours at 650°C and are shown in Fig 6.1. The low-magnification images (Fig 6.1 (a) and (b)) show the formation of intensive slip bands, indicating the occurrence of the plastic deformation at the centre region of the 3 point PBB at a maximum stress of 912 MPa (105% of the yield stress). The higher-magnification SEM images in Fig 6.1 (c), (d), (e) and (f) further illustrate the interaction between oxidation and microstructural features. The morphology of carbides after exposure for 2 hours are similar to those seen at room temperature in Fig 4.1 (c), apart from internal cracks. It indicates that although the oxidation of carbides is only minor after 2 hours exposure, the carbides start to break under the sustained stress. In comparison, “flower-like” carbides are shown in Fig 6.1 (d), after tested at 650ºC for 16 hours, and this morphology is a typical feature of oxidised carbides. The slip bands are apparently decorated with oxides after testing for 16 hours, while very few oxides are observed on the slip bands for the sample tested for 2 hours.

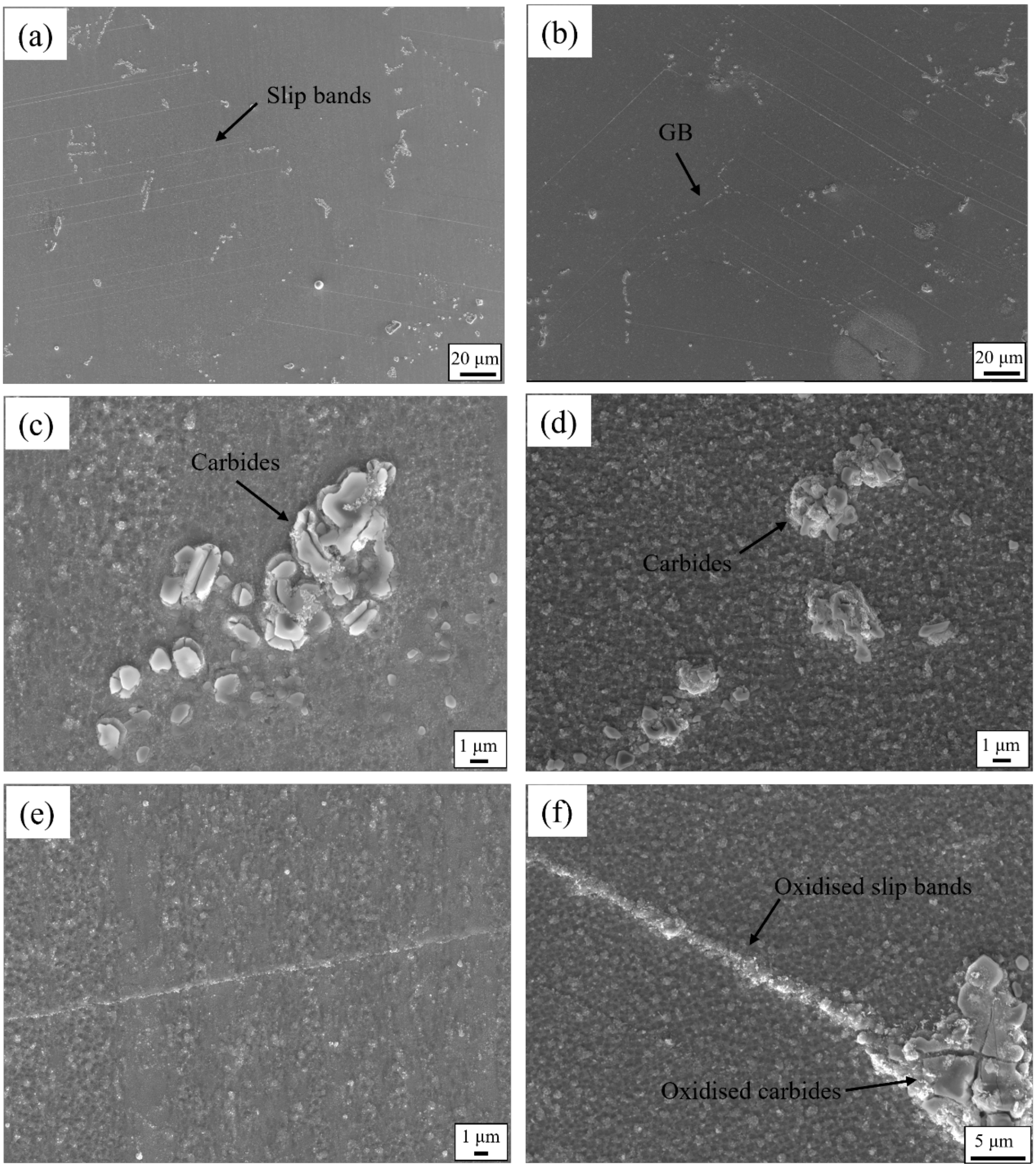

Fig 6.1 (a) the oxidized centre regions for samples tested at 650ºC after 2 hours (a), after 16 hours (b); the oxidized carbides after tested for 2 hours (c), for 16 hours (d); the oxidized slip bands tested for 2 hours (e), for 16 hours (f)

The SEM-EDX analysis performed on these severely oxidized microstructural features is shown in Fig 6.2 and 6.3. The composition of the carbides is rich in Ta, W and Hf at the centre, and Co, Ni at the edge, while some of carbides are also rich in Co at the centre.

Compared with the composition of carbides characterized at room temperature, the main difference is the enrichment of the Co and Ni elements, which is evidence that the oxygen attacks the carbides and forms the Co, Ni-rich oxides. The interesting thing is that the oxidation always occurs from the edge (maybe the interface between the carbides and matrix) in towards the centre of the centre of the carbides, as some tiny carbides are fully covered by the Co elements.

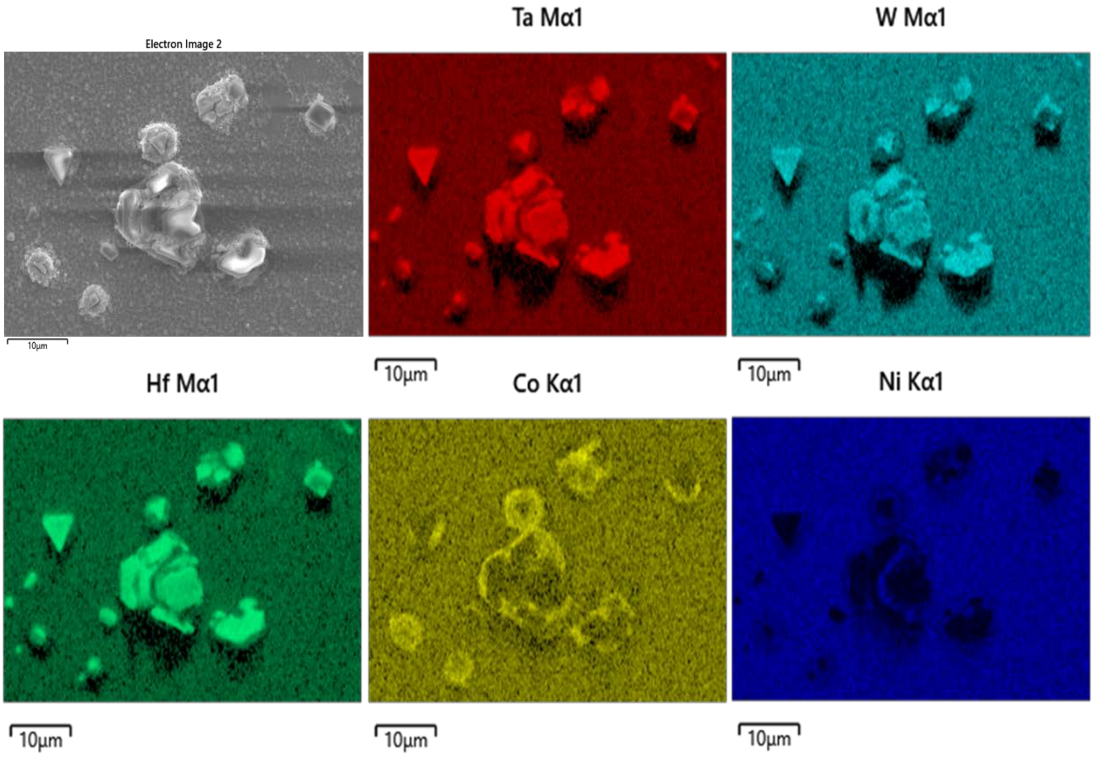

Fig 6.2 The oxidized carbides and corresponding element distribution maps

The oxidized slip bands are shown in Fig 6.3, and the Co element is segregated within the slip bands, which indicate that the preferential oxidation of the slip bands. This might be associated with fast diffusion of the elements via dislocations. An oxidised carbide is also found at one end of the dislocations. A few micro cracks could be observed on the carbides, indicating preferential crack initiation at the carbides rather than the oxidised slip bands, which is the consistent with what is found in the fatigue short crack tests at the room temperature.

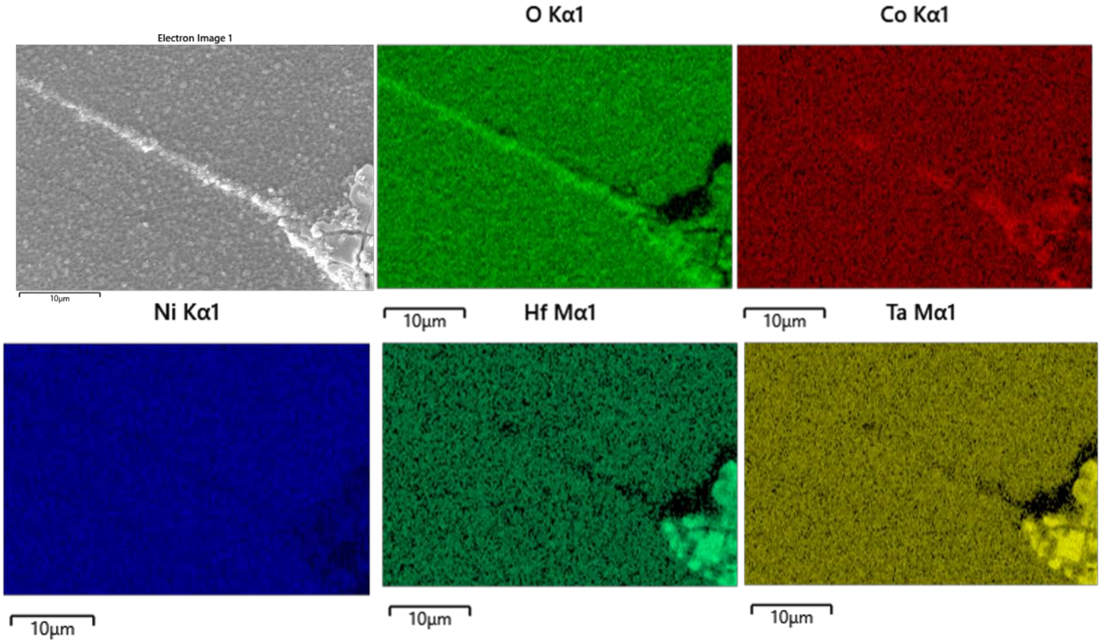

Fig 6.3 The oxidized slip bands and corresponding element distribution maps

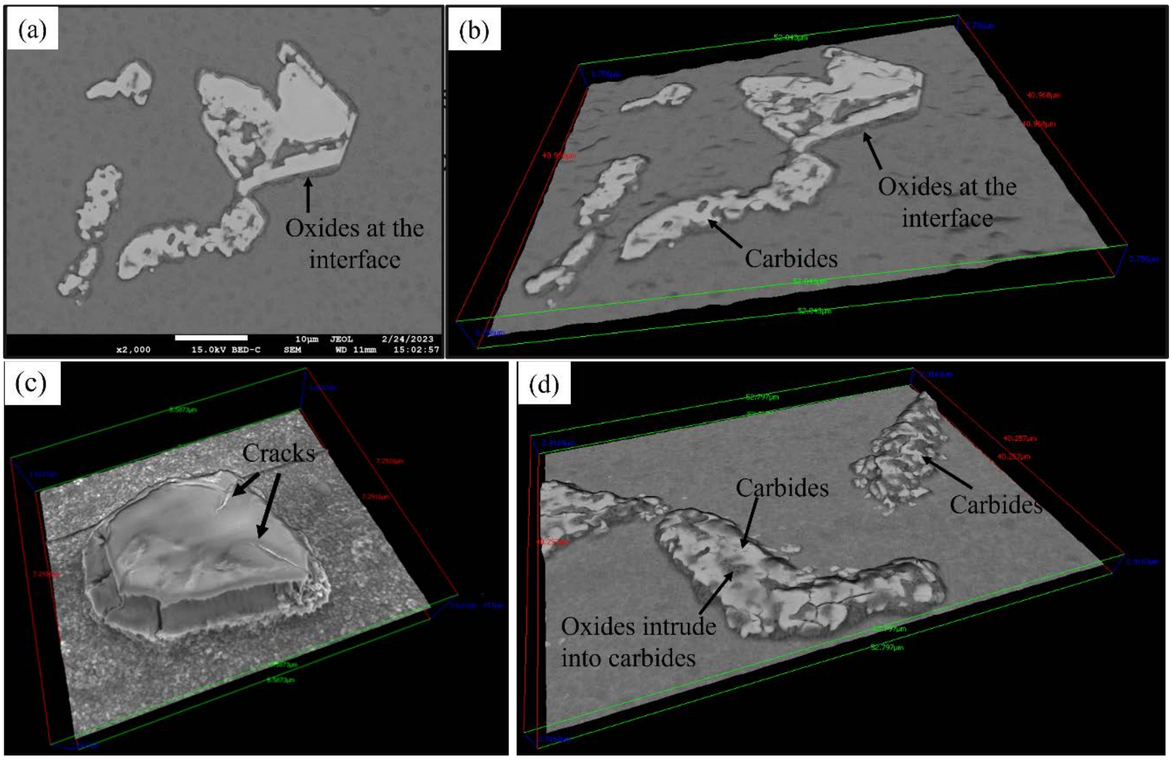

Fig 6 4 The SEM image of oxidized carbides after tested for 1 hour (a); the 3D reconstruction of oxidized carbides after 1 hour (b), 2 hours (c), 4 hours (d)

The oxidised process is further observed using the 3D tilt reconstruction techniques of the BSE (backscatter electron) images shown in Fig 6.4, apart from Fig 6.4 (c) which is reconstructed using SEI (Secondary Electron Imaging)-mode images. The BSE images facilitate the differentiation of carbides, oxides and the matrix. Fig 6.4 (a) and (b) show that the early stages of oxidation of the carbides occurs at the interface between carbides and matrix. The oxidation behaviour might be associated with the highly localized stress/strain at the interface between carbides and matrix under loading. The following images in Fig, 6.4 (c) presents the clear elevation of the oxidised carbides after testing for 2 hours, caused by the oxidation-induced volume expansion. Some microcracks are found inside the carbides, marked by arrows. With the testing time increased to 4 hours, the oxides completely intrude into the carbides as shown in Fig 6.4 (d), where the broken carbides could be clearly observed. When the testing time is increased to 16 hours, the oxidation of the carbides is more significant as shown in Fig 6.5. The carbide (located at the centre of the image) is completely separated by the intruding oxides, forming cracks. Other small carbides are also lifted by the oxidation, consistent with the observation of the specimen tested for 2 hours.

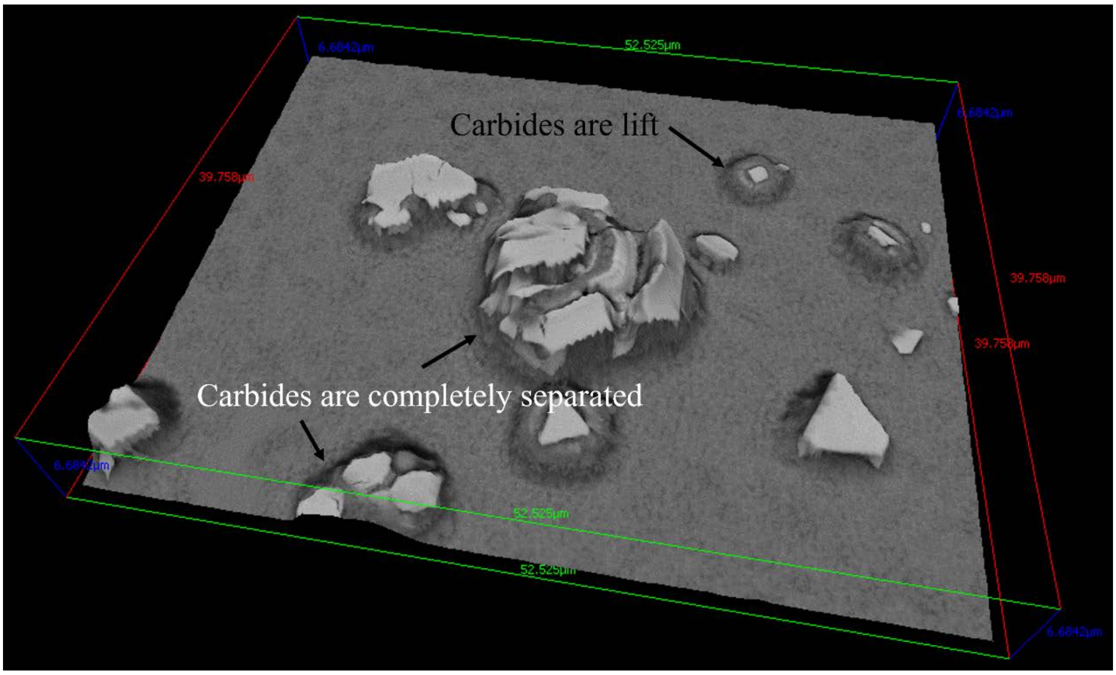

Fig 6.5 The 3D reconstruction of the oxidized carbides after testing for 16 hours

6.3 High-temperature short crack initiation and propagation

The fatigue tests were performed on the LR and RR specimens at temperatures of 650 °C, with frequencies of 10 Hz sine waveform and a 1-1-1-1 trapezoidal waveform. In addition, two levels of maximum stress are applied on the specimens: 912 MPa and 1008 MPa, corresponding to 105 % of the yield stress of the RR and LR specimens. The tested results are listed in the Table 6.1, showing that the corresponding fatigue lives of the LR and RR specimens are both reduced dramatically when the applied maximum stress decreases from 1008 MPa to 912 MPa in the high frequency tests. In comparison, the fatigue lives of the RR specimen are higher than that of the LR specimen in both high and low stress cases, but their difference is minimized with the increase of strength. In Chapter 3, lower fatigue lives for the LR specimen are found at room temperature when the applied maximum stress is close to the material's yield stress, which is consistent with the results in the current chapter. It should be noted that there are some stray grains in the LR specimen tested under 912 MPa with high frequency of 10 Hz sine waveform, which might influence the fatigue behaviours. The interesting finding is the dramatic increase of fatigue life for the LR specimen when the testing frequency changes from the 10 Hz sine waveform to the 1-1-1-1 trapezoidal waveform. The 1-1-1-1 test was interrupted after the cycles exceeded 110,000 cycles, 10 times longer than the lifetime in the high frequency test. The top surface of the interrupted specimen was then carefully examined using SEM. In contrast, the fatigue life of the RR specimen drops, when the frequency is decreased to the 1-1-1-1 trapezoidal waveform.

Table 6.1 The fatigue tests results of LR and RR specimens

Orientation	Stress	Temperature	Test Type	Frequency	Lifetime
LR	912 MPa	650 ºC	Failure	10 Hz	71,413 cycles
LR	1008 MPa	650 ºC	Failure	10 Hz	11,942 cycles
LR	1008 MPa	650 ºC	Interrupted	1-1-1-1	110,000 cycles
RR	912 MPa	650 ºC	Failure	10 Hz	136,793 cycles
RR	1008 MPa	650 ºC	Failure	10 Hz	14,842 cycles
RR	912 MPa	650 ºC	Failure	1-1-1-1	42,728 cycles

The fracture surfaces of the LR and RR specimens tested at the frequency of 10 Hz are presented in Fig 6.6. Although replicas were not employed to trace the crack, some fractography features could act as indicators to distinguish the crack initiation sites. For both the LR and RR specimens, the main fatigue crack initiation sites were located subsurface at the applied maximum stress of 912 MPa, while they changed to being at the surface at the applied maximum stress of 1008 MPa. Fig 6.6 (a), (b), (c), (f) show the subsurface cracks have initiated from a pore in the centre of the halo region marked by the red dash line. For the surface crack, it is initiated from slip bands in the LR specimen, indicated by the faceted crack presented in Fig 6.6 (c) and (d), and from surface pores in Fig 6.6 (g) and (h).

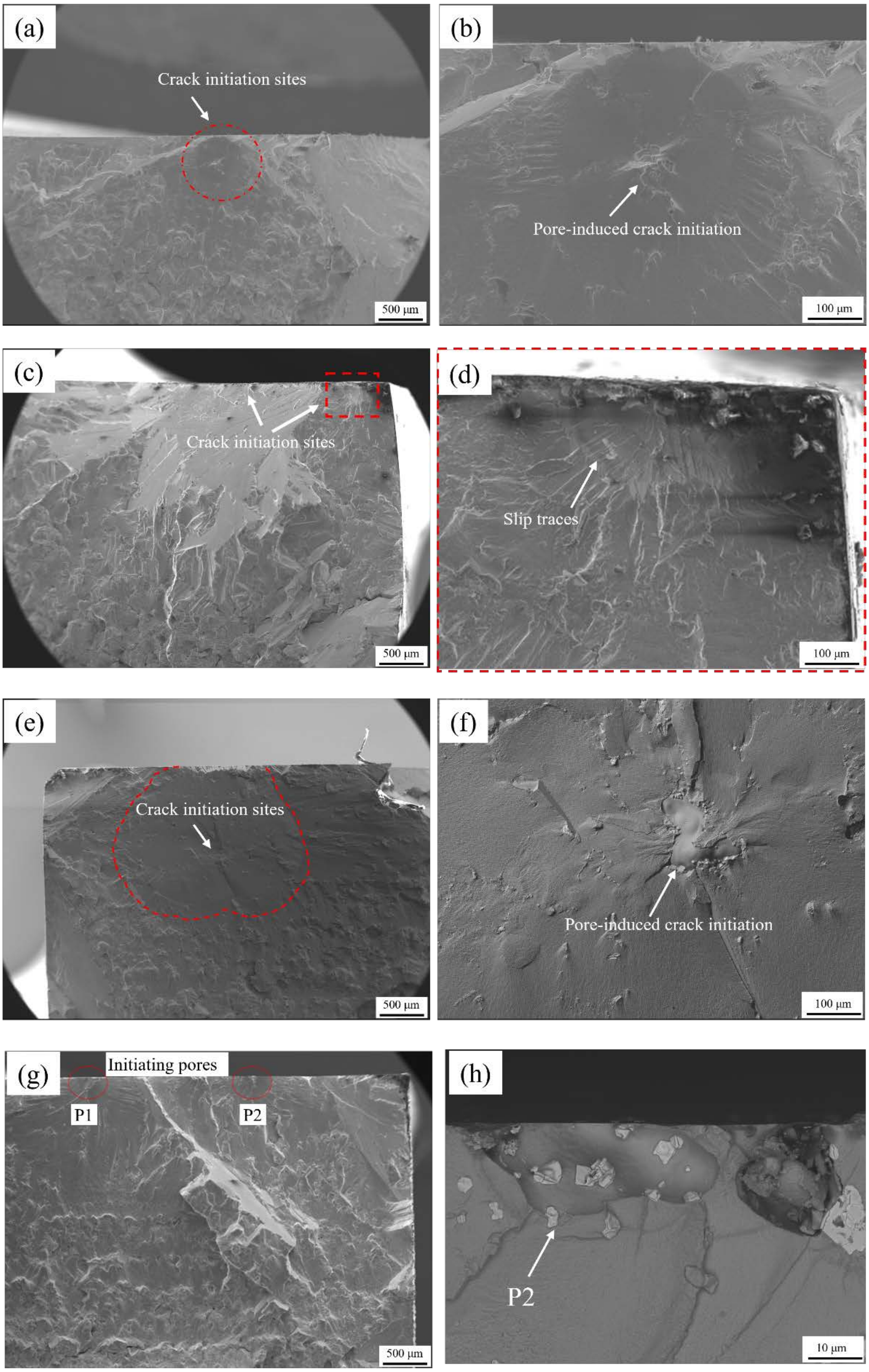

Fig 6. 6 the crack initiation sites of the LR specimen tested with the frequency of 10 Hz (a), (b); of the RR

specimen tested with the frequency of 10 Hz and applied maximum stress of 912 MPa (c) and (d); with applied maximum stress of 1008 MPa

The fracture surface of the RR specimen tested at an applied maximum stress of 1008 MPa with the 1-1-1-1 trapezoidal waveform is shown in the Fig 6.7. The fatigue crack is also thought to be initiated from the pore at the sub surface shown in Fig 6.7 (a) and (b). The high magnification images show more significant oxides forming inside the pore, compared with those tested at the high frequency. However, the dispersed tiny oxides seem not to affect the fatigue crack initiation behaviour.

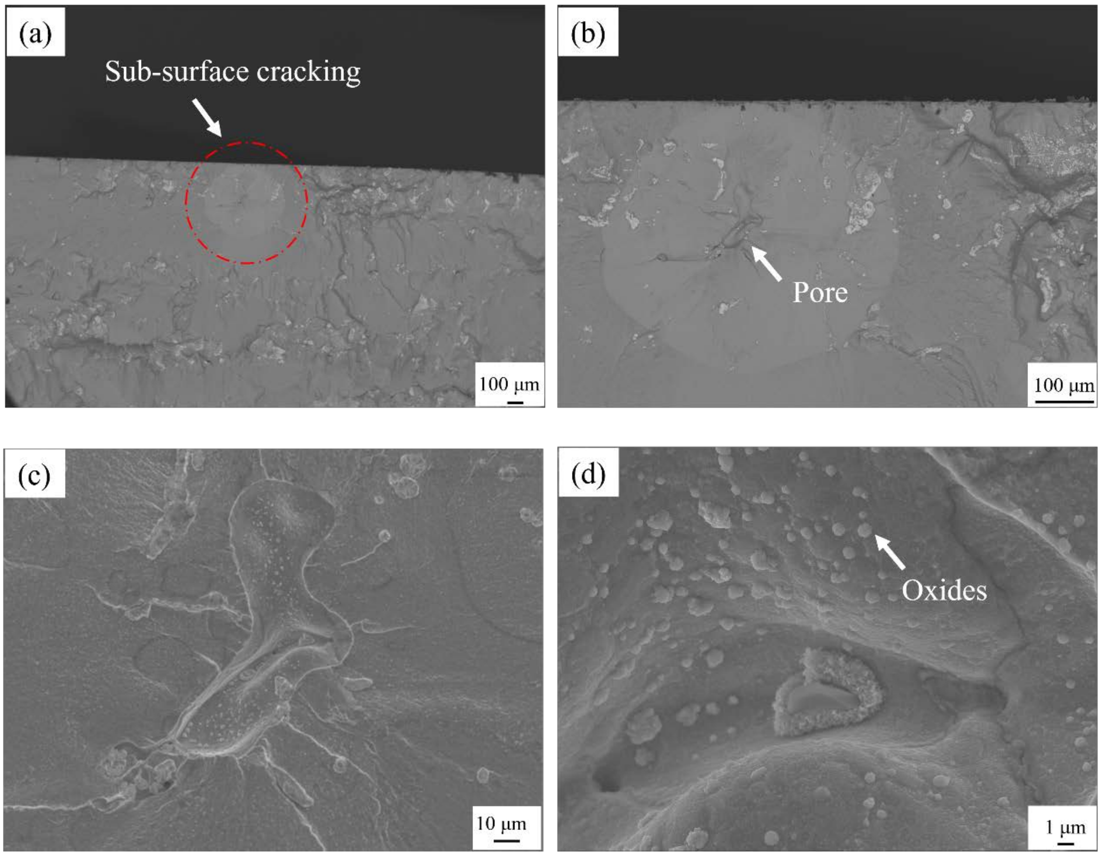

Fig 6. 7 The fracture surface of the RR specimen tested under 1008 MPa, with 1-1-1-1 trapezoidal waveform (a); the crack initiation site (b); the pore inside the crack initiation site (c); the oxides inside the pore

The top surface of the interrupted LR specimen tested with a 1-1-1-1 trapezoidal waveform is shown in Fig 6.8 (a) – (d). The low magnification image taken from the centre of the top surface, shows a large amount of slip bands and spallation, showing the occurrence of plastic deformation and significant oxidation. In the same area, all the carbides are broken as presented in Fig 6.8 (b), (c) and (d), which is attributed to the local plastic strain induced by both volume expansion and mechanical loading. The use of BSE mode in the SEM facilitates distinguishing the oxides and carbides from the matrix. All the broken carbides are observed surrounded by oxides, which is consistent with the observations in the sustained loading tests that oxides form first at the interface between carbides and matrix. The cracks forming inside the carbides do not propagate from the carbides into the surrounding oxides and finally into the matrix. This is completely different to the observations of the broken carbides in the specimen tested at high frequency, shown in Fig 6.8 (e) and (f). The cracks initiated from the carbides clearly propagate into the matrix at higher frequencies. This indicates that the formation of the oxides around the carbides is likely to increase the resistance of the materials to the crack propagation.

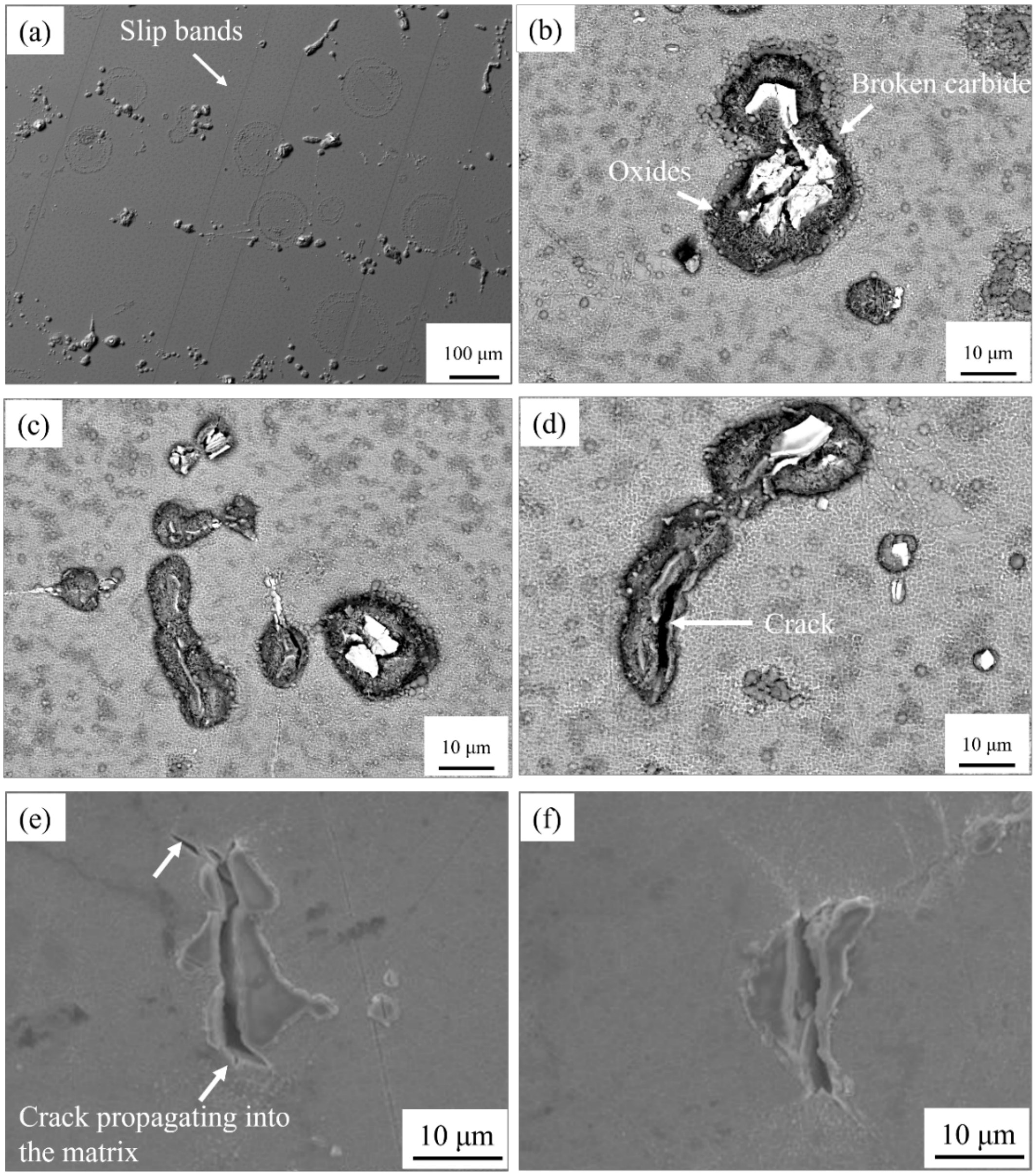

Fig 6. 8 The top surface of the interrupted LR specimen tested with frequency of 1-1-1-1 (a), the broken carbides and surrounded oxides (b), (c), (d); the broken carbides at the top surface of the LR specimen tested

with the frequency of 10 Hz

6.4 Discussion

6.4.1 Stress assisted oxidation mechanism

Stress-assisted oxidation has been studied in detail in the superalloys [106, 218, 219]. Most of the research agrees that selective oxidation occurs at the strain/stress localized regions, particularly the GBs or carbides. Jiang et. al [220] found that the preferential oxidation on GBs is closely correlated to the Schmid factor (SF) of the neighbouring grains. (Co, Ni)-rich oxides are always formed at the GBs with the high-SF neighbouring grains. It is attributed to the higher strain storage energy at these GBs facilitating easier oxide nucleation and furthermore, the piling-up dislocations provide a fast path for element diffusion. The preferential oxidation of the carbides is further discussed in the study of Connolley et. al [221]. The multi-layers of Nb_2O_5 oxides form on the carbides located at the surface, leading to volume expansion. Similar results are found in Sjoberg's study [222], and they quantitatively measured the extrusion of oxidised carbides from the surface by around 0.1 mm.

Current results show consistently that the (Co, Ni)-rich oxides preferentially formed at the slip bands and the interface between the carbides and matrix. The series of 3D reconstruction of the oxidised carbides shows a more detailed mechanism. Firstly, the oxidisation occurs at the interface, which is associated with the piling-up of dislocations. However, in comparison to the mechanisms introduced in the previous research, the oxides protrude beneath the carbides shown in the Fig 6.4 (c) and 6.5 to lift the carbides, instead of forming multi layers on the carbides. Then the oxides start to protrude into the bulk of the carbides, causing the separation of the carbides. Finally, large amounts of cracks are formed inside the oxidised carbides.

6.4.2 The effects of oxidation on the crack initiation

Compared with the crack initiation behaviours observed at room temperatures, the most significant feature of the crack initiation behaviours at elevated temperatures is the transfer from surface to subsurface crack initiation. As shown in Fig 6.6 – 6.7, almost all the fatigue cracks are initiated from subsurface pores and form a halo-shape region marked by the red dashed line. Similar results have also been observed in fatigue tests of high-strength steels [223-226]. In those studies, the halo-shape region is termed as a fish-eye zone, which always occurs in the low stress amplitude and high cycle (usually over 10^7 cycles, known as the gigacycle-domain fatigue). In comparison, fatigue cracks mainly initiate from surface slip bands in high stress-amplitude and low cycle fatigue tests. There is an applied stress range which determines the transfer of crack initiation sites from surface to the subsurface. Shiozawa et. al [227] proposed an empirical model to calculate the stress intensity for the surface and subsurface crack initiation:

$$\Delta K_{ini,\ s} = 0.65\sigma\sqrt{\pi\sqrt{area_s}} \tag{6.1}$$

$$\Delta K_{ini,\ p} = 0.5\sigma_p\sqrt{\pi\sqrt{area_p}} \tag{6.2}$$

Where $\Delta \mathrm{K}_{\mathrm{ini,\ s}}$, $\Delta K_{ini,\ p}$ refer the stress intensity for surface and subsurface crack initiation. σ is the applied stress amplitude, while σ_p is the stress amplitude applied to the subsurface pores. $area_s$ and $area_p$ refers to the area of the surface crack initiation sites and the subsurface pores. Herein, the surface crack initiation is assumed to be the oxidised carbides, and thus $area_s$ could be considered as the average area of the carbides. Owing to the quite close locations of the subsurface pores to the surface, the σ_p is regarded as the same with the σ to simplify the situation. Taking the statistical data of carbide and pore volumes into account, measured by SRCT in chapter 4, the calculated $\Delta K_{ini,\ s}$ and $\Delta K_{ini,\ p}$ are 4.14 MPa√m and 2.65 MPa√m under the applied maximum stress of 1008 MPa, respectively. If the stress gradient is considered, the $\Delta K_{ini,\ p}$ should be lower. With the decrease of the applied maximum stress to 912 MPa, the value of $\Delta K_{ini,\ s}$ and $\Delta K_{ini,\ p}$ are reduced to be 3.76 MPa√m and 2.41 MPa√m. The difference between $\Delta K_{ini,\ s}$ and $\Delta K_{ini,\ p}$ decreases from 1.49 MPa√m to 1.35 MPa√m. The trend that decreasing the applied stress induces subsurface crack initiation is also found in [227], due to the minimizing difference between $\Delta K_{ini,\ s}$ and $\Delta K_{ini,\ p}$. Although the difference is minimized, $\Delta K_{ini,\ p}$ is unable to surpass the $\Delta K_{ini,\ s}$, no matter how low the applied stress is, according to the empirical model. In this case, more physical models might need to be developed, because the transfer from surface crack to sub surface crack cannot be explained by this empirical model. Miller et. al [228] thought the crack initiation at the subsurface pores is also correlated to their positions and shapes. In their 3 point bending fatigue tests on SX CMSX-4 superalloys at 650 ºC and 725 ºC, all the cracks were initiated from subsurface pores located at inter-dendritic regions with high aspect ratios. Similarly, the pores inducing the subsurface crack initiation are also with high aspect ratios in the current study, and particularly, the ratio of the longest length to the shortest length is approximately 4. The stress concentration is closely associated with the shape of pores [229], but how to correlate the parameter to the subsurface crack initiation behaviours quantitatively needs more systematic tests.

The observation of the top surface of the failure and interrupted LR specimens at the applied maximum stress of 1008 MPa (Fig 6.8) confirm the formation of micro-cracks in the carbides. The crack propagation is prevented from going into the matrix by the oxidation observed in the low-frequency tests, compared with that in the high-frequency test (Fig 6. 8 (c), (d) and (e), (f)). The increase in the fatigue life of LR specimen in the low-frequency test should be attributed to the changes in crack propagation. There are two potential mechanisms accounting for the extended life phenomenon at lower frequencies. One is oxidation induced crack closure, which proposes that the formation of oxides inside the cracks reduce the effective ΔK, leading to crack arrest [230, 231]. However, the oxides are more preferentially forming surrounding rather than inside the cracks according to Fig 6.8 (b), (c) and (d). In this case, the prevention of the crack propagation from the carbides into the matrix might be related to the mechanical properties of these carbides. Jiang et al [232] recently reported the much higher hardness of the oxidation layers detected by nano-indentation, compared with the matrix in a superalloy. Hence, there is a possibility that as the micro cracks are formed at the surface, the stress intensity at the crack tip is quite low, which is incapable of breaking into the surrounded high-hardness oxides. While for the subsurface crack initiation, the oxidation effects are much minor, where the crack initiated from the sub-surface pores could propagate into the matrix and become the main fatigue crack, which has been observed in the RR specimen tested at the low frequency.

6.5 Summary and conclusion

The stress assisted oxidation behaviours and fatigue short crack initiation behaviours at 650 ^{o}C are studied. The different specimen types, applied maximum stress and tests frequencies are employed to assess the effects of grain orientation with respect to the loading direction, stress levels and oxidation on the fatigue crack initiation behaviours. The main conclusions are:

(1) The (Co, Ni)-rich oxides prefer to form in the stress/strain localized regions, such as the slip bands and the interface between matrix and carbides, due to the high strain storage energy at these features and the fast element diffusion path formed by dislocations.

(2) The detailed oxidation mechanism is assessed by reconstructing the 3D morphologies of the oxidised carbides. The oxides initially form at the interface between the carbides and matrix, then protrude into the carbides beneath, lifting the phases. Finally, oxides protrude into the bulk of the carbides, damaging their integrity and leading to cracks.

(3) The transfer from surface to subsurface crack is closely associated with the applied maximum stress in the high-frequency tests for both LR and RR specimens, and the threshold applied maximum stress is approximately in the range of 912 MPa to 1008 MPa. The decrease in applied maximum stress supports the formation of subsurface cracks, due to the minimized difference of stress intensity between the surface and subsurface crack and the availability of sub-surface pores to act as the critical initiating defect.

(4) The surface crack is suppressed by the oxidation observed in the low-frequency tests for LR specimen. The oxides formed surrounding the carbides preventing the microcracks propagating from the carbides into the matrix.

Chapter 7 Effects of oxidation on fatigue crack propagation behaviours

7.1 Introduction

The previous chapter was focused on fatigue crack initiation and early propagation behaviours considering the effects of both local microstructural features and increasing temperature. Early crack propagation is often variable, due to the variations of local microstructural features. When the fatigue crack further grows into the stage II (long crack) regime, its propagation rate is often more stable, following the Paris law, where a more averaged behaviour is seen across a through thickness crack front. Such stage-II crack propagation may also be important to assess when considering the whole crack propagation process over the fatigue lifetime of a component.

As introduced in the sections 2.2.5.1 and 2.2.5.2, oxidation and creep processes have significant effects on long crack propagation behaviour. They can either accelerate or decelerate the FCP rate by activating oxidation mechanisms like SAGBO, DE or OICC, and creep mechanisms, such as GB sliding or crack tip blunting. In an attempt to understand the effects of high temperature environments, systematic fatigue tests with different testing temperatures and loading frequencies have been designed. The DCPD method introduced in section 3.2.3.4 was used to monitor the crack length, and furthermore, interrupted tests were performed to analyse the interaction between the crack tip, microstructure and environmental effects, like oxidation and creep. Some aspects of the work detailed in this chapter have been published in the following paper:

Yuanguo Tan, Nong Gao, Philippa. Reed, Oxidation induced crack closure in a nickel base superalloy: A novel phenomenon and mechanism assessed via combination of 2D and 3D characterization, Materials Science and Engineering: A, 861 (2022) 144311.

7.2 High-temperature long fatigue crack growth and fracture surface observation

The high-temperature long fatigue crack growth rates versus the stress intensity factor range (*ΔK*) at 650 °C and 725 °C for a range of frequencies are plotted in Fig. 7.1 (a). Specimens were first pre-cracked at high frequency (10Hz) at the test temperature of interest before starting at the testing frequency. For the 10 Hz (high frequency) fatigue tests, the crack starts growing at the initial ΔK of 15 MPa√m for both L and T samples at 650 °C and 725 °C. However, fatigue cracks arrest at the same ΔK value, when the test frequencies are decreased to 0.25 Hz (1-1-1-1 waveform) and 0.011 Hz (1-90-1-1 waveform). One typical curve for an L sample tested under a 1-1-1-1 waveform at 650 °C is presented in Fig. 7.1 (a). After the crack arrests at a ΔK of 15 MPa√m, several steps of increasing the load range by 10% are performed to force the crack growth to re-start at the lower frequency. Nevertheless, the crack is still unable to propagate until the ΔK reaches nearly 23 MPa√m. The vertical line highlighted by a red dotted ellipse in Fig 7.1 (a) shows one example of the crack arrest process. Initially increasing the load to give a ΔK of 21 MPa√m, the fatigue crack starts to grow, but crack growth rate dramatically decreases from 10^{-5} mm/cycle to 10^{-8} mm/cycle over only a few more cycles. According to ASTM E 647, when the crack growth rate approaches 10^{-7} mm/cycle, the corresponding ΔK is taken as the threshold for fatigue crack growth (ΔK_{th}). Apparently, in this case the ΔK_{th} is increasing with the decrease of test frequency. Given that ΔK_{th} is not systematically measured in the current work, ΔK_0, denoting the initial ΔK enabling the fatigue crack to grow continuously, is used to describe the severity of crack growth arrests. Fig. 7.1 (b) shows the relationship between ΔK_0 and test frequencies, in which ΔK_0 increases notably with the decrease of test frequencies for both L and T samples tested at 650 °C and 725 °C. Also, it should be noted that the temperature has an effect on the crack growth arrests. When tested at very low frequencies (1-90-1-1), the ΔK_0 rises from 30 MPa√m at 650 °C to more than 40 MPa√m at 725 °C. Therefore, the fatigue crack growth arrest points are closely associated with both test frequencies and temperatures. Certainly, the microstructure difference between L and T samples has some effect on the fatigue crack growth behaviours. For instance, the T sample doesn't show crack growth arrests at 1-1-1-1 test frequency, 650 °C and L and T samples show much lower fatigue crack growth rates at the 1-90-1-1 test frequency, 725 °C. Compared with the significant effects on crack growth arrests, linked principally to test frequencies and temperatures, the effects of microstructure alignment are therefore seen to be relatively minor, and are not the focus of current study.

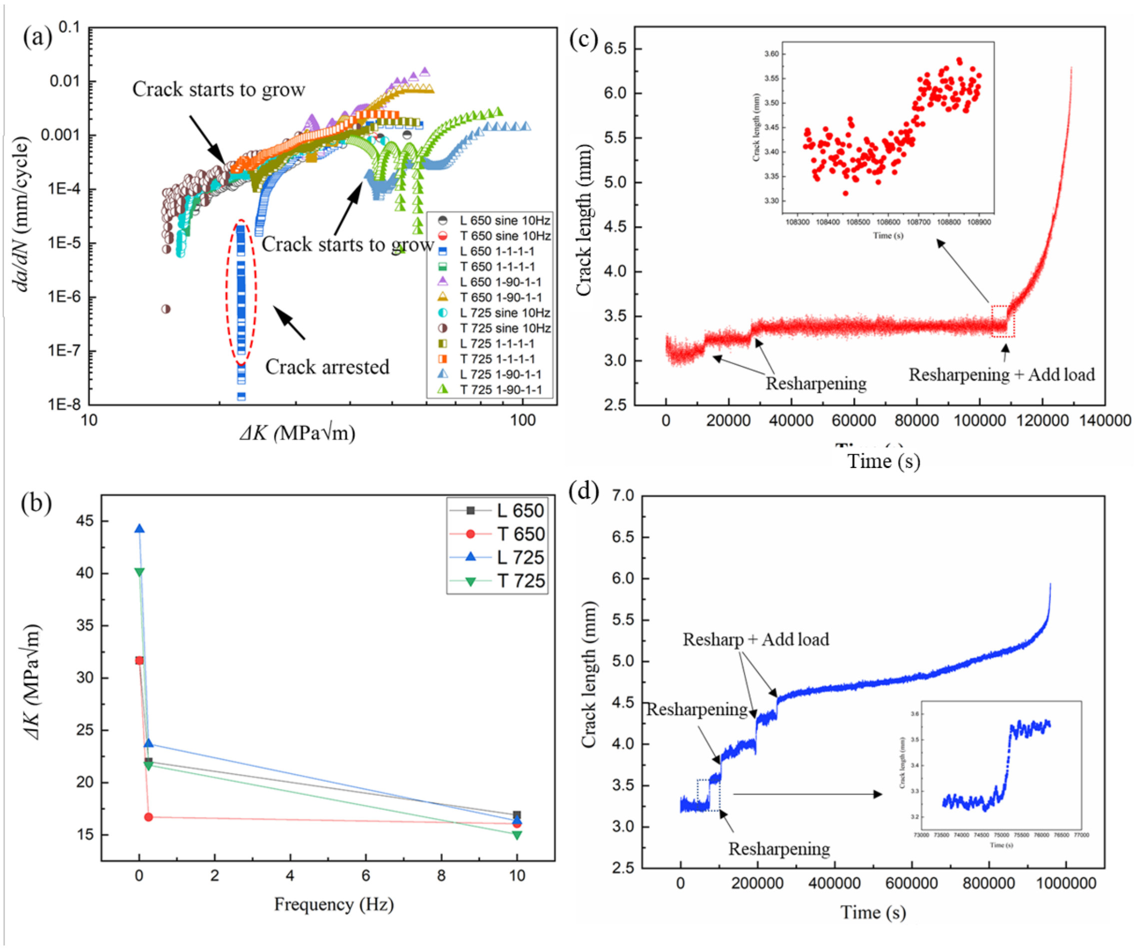

Fig 7.1 (a) Fatigue crack propagation rates of L and T samples tested at various conditions, (b) ΔK_0 variation against test frequencies, (c) crack length of L tested at 1-1-1-1 waveform, 725 °C and (d) tested at 1-90-1-1 waveform, 725 °C.

The variation of the crack length records the process of the crack arrests and growth as well as how the ΔK_0 is approached as shown in Fig. 7.1 (c) and (d) for L samples tested at 1-1-1-1 and 1-90-1-1 waveforms at 725 °C. Arrows in the figures show the points where crack-tip resharpening is performed to force the crack growth (this is where the testing frequency is switched back to a higher frequency at the same ΔK to try and re-start crack growth again and then switching back to the lower frequency). For the L sample tested under the 1-1-1-1 waveform, the first two resharpenings were conducted nearly every 8000 cycles without any detectable crack growth indicated by the stable crack length in Fig. 7.1 (c). The crack length jumps at the point of crack-tip resharpening (switching to a higher frequency), which means the crack-tip resharpening successfully forces the crack to grow. However, after the first two crack-tip resharpenings, the crack is still unable to continuously grow at the lower test frequency. The crack length is stabilized at 3.4 mm for 25000 cycles, indicating the crack is again arrested. The third time, to force the crack growth, a simple crack-tip resharpening by changing frequency could not activate crack propagation and the load range was also increased by 10%. These combined methods eventually got the crack to grow and thereafter, the fatigue crack did continuously grow. The ΔK_0 now has been achieved at 23 MPa√m. Another test for an L sample tested under the 1-90-1-1 waveform, shows a similar crack length variation in Fig. 7.1 (d). In the early stages, the crack could be forced to grow by the crack-tip resharpening by increasing frequency. The combined methods have to be conducted when the test has been sustained for a longer time at this waveform. Finally, the ΔK_0 is increased to nearly 40 MPa√m, which is an extremely high value. Both tests show that the crack-tip resharpening works when the tests have been only conducted for a short time. After a longer duration test, crack-tip resharpening (by frequency increase) should be combined with increasing the load range to obtain the crack growth. Thus, the fatigue crack arrest level is also related to the time of being tested (so very likely linked to crack wake or crack tip oxidation events which develop over time). Two typical crack length extensions caused by the resharpening are displayed as insert graphs in Fig. 7.1 (c) and (d).

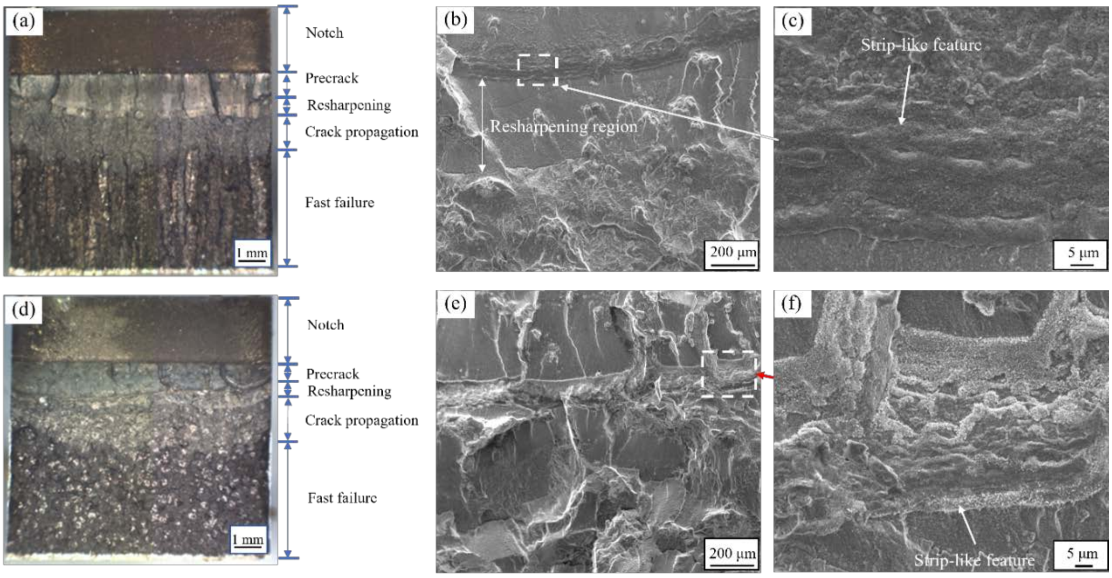

Fig 7.2 Optical microscopic (OM) image of T and L samples tested at 1-90-1-1 waveform, 650 ℃ (a, d), the low-magnification SEM images of the resharpening region for T and L samples (b, e), the high-magnification SEM images of oxidation layers for T and L samples (e, f)

Two typical fracture surfaces are shown in Fig. 7.2. They are L and T samples tested with the 1-90-1-1 waveform at 650 ℃. For both tests, cracks are arrested when the loading frequency is transfered from 10 Hz sine waveform for precrack to 1-90-1-1 trapezoidal waveform. Load range was increased in 10% increments multiple times to force the crack growth to continue, although no detectable crack growth was found. Eventually, the crack did continuously grow, after ΔK_0 is increased to nearly 30 MPa√m, combined with crack-tip resharpening. The features of these crack arrests are clearly observed on the fracture surfaces shown in Fig. 7.2 (a) and (d). Strip-like features are noticeable at the crack-arrested regions for both L and T samples shown in Fig. 7.2 (b), (c), (e) and (f). These features are inferred to be oxidation layers formed during the low-frequency tests with a width of over 10 μm. It is inferred that the crack arrest behaviour is associated with the formation of the thick oxidation layers. Thus, more interrupted tests were performed to analyse the oxidation behaviours at the crack tips in more detail.

7.3 Interrupted tests and crack tips characterization

Three interrupted tests were performed. The first one is an L specimen tested under a 1-1-1-1 waveform, 650 °C for 48 hours, without detectable crack growth. The total cycles experienced by the interrupted L sample is twice the life time of the L sample tested under a 10 Hz sine waveform. The tested and polished sample is shown in Fig. 7.3 (a). The interdendritic regions are generally perpendicular to the main crack propagation direction (indicated by the top arrow in the figure). The main crack is locally tortuous, due to the crack paths following the slip systems or being deflected by microstructure features (like carbides or pores). A higher magnification of the crack tip and element maps are shown in Fig. 7.3 (b). The morphology of the crack tip is noticeably different to the expected sharp crack tip. It shows a round-coronal morphology with oxygen filling the whole crack, indicated by the oxygen-distribution map. Obviously, the crack tip is blunted. The Ni and Co-element distribution maps demonstrate that the Ni/Co-rich oxides are mainly located within the crack tip, forming the so-called external oxidation layers. The Al/Cr-rich oxides are formed ahead of the crack tip at the coronal parts, which is potentially caused by the intrusion of oxygen species into the alloy ahead of the crack tip.

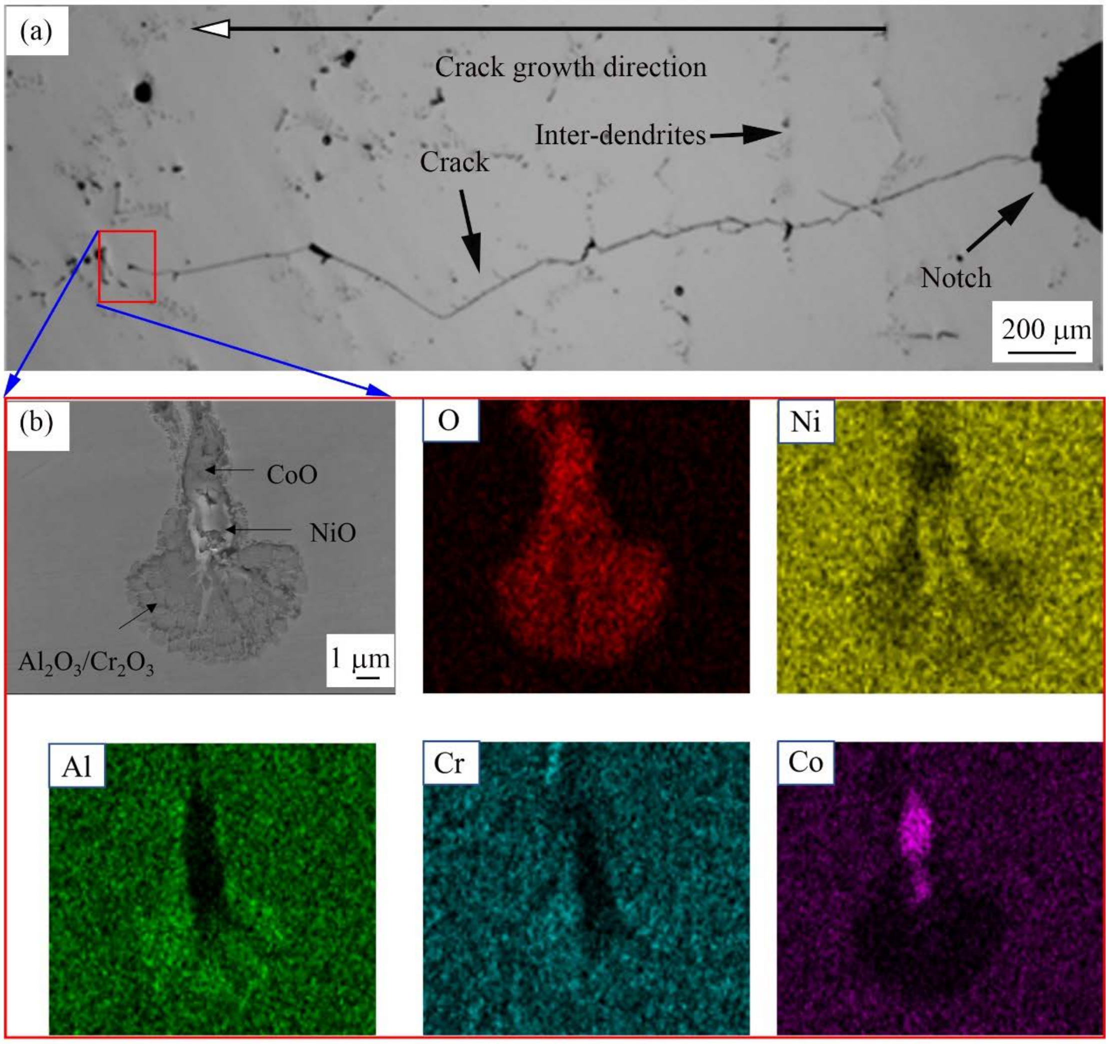

Fig 7.3 (a) the OM image of interrupted L sample after tested at 1-1-1-1 waveform, 650 °C for 48 hours, (b) the high magnification SEM image of the crack tip and associated element distribution maps.

For the second interrupted test, the T sample is interrupted after being tested under a 1-90-1-1 trapezoidal waveform, 650 °C for 12 hours, similarly without any detectable crack growth. The crack tip has a round-coronal morphology as well (Fig. 7.4 (a)), with however, a smaller size compared to the crack tip of the first interrupted-test sample. The diameter of the round-coronal region of the crack of the L specimen is approximately 6 μm, determined by measuring the longest distance between two points within the coronal region. Comparatively, the diameter of the crack tip in the second interrupted sample is only ~ 3 μm. In addition, a very minor crack is found in front of the coronal crack tip in Fig. 7.4 (a), indicating potentially the crack growth is not completely arrested, but it should be noted whether the minor crack is formed before the oxidation of the crack is uncertain due to the 2D section being assessed here. A higher-magnification SEM image of the crack wake, taken

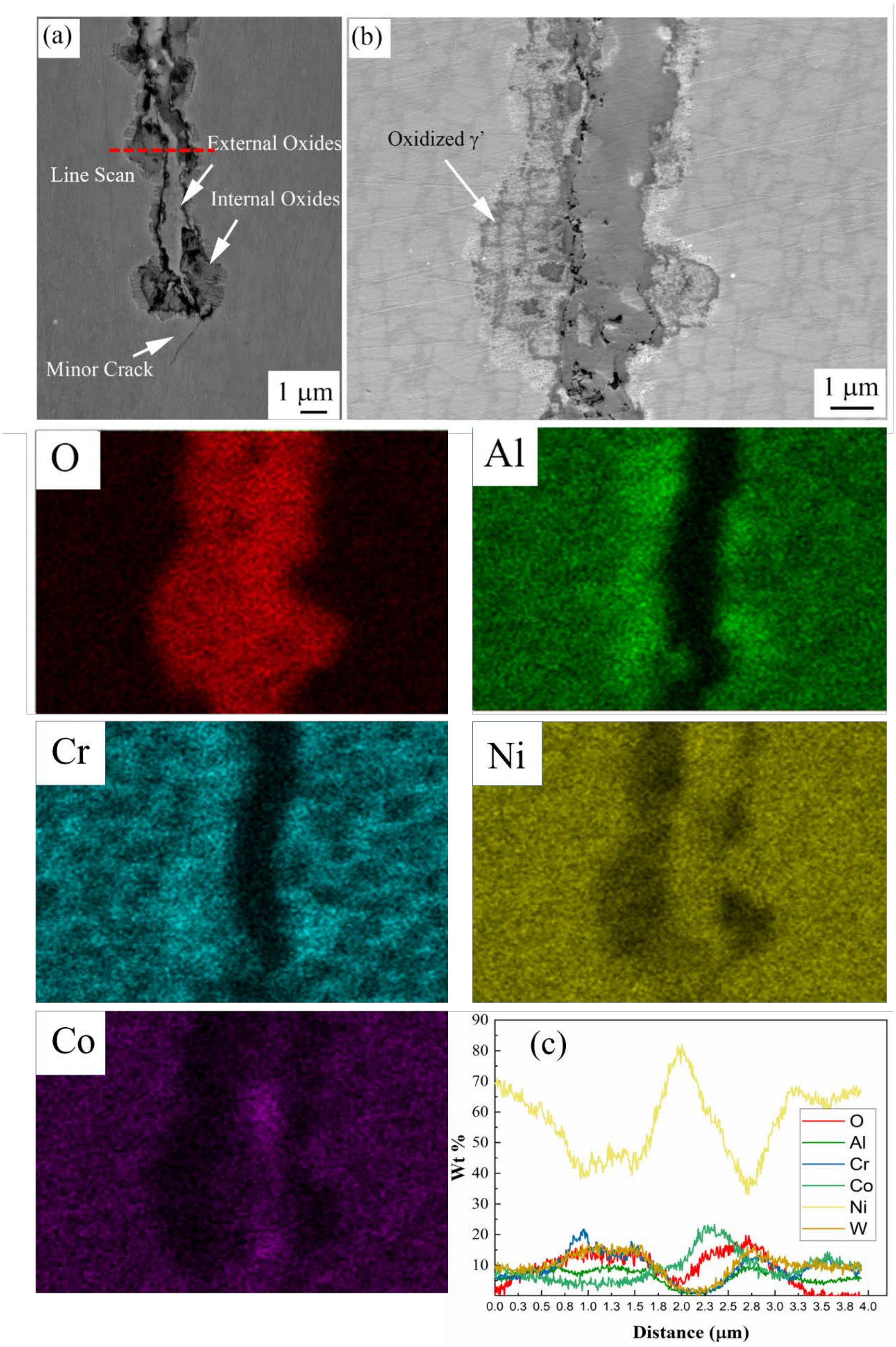

Fig 7. 4 SEM images of the crack tip of interrupted T sample, tested at 1-90-1-1, 650 °C for 12 hours (a), and the crack wake and associated element distribution maps (b), an EDX line scan perpendicularly across the crack (c)

under a lower accelerating voltage, more clearly presents the morphology of internal and external oxides in Fig. 7.4 (b). The completely oxidized γ′ precipitates and γ channel constitute the internal oxidation layers. Associated element distribution maps show the enrichment of Al and Cr elements in the same region. The composition of the external oxidation layers is as observed in the T samples, consisting of Ni/Co-rich oxides. An EDX line scan is performed at the crack wake, perpendicular to the crack propagation direction, marked in Fig. 7.4 (a). According to the element variation along the line profile in Fig. 7.4 (c), the thickness is measured to be 1.2 μm for external oxides and 2.0 μm for internal oxides. Herein, the EDX line scan is employed as a tool to measure the thickness of oxides and performed multiple times to obtain statistically consistent data.

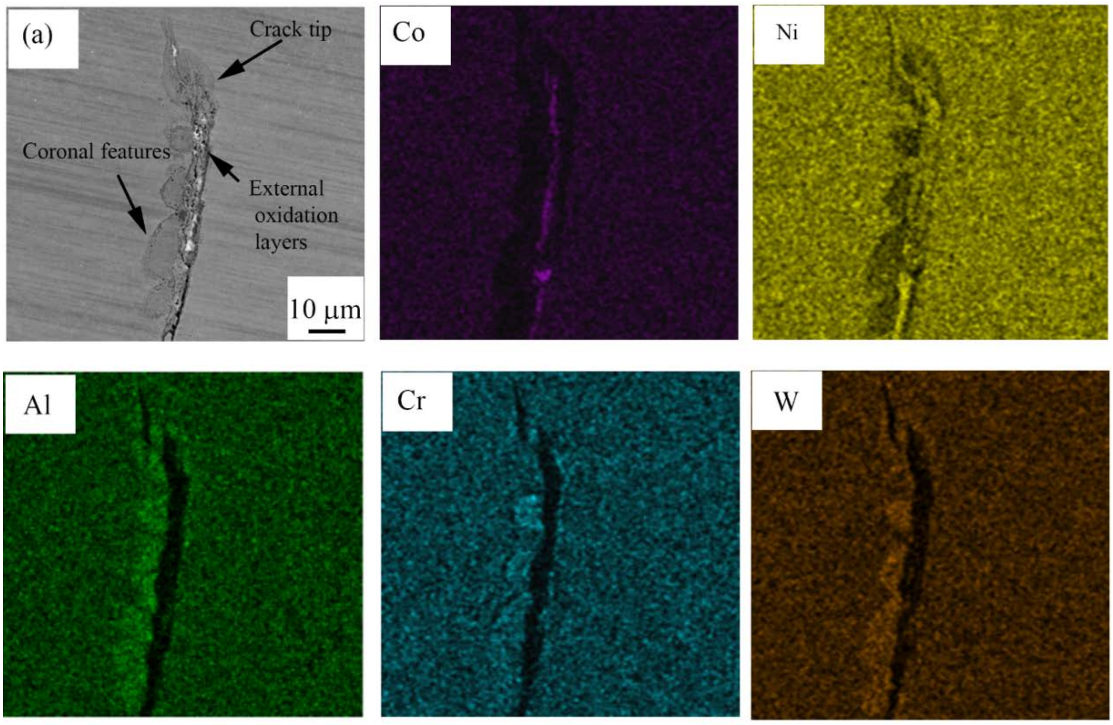

Fig 7. 5 the SEM image of the crack tip for the third interrupted T sample, tested at 1-90-1-1, 650 °C for 96 hours and associated element distribution maps.

The third interrupted test is much more complicated. The T sample was tested at 1-90-1-1 waveform, 650 °C for, in total, 96 hours. Load range was increased by 10%, during the test approximately every 16 hours, and eventually the ΔK reached 24 MPa√m. A series of round-coronal oxidized features are observed in a row along the crack tip shown in Fig. 7.5 (a). However, these features are formed at both crack tip and wake, apparently different to previous tests, where internal oxidised regions are only formed at the crack tip. It indicates that the crack did indeed grow after load was added, but the growth length is at the micron scale, undetectable by the potential drop method. After a few microns growth, the crack is arrested again, forming a new round coronal crack tip. The number of the coronal features is consistent with the number of times the load range was increased. The element distribution maps present similar oxidation layers as the last two cracks, but the thickness of the external oxidation layers is increased to approximately 4 μm. This could be attributed to the larger crack opening caused by the higher ΔK value.

7.4 Three-dimensional characterization of the crack tip via Xray-CT

The SEM-based characterization illustrates the formation of thick oxidation layers at the crack wake as well as at the crack tip. However, this two-dimensional characterization is sectioning-position dependent, and reconstructing the crack tip in three-dimensions could obtain more valuable/relevant information, especially measuring the crack opening displacement (COD) systematically. The 3D rendering of the crack tip of the interrupted L specimen tested under 1-1-1-1 waveform, 650 °C is shown in Fig. 7.6 (a). The crack propagation and loading direction is marked in the figure, and it is notable that the crack tip is not as sharp as those observed in polycrystalline superalloys using X-ray CT, tested under similar conditions [204]. Slices corresponding to the different positions of the crack tip are presented in Fig. 7.6 (b), (c), (d) and (e). All the CT slices show the rounded crack tips, consistent with the observation via SEM.

Another 3D rendering of the crack tip of the interrupted T sample tested at 1-90-1-1 waveform, 650 °C after 96 hours is shown in Fig. 7.7 (a). It is interesting that the tiny match-stick sample possesses two cracks, which is potentially associated with the large-size columnar grain structure [150]. The columnar grains aligned with the crack propagation direction facilitate crack initiation and propagation inside each grain. Similarly, the blunted crack tips are observed in both the 3D rendering and the corresponding slices. In comparison, the scale of the blunted crack tips is considerably larger than those in the L sample due to the longer time exposure to the high temperature. Also, the blunted crack tips are elongated, attributed to increasing the load range several times during the test (to try and grow the crack). The slice d (Fig. 7.7 (d)) shows the two-crack overlaid region, where both the crack tips are rounded.

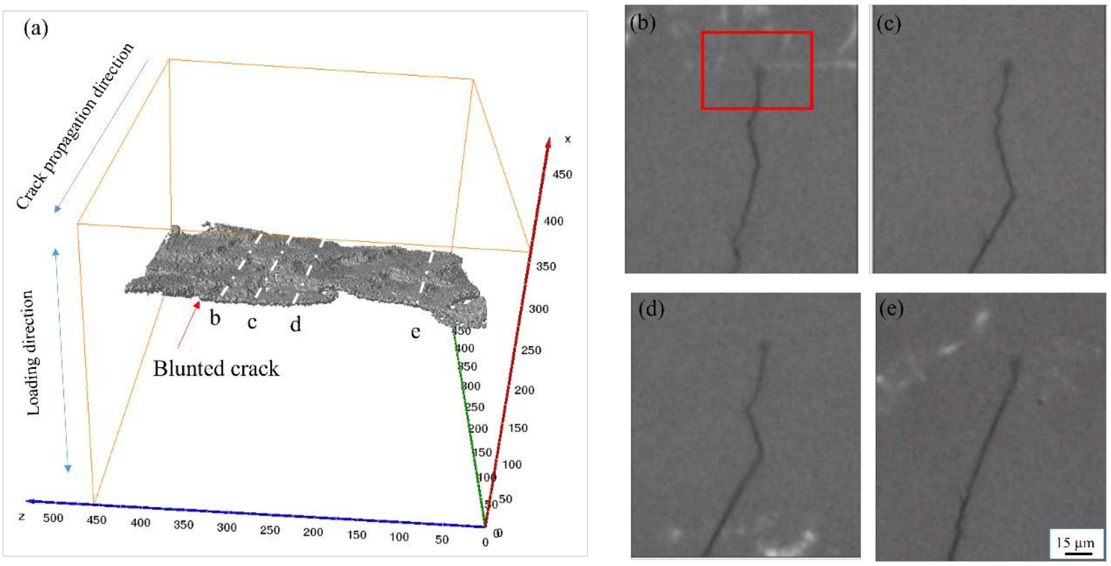

Fig 7. 6 (a) CT 3D rendering of crack profile for the interrupted L sample, tested at 1-1-1-1 650 ℃ for 48 hours, slices corresponding to the line profiles: b (b), c (c), d (d), e (e).

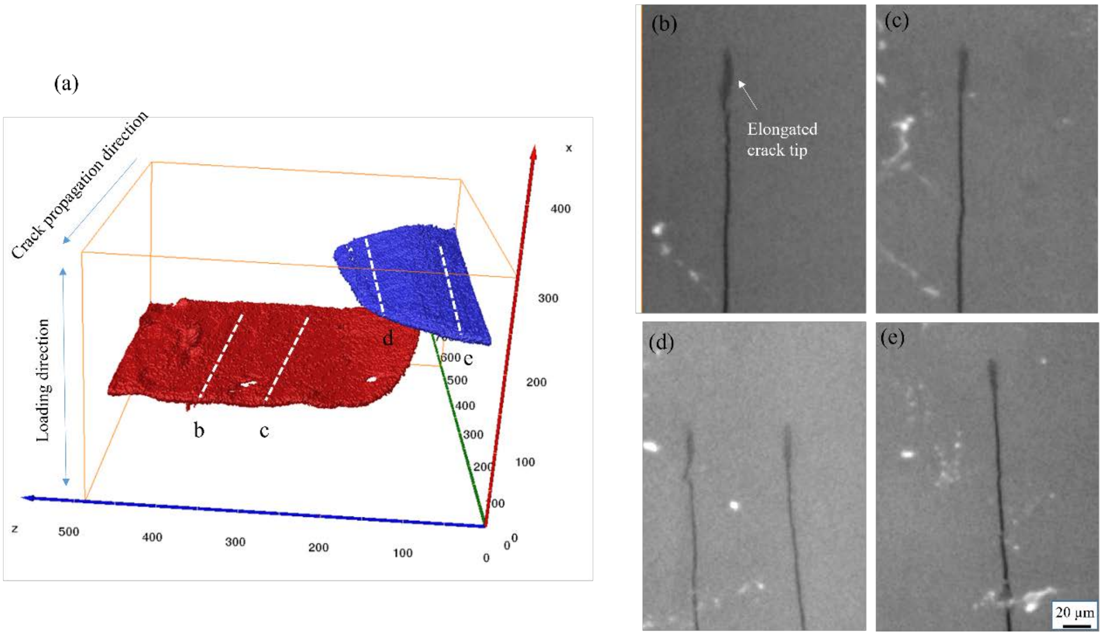

Fig 7.7 CT 3D rendering of crack profile for the interrupted T sample, tested at 1-90-1-1 650 ℃ for 96 hours, slices corresponding to the line profiles: b (b), c (c), d (d), e (e).

The COD contour maps measured perpendicular to the crack plane (Fig. 7.8 (a) and (b)) show the high values at the crack front lines for both L and T samples. In comparison, the front line of high CODs is wider in the T specimen, consistent with the elongated crack tip observed by SEM and X-ray CT. Corresponding line profiles across the crack faces are shown in Fig. 7.8 (c) and (d). The peak COD values are presented at the interface between the crack faces and the materials matrix, confirming the formation of the round crack tips for both L and T samples. It is notable that the peak COD values of the crack tip are over 12 μm for the T sample, while around 7 μm for the L sample. This is potentially caused by the longer duration and higher K_{max} of the test leading to the larger oxidised region at the wake of the crack tip. The line profiles of the L sample are noisier, and at some points, the COD reaches zero, indicating direct contact between crack faces without oxidation formation. The CODs of the crack wake vary with the distance to the crack tip. The values rise from 0 - 2 μm, within the distance of 50 μm to the crack front line (herein, the crack front line is considered at the COD peak point) to 4 - 6 μm, with the distance increasing to 200 to 300 μm. T sample exhibits the similar trend for the CODs, as they are nearly 4 - 6 μm within the distance of nearly 100 μm, while increase to 6 - 8 μm at a larger distance. Therefore, the difference of CODs is mainly concentrated at the crack wake within a short distance (less than 50 μm) to the crack tips for L and T samples.

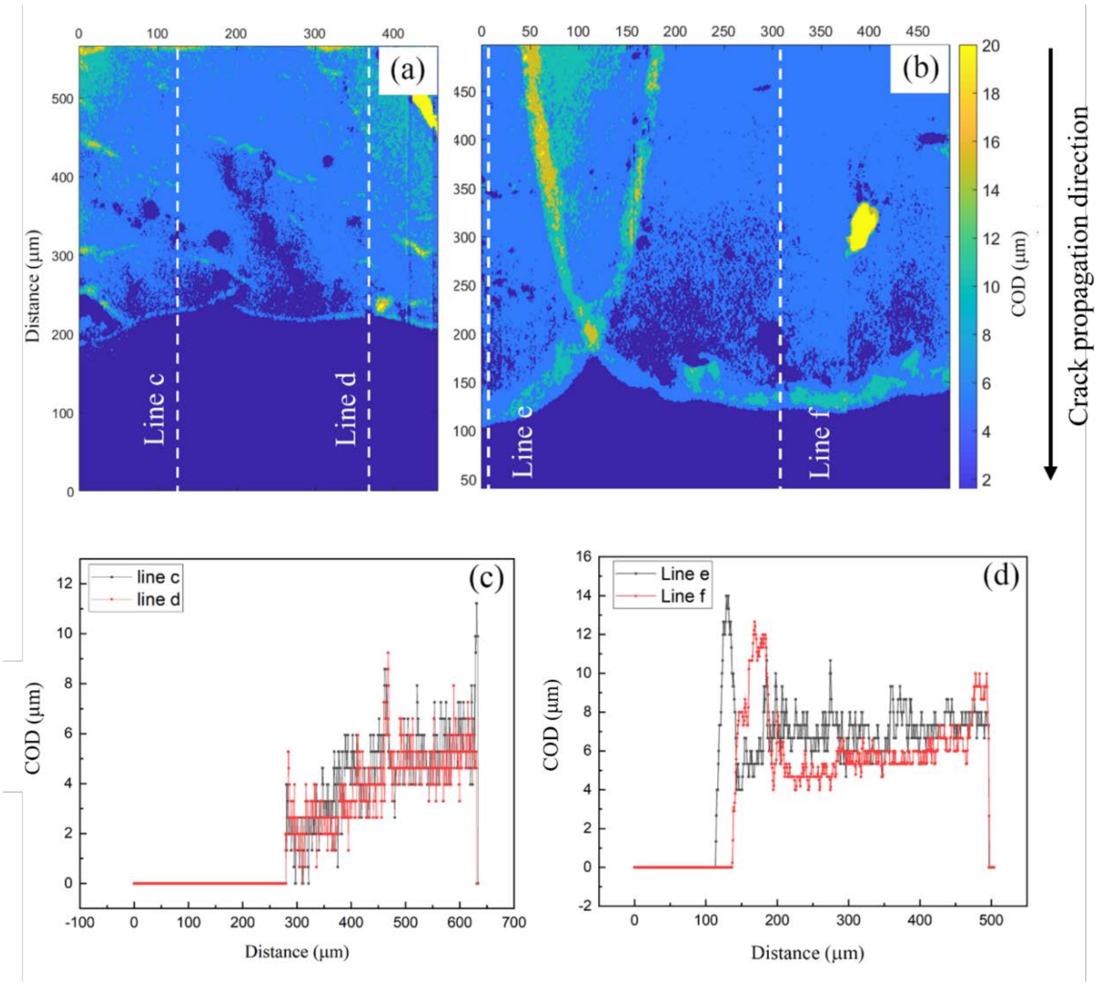

Fig 7.8 crack opening displacement plots across the crack face for interrupted L sample, tested at 1-1-1-1 650 ℃ for 48 hours (a) and T sample, tested at 1-90-1-1 650 ℃ for 96 hours (b), COD line profile plots as measured across the white dotted lines for L (c) and T (d)

7.5 Discussion

The above work provides clear experimental results confirming the existence of significant oxidation-induced crack closure (OICC) under high temperature and low frequency testing conditions in a Ni base superalloy. Over the past few decades, oxidation has tended to be regarded as a purely detrimental process prompting fatigue crack initiation and propagation at high temperatures [233-238]. Although some research shows evidence of oxidation-induced crack closure results [121-125, 239], particularly in the 1980s, the underlying mechanism was somewhat ambiguous due to the lack of characterization techniques of high enough spatial resolution and inability to consider the full 3 dimensional process. A question also arises as to whether the deceleration of the crack propagation is caused by the oxides filling the crack wake or the effective increase of fracture surface roughness by the oxidation (roughness-induced crack closure). Current work rationalises the crack closure results based on the OICC mechanism combined with the benefits of detailed characterization. Modified models and solutions are proposed and discussed to understand the physical mechanisms and chemical reactions behind the OICC.

7.5.1 Complete or partial oxidation-induced crack closure ?

In considering general fatigue crack propagation without oxidation, the crack opening displacement (COD, δ) reaches a peak under the maximum load, denoted as δ_{max}, while the lowest value is seen at the minimum load, δ_{min}. The difference between the CODs ($\Delta\delta$) at the maximum and minimum loads could act as the parameter indicating the driving force for the crack advancing [240]. However, once the oxidation film is formed at the crack flanks, the δ_{min} is accordingly increased, decreasing the $\Delta\delta$ and driving force for the crack propagation. The whole process is shown in the schematic diagram Fig. 7.8. Although the mechanism was proposed a few decades ago [121-123, 239], quantitatively evaluating the effects of OICC on fatigue crack propagation is still a challenge. According to N. Louat et. al [126, 241, 242], there are at least two cases that need to be considered when evaluating the OICC. They are termed as complete oxidation-induced crack closure (COICC) and partial oxidation-induced crack closure (POICC), this was termed as asperity induced crack closure in some literature [126, 241]), respectively. Whether the formed oxides inside the crack wake are continuous or discrete is the critical difference between COICC and POICC. Researchers think COICC is an idealised model [241], as usually the oxides inside the crack are believed to be formed by ‘fretting oxidation’, which means the oxide scale is repeatedly breaking and reforming under the cyclic loading. In this case, a continuous oxide film is rarely formed, and hence very few models have been proposed to assess the effects of COICC. Nevertheless, the current study clearly shows the continuous external oxidation layers formed within the crack for our 1-90-1-1 tests in Fig. 7.4 (a), (b) and Fig. 7.5 (a). It should be noted that these SEM images are at high magnifications, only showing local oxides within the crack. In addition, the 2D observation is sectioning-position dependent, thus requiring a more systematic characterization evidencing the occurrence of COICC. The COD measured using X-ray CT could provide such systematic data, proposed by Toda et. al [151, 152]. For the tests of 1-90-1-1 loading frequencies, the randomly selected line profiles of the crack faces indeed show stable and high COD values, as shown in Fig. 7.8 (d), indicating the formation of continuous oxides wedging the crack opening. In contrast, for the tests under the 1-1-1-1 loading frequencies, the COD values fluctuate significantly, and at some points of the line profiles, the COD values reach zero in Fig. 7.8 (c), indicating the contact of the crack faces. The stitched image of the crack path of the 1-1-1-1 test also confirms this in Fig. 7.10 (a), (b) and (c). Therefore, the occurrence of COICC or POICC is highly dependent on the test frequencies for the alloy. The relatively high-frequency tests are more likely to smash the oxides repeatedly, resulting in POICC, while low-frequency tests will facilitate the formation of thick and continuous oxides, leading to COICC. Based on the results, different models and solutions are proposed to evaluate the effects of COICC and POICC.

7.5.2 The effects of COICC

Firstly, for the COICC, where the COD is rather stable, the following simplified assumptions are made:

(i) The δ_{max} is only related to the maximum load, not affected by the oxidation.

(ii) The δ_{min} is equal to the thickness of the external oxidation layers, as the oxides are assumed to be rigid bodies.

(iii) The thickness of the external oxides is taken as the average oxide thickness within 10 μm behind the crack tip.

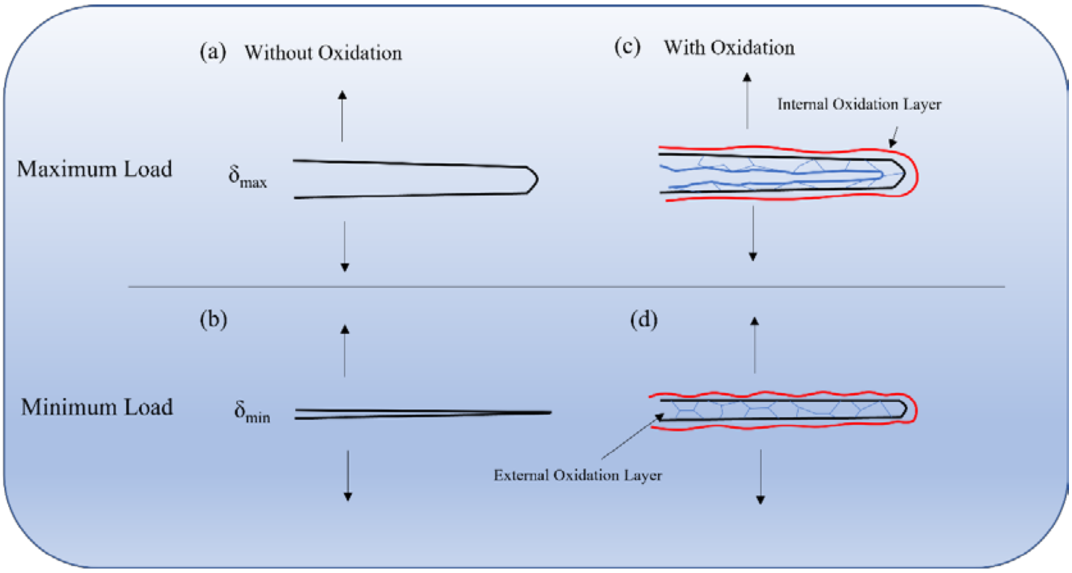

Fig 7.9 Schematic diagram of fatigue crack opening at maximum load (a) and minimum load (b) without oxidation, maximum load (c) and minimum load (d) with oxidation

From the SEM characterization results, internal oxides are formed by the oxygen intrusion into materials, slightly affecting the crack opening. Thus, the effects of internal oxides are not considered here, but will be discussed later. Approximating the δ_{min} with the oxide's thickness is supported by Suresh et. al [121], but theoretically, calculating the δ_{min} should consider the external oxide's thickness as well as the CODs induced by the minimum load. Given that the load ratio, R is only 0.1, the δ_{min} induced by minimum load is negligible compared with the δ_{max} and the oxide's thickness in the second assumption. The third assumption is associated with the definition of COD, as the values always increase from the crack tip to the crack end. Most researchers think that the driving force for the fatigue crack propagation is mainly influenced by the COD near the crack tip, termed as CTOD. In most cases, the CTOD is defined at the points where a 90° angle at the crack tip intersects with the crack sides [243]. However, due to the oxygen intrusion, the crack tip is blunted and forms a distinctive rounded shape, completely different to the normal sharp crack tip (Fig. 7.3, 4, 5, 6, 7). Thereby, using the method of 90°-intersected lines might overestimate the CTOD. According to the CODs measured from X-ray CT in Fig. 7.9 (c) and (d), the δ_{min} is stable within distance of 50 μm to the crack tip. Herein, the δ_{min} (external oxides thickness) is measured in two ways. The first way is measuring the δ_{min} by averaging the thickness of external oxides within 10 μm to the crack tip via SEM-EDX. The other is directly measuring the average δ_{min} of the equal region using X-ray CT. It should be noted that there is an obvious oxidation intrusion ahead of the crack tip, which is incapable of being distinguished by X-ray CT. To avoid counting the oxidation intrusion into crack, all the COD measurements by X-ray CT are extracted 10 μm behind the segmented crack tip. The averaged oxidation intrusion size is in the range of 6 μm to 9 μm. The stress intensity factor K_c, when crack flanks contact oxides, and effective stress intensity range (ΔK_{eff}) are

$$K_{max} = \frac{P_{max}}{B \times W^{1/2}} \times Y \times 10^{1.5} \tag{7.1}$$

$$\delta_{oxides} = \frac{K_c^2}{m\sigma_Y E'} \tag{7.2}$$

$$m = 1.517\left(\frac{\sigma_Y}{\sigma_U}\right)^{-0.3188} \tag{7.3}$$

$$\Delta K_{eff} = K_{max} - K_c \tag{7.4}$$

where K_{max} is the stress intensity factor at the maximum load, P_{max} is the applied maximum stress, B is the breadth of the cross-section of the bend bar, W is the height of the cross-section of the bend bar, Y is the stress intensity factor function given by British Standards [244], m is the parameter associated with the material's yield stress, σ_Y and ultimate failure stress, σ_U. E' is the Young's modulus under plane strain conditions [245]. δ_{oxides} is the thickness of oxides measured using SEM-EDX. They have been compared with COD data extracted from X-ray CT in Fig. 7.10 (d). It is obvious that the data from X-ray CT overestimates the COD values, potentially caused by two factors. The first one is the partial volume effect existing in segmenting the crack [151], causing an error of half the voxel size at maximum (0.3 μm in the current work). The second one is the oxygen intrusion along the crack, leading to the formation of internal oxidation layers with width of nearly 2 μm in Fig. 7.4 (a), (b) and Fig. 7.5 (a). Completely segmenting the crack from the internal oxidation layers is unachievable due to their extremely close grey values, and hence resulting in the overestimation of COD.

Table 7.1 δ_{oxides} from SEM and $\Delta\delta$ calculated from the ΔK applied for the fatigue tests, ΔK_{eff} and ΔK

	*Thickness of oxides	Δδ calculated from ΔK	ΔK_{eff}	ΔK
T interrupted after 12 h	1.09	1.53	3.88	15.07
T interrupted after 96 h	2.61	3.30	4.75	22.18

* The unit for thickness of oxides and COD are μm, for ΔK_{eff} and ΔK is MPa$\sqrt{m}$

The measured average thickness of external oxides is quite close to the $\Delta\delta$ calculated from ΔK in Table 7.1, indicating the significant effects of crack closure induced by external oxides. Calculated ΔK_{eff} values directly confirm the hypothesis, as the markedly reduced ΔK_{eff} is apparently lower than the common ΔK_{th} quoted for superalloys [246-248], explaining the arrest of the crack growth at low frequency. The good fit of experimental results and calculations validates the use of this simplified geometrical model, which could be employed in other similar material systems for evaluating COICC.

7.5.3 The effects of the POICC

As discussed above, POICC occurred during the test at 1-1-1-1 frequency. Fig. 12 show the locations of these asperities. It is worth noting that oxidation intrusion along the crack wake is much slighter compared with the test of 1-90-1-1, and thus COD from X-ray CT is comparable with the oxide's thickness measured from SEM-EDX in Fig. 7.10 (e). Evaluating the POICC is far more complicated than COICC, and so far, only two models have been proposed, which attempt to quantitively correlate the thickness of oxides on the driving force for fatigue propagation. One of them is proposed by Suresh et. al [121, 249], where only a mechanical closure phenomenon arising from the oxide wedge is considered. The K_c at the crack tip is calculated based on elastic superposition using the Westergaard stress function:

$$K_c = \frac{E'd}{4\sqrt{\pi l}} \tag{7.5}$$

$$\Delta K_{eff} = K_{max} - K_c \tag{7.6}$$

where d is the height of the rigid wedge, $2l$ is the location behind the crack tip. Herein, the COD data measured using X-ray CT is utilized to calculating the ΔK_{eff} under the effects of oxides in different positions. The scattered ΔK_{eff} shown in Fig. 7.10 (f) is due to the thickness variation of oxides within the crack, which is the feature of POICC. Some points with fine-scale oxides lead to a high ΔK_{eff} value, while some points with large-size cause a significant crack closure (low ΔK_{eff} value). However, the scatter in ΔK_{eff} tends to converge to 0 with oxides positioned close to the crack, indicating even small oxides forming at the crack tip will exert a significant closure effect on the crack propagation. This is consistent with the experimental results that the fatigue crack is arrested with external oxides forming extremely close to the crack tip in Fig. 7.10 (d). The ΔK_{eff}, resulting from the oxides located more than 200 μm behind the crack tip, becomes more stable, varying in the band between 8 MPa$\sqrt{m}$ to 12 MPa$\sqrt{m}$. This is attributed to the more stabilized COD data measured at these positions shown in Fig. 10 (d). Although the COD data far behind the crack tip is higher, their effect on crack closure is much slighter. It is worth noting that Suresh's model is based on linear elastic theory, which is unable to describe the K_c in the plastic region. The radius of cyclic plastic region is estimated to be 9.1 μm [250]. In this case, using the data obtained 10 μm behind the crack tip to calculate ΔK_{eff} is reasonable.

Louat et. al [241, 242, 251] proposed a nonlinear elastic model to calculate POICC, based on the dislocation continuum theory. In Suresh's model, they thought once the crack faces contact with the rigid body during the unloading process, the whole crack is blocked from further closing. In comparison, Louat et. al thought that the contacted parts of the crack are open, while other indirectly contacted parts are going to further close. It results in the dislocation density for indirectly contacted parts being considered to be zero, but for contacting parts should be related to the Burgers vector and heights of the oxide. Based on the hypothesis and some simplified assumptions, the ΔK_{eff} could be calculated using following equations:

$$\Delta K_{eff} = K_{max} - 0.25K_i[1 + 0.75\left(\frac{K_{min}}{K_i}\right)] \tag{7.7}$$

They thought when the crack faces contact the oxides, there should be a slope change of the cyclic strain-stress at the unloading phase. The stress intensity factor corresponding to the inflection point is K_i. Nevertheless, the inflection point is hard to distinguish in the experiments for the material [252], as the effects of the local crack closure on the global mechanical response of the material should be minor, particularly at the initial stage of crack propagation tests. Herein, another experimental solution to estimate the K_i is proposed based on the COD data obtained using X-ray CT. K_i is exactly the point when oxides are contacting with crack faces, hence it could be calculated if the CTOD of that point could be measured. In the model shown in Fig. 7.10 (g), the initial contact between crack faces and oxides is considered, and thus the CTOD at the position 10 μm behind the crack tip could be calculated using following equation:

$$\delta_{10} = \delta_{COD}\frac{10}{l} \tag{7.8}$$

where δ_{10} is the CTOD at the position 10 μm behind the crack tip, δ_{COD} is the COD at the position with distance of l μm to the crack tip. Then the K_c could be calculated using equation (2) and (3). The contact between oxides and crack faces could occur at many points within the crack, and consequently a series of K_c is calculated based on the CTOD estimated from oxides at different position along the crack. K_i should be in the range of these K_c, and hence the range of ΔK_{eff} could be calculated by replacing K_i with the series of K_c. The calculated ΔK_{eff} is in the range of 10 MPa√m (near the crack tip) to 15 MPa√m (far away from the crack tip) in Fig. 7.10 (d), which is much higher than that calculated from Suresh's model. It indicates that although the formation of external oxides indeed reduces the driving force, but their effects are not as significant as proposed by Suresh et al. So far, it is still quite a challenge to directly measure the driving force variation in high-temperature fatigue tests, leading to difficulty in validating and developing these models. However, the data calculated from both models show that oxides forming near to the crack tip exert a significant retardation effect on the crack propagation, which is consistent with the current experimental results. It should be noted that the calculated ΔK_{eff} is highly oxide-position dependent according to the two models and thus, systematic data of oxide thickness and position is required. Current work proves that X-ray CT could be appropriately employed to characterize the POICC, particularly in materials or test conditions where oxygen intrusion is minor.

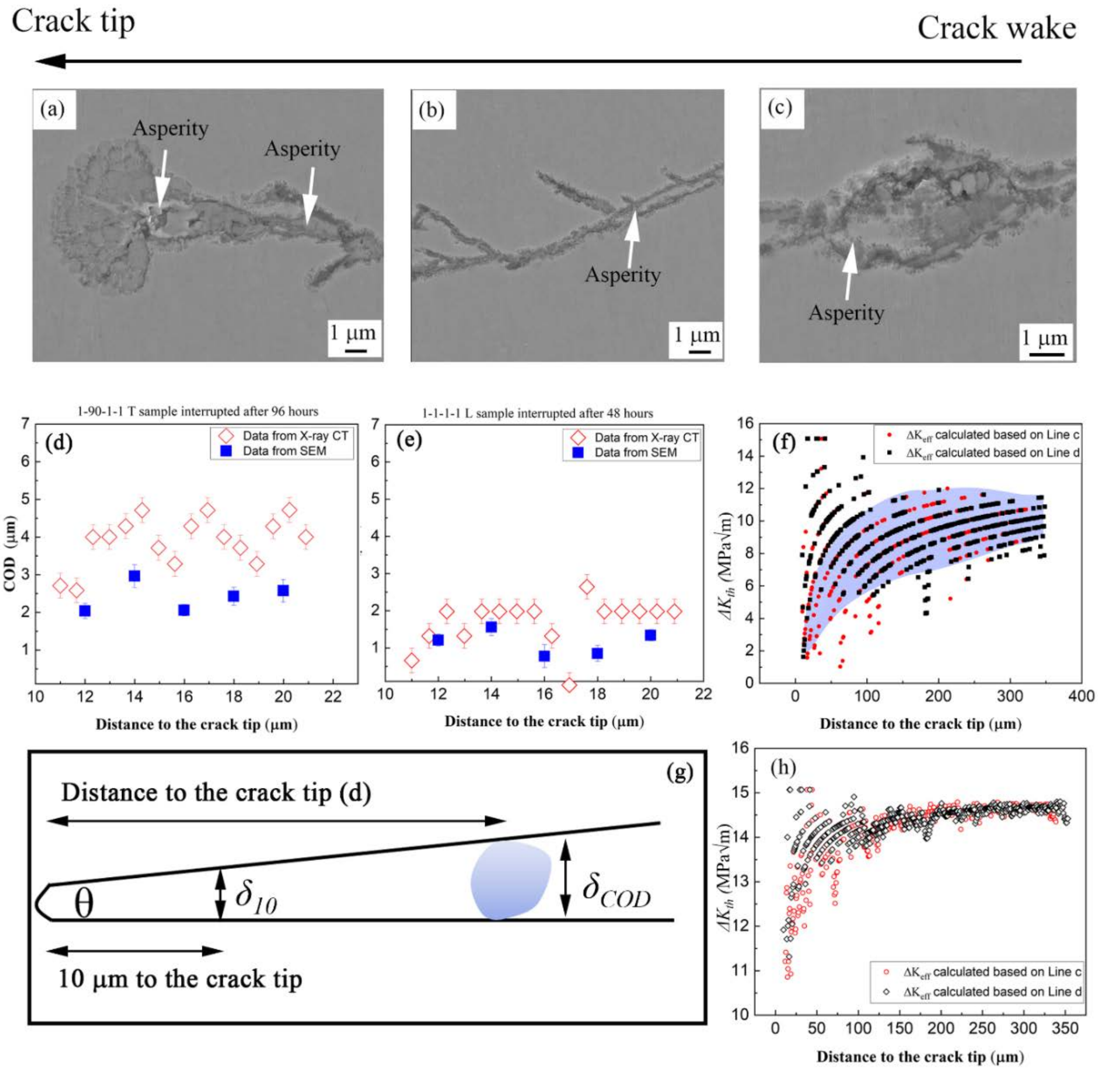

Fig 7.10 the SEM images from the crack tip to the crack wake of the interrupted L sample, tested at 1-1-1-1 650 ℃ for 48 hours: (a), (b), (c); COD measured by X-ray CT and SEM-EDX for the test of 1-90-1-1 (d) and

1-1-1-1 (e); ΔK_{eff} calculated based on Suresh's model (f); Schematic diagram of the model to estimate the CTOD (g); ΔK_{eff} calculated based on Louat's model

7.5.4 The effects of the microstructures

As discussed above, external oxides play a significant role in arresting the fatigue crack propagation for both L and T samples. However, it should be noted that the T sample does not show any crack-arrest phenomenon, tested at 650 ℃ and 1-1-1-1 waveform. This is in contrast to the situation of the L sample, where ΔK needs to be increased to nearly 22 MPa√m to allow crack growth. To confirm this, these tests have been repeatedly performed and show the same results consistently, indicating the crack arrest is also affected by the underlying microstructure. The precrack path of L and T samples are compared in Fig 7.11, derived from 2D X-ray CT tomograph slices. It is obvious that the pre-cracks of the L samples (Fig 7.11 (a) and (b)) are much more tortuous than those of the T samples (Fig 7.11 (c) and (d)). This should be attributed to the relationship between dendrite orientations and crack propagation direction. For the L direction, the fatigue crack propagates generally perpendicular to the dendrites, and hence, it needs to go across the carbides, located in the inter-dendritic region, e.g. marked by the black arrow in Fig. 7.11 (a). Obviously, these carbides deflect the crack, resulting in a more tortuous crack path. Comparing with the crack propagation in the L sample, the crack in the T sample can propagate in much straighter trajectory within (and along) the main dendritic regions and largely avoid being deflected by carbides, as shown in Fig 7.11 (c) and (d). According to [253, 254], these deflection points could act as contact points to induce the crack closure, and hence reduce the effective stress intensity. From this point of view, it is reasonable to deduce that the crack arrest only occurs in L sample at 650 ℃ and 1-1-1-1 waveform, due to the occurrence of both POICC and roughness-induced crack closure acting together.

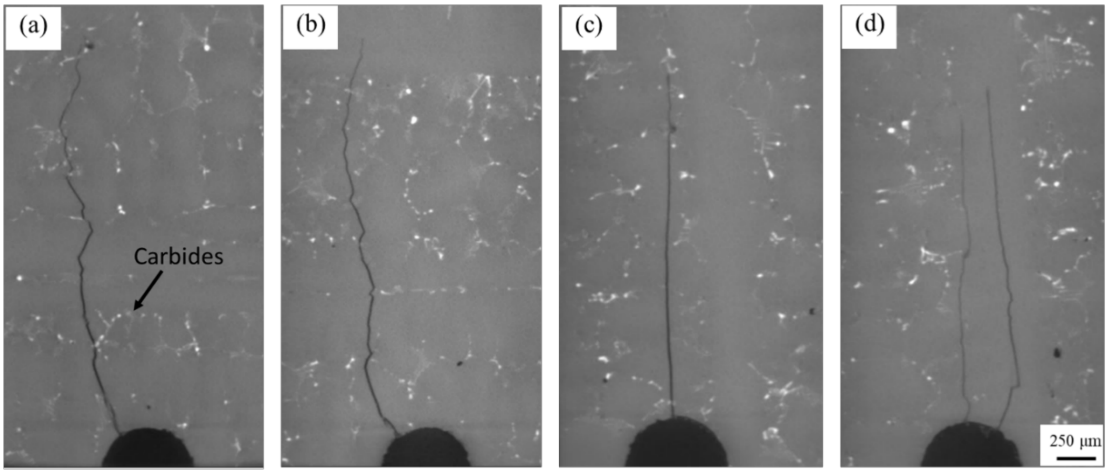

Fig 7. 11 the precrack path revealed in X-ray CT 2D tomographs of L, tested at 1-1-1-1, 650 °C, (a) and (b); of T tested at 1-90-1-1, 650 °C (c) and (d)

It should be noted the crack paths in Fig. 7.11 are produced from pre-cracking at high frequency, as both L and T samples were arrested after pre-cracking. The pre-cracking is performed at the same test conditions 650 ºC and 10 Hz waveform. Therefore, this comparable pre-crack test condition can be used to analyse the effects of microstructures on crack paths and consequent crack closure behaviours. Here we have only considered the deflection of the crack path by interdendritic carbides. The crack deflection by propagating into neighbouring grains is not discussed. This is because firstly, the grains of the DS materials are quite large (several hundreds of microns), and the precrack path considered here is ~ 2 mm, therefore in this case grain orientation influence is minor compared to the role of inter-dendritic regions within the large columnar grains. Secondly, the effects of grain orientation are likely to be more complicated, associated with the slip systems and misorientations between neighbouring grains, the current work and cases presented here are therefore mainly focused on the oxidation process. Future studies are also planned to evaluate the effect of these DS microstructures on a wider set of fatigue crack propagation cases in more detail.

7.6 Summary and conclusion

The following conclusions can be drawn based on the current work:

(1) Fatigue crack growth is arrested in the low-frequency fatigue tests at 650 °C and 725 °C in both L and T samples, except for the T sample tested at 650 °C and 1-1-1-1 waveform. It has been determined that the external oxides consist of Ni/Co-rich oxides which induce crack closure.

(2) The complete oxidation induced crack closure effects can be quantitatively evaluated based on the simplified assumptions and the thickness of oxides measured using SEM. Significant reduction in ΔK is induced by the thick external oxides, which should be the primary factor causing the fatigue crack arrest.

(3) X-ray CT is able to capture the morphology of the oxidized fatigue crack in three dimensions. Crack opening displacement (COD) measured using the segmented crack could be used to assess the crack closure effects induced by oxidation. It should be noted the COD data is overestimated in the situation of significant oxidation intrusion, such as the test at 1-90-1-1 frequency.

(4) The partial oxidation induced crack closure effect is evaluated based on the model of Suresh and Louat et. al as well as by evaluating the COD data from X-ray CT for the 1-1-1-1 frequency test. An obvious reduction in ΔK results from the oxides formed close to the crack tip and is confirmed by both models, though the degree of reduction in ΔK is different according to the two models.

(5) The carbides located at the inter-dendritic regions significantly deflect the fatigue crack path for L sample in the pre-cracking stage. Subsequently, the roughness-induced and oxidation-induced crack closure co-result in the crack arrest of L sample tested at 650 ℃ and 1-1-1-1 waveform.

Chapter 8 Detailed analysis on the oxidation and creep process on the arrested crack

8.1 Introduction

In the last section, fatigue crack closure in low-frequency tests is observed and explained in the view of the OICC that occurred at the crack wake. However, there are still some results that are not fully understood. Firstly, crack blunting is observed, which is potentially correlated to a creep process when holding at the maximum loading according to previous work reported in the literature review. Secondly, large-scale external oxides are formed, which is regarded as the main reason for the crack closure. Reported in [238], the oxidation process is competing with the cyclic mechanical damage, therefore, significant OICC would indicate that the stress-assisted oxidation process is quite fast in this DS-materials system. The question is whether any fast stress-assisted oxidation mechanism is correlated to material characteristics such as composition or microstructural features? Thirdly, although large-scale internal oxides are also formed ahead of the crack tip, their role in fatigue crack propagation is not well understood.

In this section, the crack tips of the interrupted tests are characterized using SEM-EBSD, nano-indentation and FIB-STEM, in an attempt to provide a deeper understanding of the role of oxidation and creep in fatigue crack closure. This work is currently being prepared as a journal paper, and we wish to acknowledge the contributions of the co-authors accordingly in this dissertation:

Yuanguo Tan, Ian Griffiths, Gareth Hughes, Neil Young, Nong Gao, Philippa Reed. The oxidation mechanisms for the oxidation induced crack closure in a directionally solidified superalloy, in preparation.

8.2 Results

8.2.1 Strain and mechanical property analysis at the crack tips in the interrupted tests

Crystal misorientation has been characterized via EBSD to semi-quantitatively measure the strain distribution along cracks under the influence of oxides in the second interrupted sample in Fig. 7.4 (T specimen was tested for 12 hours at 650 ºC, 1-1-1-1 waveform). The overlaid X-axis inverse map and SEM figure (Fig. 8.1 (a)) shows that the crack has propagated intragranularly. The notable difference of inverse pole colour marked in the black rectangle indicates the potential distortion of crystal orientation ahead of the crack tip. A higher resolution SEM image shows the crack is bifurcated at the tip covered by oxides (Fig. 8.1 (b)). The kernel average misorientation (KAM) map in Fig. 8.1 (c) confirms that the concentrated high-misorientation angle is localized at the crack tip, particularly between the two branches, which could be induced by plastic deformation. Consistently, the total geometrically necessary dislocation (GND) energy map (Fig .8.1 (d)) shows a localized high dislocation energy at the crack tip. Although both maps are unable to capture the strain accurately, the high KAM and GND energy could be correlated to the high plastic strain ahead of the crack tip at the unloading condition. In most cases, such high plastic deformation induces crack growth, but herein the crack is arrested during the fatigue test. It should be noted that some of the material ahead of the crack tip is oxidized in an oxide protrusion and hence is not indexed for EBSD mapping. The mechanical properties of these oxidized regions might also have effects on the strain localization or crack growth process, which needs more detailed analysis.

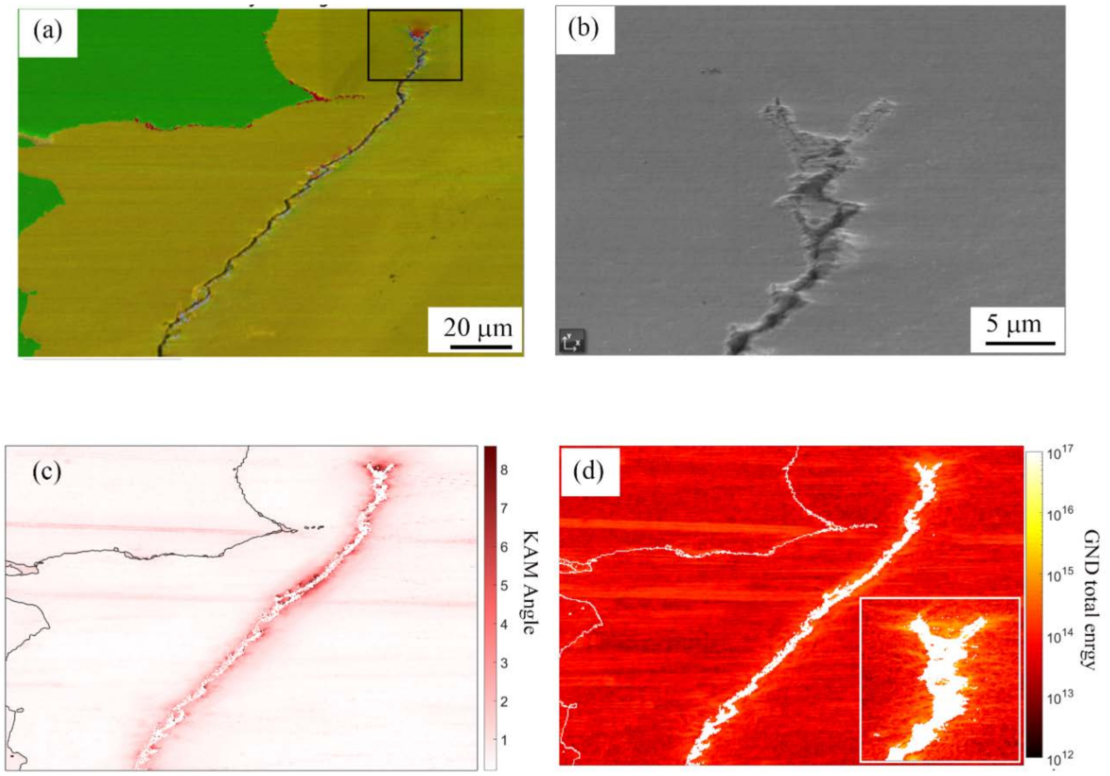

Fig 8.1 T Specimen tested at 650 °C for 12 hours: (a) Overlaid IPF (x) map and SEM image of the crack, (b) a higher SEM image of the crack tip, (c) KAM of the crack, (d) total GND energy map

of the crack and crack tip

Nanoindentation testing was performed on the crack tip and its close vicinity for the third interrupted test (L specimen was tested for 96 hours at 650 oC, 1-90-1-1 waveform) as shown in the Fig 7.5. For this relatively longer-term test, both internal and external oxidation layers are sufficiently large to allow nanoindentation testing. The nano indents can be clearly seen in Fig 8.2 (a). The hardness map (Fig 8.2 (b)) shows a good fit with the known crack tip morphology. The internal oxides present a much higher hardness value, where the average value is more than 14 GPa, while the maximum value reaches 24 GPa. The internal oxides are mainly composed of Al, Cr, W oxides, among which, Cr2O3 is the hardest oxide with 26 GPa hardness quoted in the literature [255, 256]. The hardness of Al2O3 and WO3 are quoted as nearly 15 and 8 GPa respectively [257, 258]. The hardness of the γ matrix is estimated here from our nanohardeness testing to be 6 to 10 GPa, which is a reasonable value compared with literature [259]. In comparison, the hardness value of external oxidation layers appears rather low, nearly 2 to 4 GPa. Nevertheless, it should be noted the roughness of the external oxides is quite high compared to the matrix and internal oxide, as they are formed inside of the crack. This potentially causes poor contact between the indenter and the oxides. The reduced elastic modulus map (Fig. 8.2 (c)) does not show much difference between the matrix and the internal oxides, apart from a very low modulus value at the external oxides. Similarly, this might be caused by the large height variation between the matrix and the external oxides. Another issue that should be taken into account is the indentation interaction volume. According to Bückle-Rule [260], the indentation depth is approximately 10% of the indentation interaction volume depth. Considering that the oxides in Fig 8.2 (b) closely surround the fatigue crack, the interaction volume might consist of oxides, material matrix and the fatigue cracks. This explains the hardness variation within these internal oxides in Fig 8.2 (b), as some points show the higher hardness than others due to the potentially different makeup of the interaction volumes. Further to this the external oxides within the fatigue cracks are largely unsupported when compared to the internal oxides and matrix and low hardness values could be as a result of increased compliance due to the oxide ability to move under the indentation loading.

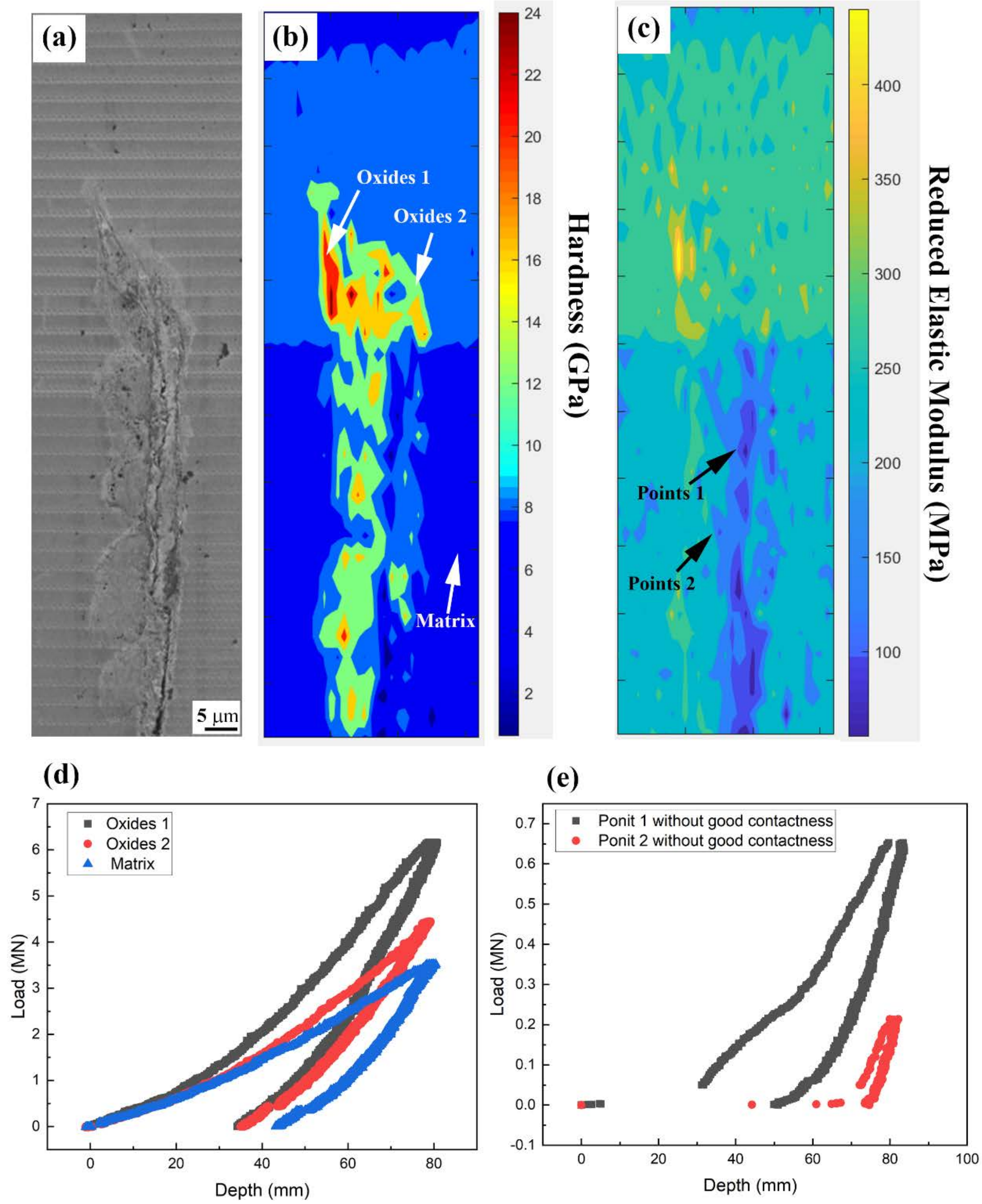

Fig 8. 2 (a) the SEM image of the crack tip after the nano-indentation test, (b) hardness map, (c) reduced elastic modulus map, (d) load-displacement curves of internal oxides and matrix, (e) load-displacement curves of external oxides

The load-displacement curves of some typical points are picked from the hardness map, shown in Fig. 8.2 (d) and (e). This shows that to obtain an 80 nm depth of the indenter, the required loads for internal oxide regions are quite a lot higher than for the matrix, further indicating the hardening of the crack tip by the internal oxidization. For the external oxide regions (points picked out from the reduced elastic modulus map), the curves show the poor contact, as the indenter initially contacted the oxides at the 30-μm depth for points 1, 70-μm depth for points 2.

8.2.2 Oxidation mechanism characterization via FIB and STEM

The SEM and X-ray CT characterize the potential relationship between oxidation and crack arrest, as the oxides fill the crack wake, wedging the crack opening, blunting and hardening the crack tip. However, the oxidation layers are complex, composed of sublayers of Co/Ni/W/Cr/Al oxides at the sub-micron scale. Each oxidation layer might play different roles in fatigue crack propagation. Therefore, a higher resolution characterization technique (FIB-STEM) has been used to investigate the oxidation layer growth mechanisms and associated effects on the fatigue crack growth behaviour. This work has been conducted with Dr Neil Young (managing the whole project), Dr Gareth Hughes (FIB cutting) and Dr Ian Griffiths (STEM analysis).

Two regions of interest (ROIs) were coated and extracted as shown in Fig. 8.3 (a). Region 1 (ROI-1) is located at the crack wake, perpendicular to the crack propagation direction, and Region 2 (ROI-2) is at the crack tip, parallel to the crack propagation direction. Strip-like external oxides with a homogenous width of 2 μm wedge the crack opening as shown in Fig. 8.3 (b). The internal oxides are heterogeneously distributed at both sides of the crack due to the oxygen intrusion. However, the internal oxides at the left side of the crack are more obvious than the right side, and a clear interfacial crack is observed between the external oxides and right-side internal oxides. Thus, it is inferred that the external oxides have predominantly formed and grown most extensively from the left crack flank. The external oxides at the crack tips also show this somewhat one-side dependent growth, as an interfacial crack is also observed at the bottom of the crack tips in Fig. 8.3 (c) and (d). Left and right views of the ROI-2 exhibit different crack tip morphologies (marked by the red-dashed line), as the crack appears to have a round shape in the left view, while it becomes branched in the right view. Similarly, the large-scale external oxides fill the crack tips with internal oxides protruding into the surrounding material.

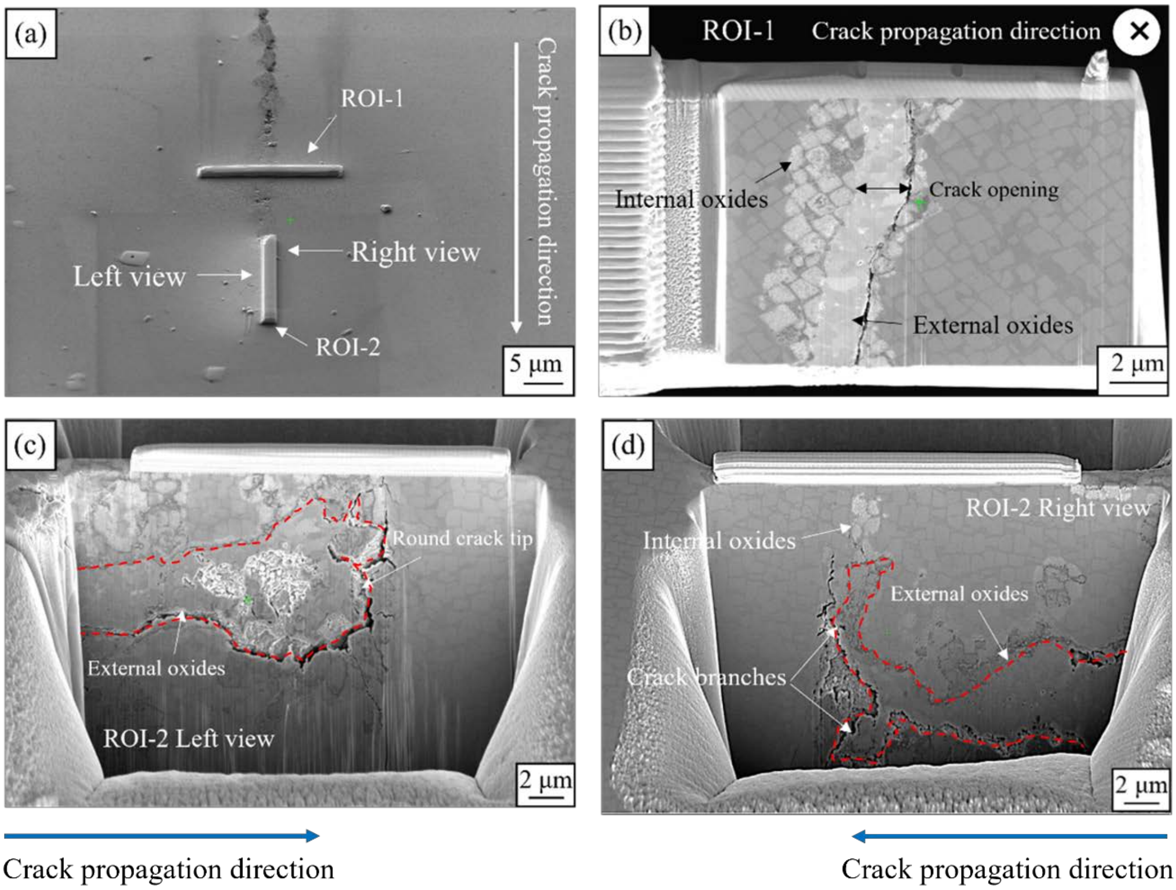

Fig 8.3 (a) the SEM image showing the coated regions of interests, (b) cross-section of the crack wake, (c) cross-section of the crack tip from left view, (d) cross-section of the crack tip from the right view

The dark and bright view of the ROI-1 under STEM are presented in Fig. 8.4 (a) and (b). The strip-like external oxides comprise polycrystalline grains, clearly shown in the bright view. The element distribution maps show that the external oxidation layers consist of Co/Ni oxides. The two elements are not homogeneously distributed, Co is more enriched in the centre of the external oxidation layers, where Ni is depleted. However, no microstructure variation is observed at the external oxidation layers. According to the O element distribution map, the internal oxidation layers can be divided into two regions. In region 1, the internal oxidation layers are composed of Al oxides in the γ', Cr oxides are concentrated in the γ channel, and W oxides are homogeneously distributed. In comparison, only Al oxides inside the γ' are observed in region 2. Also, the Ni-rich line is formed at the interface between region 2 and the remaining matrix, indicating the Ni elements are rejected by the oxidation of the γ' precipitates. A higher resolution EDX map was conducted within the red-rectangle region within region 2 as shown in Fig. 8.4 (b) and then (c) at higher magnification. The γ' directly sheared by the crack is enriched in finger-like Al-rich oxides, and Ni has been rejected by the growth of the finger-like phases, thereby forming a Ni-rich line at the tips of the finger-like Al-rich oxides. Oxygen is depleted in the γ channel, indicating that the Al-rich oxides are formed prior to Cr-rich oxides in the γ channel.

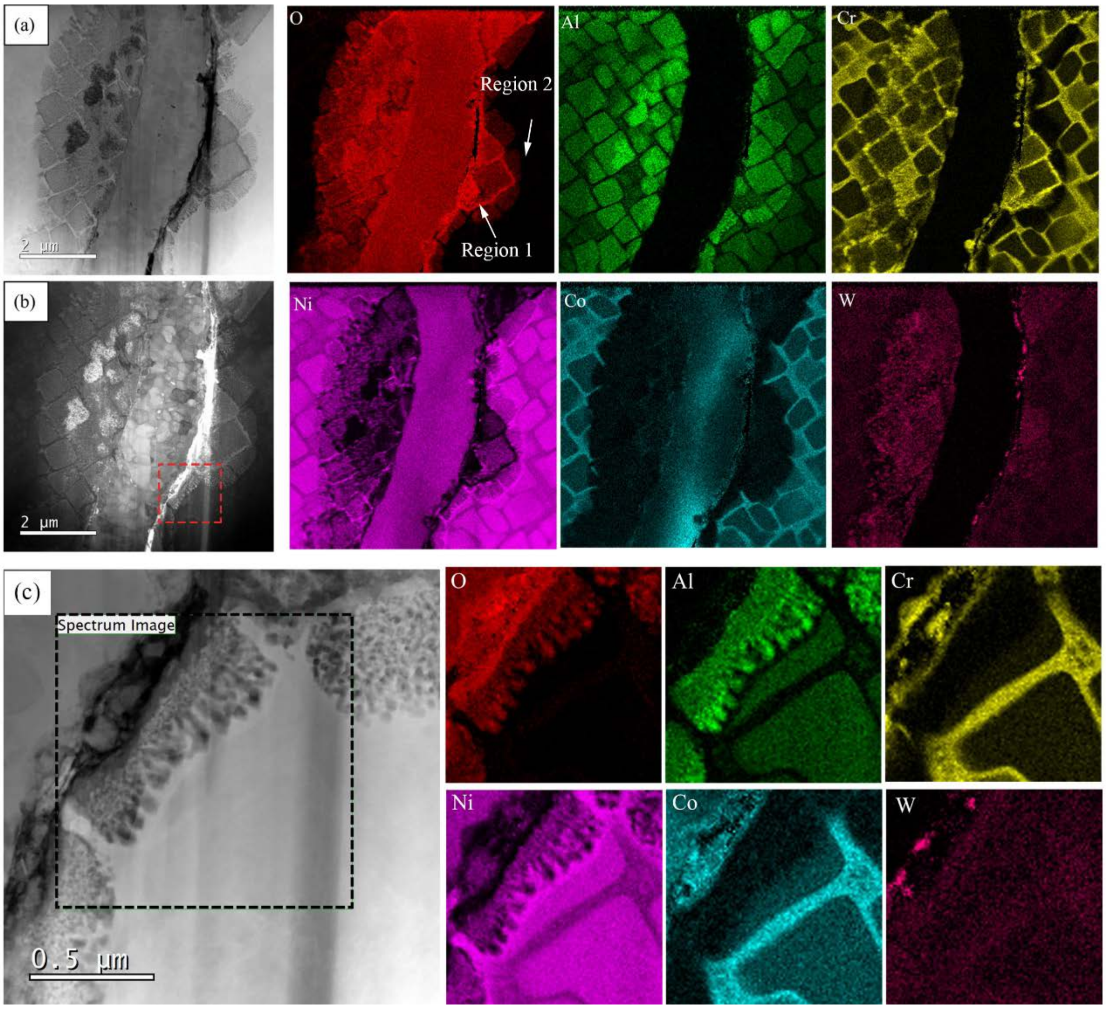

Fig 8.4 Dark (a) and bright (b) views of the crack wake cross-section and associated element distribution maps, (c) a high-resolution image of the sheared γ′ and associated element distribution maps from the red rectangle ROI identified in (b).

An overview of the cross-section of the crack tip (RO1-2, right view) under STEM is presented in Fig. 8.5 (a). The crack with the filled external oxides is located at the right-bottom corner as marked in the figure. The relatively dark regions are caused by the oxygen intrusion, which is quite large, compared with the equivalent region of the crack tip in our previous study [238]. The higher-magnification images show the morphologies of the internal oxides – strip-like Cr-rich oxides in the γ channel and speckle-shape Al-rich oxides inside the γ′ precipitates in Fig 8.5 (b) and (c). The bright region should be the matrix where the oxygen intrusion is slight. Element distribution maps show that the oxygen is enriched in both the γ′ precipitates and γ channel in the left side of Fig. 8.5 (d). Al-rich and Cr-rich oxides are thereby formed, whereas Ni and Co are rejected. In contrast, at the right side of the map, where the region is closer to the matrix, only oxygen intrusion into γ′ precipitates is observed. The result is consistent with the observation of the crack wake, that for the internal oxides, there are still two sub-layers, one is fully oxidized with Al-oxides and Cr-oxides and the other is partially oxidized, which we term as the oxygen diffused region with only Al-oxides present. The final EDX map is focussed on the secondary crack tip in Fig. 8.5 (e). The oxygen is concentrated at the right side of the map and no oxygen content is

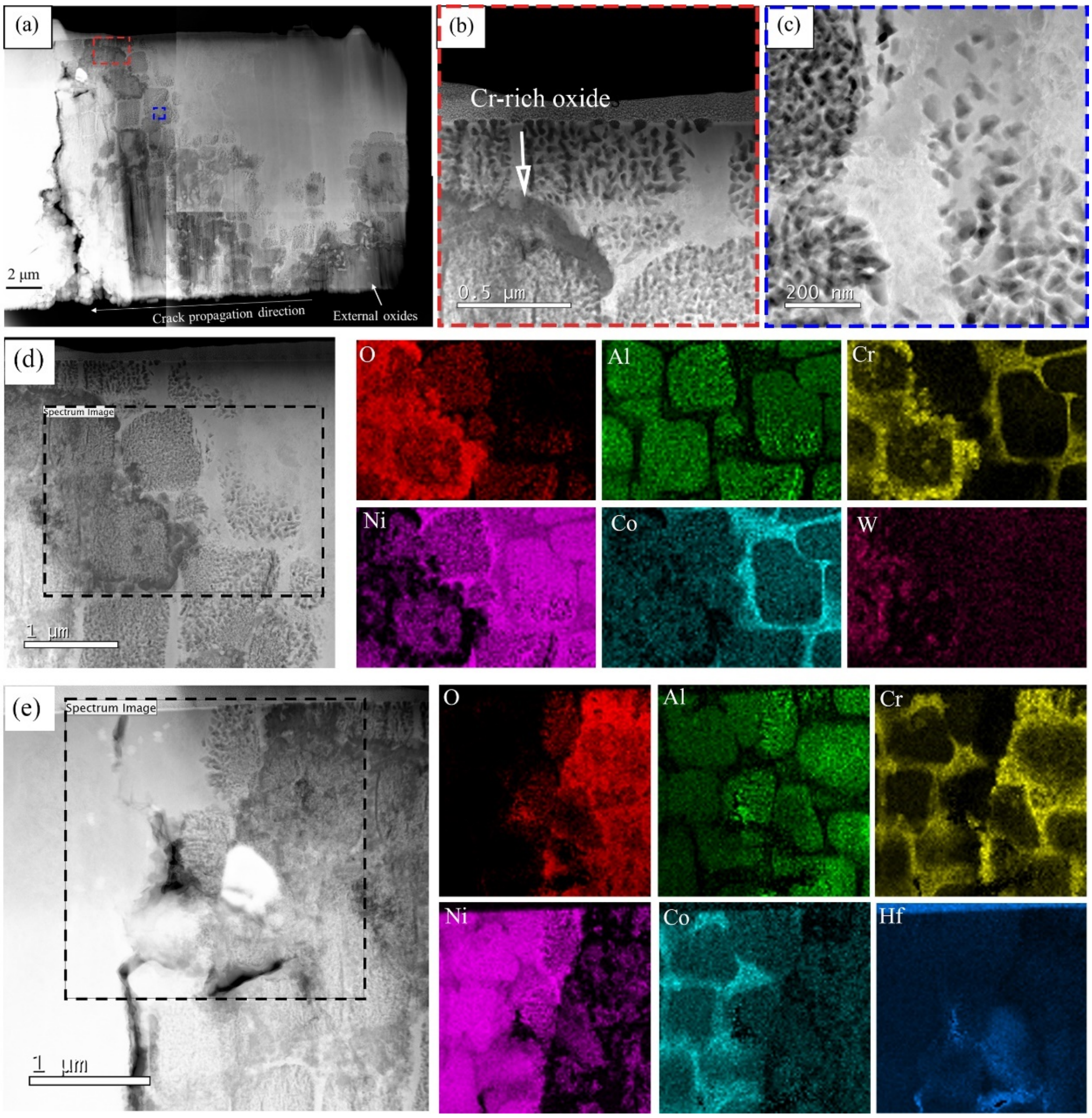

Fig 8.5 (a) an overview of the cross-section of the crack tip (RO1-2 right view from Fig 8.3 (a)) high-resolution images of the Cr-rich oxides (red box) (b) and Al-rich oxides (blue box) (c). A higher magnification image of the oxidized region and matrix and associated element distribution maps (d), a higher magnifciation image of the secondary crack and associated element distribution map (e)

determined around the secondary crack tip at this magnification. Also, the depletion of Ni and Co inside the crack, indicates the non-existence of the external oxides within the crack.

8.3 Discussion

8.3.1 Crack blunting by creep?

Blunted crack tips are repeatedly observed in the interrupted tests. Reported in [261], once the crack tip is blunted, the FCP rate is largely reduced due to the change of the strain state ahead of the crack tip. To verify whether the blunt crack tip is caused by the creep or oxidation, the observation of the associated crack tip dislocations is of great importance, as the creep process will be confirmed by dislocation network observations. The second TEM foil of ROI-2 was further thinned down for a better view of dislocations. No single dislocations were observed ahead of the crack tip as shown in Fig 8.6. There might be several reasons accounting for this. Firstly, the plastic deformation is so great this has led to the formation of substructures which incorporate the dislocations. Secondly, dislocation climb is not activated due to the low test temperature (650 ºC), which is a relatively low temperature for creep in this system. In this case, dislocations might not be easily viewed, especially if the TEM foil is not thin enough. Based on the current observations, the crack blunting process seems not directly related to creep. However, to validate this hypothesis, more characterization work is needed in the future.

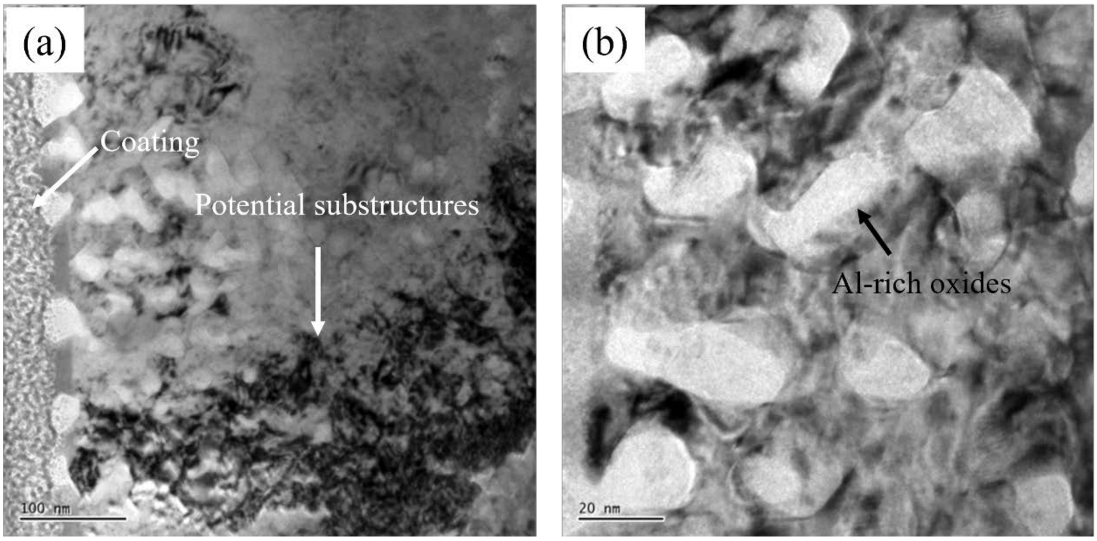

Fig 8.6 the TEM foil of the crack tip at low magnification (a), at high magnification (b)

8.3.2 The effects of oxidation intrusion

Most of the research considers the OICC from the external oxides formed inside the crack, but in Ni-based superalloys, the internal oxides are a non-negligible factor. In polycrystalline alloys [105, 106, 262-264], the fine-scale internal Al/Ti/Cr-rich oxides are formed along the GBs as well as at the interface between primary γ' and γ, which enhances the inter-granular crack due to their brittle nature [256, 265]. Indeed, the secondary cracks inside the internal oxides are observed ahead of the crack tip in the cross-section of the FIB-sample (Fig. 8.3 (c) and (d)). However, whether these cracks are formed prior to or post the formation of the internal oxides are not certain. According to the studies of Jiang et. al [204], secondary cracks are largely formed ahead of the crack tip under low-frequency test (1-90-1-1). These secondary cracks connected to the main crack in the further cyclic loading, prompting the crack propagation in polycrystalline superalloys. Considering the increased hardness of the internal oxides in this material, these secondary cracks are perhaps harder to form after the formation of internal oxides. Allowing for the hardening effects of internal oxides, the proposed mechanism for OICC is modified as shown in Fig. 8.7. Firstly, the main crack is open at the maximum load stage with a few secondary cracks formed ahead of the crack tip. External oxides are then formed at crack flanks, reducing the $\Delta\delta$ and ΔK_{eff}. The oxidation sequence of external oxides being produced prior to the formation of internal oxides has been proved in several studies [266-268] considering both thermodynamics and kinetics principles. Finally, the hardening of the crack tip via the formation of the internal oxides, completely arrests the growth of the main crack and any secondary cracks.

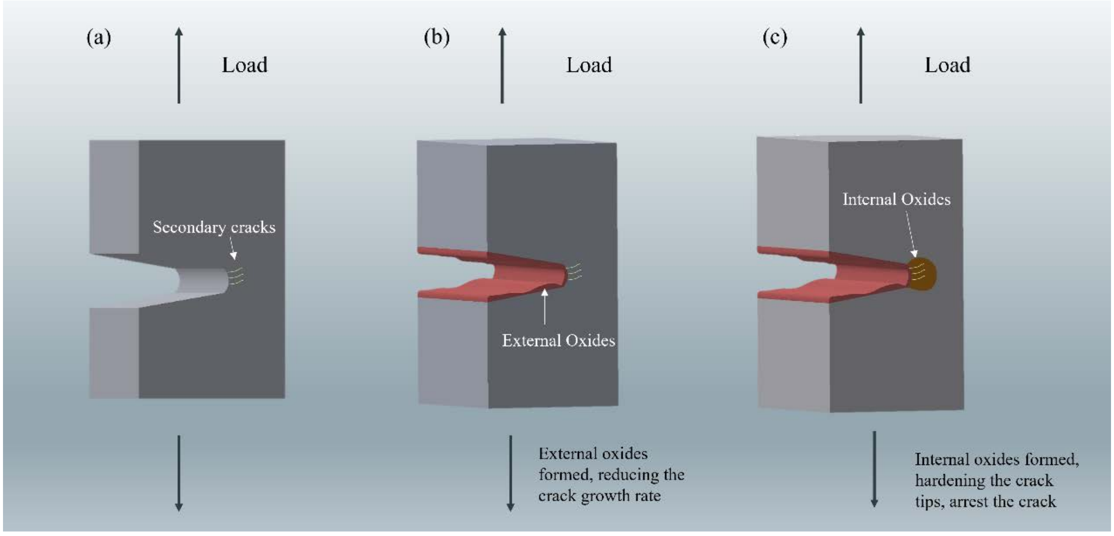

Fig 8. 7 the schematic diagram of crack opening without oxides (a), with external oxides (b), with internal oxides (c).

Here we propose for the first time, that internal oxides may actually harden the crack tip affecting subsequent crack propagation. It should be noted that the high hardness of internal oxides, particularly Cr-rich oxides, has also been confirmed by Jiang et. al [232] in high-temperature sustained load tests. Comparing with the mechanisms of SAGBO and DE [120, 263, 269], quite different effects of oxides might be attributed to their spatial distribution and physical scale. Oxides tend to be localized at the GBs in polycrystalline superalloys, as the GBs act as element fast diffusion paths [270, 271]. Thus, the oxide growth rate along GBs is much faster than at the two flanks of the crack, which potentially will decrease any effects of OICC due to oxide wedging effects. Vsikari et. al [272] confirmed this by finding that the length of oxides is nearly 10 μm along GBs in wrought Ni-base alloy Allvac 718Plus, while the thickness of the oxides at the crack flanks is in the nano-meter scale in a sustained-load oxidation test at 700 ºC. Due to the anisotropic deformation behaviour of neighbouring grains, the internal oxides at GBs also experience a higher strain/stress concentration [273-275]. Brittle fracture then initiates from the voids inside these oxides and connects to the main crack, accelerating the FCP [82]. In this work, current results show the clearly transgranular crack propagation in the very coarse columnar grained DS material (Fig 7.3 – 7.5), and thus SAGBO hardly occurs during the fatigue tests, and the system is far closer to a single crystal system. DE has instead been found in the single crystalline superalloys CMSX-4 at lower temperatures (550 ºC) 1-90-1-1 waveform [238], where oxygen intrusion into the interface between γ and γ' has been observed, decreasing the cohesion along this interface and inducing subsequent crack propagation along the γ channel. In that study, the occurrence of DE led to development of a sharp crack tip without micro-scale oxides forming ahead. In contrast, the current study clearly shows a blunted crack tip surrounded by several-micron internal oxides (Fig. 7.3 – 7.5). Particularly, the hardest oxides – Cr-rich oxides [256] forming in the γ channel are very likely to block dislocation sliding and climbing. The accumulation of dislocations on the one hand causes some strain localization as shown by the KAM map in Fig. 8.1 (c), but on the other hand, increases the difficulty in further dislocation movement in the plastic zone. This is similar to the mechanism of strain hardening [276], where the accumulated dislocations tangle around precipitates or GBs to form dislocation nets, adding to the difficulty of plastic deformation. Although physical dislocation is not directly observed in this work (as discussed in 8.3.1, this might be due to the formation of substructures or the sample is simply not thin enough), the calculated GND total energy localized around the internal oxides ahead of the crack tip supports the hypothesis. Finally, under the co-effects of external and internal oxides, crack growth is completely arrested. In our tests, the crack-tip resharpening method (by reverting to a high frequency to re-start the crack) can obtain crack growth after a short time duration of crack arrest at a lower frequency if the OICC effects are relatively minor due to the small scale of external and internal oxides. After a longer duration of crack arrest at lower frequency, the crack growth can only be re-started by increasing the ΔK as well as the frequency to overcome the significant OICC brought by the large scale of oxides.

8.3.3 The mechanism of internal oxidation

The above results and discussion show the significant role of oxides in resisting crack propagation. Comparing with other DS and SX superalloys under similar load conditions [106, 238], the large-scale (in the micron scale) oxides formed both at the crack tip and wake are the major factor leading to an obvious OICC phenomenon. To utilize OICC to improve crack propagation resistance requires a better understanding of the oxidation mechanism. The sequence proposed by Viskari et. al [272] (in wrought Ni-base superalloy Allvac 718Plus sustained loaded at ΔK 20 MPa√m for 600s at 700 °C) is that the most active element Ni firstly reacts with oxygen and forms the outermost Ni-rich oxides layer. The formed oxidation layer is not sufficiently dense [116, 272], facilitating the continued transportation of oxygen through the Ni-rich oxide. Cr-rich oxides are then formed, and this oxidation layer is quite dense [277], inhibiting both oxygen and Ni element further transport, and hence, the growth of external and internal oxides is blocked. Although Al-rich oxides are found below the Cr-rich oxidation layer [235, 264, 278], their thickness is mostly in nano-meter scale, also indicating the inhibition of oxygen transportation by Cr-rich oxides.

In contrast, the detailed analysis here of internal oxidation layers via FIB-STEM shows different results, whereby the dense Cr-rich and Al-rich oxidation layers are actually not separately formed in the material. Fig. 8.4 (e) and 8.5 (d) clearly shows the internal oxidation layers are consist of Al-rich speckle-shape and Cr-rich strip-like oxides. In the literature [279], mixed Cr-rich/Al-rich oxides are also found, but their morphologies are not illustrated/discussed. Also, the oxidation sequence we observe is quite different to the previous proposed mechanism of Cr-rich oxides forming prior to Al-rich oxides. Our work may agree that the external oxidation process might be as discussed in [237, 280], but the internal oxidation behaviour is proposed to be as shown in Fig. 8.8. The external nano-crystalline (Ni, Co)-rich oxides are thought to form by depleting the Ni element of γ' [272], which causes instability in the $Ni_3(Al, Ti)$-γ' precipitates. Hence, the γ' precipitates near the crack are oxidized, yielding speckle-shaped Al-rich oxides, represented by the green triangles in Fig. 8.8 (a). These speckles grow from the crack-tip into the bulk material, forming the finger-like morphology and Ni-rich line ahead, as shown in Fig 8.4 (c). At this stage, Cr-rich oxides are not formed, but with the oxidation progress, γ′ precipitates near the crack tip are fully oxidized, and then oxygen protrudes into the γ channel, forming strip-like Cr-rich oxides shown in Fig. 8.5 (b) and Fig. 8.8 (b). Therefore, Al-rich oxides and Cr-rich oxides are formed alternately in this DS material system and they are overlaid to form the internal oxidation layer. As the partial pressure of oxygen required for Al-rich oxide formation is lower than for Cr-rich oxides, the intrusion of Al-rich oxides is deeper into the materials (Fig. 8.8 (c)), which has also been acknowledged in similar alloy systems [281].

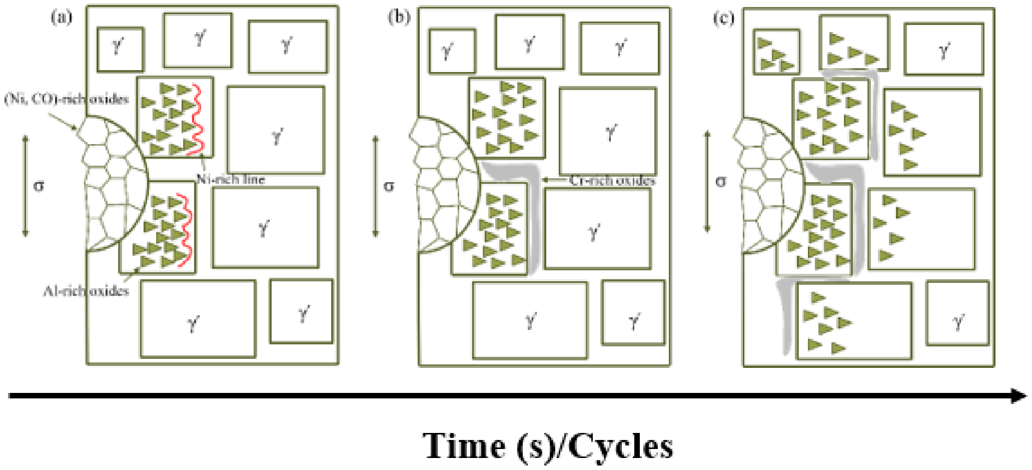

Fig 8. 8 the schematic diagram of internal oxidation process: (a) partially oxidized γ′, (b) fully oxidized γ′ and partially oxidized γ, (c) fully oxidized γ

The reason that Al-rich oxides are formed prior to the Cr-rich oxides is inferred to be associated with the presence of dislocations. According to [282] , dislocations can move via slipping into γ′ precipitates rather than climbing within the γ channel at these test temperatures (650 °C and 725 °C). The high anti-boundary energy of γ′ blocks the dislocation motion and causes their accumulation. As illustrated in many studies [283-285], dislocations can act as ‘pipes’ for fast element transportation, leading to the preferential oxidation of the γ′ precipitates. It could also help to explain the strong OICC effects observed in this series of high-temperature low-frequency tests. Instead of forming a dense Cr-rich oxidation layer, the dislocation pipes in γ′ not only transport oxygen, but also transport out the Ni and Co to produce the substantial external oxidation layer filling the crack. This results in the significantly reduced ΔK_{eff}. However, observing the dislocations and analysing their interaction with oxidation behaviour in the oxidized region is quite a challenge, which is proposed as the next step of our research.

8.4 Summary and conclusions

Detailed characterization analysis has been performed on the arrested crack in this chapter, including evaluating the strain localization around the crack, the mechanical properties of the oxides and matrix, as well as the composition and dislocation analysis ahead of the crack tip. Thus, the following conclusions could be drawn:

(1) The blunted crack tip is inferred not to be caused by the creep process, as creep dislocation networks are not observed in the region ahead of the crack tip.

(2) Crack tip hardening is found, and is caused by the formation of the hardest oxides - Cr-rich oxides in the γ channel. It is proposed that the increased hardness of the materials ahead of the crack tip add to the difficulty of dislocation movement, further arresting the fatigue crack propagation via inhibiting the connection between secondary cracks and the main crack.

(3) A new internal oxidation mechanism is illustrated that the Cr-rich oxidation layers and Al-rich oxidation layers are mixed instead of forming separately. Oxygen preferentially attacks the γ' precipitates forming the Al-rich oxides due to the dislocations providing a fast element-diffusion path to γ' precipitates at these intermediate test temperatures. After the γ' precipitates are fully oxidized, the surrounding γ channels are oxidized by oxygen protrusions, forming Cr-rich oxides.

Chapter 9 General discussion and Conclusions

9.1 General discussion

As stated in the literature review, fatigue damage is an important damage mode for superalloys serving in turbomachinery applications, but the mode is often coupled with other damage modes like oxidation and creep. In order to comprehensively understand the fatigue behaviours under the real service operating conditions, the following two steps have been taken:

1. Finding and evaluating the intrinsic parameters influencing the fatigue behaviours. To achieve this, fatigue tests at room temperatures were performed. Typically, the intrinsic parameters affecting the fatigue behaviours of superalloys are considered to be microstructural features, such as slip bands, precipitates, secondary phases, pores/defects and grain boundaries. Considering that DS superalloys will always exhibit mechanical anisotropy, specimens with different relationships between columnar grain elongation direction, loading direction and crack growth direction have been designed. In these tests, it was found that the general fatigue lives are most strongly affected by the differences in Young's modulus when the maximum applied stress is close to the yield stress. The local crack initiation and propagation behaviours are influenced by microstructural features, particularly carbides, slip bands and GBs. Further fatigue tests at room temperature were combined with advanced characterization approaches such as ex-situ DIC and in-situ SRCT to assess the contribution of these factors to the fatigue crack initiation and propagation behaviours. Carbides and slip bands are determined to be the main fatigue crack initiation sources, due to early strain localization at these features. The results are consistent with the results presented in the previous research [51, 220]. In comparison, GBs can facilitate strain bands transferring from one grain to the neighbouring one, as shown in Fig 5.4, which is correlated to the high compatibility of the GB in this specimen orientation. Considering the large grain size of the DS superalloy, the density of GBs is much less than that of carbides and slip bands, therefore, GBs are not regarded as the main crack initiation source in this system.

In terms of crack propagation, surface SEM observation illustrates that at room temperature the crack grows along one main slip trace in both stage I and II and is deflected by pores and carbides. Crack growth following one main slip trace is thought to be caused by the high resolved shear stress on the highest-Schmid factor slip plane [73]. Similar results including the deflection of the crack by carbides are also captured in the 3D characterization using X-ray CT, but a difference is that crack growth is found to occur along several slip planes simultaneously when viewing the process in 3D. The slip planes might be equivalent because of the close Schmid factors, but this needs more characterization on determining the crystal orientation in the future work. In general, the intrinsic parameters that affect the crack initiation and propagation at room temperature are the carbides, pores and slip bands, and thus, these microstructural features are also focussed upon when moving on to assess the coupled fatigue-environment damage.

2. Assessing the interaction between the extrinsic and intrinsic parameters. Herein, the extrinsic parameters are considered as the loading condition (including the applied maximum stress and loading frequencies) and the higher testing temperatures (650 and 725°C). The occurrence of the subsurface crack initiation at elevated temperatures, when the applied maximum stress exceeds the yield stress of the T specimen, indicates suppression of the surface crack, potentially attributed to oxidation on the surface. The phenomenon is more obvious at lower loading frequencies (1-1-1-1 trapezoidal waveform). Although micro cracks are formed inside the carbides, they are unable to propagate into the matrix due to the oxidation at the carbide interface. It is consistent with our room temperature work, that carbides still act as the main crack initiation sites, but the crack propagation behaviours seem strongly affected at the elevated temperature. Based on this, fatigue long crack propagation tests have been performed. These also show that fatigue crack growth is arrested on changing frequencies from higher levels (10 Hz sine waveform) to lower levels (1-1/90-1-1 trapezoidal waveforms). These results are also thought most likely correlated to the oxidation process, as the crack arrest is more significant in the lower-frequency and higher-temperature tests. Similar findings are reported in the single crystal superalloy [230], in which the lower crack propagation rate in air condition is caused by oxidation induced crack closure. The current work also quantitatively assesses the crack closure induced by oxidation, using a modified model with the oxidation thickness measured by SEM and X-ray CT. At the same time, the crack tip is blunted surrounded by the high-hardness internal oxides. These oxides might also play the role in prohibiting the crack propagation, particularly when the crack tip driving force is also reduced by OICC.

Why is the crack arrest phenomenon so marked in the superalloy DS CM247LC? From the current characterization work, the underlying mechanism could be that at these intermediate service temperatures, dense internal oxides are not formed, as Al-rich oxides only form in the γ' in the form of nano particles. In this case, the overall oxidation is then quite severe as the "usual" protective oxide layers are not formed. This might be correlated to the composition of alloy and the particular test temperatures investigated, which needs further investigation.

9.2 Overall Summary and Conclusions

The microstructures have been investigated by using the 2D and 3D characterization techniques. Columnar grains and primary dendrites are aligned parallel to the solidification direction. Pores and carbides are mainly co-segregated at the inter-dendritic regions, except for the very tiny chain-like carbides which are precipitated at the grain boundaries. The size variation and volume fraction of carbides and pores are quantitatively measured and analysed using SRCT, which confirms the higher volume fraction of carbides compared with pores.

Fatigue short crack tests were performed at room temperature to study the effects of mechanical anisotropy and microstructural features in the DS system. Two types of tension-tension and three types of three-point bending fatigue specimens were designed. The specimens with columnar grains elongation direction parallel to the loading direction is termed as L specimen in the tension-tension tests, as LR in the three-point bending tests. The specimens with columnar grain transverse to the loading direction is termed as T specimen in the tension-tension tests. According to the relationship between columnar grains elongation direction and normal direction of the top surface, the T specimens are divided into RL and RR specimens with columnar grain aligned parallel and transverse to the normal direction of the top surface respectively. The fatigue lives of the L and LR specimens decreases significantly with the increase of the applied maximum stress and is surpassed by the RR and RL specimens when the maximum applied stress is increased to 95% of the yield of the L specimen. This is attributed to the lower elastic modulus which induces a higher local plastic strain, resulting in the much fewer cycles to cause fatigue crack initiation. Multiple crack initiations at the grain boundaries are observed in the RL specimen, which is inferred to be associated with the high misalignment of activated slip systems of neighbouring grains calculated using a modified m' model. Early crack propagation follows the slip system with the maximum Schmid factor (SF). Owing to the different crack initiation behaviours, the final long crack is formed by single crack propagation in the LR and RR specimens, but coalescence of multiple short cracks in the RL specimen.

In-depth analysis of the interaction among the microstructural features, localized strain and fatigue short crack is performed in the RL specimen. A data-rich imaging approach is employed to more deeply understand the mechanism of short crack initiation and early propagation, which combines traditionally well-established with recently emerging characterization techniques. Strain is localized at the slip bands and intersection between the slip bands and carbides. Although the intensity of strain is of the same level within slip bands and at the carbides, characterized by SEM-DIC, the cracks preferentially initiate from the carbides at the initial stages of fatigue. With increased loading cycles, slip band cracking becomes the dominant mode of the crack initiation. At the final stage of the fatigue, opening mode carbide cracking is the primary mode of the crack initiation. This process is associated with the enhanced plastic zone size and plastic strain intensity after more loading cycles. The 3D segmentation of cracks illustrates that the initiated cracks could simultaneously propagate on several slip planes in the early stages, as observed in the in-situ fatigue tests obtained under the SRCT. In comparison, the crack can seem to only propagate following one favoured slip system, if only making 2D observations on the surface, which confirms the necessity of analysing the crack growth behaviours using 3D characterization techniques.

Following the room-temperature tests, which are focused on the effects of intrinsic factors (like microstructures and mechanical anisotropy) on the fatigue crack growth behaviours, the effects of environment (regarded as extrinsic factors) are assessed by performing fatigue tests at elevated temperatures. Sustained load and fatigue short crack tests are performed on the LR and RR specimens at 650 °C. Oxidation preferentially occurs at the stress/strain localized microstructures, forming (Co, Ni)-rich oxides. Particularly, the oxides form at the interface between carbides and matrix first, and then protrude into the carbides beneath, lifting the phase, finally protruding into the bulk of the carbides, leading to crack initiation inside the carbides. The initiated cracks are in turn prohibited from propagating into the matrix by the surrounding formed oxidation layers, leading to the supression of the surface cracks in the low-frequency (1-1-1-1) fatigue tests. For the high-frequency (10 Hz sine waveform) tests, the effects of oxidation and grain orientation with respect to the loading direction are not as significant, while the applied maximum stress plays an important role. The transfer from surface to subsurface crack initiation is observed when the applied maximum stress decreases from 1008 MPa to 912 MPa, due to the decreasing difference of stress intensity between the surface and subsurface crack, making the subsurface initiation from pores/carbides that have not been oxidised more favourable.

To further assess the effects of environment on fatigue crack propagation behaviour, fatigue long crack tests are performed on L and T specimens with different frequencies (10 Hz sine waveform, 1-1/90-1-1 trapezoidal waveform) and temperatures (650 ºC and 725 ºC). Crack arrest is observed in the low frequency (1-1/90-1-1) tests, except for the T specimen tested at 1-1-1-1 waveform, 650 ºC. The initial $\varDelta K$ ($\varDelta K_0$) needed to continue to propagate the crack (without it arresting) increases with both the decrease of test frequency and increase of test temperatures, indicating the most severe crack closure occurs in the lower-frequency and higher-temperature tests. Oxidised blunted crack tips as well as thick oxidation layers inside the crack wake are observed in the low-frequency interrupted tests. According to SEM-EDX analysis, the external oxidation layers filling the crack wake consist of (Co, Ni)-rich oxides and the internal oxidation layers, protruding into the matrix, consist of (Al, Cr)-rich oxides. In the oxidation-induced crack closure, the external oxides play the main role in reducing the effective stress intensity and causing the crack closure. A modified model based on the external oxidation thickness measured from SEM-EDX and X-ray CT is proposed to quantitatively calculate the effective stress intensity. This explains well how the more severe crack closure in the low-frequency test can be attributed to the lower effective stress intensity caused by the thicker external oxidation layers.

The roles of the blunted crack tip and internal oxides in crack arrest are further studied. The localized strain at the crack tip is semi-quantified by EBSD, but at the same time, higher hardness regions are also found around the crack tip caused by the formation of internal oxidation layers. A competing mechanism is proposed that if the localized strain is high enough to break the brittle oxides, the crack propagation is accelerated, similar to the SAGBO mechanism, otherwise, the crack will be arrested. The arrested crack due to the oxides are also observed in the low-frequency high-temperature short crack tests. Al-rich oxides are formed inside the γ' phases in the form of nano-scale particles, while Cr-rich oxides are formed in the γ channels with a strip morphology. The expected continuous and dense internal oxidation layers are not formed, weakening their roles in prohibiting element diffusion at the elevated temperatures, and causing the severe oxidation at this intermediate service temperature. The severe oxidation, especially in the low frequency and high temperature tests, leads to the crack arrest from two aspects: firstly, the thick external oxides in the crack wake reduce the effective intensity, and then the harder internal oxides prohibit the crack propagating into the matrix. Very few dislocations are observed in the region ahead of the crack tip, indicating the blunted crack tip is more likely caused by oxidation rather than creep.

Generally, the work builds a systematic fatigue study on the DS CM247LC superalloy step by step. The elastic anisotropy has the most significant effect on the fatigue lives at the room temperature, with the maximum applied stress lower than the yield stress. Microstructural features (like carbides and pores) act as the main crack initiation sites at both room and elevated temperatures, therefore reducing the volume fractions of these features will be significant for prolonging fatigue lives. Severe oxidation occurs in the alloy at the intermediate elevated temperatures studied here, which influence the crack propagation behaviours, leading to significant fatigue crack arrest. The severe oxidation and associated crack arrest is not linked with the columnar grains orientation with the respect to the loading direction, or microstructural features such as GBs or carbides, but correlated more to the oxidation process of forming the mixed and dispersed Al-rich and Cr-rich oxides. Providing that the mechanism could be utilized potentially by careful design of composition, the fatigue lives of superalloys at the relevant elevated temperatures could be largely enhanced by such “crack-healing” mechanisms.

Chapter 10 Future work

10.1 In-situ high-temperature fatigue long crack tests

Fatigue crack arrest occurs in the high-temperature and low-frequency tests, and the phenomenon is correlated to the oxidation process discussed in the Chapter 7 and 8 by performing characterizations on the failed and interrupted specimens. However, in-situ observation of the crack arrest process will provide more information to illustrate the underlying mechanism. Currently, carrying out in-situ high-temperature fatigue tests under SEM is achievable, but the bending fatigue tests needs to be changed to tension-tension fatigue tests. The dog-bone samples (with dimensions the same with those used in the previous fatigue tests) with a single edge semicircle notch can be machined in the gauge section of the specimen by micro-milling. Constant ΔK (15 MPa√m) fatigue tests can be performed on the L-type specimens with different frequencies of 10 Hz sine, 1-1/90-1-1 trapezoidal waveforms. At the beginning of the tests, a high frequency of 10 Hz will be applied to ensure crack growth and subsequently, a trapezoidal waveform of 1-1-1-1 waveform is applied. Theoretically, the crack should then become blunt and arrested based on the previous results, then the frequency will be transferred back to 10 Hz to resharpen the crack tip and force crack growth, then a 1-90-1-1 loading waveform will be applied to the specimen, this will provide interesting crack propagation transitions, development of crack wakes and crack-tips that can be observed in-situ. It should be noted that the in-situ SEM tests are focussed on a surface crack, where oxidation is much more significant than for cracks inside the material. Therefore, the surface crack propagation behaviours might not be fully representative. The ideal situation is performing a high-temperature in-situ fatigue test on the SRCT. However, few high-temperature fatigue tests have been successfully performed on the SRCT so far, the main problem should be the heating process, particularly for superalloys, for which the testing temperatures are quite high.

10.2 Crystal plasticity finite element analysis

The effects of mechanical anisotropy on fatigue behaviours are investigated experimentally in the Chapter 4 and are correlated to the applied maximum stress. For instance, the fatigue lives of the L (LR) specimens are much longer at the lower applied maximum stress but lower when the stress is close to the yield stress of the L specimen. However, to illustrate how the stress levels affect the effects of mechanical anisotropy experimentally is time consuming and expensive. Therefore, using simulation combined with experiments to validate the simulation results will be more effective.

Crystal plasticity finite element analysis (CPFEA) is a recently developed mechanical simulation method, which considers the anisotropic behaviours of individual grains caused by the crystal orientation with the respect to the loading directions. The simulation method has been widely used in polycrystalline aggregates, particularly those with strong textures. Mostly, the simulations are used to show the intensity and heterogeneous distribution of strain in the mesoscale, but recently models calculating fatigue indicator parameters (FIPs) based on CPFEA have been developed. These FIPs such as accumulated shear-strain energy dissipation density (ASSEDD) and the Fatemi-Socie parameter which could represent the driving forces for fatigue crack nucleation and early stages of crack growth which are very microstructurally dependent.

In this study, preliminary simple models of L and T tensile samples have been developed, with aspect ratios (length to width ratio) of 1:2, 1:3, 1:4 to mimic the elongated strain gauge section of the physical samples. The number of columnar grains in each virtual sample was simply estimated via dividing the cross-sectional area, normal to elongated grains, by average observed grain diameters. There are 15 columnar grains in the L virtual specimen, while 30, 45, 60 columnar grains were simulated in the T specimens with 1:2, 1:3, 1:4 aspect ratios respectively. Fig 10.1 shows the virtual L and T samples with the ratio of 1:2. The monotonic tensile strain extending beyond the onset of plastic yielding (approximately 1% strain) has been performed on the two sample types, at a strain rate of 1.0×10^{-4}/s. Model parameters were gathered from associated studies [252, 286, 287]. Single crystal elastic constants are outlined in Table 10.1. The initial and saturation slip system strength, which determine the plastic flow stress regime of the strain-stress curve, vary between different superalloys. These parameters are thought to be closely associated with the strengthening mechanisms, such as precipitation strengthening (the volume, size and shape of γ'), solution strengthening (the content of solution strengthening elements). Thus, the slip strength of some other nickel based superalloys [252, 286, 287] were set as the initial parameters to fit with the strain-stress curves of one type of specimen (L or T). The fitting parameters are then used in the simulation of the other type of specimen. If the slip strength also fit wells with the other sample orientation (i.e. with the strain-stress curves of both specimen types simultaneously) it is thought to adequately represent the intrinsic parameters of the alloy shown in Table 10.2.

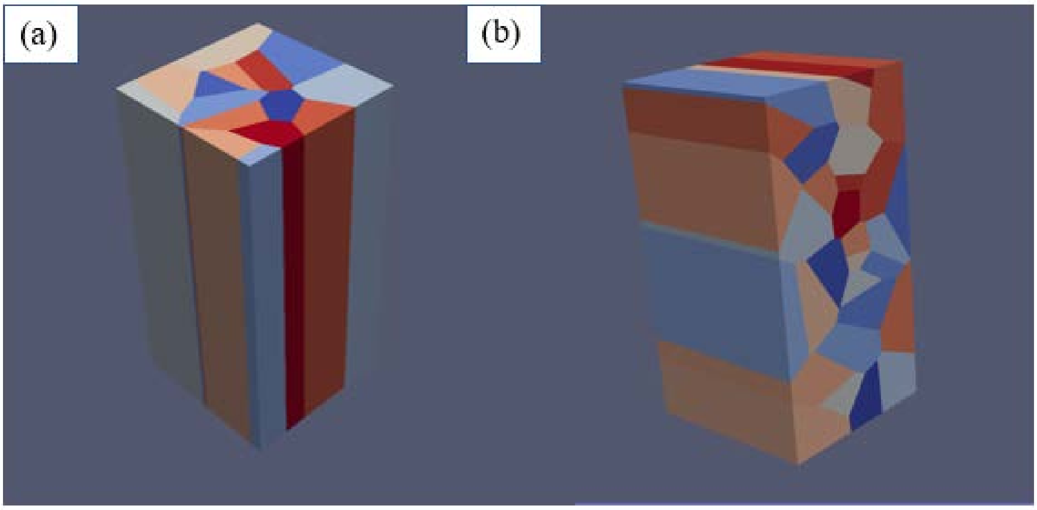

Fig 10. 1 Virtual L (a) and T (b) samples with ratio of 1:2

Table 10.1 Single crystal elastic constants for DS CM247LC superalloys

C11(GPa)	C12(GPa)	C44(GPa)
250.1	161.4	129.3

Table 10.2 Plastic parameters used for DS CM247LC superalloys

h_0(MPa)	g_0(MPa)	g_{s0}(MPa)	m	$\dot{\gamma}_0$	$\dot{\gamma}_{s0}$
195.0	450.0	500.0	0.005	1.0	120.0

The initial simulation results are shown in the Fig 10.2, with good agreement with the experimental tensile results. Also, the simulation for assessing the mesh sensitivity and effects of width-to-length ratio are performed in the Fig 10.3, validating the use of virtual sample with ratio of 1:2.

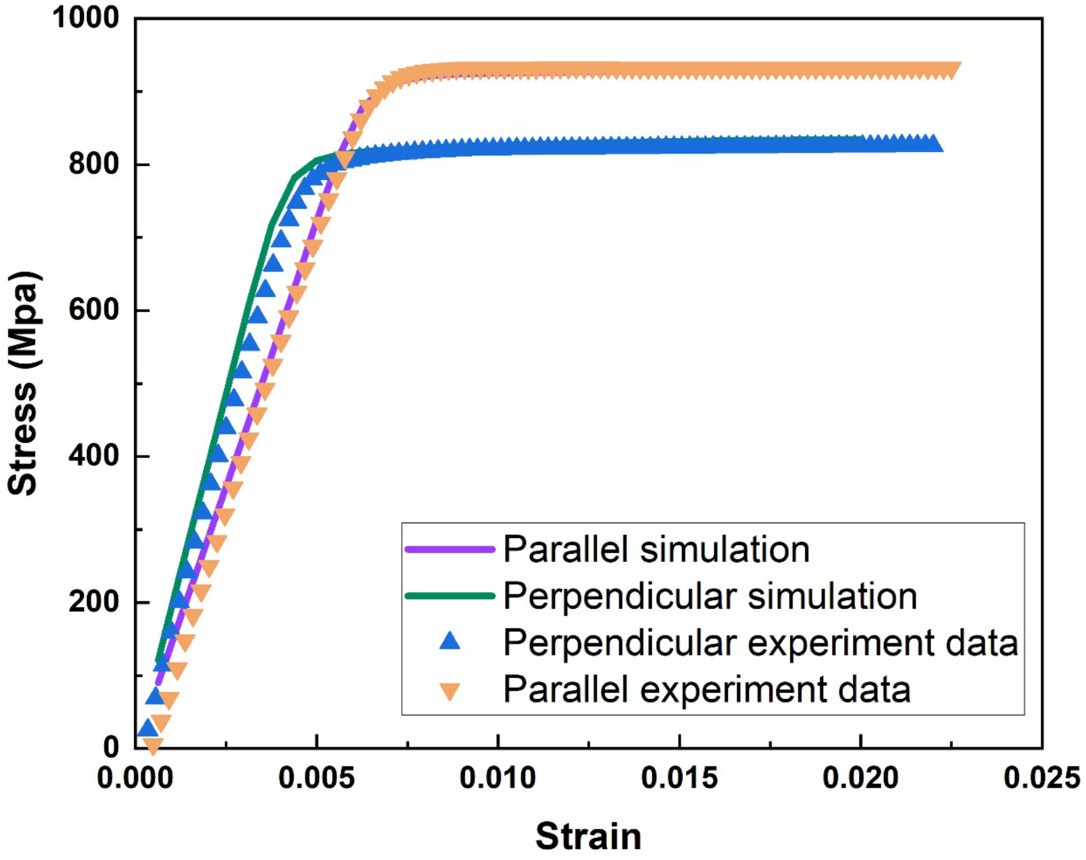

Fig 10. 2 Tensile properties of L and T specimen from experiments and CPFEA

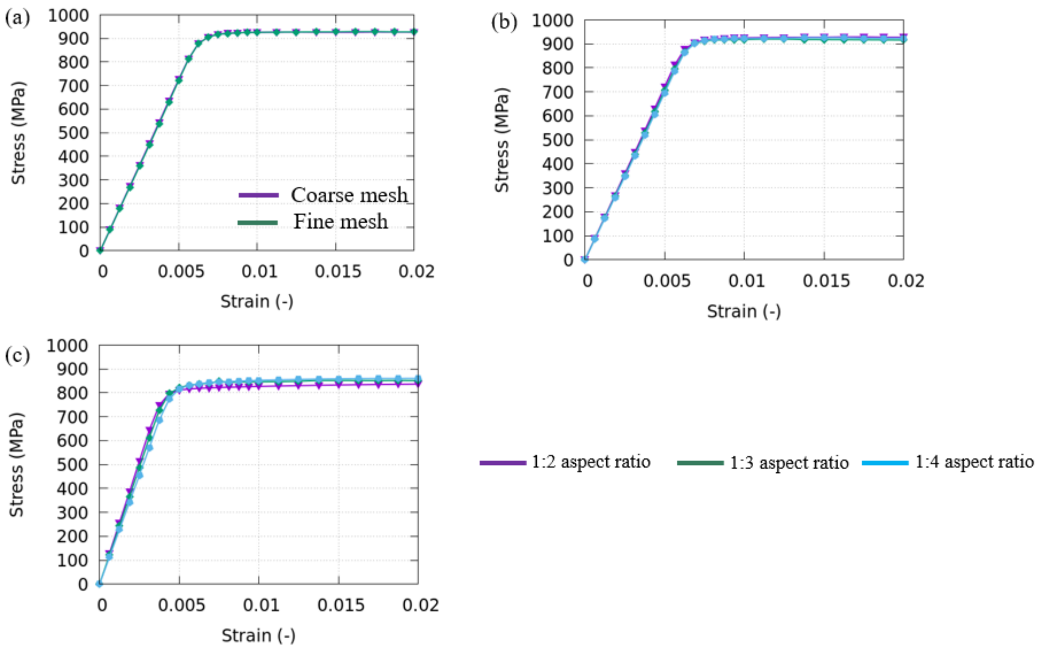

Fig 10.3 (a) strain-stress curve of L specimen via coarse and fine mesh; strain-stress curve of L specimen (b) and T specimen (c) with aspect ratio of 1:2, 1:3, 1:4

The strain distribution in the mesoscale is obtained in Fig 10.4 under tensile loading.

So far, this all that has been carried out for CPFEA as part of this PhD (partly due to COVID mitigation requirements there was an initial focus on modelling in my first year). Future work is expected to be based on the CPFEA framework, and we plan to carry out cyclic loading at different stress levels (mainly focussed on the applied maximum stress, ranging from 85% yield stress to 120% yield stress of the L specimen) on the L and T specimen and to calculate their FIPs. The aim is that using this approach, the effects of anisotropy on the fatigue behaviours could be well understood. In addition, the actual grain morphology and the discontinuity of GBs induced by the tiny carbides are not considered in the current work. Further consideration of these microstructural features should also be carried out.

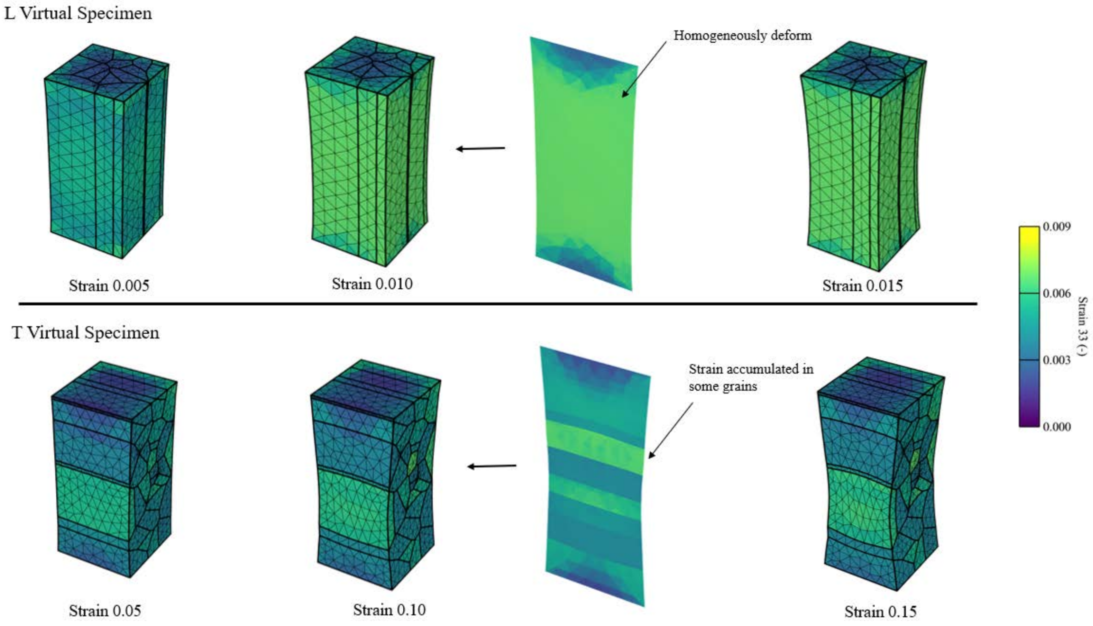

Fig 10.4 Deformation virtual samples at 0.5%, 1% and 1.5% axial strain coloured by elastic strain, ϵ_{33}

10.3 Further study on the internal oxidation ahead of the crack tip

The oxidation mechanism is investigated in Chapter 7 and 8 in detail. However, there is still one key issue to establish: why the Al-rich oxides are only formed in the γ' phases. Although this question could be explained to some extent in terms of the composition of γ' containing a higher Al content, it should be considered that the Al atoms react with the Ni atoms to form the stable Ni_3Al-structure phase (γ'), while Al atoms are also dissolved into the matrix. Thus, forming the Al-rich oxides in γ' or γ is not only associated with the composition, but also correlated to the phase transition. Both more detailed characterization and thermodynamic/kinetics calculations are required. The characterization work mainly includes two parts: Firstly, a detailed analysis on the orientation relationship between Al-rich oxides and γ' phase should be performed on extracted TEM foils of the crack tip.

Secondly, a further FIB-milling of the crack tip is required for the interrupted sample tested for 96 hours to check whether, with the extension of testing time, the Al-rich oxides will be formed in the γ channel. In terms of thermodynamic calculations, the Gibbs energy for producing the Al-rich oxides is needed, considering the composition difference in the γ and γ' initially. In considering the phase transition, a first-principles calculation is suggested to calculate the required energy. This future study will require cooperation with other research groups, who major more in the theoretical calculations of the phase transitions.

References

[1] K. Harris, High-ductility nickel alloy directional casting of parts for high-temperature and stress operation, Off. Gaz. (1984).

[2] R.A. Kupkovits, Thermomechanical fatigue behavior of the directionally-solidified nickel-base superalloy CM247LC, Georgia Institute of Technology, 2009.

[3] Z.J. Moore, Life modeling of notched CM247LC DS nickel-base superalloy, Georgia Institute of Technology, 2008.

[4] D.G. Leo Prakash, M.J. Walsh, D. Maclachlan, A.M. Korsunsky, Crack growth micro-mechanisms in the IN718 alloy under the combined influence of fatigue, creep and oxidation, International Journal of Fatigue 31(11) (2009) 1966-1977.

[5] A. Pineau, S.D. Antolovich, High temperature fatigue of nickel-base superalloys – A review with special emphasis on deformation modes and oxidation, Engineering Failure Analysis 16(8) (2009) 2668-2697.

[6] R.R. Stephens, L. Grabowski, D.W. Hoeppner, The effect of temperature on the behaviour of short fatigue cracks in Waspaloy using an in situ SEM fatigue apparatus, International Journal of Fatigue 15(4) (1993) 273-282.

[7] B. Ruttert, C. Meid, L. Mujica Roncery, I. Lopez-Galilea, M. Bartsch, W. Theisen, Effect of porosity and eutectics on the high-temperature low-cycle fatigue performance of a nickel-base single-crystal superalloy, Scripta Materialia 155 (2018) 139-143.

[8] Y. Jiao, Y. Zhang, S. Ma, D. Sang, Y. Zhang, J. Zhao, Y. Liu, S. Yang, Role of secondary phase particles in fatigue behavior of high-speed railway gearbox material, International Journal of Fatigue 131 (2020) 105336.

[9] L. Wang, Studies on recrystallization in directionally solidified nickel-base superalloys, Superalloys, Institute of Metal Research, 2006.

[10] R.C. Reed, The superalloys: fundamentals and applications, Cambridge university press2008.

[11] F. VerSnyder, R. Guard, Directional grain structure for high temperature strength, Trans. ASM 52 (1960) 485.

[12] K. Harris, G. Erickson, R. Schwer, MAR M 247 derivations—CM 247 LC DS alloy, CMSX® single crystal alloys, properties and performance, 5th Int. Symp, 1984, pp. 221-230.

[13] Z. Moore, R. Neu, Creep fatigue of a directionally solidified Ni-base superalloy–smooth and cylindrically notched specimens, Fatigue & Fracture of Engineering Materials & Structures 34(1) (2011) 17-31.

[14] J. Zhang, L. Lou, Directional solidification assisted by liquid metal cooling, Journal of Materials Science and Technology 23(3) (2007) 289-300.

[15] D. Ma, Q. Wu, A. Bührig-Polaczek, Some New Observations on Freckle Formation in Directionally Solidified Superalloy Components, Metallurgical and Materials Transactions B 43(2) (2012) 344-353.

[16] K. Kubiak, D. Szeliga, J. Sieniawski, A. Onyszko, 11 - The Unidirectional Crystallization of Metals and Alloys (Turbine Blades), in: P. Rudolph (Ed.), Handbook of Crystal Growth (Second Edition), Elsevier, Boston, 2015, pp. 413-457.

[17] H. Fu, J. Shen, L. Liu, Q. Hao, S. Li, J. Li, Electromagnetic shaping and solidification control of Ni-base superalloys under vacuum, Journal of materials processing technology 148(1) (2004) 25-29.

[18] J. Zhang, Y. Tan, S. Li, J. Li, H. Fu, The frequency effect on electromagnetic confinement and shaping of liquid metal, Science and Technology of Advanced Materials 2(1) (2001) 205.

[19] A. Elliott, G. Karney, M. Gigliotti, T. Pollock, Issues in processing by the liquid-Sn assisted directional solidification technique, Superalloys (2004) 421-430.

[20] H. Fu, X. Geng, High rate directional solidification and its application in single crystal superalloys, Science and Technology of Advanced Materials 2(1) (2001) 197-204.

[21] A.F. Giamei, J.G. Tschinkel, Liquid metal cooling: A new solidification technique, Metallurgical Transactions A 7(9) (1976) 1427-1434.

[22] M. Torfeh, S.M.H. Mirbagheri, J. Cormier, J. Aghazadeh Mohandesi, S. Nakhodchi, Intermediate temperature creep damage mechanisms of a directionally solidified Ni-based superalloy, Materials at High Temperatures 39(3) (2022) 193-205.

[23] K. Safaei, N.T. Andani, B. Poorganji, M.T. Andani, M. Elahinia, Controlling texture of NiTi alloy processed by laser powder bed fusion: Smart build orientation and scanning strategy, Additive Manufacturing Letters 5 (2023) 100126.

[24] N. D'Souza, M.G. Ardakani, A. Wagner, B.A. Shollock, M. McLean, Morphological aspects of competitive grain growth during directional solidification of a nickel-base superalloy, CMSX4, Journal of Materials Science 37(3) (2002) 481-487.

[25] Y.-G. Tan, F. Liu, A.-W. Zhang, D.-W. Han, X.-Y. Yao, W.-W. Zhang, W.-R. Sun, Element Segregation and Solidification Behavior of a Nb, Ti, Al Co-Strengthened Superalloy ЭК151, Acta Metallurgica Sinica (English Letters) 32(10) (2019) 1298-1308.

[26] W. Zhang, Y. Tan, N.H. Tariq, T. Si, Z. Wang, X. Xin, W. Sun, The Effect of Primary Laves Phase on Notch Sensitivity in Thermo-span Superalloy, Journal of Materials Engineering and Performance 32(8) (2023) 3420-3430.

[27] A. Wagner, B.A. Shollock, M. McLean, Grain structure development in directional solidification of nickel-base superalloys, Materials Science and Engineering: A 374(1) (2004) 270-279.

[28] L. Li, R.A. Overfelt, Influence of directional solidification variables on the cellular and primary dendrite arm spacings of PWA1484, Journal of Materials Science 37(16) (2002) 3521-3532.

[29] C.A. Gandin, M. Rappaz, D. West, B.L. Ada, Grain texture evolution during the columnar growth of dendritic alloys, Metallurgical and Materials Transactions A 26(6) (1995) 1543-1551.

[30] S.S. Hwang, Y.S. Lim, S.W. Kim, D.J. Kim, H.P. Kim, ROLE OF GRAIN BOUNDARY CARBIDES IN CRACKING BEHAVIOR OF Ni BASE ALLOYS, Nuclear Engineering and Technology 45(1) (2013) 73-80.

[31] F. Theska, R. Buerstmayr, H. Liu, M. Lison-Pick, S.R. Street, S. Primig, Influence of grain boundary precipitation and segregation on cracking of cast and wrought superalloys containing B and Zr, Materials Characterization 187 (2022) 111881.

[32] H. Cui, J. Zhang, Y. Murata, M. Morinaga, N. Yukawa, Hot Corrosion Behavior of Ni-based Superalloy with High Cr Contents-Part 1. Experimental Study, JOURNAL OF UNIVERSITY OF SCIENCE AND TECHNOLOGY BEIJING (ENGLISH EDITION) (2) (1996) 02.

[33] M. Nathal, L. Ebert, Gamma prime shape changes during creep of a nickel-base superalloy, Scripta metallurgica 17(9) (1983) 1151-1154.

[34] M. Nathal, R. MacKay, R. Garlick, Lattice parameter variations during aging in nickel-base superalloys, (1988).

[35] H. Long, S. Mao, Y. Liu, Z. Zhang, X. Han, Microstructural and compositional design of Ni-based single crystalline superalloys—A review, Journal of Alloys and Compounds 743 (2018) 203-220.

[36] K. Park, P. Withey, Compositions of Gamma and Gamma Prime Phases in an As-Cast Nickel-Based Single Crystal Superalloy Turbine Blade, Crystals, 2022.

[37] M. Rozmus-Górnikowska, J. Kusiński, Ł. Cieniek, J. Morgiel, The Microstructure and Properties of Laser Shock Peened CMSX4 Superalloy, Metallurgical and Materials Transactions A 52(7) (2021) 2845-2858.

[38] C.L. Qiu, P. Andrews, On the formation of irregular-shaped gamma prime and serrated grain boundaries in a nickel-based superalloy during continuous cooling, Materials Characterization 76 (2013) 28-34.

[39] N. Mrozowski, G. Hénaff, F. Hamon, A.-L. Rouffié, J.-M. Franchet, J. Cormier, P. Villechaise, Aging of γ' Precipitates at 750 °C in the Nickel-Based Superalloy AD730TM: A Thermally or Thermo-Mechanically Controlled Process?, Metals, 2020.

[40] D. Wang, Investigation of microstructure and creep mechanism of two directionally solidified Ni-base superalloys, Institute of Metal Research, 2010, pp. 5-6.

[41] A. Wasson, G. Fuchs, The effect of carbide morphologies on elevated temperature tensile and fatigue behavior of a modified single crystal Ni-base superalloy, Superalloys 2008 (2008) 489-497.

[42] L.Z. He, Q. Zheng, X.F. Sun, H.R. Guan, Z.Q. Hu, A.K. Tieu, C. Lu, H.T. Zhu, Effect of carbides on the creep properties of a Ni-base superalloy M963, Materials Science and Engineering: A 397(1) (2005) 297-304.

[43] S. Sui, J. Chen, L. Ma, W. Fan, H. Tan, F. Liu, X. Lin, Microstructures and stress rupture properties of pulse laser repaired Inconel 718 superalloy after different heat treatments, Journal of Alloys and Compounds 770 (2019) 125-135.

[44] D.A. Gurianov, S.V. Fortuna, K.S. Osipovich, Defects formation features of nickel-based superalloy product obtained by wire-feed electron beam additive manufacturing, AIP Conference Proceedings 2167(1) (2019) 020125.

[45] A. Epishin, U. Brückner, P.D. Portella, T. Link, Influence of small rhenium additions on the lattice spacing of nickel solid solution, Scripta Materialia 48(4) (2003) 455-459.

[46] D.L. Anton, A.F. Giamei, Porosity distribution and growth during homogenization in single crystals of a nickel-base superalloy, Materials Science and Engineering 76 (1985) 173-180.

[47] K. Prasad, R. Sarkar, K. Gopinath, Role of shrinkage pores, carbides on cyclic deformation behaviour of conventionally cast nickel base superalloy CM247LC® at 870°C, Materials Science and Engineering: A 654 (2016) 381-389.

[48] L. Kunz, P. Lukáš, R. Konečná, S. Fintová, Casting defects and high temperature fatigue life of IN 713LC superalloy, International Journal of Fatigue 41 (2012) 47-51.

[49] A. Defresne, L. Remy, Fatigue behaviour of CMSX 2 superalloy [001] single crystals at high temperature I: Low cycle fatigue of notched specimens, Materials Science and Engineering: A 129(1) (1990) 45-53.

[50] R.J. Morrissey, R. John, W. John Porter, Fatigue variability of a single crystal superalloy at elevated temperature, International Journal of Fatigue 31(11) (2009) 1758-1763.

[51] R. Jiang, D.J. Bull, A. Evangelou, A. Harte, F. Pierron, I. Sinclair, M. Preuss, X.T. Hu, P.A.S. Reed, Strain accumulation and fatigue crack initiation at pores and carbides in a SX superalloy at room temperature, International Journal of Fatigue 114 (2018) 22-33.

[52] D. Shi, C. Dong, X. Yang, Constitutive modeling and failure mechanisms of anisotropic tensile and creep behaviors of nickel-base directionally solidified superalloy, Materials & Design 45 (2013) 663-673.

[53] X. Wang, J. Li, J. Yu, S. LIU, Z. SHI, X. YUE, Tensile anisotropy of single crystal superalloy DD9, Acta Metall Sin 51(10) (2015) 1253-1260.

[54] G. Erickson, K. Harris, DS and SX superalloys for industrial gas turbines, Materials for Advanced Power Engineering. Part II. Proc. of a Conf. Belgium, Kluwer Academic Publishers, 1994, pp. 1055-1074.

[55] K. Harris, G. Erickson, R. Schwer, MAR-M247 derivations—CM247 LC DS alloy, CMSX single crystal alloys, properties and performance, Superalloys 1984 (1984) 221-230.

[56] W. Kurz, D.J. Fisher, Fundamentals of solidification, (1989).

[57] H. Jeong, S. Seo, B. Choi, Y. Yoo, Y. Ahn, J. Lee, Effect of long-term thermal exposures on microstructures and mechanical properties of directionally solidified CM247LC alloy, Metals and Materials International 19(5) (2013) 917-925.

[58] C. Shao, Investigations on the low-cycle fatigue behaviors of Fe-Mn-C twinning-induced plasticity steels, Institute of Metal Research, Chinese Academy of Sciences, 2017.

[59] S. Suresh, Fatigue of Materials, Cambridge University Press, Cambridge, England (1998).

[60] U. Krupp, Fatigue crack propagation in metals and alloys: microstructural aspects and modelling concepts, John Wiley & Sons2007.

[61] J. Schijve, Fatigue of structures and materials, Springer Science & Business Media2001.

[62] W.C. Oliver, G.M. Pharr, Nanoindentation in materials research: Past, present, and future, MRS Bulletin 35(11) (2010) 897-907.

[63] O. Basquin, The exponential law of endurance tests, Proc Am Soc Test Mater, 1910, pp. 625-630.

[64] L. Coffin, The problem of thermal stress fatigue in austenitic steels at elevated temperatures, Symposium on Effect of Cyclic Heating and Stressing on Metals at Elevated Temperatures, ASTM International, 1954.

[65] S. Manson, Behaviour of materials under conditions of thermal stress, 1953, NACA TN-2933 and Coffin LF Jr, Transactions of the ASME 76 (1954) 931.

[66] J.A. Ewing, J. Humfrey, VI. The fracture of metals under repeated alternations of stress, Philosophical Transactions of the Royal Society of London. Series A, Containing Papers of a Mathematical or Physical Character 200(321-330) (1903) 241-250.

[67] R. Cahn, P. Haasen, Metallurgy, Physical, North-Holland, Amsterdam, 1983.

[68] R. Jiang, F. Pierron, S. Octaviani, P.A.S. Reed, Characterisation of strain localisation processes during fatigue crack initiation and early crack propagation by SEM-DIC in an advanced disc alloy, Materials Science and Engineering: A 699 (2017) 128-144.

[69] J.C. Stinville, N. Vanderesse, F. Bridier, P. Bocher, T.M. Pollock, High resolution mapping of strain localization near twin boundaries in a nickel-based superalloy, Acta Materialia 98 (2015) 29-42.

[70] L. Zhang, L.G. Zhao, A. Roy, V.V. Silberschmidt, G. McColvin, In-situ SEM study of slip-controlled short-crack growth in single-crystal nickel superalloy, Materials Science and Engineering: A 742 (2019) 564-572.

[71] Y. Zhang, H.J. Shi, J. Gu, C. Li, K. Kadau, O. Luesebrink, Crystallographic analysis for fatigue small crack growth behaviors of a nickel-based single crystal by in situ SEM observation, Theoretical and Applied Fracture Mechanics 69 (2014) 80-89.

[72] M. Sakaguchi, R. Komamura, X. Chen, M. Higaki, H. Inoue, Crystal plasticity assessment of crystallographic Stage I crack propagation in a Ni-based single crystal superalloy, International Journal of Fatigue 123 (2019) 10-21.

[73] R. Jiang, N. Karpasitis, N. Gao, P.A.S. Reed, Effects of microstructures on fatigue crack initiation and short crack propagation at room temperature in an advanced disc superalloy, Materials Science and Engineering: A 641 (2015) 148-159.

[74] L.C. Zhang, R. Jiang, Y.C. Wang, L. Zhang, J.T. Liu, Y.W. Zhang, Y.D. Song, Effects of microstructure and temperature on short fatigue crack propagation behaviour of powder metallurgy superalloy FGH4098 in vacuum, Materials Science and Engineering: A 852 (2022) 143637.

[75] L. Zhang, L.G. Zhao, A. Roy, V.V. Silberschmidt, G. McColvin, Low-cycle fatigue of single crystal nickel-based superalloy – mechanical testing and TEM characterisation, Materials Science and Engineering: A 744 (2019) 538-547.

[76] H. Long, Y. Liu, D. Kong, H. Wei, Y. Chen, S. Mao, Shearing mechanisms of stacking fault and anti-phase-boundary forming dislocation pairs in the γ' phase in Ni-based single crystal superalloy, Journal of Alloys and Compounds 724 (2017) 287-295.

[77] Y. Tang, M. Huang, J. Xiong, J. Li, J. Zhu, Evolution of superdislocation structures during tertiary creep of a nickel-based single-crystal superalloy at high temperature and low stress, Acta Materialia 126 (2017) 336-345.

[78] H.T. Pang, P.A.S. Reed, Fatigue crack initiation and short crack growth in nickel-base turbine disc alloys—the effects of microstructure and operating parameters, International Journal of Fatigue 25(9) (2003) 1089-1099.

[79] R.W. Neu, Crack paths in single-crystal Ni-base superalloys under isothermal and thermomechanical fatigue, International Journal of Fatigue 123 (2019) 268-278.

[80] L.Z. He, Q. Zheng, X.F. Sun, H.R. Guan, Z.Q. Hu, A.K. Tieu, C. Lu, H.T. Zhu, High temperature low cycle fatigue behavior of Ni-base superalloy M963, Materials Science and Engineering: A 402(1) (2005) 33-41.

[81] L.R. Liu, T. Jin, N.R. Zhao, X.F. Sun, H.R. Guan, Z.Q. Hu, Formation of carbides and their effects on stress rupture of a Ni-base single crystal superalloy, Materials Science and Engineering: A 361(1) (2003) 191-197.

[82] R. Jiang, Y.D. Song, P.A. Reed, Fatigue crack growth mechanisms in powder metallurgy Ni-based superalloys—A review, International Journal of Fatigue 141 (2020) 105887.

[83] C. Zhaokuang, Y. Jinjiang, S. Xiaofeng, G. Hengrong, H. Zhuangqi, High cycle fatigue behavior of a directionally solidified Ni-base superalloy DZ951, Materials Science and Engineering A 496(1-2) (2008) 355-361.

[84] M. Goto, D.M. Knowles, Initiation and propagation behaviour of microcracks in Ni-base superalloy Udimet 720 LI, Engineering Fracture Mechanics 60(1) (1998) 1-18.

[85] J. Reuchet, L. Remy, High temperature low cycle fatigue of MAR-M 509 superalloy I: The influence of temperature on the low cycle fatigue behaviour from 20 to 1100°C, Materials Science and Engineering 58(1) (1983) 19-32.

[86] R.J. Morrissey, R. John, W. John Porter Iii, Fatigue variability of a single crystal superalloy at elevated temperature, International Journal of Fatigue 31(11-12) (2009) 1758-1763.

[87] P.S. Karamched, A.J. Wilkinson, High resolution electron back-scatter diffraction analysis of thermally and mechanically induced strains near carbide inclusions in a superalloy, Acta Materialia 59(1) (2011) 263-272.

[88] J. Litz, A. Rahmel, M. Schorr, Selective carbide oxidation and internal nitridation of the Ni-base superalloys IN 738 LC and IN 939 in air, Oxidation of Metals 30(1) (1988) 95-105.

[89] L. Fournier, D. Delafosse, T. Magnin, Oxidation induced intergranular cracking and Portevin–Le Chatelier effect in nickel base superalloy 718, Materials Science and Engineering: A 316(1) (2001) 166-173.

[90] S. Cruchley, H.Y. Li, H.E. Evans, P. Bowen, D.J. Child, M.C. Hardy, The role of oxidation damage in fatigue crack initiation of an advanced Ni-based superalloy, International Journal of Fatigue 81 (2015) 265-274.

[91] J. Miao, T.M. Pollock, J. Wayne Jones, Microstructural extremes and the transition from fatigue crack initiation to small crack growth in a polycrystalline nickel-base superalloy, Acta Materialia 60(6-7) (2012) 2840-2854.

[92] J.D. Livingston, B. Chalmers, Multiple slip in bicrystal deformation, Acta Metallurgica 5(6) (1957) 322-327.

[93] Z. Shen, R.H. Wagoner, W.A.T. Clark, Dislocation and grain boundary interactions in metals, Acta Metallurgica 36(12) (1988) 3231-3242.

[94] J. Luster, M.A. Morris, Compatibility of deformation in two-phase Ti-Al alloys: Dependence on microstructure and orientation relationships, Metallurgical and Materials Transactions A 26(7) (1995) 1745-1756.

[95] D. Mercier, C. Zambaldi, T. Bieler, STABiX Toolbox documentation, 2015.

[96] R. Jiang, W. Zhang, L. Zhang, Y. Zhao, L. Zhang, Y. Song, Strain localization and crack initiation behavior of a PM Ni-based superalloy: SEM-DIC characterization and crystal plasticity simulation, Fatigue & Fracture of Engineering Materials & Structures 45(6) (2022) 1635-1651.

[97] J. Tong, S. Dalby, J. Byrne, M.B. Henderson, M.C. Hardy, Creep, fatigue and oxidation in crack growth in advanced nickel base superalloys, International Journal of Fatigue 23(10) (2001) 897-902.

[98] G. Chen, Y. Zhang, D.K. Xu, Y.C. Lin, X. Chen, Low cycle fatigue and creep-fatigue interaction behavior of nickel-base superalloy GH4169 at elevated temperature of 650°C, Materials Science and Engineering: A 655 (2016) 175-182.

[99] A. Cervellon, J.Z. Yi, F. Corpace, Z. Hervier, J. Rigney, P.K. Wright, C.J. Torbet, J. Cormier, J.W. Jones, T.M. Pollock, Creep, Fatigue, and Oxidation Interactions During High and Very High Cycle Fatigue at Elevated Temperature of Nickel-Based Single Crystal

Superalloys, in: S. Tin, M. Hardy, J. Clews, J. Cormier, Q. Feng, J. Marcin, C. O'Brien, A. Suzuki (Eds.) Superalloys 2020, Springer International Publishing, Cham, 2020, pp. 185-195.

[100] L.G. Zhao, Modeling of Oxygen Diffusion Along Grain Boundaries in a Nickel-Based Superalloy, Journal of Engineering Materials and Technology 133(3) (2011).

[101] A. Karabela, L.G. Zhao, B. Lin, J. Tong, M.C. Hardy, Oxygen diffusion and crack growth for a nickel-based superalloy under fatigue-oxidation conditions, Materials Science and Engineering: A 567 (2013) 46-57.

[102] J.D. Ramsay, H.E. Evans, D.J. Child, M.P. Taylor, M.C. Hardy, The influence of stress on the oxidation of a Ni-based superalloy, Corrosion Science 154 (2019) 277-285.

[103] A. Evangelou, Oxidation-fatigue mechanisms at moderate service temperatures in single crystal turbine blade materials, University of Southampton, 2017.

[104] A. Encinas-Oropesa, G. Drew, M. Hardy, A. Leggett, J.R. Nicholls, N.J. Simms, Effects of oxidation and hot corrosion in a nickel disc alloy, (2008).

[105] H.E. Evans, H.Y. Li, P. Bowen, A mechanism for stress-aided grain boundary oxidation ahead of cracks, Scripta Materialia 69(2) (2013) 179-182.

[106] R. Jiang, D. Proprentner, M. Callisti, B. Shollock, X.T. Hu, Y.D. Song, P.A.S. Reed, Role of oxygen in enhanced fatigue cracking in a PM Ni-based superalloy: Stress assisted grain boundary oxidation or dynamic embrittlment?, Corrosion Science 139 (2018) 141-154.

[107] J.A. Pfaendtner, C.J. McMahon Jr, Oxygen-induced intergranular cracking of a Ni-base alloy at elevated temperatures—an example of dynamic embrittlement, Acta Materialia 49(16) (2001) 3369-3377.

[108] U. Krupp, W.M. Kane, C. Laird, C.J. McMahon, Brittle intergranular fracture of a Ni-base superalloy at high temperatures by dynamic embrittlement, Materials Science and Engineering: A 387-389 (2004) 409-413.

[109] R. Jiang, S. Everitt, N. Gao, K. Soady, J.W. Brooks, P.A.S. Reed, Influence of oxidation on fatigue crack initiation and propagation in turbine disc alloy N18, International Journal of Fatigue 75 (2015) 89-99.

[110] H.E. Evans, Stress effects in high temperature oxidation of metals, International Materials Reviews 40(1) (1995) 1-40.

[111] P. Kontis, Z. Li, M. Segersäll, J.J. Moverare, R.C. Reed, D. Raabe, B. Gault, The Role of Oxidized Carbides on Thermal-Mechanical Performance of Polycrystalline Superalloys, Metallurgical and Materials Transactions A 49(9) (2018) 4236-4245.

[112] P. Li, B. Zhou, Y. Zhou, Z. Zhang, Effect of orientation on low-cycle fatigue behaviour of single crystal superalloys at 900°C, Materials Science and Technology 35(7) (2019) 767-774.

[113] Z. Wang, W. Wu, J. Liang, X. Li, Creep–fatigue interaction behavior of nickel-based single crystal superalloy at high temperature by in-situ SEM observation, International Journal of Fatigue 141 (2020) 105879.

[114] D. Hu, R. Wang, Experimental study on creep–fatigue interaction behavior of GH4133B superalloy, Materials Science and Engineering: A 515(1) (2009) 183-189.

[115] Y.L. Lu, P.K. Liaw, L.J. Chen, G.Y. Wang, M.L. Benson, S.A. Thompson, J.W. Blust, P.F. Browning, A.K. Bhattacharya, J.M. Aurrecoechea, D.L. Klarstrom, Tensile-hold effects on high-temperature fatigue-crack growth in nickel-based HASTELLOY® X alloy, Materials Science and Engineering: A 433(1) (2006) 114-120.

[116] E. Andrieu, R. Molins, H. Ghonem, A. Pineau, Intergranular crack tip oxidation mechanism in a nickel-based superalloy, Materials Science and Engineering: A 154(1) (1992) 21-28.

[117] R. Jiang, D. Bull, D. Proprentner, B. Shollock, P. Reed, Effects of oxygen-related damage on dwell-fatigue crack propagation in a P/M Ni-based superalloy: from 2D to 3D assessment, International Journal of Fatigue 99 (2017) 175-186.

[118] R. Jiang, S. Everitt, M. Lewandowski, N. Gao, P. Reed, Grain size effects in a Ni-based turbine disc alloy in the time and cycle dependent crack growth regimes, International Journal of Fatigue 62 (2014) 217-227.

[119] R. Jiang, D. Proprentner, M. Callisti, B. Shollock, X. Hu, Y. Song, P. Reed, Role of oxygen in enhanced fatigue cracking in a PM Ni-based superalloy: Stress assisted grain boundary oxidation or dynamic embrittlment?, Corrosion Science 139 (2018) 141-154.

[120] C.J. McMahon, Comments on "Identification of SAGBO-induced damage zone ahead of crack tip to characterize sustained loading crack growth in alloy 783", Scripta Materialia 54(2) (2006) 305-307.

[121] S. Suresh, G.F. Zamiski, D.R.O. Ritchie, Oxide-Induced Crack Closure: An Explanation for Near-Threshold Corrosion Fatigue Crack Growth Behavior, Metallurgical and Materials Transactions A 12(8) (1981) 1435-1443.

[122] A.T. Stewart, The influence of environment and stress ratio on fatigue crack growth at near threshold stress intensities in low-alloy steels, Engineering Fracture Mechanics 13(3) (1980) 463-478.

[123] P.K. Liaw, T.R. Leax, R.S. Williams, M.G. Peck, Influence of oxide-induced crack closure on near-threshold fatigue crack growth behavior, Acta Metallurgica 30(12) (1982) 2071-2078.

[124] P. Paris, R. Bucci, E. Wessel, W. Clark, T. Mager, Extensive study of low fatigue crack growth rates in A533 and A508 steels, ASTM STP 513 (1972) 141-176.

[125] J.M. Martínez-Esnaola, A. Martín-Meizoso, E.E. Affeldt, A. Bennett, M. Fuentes, HIGH TEMPERATURE FATIGUE IN SINGLE CRYSTAL SUPERALLOYS, Fatigue & Fracture of Engineering Materials & Structures 20(5) (1997) 771-788.

[126] N. Louat, K. Sadananda, M. Duesbery, A.K. Vasudevan, A Theoretical Evaluation of Crack Closure, Metallurgical and Materials Transactions A 24(10) (1993) 2225-2232.

[127] G. Onofrio, G.A. Osinkolu, M. Marchionni, Fatigue crack growth of UDIMET 720 Li superalloy at elevated temperature, International Journal of Fatigue 23(10) (2001) 887-895.

[128] D.M. Knowles, D.W. Hunt, The influence of microstructure and environment on the crack growth behavior of powder metallurgy nickel superalloy RR1000, Metallurgical and Materials Transactions A: Physical Metallurgy and Materials Science 33(10) (2002) 3165-3172.

[129] S. Everitt, R. Jiang, N. Gao, M.J. Starink, J.W. Brooks, P.A.S. Reed, Comparison of fatigue crack propagation behaviour in two gas turbine disc alloys under creep–fatigue conditions: evaluating microstructure, environment and temperature effects, Materials Science and Technology 29(7) (2013) 781-787.

[130] K.-S. Li, R.-Z. Wang, G.-J. Yuan, S.-P. Zhu, X.-C. Zhang, S.-T. Tu, H. Miura, A crystal plasticity-based approach for creep-fatigue life prediction and damage evaluation in a nickel-based superalloy, International Journal of Fatigue 143 (2021) 106031.

[131] B. Ding, W. Ren, K. Deng, H. Li, Y. Liang, An Abnormal Increase of Fatigue Life with Dwell Time during Creep-Fatigue Deformation for Directionally Solidified Ni-Based Superalloy DZ445, 37(3) (2018) 277-284.

[132] B. Ding, W. Ren, J. Peng, Y. Zhong, J. Yu, Influence of dwell time on the creep–fatigue behavior of a directionally solidified Ni-based superalloy DZ445 at 850 °C, Materials Science and Engineering: A 725 (2018) 319-328.

[133] D. Shi, J. Liu, X. Yang, H. Qi, J. Wang, Experimental investigation on low cycle fatigue and creep–fatigue interaction of DZ125 in different dwell time at elevated temperatures, Materials Science and Engineering: A 528(1) (2010) 233-238.

[134] R. Pippan, A. Hohenwarter, Fatigue crack closure: a review of the physical phenomena, Fatigue & Fracture of Engineering Materials & Structures 40(4) (2017) 471-495.

[135] M. Miller, P. Reed, M. Joyce, Effect of temperature and secondary orientation on notch fatigue resistance of CMSX4, International Journal of Fatigue (2005).

[136] P.A.S. Reed, P.H. Tucker, M.R. Joyce, Effects of mixed mode loading on fatigue and creep–fatigue in SRR-99 single crystals, Materials Science and Engineering: A 394(1) (2005) 256-265.

[137] A. Cervellon, C.J. Torbet, T.M. Pollock, Crack initiation anisotropy of Ni-based SX superalloys in the very high cycle fatigue regime, Materials Science and Engineering: A 825 (2021) 141920.

[138] J. Yu, Y. Sun, X. Sun, T. Jin, Z. Hu, Anisotropy of high cycle fatigue behavior of a Ni-base single crystal superalloy, Materials Science and Engineering: A 566 (2013) 90-95.

[139] M. Okazaki, T. Tabata, S. Nohmi, Intrinsic stage i crack growth of directionally solidified Ni-Base superalloys during low-cycle fatigue at elevated temperature, Metallurgical Transactions A 21(8) (1990) 2201-2208.

[140] Z.J. Moore, R.W. Neu, Creep fatigue of a directionally solidified Ni-base superalloy – smooth and cylindrically notched specimens, Fatigue & Fracture of Engineering Materials & Structures 34(1) (2011) 17-31.

[141] R.A. Kupkovits, R.W. Neu, Thermomechanical Fatigue of a Directionally-Solidified Ni-Base Superalloy in the Presence of Stress Concentrations, 2009, pp. 163-173.

[142] R.A. Kupkovits, R.W. Neu, Thermomechanical fatigue of a directionally-solidified Ni-base superalloy: Smooth and cylindrically-notched specimens, International Journal of Fatigue 32(8) (2010) 1330-1342.

[143] F. Bachmann, R. Hielscher, H. Schaeben, Texture analysis with MTEX- Free and open source software toolbox, Solid State Phenomena, 2010, pp. 63-68.

[144] Z.W. Lian, J.J. Yu, X.F. Sun, H.R. Guan, Z.Q. Hu, Temperature dependence of tensile behavior of Ni-based superalloy M951, Materials Science and Engineering: A 489(1) (2008) 227-233.

[145] X. Xiong, D. Quan, P. Dai, Z. Wang, Q. Zhang, Z. Yue, Tensile behavior of nickel-base single-crystal superalloy DD6, Materials Science and Engineering: A 636 (2015) 608-612.

[146] Y. Tan, D. Bull, R. Jiang, A. Evangelou, S. Chauduri, S. Octaviani, F. Pierron, N. Gao, H. Toda, S. Ian, P. Reed, Data rich imaging approaches assessing fatigue crack initiation and early propagation in a DS superalloy at room temperature, submited to Materials Science and Engineering: A (2020).

[147] H.W. Schreier, M.A. Sutton, Systematic errors in digital image correlation due to undermatched subset shape functions, Exp Mech 42(3) (2002) 303-310.

[148] W. Pantleon, Resolving the geometrically necessary dislocation content by conventional electron backscattering diffraction, Scripta Materialia 58(11) (2008) 994-997.

[149] M. Doyama, R.M.J. Cotterill, Energy and Atomic Configurations of Complete and Dissociated Dislocations. II. Screw Dislocation in an fcc Metal, Physical Review 150(2) (1966) 448-455.

[150] Y.G. Tan, D.J. Bull, R. Jiang, A. Evangelou, S. Chaudhuri, S. Octaviani, F. Pierron, N. Gao, H. Toda, I. Sinclair, P.A.S. Reed, Data rich imaging approaches assessing fatigue crack initiation and early propagation in a DS superalloy at room temperature, Materials Science and Engineering: A 805 (2021) 140592.

[151] H. Toda, I. Sinclair, J.Y. Buffière, E. Maire, T. Connolley, M. Joyce, K.H. Khor, P. Gregson, Assessment of the fatigue crack closure phenomenon in damage-tolerant aluminium alloy by in-situ high-resolution synchrotron X-ray microtomography, Philosophical Magazine 83(21) (2003) 2429-2448.

[152] H. Toda, I. Sinclair, J.Y. Buffière, E. Maire, K.H. Khor, P. Gregson, T. Kobayashi, A 3D measurement procedure for internal local crack driving forces via synchrotron X-ray microtomography, Acta Materialia 52(5) (2004) 1305-1317.

[153] L. Agudo Jácome, P. Nörtershäuser, J.K. Heyer, A. Lahni, J. Frenzel, A. Dlouhy, C. Somsen, G. Eggeler, High-temperature and low-stress creep anisotropy of single-crystal superalloys, Acta Materialia 61(8) (2013) 2926-2943.

[154] P. Nörtershäuser, J. Frenzel, A. Ludwig, K. Neuking, G. Eggeler, The effect of cast microstructure and crystallography on rafting, dislocation plasticity and creep anisotropy of single crystal Ni-base superalloys, Materials Science and Engineering: A 626 (2015) 305-312.

[155] T. Khan, P. Caron, Y.G. Nakagawa, Mechanical Behavior and Processing of DS and Single Crystal Superalloys, JOM 38(7) (1986) 16-19.

[156] T. Hasebe, M. Sakane, M. Ohnami, Elastic Anisotropy of Directionally Solidified Superalloy, Journal of Engineering Materials and Technology 114(2) (1992) 141-146.

[157] C. Dong, H. Yu, Y. Li, X. Yang, D. Shi, Life modeling of anisotropic fatigue behavior for a single crystal nickel-base superalloy, International Journal of Fatigue 61 (2014) 21-27.

[158] C. Dong, X. Yang, D. Shi, H. Yu, Modeling of anisotropic tensile and cyclic viscoplastic behavior of a nickel-base directionally solidified superalloy, Materials & Design 55 (2014) 966-978.

[159] M. Yamamoto, T. Kitamura, T. Ogata, Influence of microscopically distributed inhomogeneity and anisotropy of grains on high-temperature crack propagation properties of directionally solidified superalloy, Engineering Fracture Mechanics 75(3) (2008) 779-789.

[160] N. Shirafuji, K. Shimomizuki, M. Sakane, M. Ohnami, Tension-Torsion Multiaxial Low Cycle Fatigue of Mar-M247LC Directionally Solidified Superalloy at Elevated Temperature, Journal of Engineering Materials and Technology 120(1) (1998) 57-63.

[161] T. Lindström, D. Nilsson, K. Simonsson, R. Eriksson, J.-E. Lundgren, D. Leidermark, Accounting for anisotropic, anisothermal, and inelastic effects in crack initiation lifing of additively manufactured components, Fatigue & Fracture of Engineering Materials & Structures 46(2) (2023) 396-415.

[162] M.F. Borges, F.V. Antunes, P.A. Prates, R. Branco, T. Vojtek, Effect of Young’s modulus on fatigue crack growth, International Journal of Fatigue 132 (2020) 105375.

[163] J. Wasén, E. Heier, Fatigue crack growth thresholds—the influence of Young's modulus and fracture surface roughness, International Journal of Fatigue 20(10) (1998) 737-742.

[164] M. Segersäll, D. Leidermark, J.J. Moverare, Influence of crystal orientation on the thermomechanical fatigue behaviour in a single-crystal superalloy, Materials Science and Engineering: A 623 (2015) 68-77.

[165] S. Suzuki, M. Sakaguchi, H. Inoue, Temperature dependent fatigue crack propagation in a single crystal Ni-base superalloy affected by primary and secondary orientations, Materials Science and Engineering: A 724 (2018) 559-565.

[166] T. Hasebe, M. Sakane, M. Ohnami, High Temperature Low Cycle Fatigue and Cyclic Constitutive Relation of MAR-M247 Directionally Solidified Superalloy, Journal of Engineering Materials and Technology 114(2) (1992) 162-167.

[167] Y. Tan, N. Gao, P. Reed, Oxidation induced crack closure in a nickel base superalloy: A novel phenomenon and mechanism assessed via combination of 2D and 3D characterization, Materials Science and Engineering: A 861 (2022) 144311.

[168] L. Zhang, P. Yan, M. Zhao, J. Li, J. Zhao, Q. Zeng, F. Han, Tensile Anisotropy of a Single Crystal Superalloy, in: F. Marquis (Ed.) Proceedings of the 8th Pacific Rim International Congress on Advanced Materials and Processing, Springer International Publishing, Cham, 2016, pp. 475-484.

[169] W.-p. Yang, J.-r. Li, S.-z. Liu, Z.-x. Shi, J.-q. Zhao, X.-g. Wang, Orientation dependence of transverse tensile properties of nickel-based third generation single crystal superalloy DD9 from 760 to 1100 °C, Transactions of Nonferrous Metals Society of China 29(3) (2019) 558-568.

[170] R.B. Sills, N. Bertin, A. Aghaei, W. Cai, Dislocation Networks and the Microstructural Origin of Strain Hardening, Physical Review Letters 121(8) (2018) 085501.

[171] Z. Tong, G. Nagy, Surface tortuosity and its application to analyzing cracks in concrete, Proceedings of the 17th International Conference on Pattern Recognition, 2004. ICPR 2004., 2004, pp. 851-854 Vol.2.

[172] A. Rezaei, A. Rezaeian, A. Kermanpur, M. Badrossamay, E. Foroozmehr, M. Marashi, A. Foroozmehr, J. Han, Microstructural and mechanical anisotropy of selective laser melted IN718 superalloy at room and high temperatures using small punch test, Materials Characterization 162 (2020) 110200.

[173] X. Zhang, H. Xu, Z. Li, A. Dong, D. Du, L. Lei, G. Zhang, D. Wang, G. Zhu, B. Sun, Effect of the scanning strategy on microstructure and mechanical anisotropy of Hastelloy X superalloy produced by Laser Powder Bed Fusion, Materials Characterization 173 (2021) 110951.

[174] R.V. Miner, T.P. Gabb, J. Gayda, K.J. Hemker, Orientation and temperature dependence of some mechanical properties of the single-crystal nickel-base superalloy René N4: Part III. Tension-compression anisotropy, Metallurgical Transactions A 17(3) (1986) 507-512.

[175] D. Siebörger, H. Knake, U. Glatzel, Temperature dependence of the elastic moduli of the nickel-base superalloy CMSX-4 and its isolated phases, Materials Science and Engineering: A 298(1) (2001) 26-33.

[176] R. Muñoz-Moreno, V.D. Divya, S.L. Driver, O.M.D.M. Messé, T. Illston, S. Baker, M.A. Carpenter, H.J. Stone, Effect of heat treatment on the microstructure, texture and elastic anisotropy of the nickel-based superalloy CM247LC processed by selective laser melting, Materials Science and Engineering: A 674 (2016) 529-539.

[177] Z. Chen, S. Chen, Z. Wei, L. Zhang, P. Wei, B. Lu, S. Zhang, Y. Xiang, Anisotropy of nickel-based superalloy K418 fabricated by selective laser melting, Progress in Natural Science: Materials International 28(4) (2018) 496-504.

[178] S. Zhang, X. Lin, L. Wang, X. Yu, Y. Hu, H. Yang, L. Lei, W. Huang, Strengthening mechanisms in selective laser-melted Inconel718 superalloy, Materials Science and Engineering: A 812 (2021) 141145.

[179] J.F.S. Markanday, M.A. Carpenter, N.G. Jones, R.P. Thompson, S.E. Rhodes, C.P. Heason, H.J. Stone, Occurrence of a brass texture and elastic anisotropy in laser blown powder processed superalloy IN718, Materials Science and Engineering: A 825 (2021) 141781.

[180] A.A. Roostaei, A. Pahlevanpour, S.B. Behravesh, H. Jahed, On the definition of elastic strain energy density in fatigue modelling, International Journal of Fatigue 121 (2019) 237-242.

[181] Y.C. Lin, X.-M. Chen, Z.-H. Liu, J. Chen, Investigation of uniaxial low-cycle fatigue failure behavior of hot-rolled AZ91 magnesium alloy, International Journal of Fatigue 48 (2013) 122-132.

[182] J. Dallmeier, J. Denk, O. Huber, H. Saage, K. Eigenfeld, Deformation Behavior and Fatigue Analysis of Magnesium Wrought Alloys under Variable Amplitude Loading, Materials Today: Proceedings 2 (2015) S119-S124.

[183] S.K. Koh, Fatigue damage evaluation of a high pressure tube steel using cyclic strain energy density, International Journal of Pressure Vessels and Piping 79(12) (2002) 791-798.

[184] F. Berto, P. Lazzarin, A review of the volume-based strain energy density approach applied to V-notches and welded structures, Theoretical and Applied Fracture Mechanics 52(3) (2009) 183-194.

[185] D.J. Nicholls, THE RELATION BETWEEN CRACK BLUNTING AND FATIGUE CRACK GROWTH RATES, Fatigue & Fracture of Engineering Materials & Structures 17(4) (1994) 459-467.

[186] K.-H. Schwalbe, Comparison of several fatigue crack propagation laws with experimental results, Engineering Fracture Mechanics 6(2) (1974) 325-341.

[187] M. Clavel, A. Pineau, Fatigue behaviour of two nickel-base alloys I: Experimental results on low cycle fatigue, fatigue crack propagation and substructures, Materials Science and Engineering 55(2) (1982) 157-171.

[188] F. Bachmann, R. Hielscher, H. Schaeben, Texture analysis with MTEX–free and open source software toolbox, Solid state phenomena, Trans Tech Publ, 2010, pp. 63-68.

[189] Y. Zhou, Formation of stray grains during directional solidification of a nickel-based superalloy, Scripta Materialia 65(4) (2011) 281-284.

[190] G. Winther, X. Huang, Dislocation structures. Part II. Slip system dependence, Philosophical Magazine 87(33) (2007) 5215-5235.

[191] J. Kacher, I.M. Robertson, Quasi-four-dimensional analysis of dislocation interactions with grain boundaries in 304 stainless steel, Acta Materialia 60(19) (2012) 6657-6672.

[192] T.R. Bieler, P. Eisenlohr, F. Roters, D. Kumar, D.E. Mason, M.A. Crimp, D. Raabe, The role of heterogeneous deformation on damage nucleation at grain boundaries in single phase metals, International Journal of Plasticity 25(9) (2009) 1655-1683.

[193] F. Schaefer, E.P.W. Lang, M. Bick, A.F. Knorr, M. Marx, C. Motz, Assessing the intergranular crack initiation probability of a grain boundary distribution by an experimental misalignment study of adjacent slip systems, Procedia Structural Integrity 5 (2017) 547-554.

[194] Y. Chen, Z. Wu, G. Wu, N. Wang, Q. Zhao, J. Luo, Investigation on micromechanism of ferrite hardening after pre-straining with different strain rates of dual-phase steel, Materials Science and Engineering: A 802 (2021) 140657.

[195] F. Di Gioacchino, J. Quinta da Fonseca, Plastic Strain Mapping with Sub-micron Resolution Using Digital Image Correlation, Experimental Mechanics 53(5) (2013) 743-754.

[196] A.L. Hijazi, A Novel Approach for the Determination of Surface Tilt Angles in Two-Dimensional Digital Image Correlation Experiments, Experimental Mechanics 60(3) (2020) 267-282.

[197] W.Z. Abuzaid, M.D. Sangid, J.D. Carroll, H. Sehitoglu, J. Lambros, Slip transfer and plastic strain accumulation across grain boundaries in Hastelloy X, Journal of the Mechanics and Physics of Solids 60(6) (2012) 1201-1220.

[198] T.F. Morgeneyer, L. Helfen, I. Sinclair, H. Proudhon, F. Xu, T. Baumbach, Ductile crack initiation and propagation assessed via in situ synchrotron radiation-computed laminography, Scripta Materialia 65(11) (2011) 1010-1013.

[199] E. Maire, P.J. Withers, Quantitative X-ray tomography, International Materials Reviews 59(1) (2014) 1-43.

[200] H.T. Pang, P.A.S. Reed, Effects of microstructure on room temperature fatigue crack initiation and short crack propagation in Udimet 720Li Ni-base superalloy, International Journal of Fatigue 30(10) (2008) 2009-2020.

[201] C. Altenbach, C. Schnatterer, U.A. Mercado, J.-P. Suuronen, D. Zander, G. Requena, Synchrotron-based holotomography and X-ray fluorescence study on the stress corrosion cracking behavior of the peak-aged 7075 aluminum alloy, Journal of Alloys and Compounds 817 (2020) 152722.

[202] L. Wang, N. Limodin, A. El Bartali, J.-F. Witz, R. Seghir, J.-Y. Buffiere, E. Charkaluk, Influence of pores on crack initiation in monotonic tensile and cyclic loadings in lost foam casting A319 alloy by using 3D in-situ analysis, Materials Science and Engineering: A 673 (2016) 362-372.

[203] D.J. Bull, S.M. Spearing, I. Sinclair, L. Helfen, Three-dimensional assessment of low velocity impact damage in particle toughened composite laminates using micro-focus X-ray computed tomography and synchrotron radiation laminography, Composites Part A: Applied Science and Manufacturing 52 (2013) 62-69.

[204] R. Jiang, D.J. Bull, D. Proprentner, B. Shollock, P.A.S. Reed, Effects of oxygen-related damage on dwell-fatigue crack propagation in a P/M Ni-based superalloy: From 2D to 3D assessment, International Journal of Fatigue 99 (2017) 175-186.

[205] M. Hassanipour, S. Watanabe, K. Hirayama, H. Li, H. Toda, K. Uesugi, A. Takeuchi, Assessment of predominant microstructural features controlling 3D short crack growth behavior via a surrogate approach in Ti-6Al-4V, Materials Science and Engineering: A 751 (2019) 351-362.

[206] J. Gayda, R.V. Miner, The effect of microstructure on 650 °C fatigue crack growth in P/M astroloy, Metallurgical Transactions A 14(11) (1983) 2301.

[207] Q. Han, Y. Gu, S. Soe, F. Lacan, R. Setchi, Effect of hot cracking on the mechanical properties of Hastelloy X superalloy fabricated by laser powder bed fusion additive manufacturing, Optics & Laser Technology 124 (2020) 105984.

[208] Z. Liao, B. Yang, Y. Qin, S. Xiao, G. Yang, T. Zhu, N. Gao, Short fatigue crack behaviour of LZ50 railway axle steel under multi-axial loading in low-cycle fatigue, International Journal of Fatigue 132 (2020) 105366.

[209] X. Meng, D. Zhang, Z. Weiwen, Q. Cheng, G. Liang, J. Chen, Microstructure and mechanical properties of a high-Zn aluminum alloy prepared by melt spinning and extrusion, Journal of Alloys and Compounds 819 (2020) 152990.

[210] S.W. Chen, C. Zhang, Z.X. Xia, H. Ishikawa, Z.G. Yang, Precipitation behavior of Fe2Nb Laves phase on grain boundaries in austenitic heat resistant steels, Materials Science and Engineering: A 616 (2014) 183-188.

[211] A. Bergsmo, F.P.E. Dunne, Competing mechanisms of particle fracture, decohesion and slip-driven fatigue crack nucleation in a PM nickel superalloy, International Journal of Fatigue 135 (2020) 105573.

[212] C. Lakavath, S.S. Joshi, S.S. Prakash, Investigation of the effect of steel fibers on the shear crack-opening and crack-slip behavior of prestressed concrete beams using digital image correlation, Engineering Structures 193 (2019) 28-42.

[213] K. Suzuki, M. Koyama, S. Hamada, K. Tsuzaki, H. Noguchi, Planar slip-driven fatigue crack initiation and propagation in an equiatomic CrMnFeCoNi high-entropy alloy, International Journal of Fatigue 133 (2020) 105418.

[214] T.C. Lindley, G. Oates, C.E. Richards, A critical of carbide cracking mechanisms in ferride/carbide aggregates, Acta Metallurgica 18(11) (1970) 1127-1136.

[215] A. Kelly, The Strengthening of Metals by Dispersed Particles, Proceedings of The Royal Society A: Mathematical, Physical and Engineering Sciences 282 (1964) 63-79.

[216] S.H. Goods, L.M. Brown, Overview No. 1: The nucleation of cavities by plastic deformation, Acta Metallurgica 27(1) (1979) 1-15.

[217] M. Hassanipour, S. Watanabe, K. Hirayama, H. Toda, K. Uesugi, A. Takeuchi, Short crack growth behavior and its transitional interaction with 3D microstructure in Ti-6Al-4V, Materials Science and Engineering: A 738 (2018) 229-237.

[218] M. Sarvghad, S. Bell, R. Raud, T.A. Steinberg, G. Will, Stress assisted oxidative failure of Inconel 601 for thermal energy storage, Solar Energy Materials and Solar Cells 159 (2017) 510-517.

[219] L.G. Zhao, J. Tong, M.C. Hardy, Prediction of crack growth in a nickel-based superalloy under fatigue-oxidation conditions, Engineering Fracture Mechanics 77(6) (2010) 925-938.

[220] R. Jiang, Study of fatigue crack initiation and propagation mechanisms in an advanced Ni-based superalloy: effects of microstructures and oxidation, University of Southampton, 2015.

[221] T. Connolley, M. Starink, P. Reed, Effect of oxidation on high temperature fatigue crack initiation and short crack growth in Inconel 718, Superalloys 5(2000) (2000) 435-444.

[222] G. Sjoberg, N. Ingesten, V.F. AB, R. Carlson, Grain Boundary□-Phase Morphologies, Carbides and Notch Rupture Sensitivity of Cast Alloy 718, Superalloys 718 625.

[223] Y. Murakami, T. Nomoto, T. Ueda, Factors influencing the mechanism of superlong fatigue failure in steels, Fatigue and Fracture of Engineering Materials and Structures 22(7) (1999) 581-590.

[224] Y. Murakami, M. Takada, T. Toriyama, Super-long life tension-compression fatigue properties of quenched and tempered 0.46% carbon steel, International Journal of Fatigue 20(9) (1998) 661-667.

[225] M. Nakajima, T. Sakai, T. Shimizu, An observation of fish-eye fracture process in high strength steel SUJ2, Nihon Kikai Gakkai Ronbunshu, A Hen/Transactions of the Japan Society of Mechanical Engineers, Part A 65(640) (1999) 2504-2510.

[226] Q.Y. Wang, J.Y. Berard, A. Dubarre, G. Baudry, S. Rathery, C. Bathias, Gigacycle fatigue of ferrous alloys, Fatigue and Fracture of Engineering Materials and Structures 22(8) (1999) 667-672.

[227] K. Shiozawa, Y. Morii, S. Nishino, L. Lu, Subsurface crack initiation and propagation mechanism in high-strength steel in a very high cycle fatigue regime, International Journal of Fatigue 28(11) (2006) 1521-1532.

[228] M.D. Miller, P.A.S. Reed, M.R. Joyce, M.B. Henderson, J.W. Brooks, I. Wilcock, X. Wu, Effect of environment on notch fatigue behaviour in CMSX4, Materials Science and Technology 23(12) (2007) 1439-1445.

[229] T. Davis, D. Healy, A. Bubeck, R. Walker, Stress concentrations around voids in three dimensions: The roots of failure, Journal of Structural Geology 102 (2017) 193-207.

[230] S. Suresh, G.F. Zamiski, D.R.O. Ritchie, Oxide-Induced Crack Closure: An Explanation for Near-Threshold Corrosion Fatigue Crack Growth Behavior, Metallurgical Transactions A 12(8) (1981) 1435-1443.

[231] J. Maierhofer, D. Simunek, H.P. Gänser, R. Pippan, Oxide induced crack closure in the near threshold regime: The effect of oxide debris release, International Journal of Fatigue 117 (2018) 21-26.

[232] R. Jiang, L.C. Zhang, Y. Zhao, X.H. Chen, B. Gan, X.C. Hao, Y.D. Song, Effects of Hot Corrosion on Fatigue Performance of GH4169 Alloy, Journal of Materials Engineering and Performance 30(3) (2021) 2300-2308.

[233] J.C. Stinville, E. Martin, M. Karadge, S. Ismonov, M. Soare, T. Hanlon, S. Sundaram, M.P. Echlin, P.G. Callahan, W.C. Lenthe, V.M. Miller, J. Miao, A.E. Wessman, R. Finlay, A. Loghin, J. Marte, T.M. Pollock, Fatigue deformation in a polycrystalline nickel base superalloy at intermediate and high temperature: Competing failure modes, Acta Materialia 152 (2018) 16-33.

[234] A. Sato, Y.L. Chiu, R.C. Reed, Oxidation of nickel-based single-crystal superalloys for industrial gas turbine applications, Acta Materialia 59(1) (2011) 225-240.

[235] H.Y. Li, J.F. Sun, M.C. Hardy, H.E. Evans, S.J. Williams, T.J.A. Doel, P. Bowen, Effects of microstructure on high temperature dwell fatigue crack growth in a coarse grain PM nickel based superalloy, Acta Materialia 90 (2015) 355-369.

[236] M.Y. He, A.G. Evans, A model for oxidation-assisted low cycle fatigue of superalloys, Acta Materialia 58(2) (2010) 583-591.

[237] A.G. Evans, M.Y. He, A. Suzuki, M. Gigliotti, B. Hazel, T.M. Pollock, A mechanism governing oxidation-assisted low-cycle fatigue of superalloys, Acta Materialia 57(10) (2009) 2969-2983.

[238] A. Evangelou, K.A. Soady, S. Lockyer, N. Gao, P.A.S. Reed, On the mechanism of oxidation-fatigue damage at intermediate temperatures in a single crystal Ni-based superalloy, Materials Science and Engineering: A 742 (2019) 648-661.

[239] L. Ma, K.-M. Chang, S.K. Mannan, Oxide-induced crack closure: an explanation for abnormal time-dependent fatigue crack propagation behavior in INCONEL alloy 783, Scripta Materialia 48(5) (2003) 583-588.

[240] X.-K. Zhu, J.A. Joyce, Review of fracture toughness (G, K, J, CTOD, CTOA) testing and standardization, Engineering Fracture Mechanics 85 (2012) 1-46.

[241] A.K. Vasudeven, K. Sadananda, N. Louat, A review of crack closure, fatigue crack threshold and related phenomena, Materials Science and Engineering: A 188(1) (1994) 1-22.

[242] A. Vasudevan, K. Sadananda, N. Louat, Reconsideration of fatigue crack closure, Scripta metallurgica et materialia 27(11) (1992) 1673-1678.

[243] C.F. Shih, Relationships between the J-integral and the crack opening displacement for stationary and extending cracks, Journal of the Mechanics and Physics of Solids 29(4) (1981) 305-326.

[244] I.O.f. Standardization, Metallic Materials: Fatigue Testing: Fatigue Crack Growth Method. ISO 12108, ISO2002.

[245] C.S. Wiesner, S.J. Maddox, W. Xu, G.A. Webster, F.M. Burdekin, R.M. Andrews, J.D. Harrison, Engineering critical analyses to BS 7910 — the UK guide on methods for assessing the acceptability of flaws in metallic structures, International Journal of Pressure Vessels and Piping 77(14) (2000) 883-893.

[246] Y. Gao, R.O. Ritchie, M. Kumar, R.K. Nalla, High-cycle fatigue of nickel-based superalloy ME3 at ambient and elevated temperatures: Role of grain-boundary engineering, Metallurgical and Materials Transactions A 36(12) (2005) 3325-3333.

[247] L. Garimella, P. Liaw, D. Klarstrom, Fatigue behavior in nickel-based superalloys: A literature review, Jom 49(7) (1997) 67-71.

[248] J.M. Schooling, M. Brown, P.A.S. Reed, An example of the use of neural computing techniques in materials science—the modelling of fatigue thresholds in Ni-base superalloys, Materials Science and Engineering: A 260(1) (1999) 222-239.

[249] S. Suresh, R.O. Ritchie, Some considerations on the modelling of oxide-induced fatigue crack closure using solutions for a rigid wedge inside a linear elastic crack, Scripta Metallurgica 17(4) (1983) 575-580.

[250] S. Suresh, Fatigue of Materials, 2 ed., Cambridge University Press, Cambridge, 1998.

[251] Z. Shan, Y. Leng, Analytical estimation of asperity-induced crack closure, Scripta Materialia 36(1) (1997) 137-143.

[252] R.J. Kashinga, L.G. Zhao, V.V. Silberschmidt, F. Farukh, N.C. Barnard, M.T. Whittaker, D. Proprentner, B. Shollock, G. McColvin, Low cycle fatigue of a directionally solidified nickel-based superalloy: Testing, characterisation and modelling, Materials Science and Engineering: A 708 (2017) 503-513.

[253] G.T. Gray, J.C. Williams, A.W. Thompson, Roughness-Induced Crack Closure: An Explanation for Microstructurally Sensitive Fatigue Crack Growth, Metallurgical Transactions A 14(2) (1983) 421-433.

[254] S. Suresh, R.O. Ritchie, A geometric model for fatigue crack closure induced by fracture surface roughness, Metallurgical Transactions A 13(9) (1982) 1627-1631.

[255] P. Hones, M. Diserens, F. Lévy, Characterization of sputter-deposited chromium oxide thin films, Surface and Coatings Technology 120-121 (1999) 277-283.

[256] G.V. Samsonov, Mechanical Properties, in: G.V. Samsonov (Ed.), The Oxide Handbook, Springer US, Boston, MA, 1973, pp. 224-262.

[257] T. Polcar, N.M.G. Parreira, A. Cavaleiro, Tungsten oxide with different oxygen contents: Sliding properties, Vacuum 81(11) (2007) 1426-1429.

[258] J.R. Nicholls, D.J. Hall, P.F. Tortorelli, Hardness and modulus measurements on oxide scales, Materials at High Temperatures 12(2-3) (1994) 141-150.

[259] C. Tromas, M. Arnoux, X. Milhet, Hardness cartography to increase the nanoindentation resolution in heterogeneous materials: Application to a Ni-based single-crystal superalloy, Scripta Materialia 66(2) (2012) 77-80.

[260] H. Bückle, Mikrohärteprüfung und ihre Anwendung, Berliner Union1965.

[261] P. Peralta, S.H. Choi, J. Gee, Experimental quantification of the plastic blunting process for stage II fatigue crack growth in one-phase metallic materials, International Journal of Plasticity 23(10) (2007) 1763-1795.

[262] C.J. McMahon, L.F. Coffin, Mechanisms of damage and fracture in high-temperature, low-cycle fatigue of a cast nickel-based superalloy, Metallurgical Transactions 1(12) (1970) 3443-3450.

[263] L. Ma, K.-M. Chang, Identification of SAGBO-induced damage zone ahead of crack tip to characterize sustained loading crack growth in alloy 783, Scripta Materialia 48(9) (2003) 1271-1276.

[264] H.S. Kitaguchi, H.Y. Li, H.E. Evans, R.G. Ding, I.P. Jones, G. Baxter, P. Bowen, Oxidation ahead of a crack tip in an advanced Ni-based superalloy, Acta Materialia 61(6) (2013) 1968-1981.

[265] B.J. Hockey, B.R. Lawn, Electron microscopy of microcracking about indentations in aluminium oxide and silicon carbide, Journal of Materials Science 10(8) (1975) 1275-1284.

[266] T.D. Reynolds, D.M. Collins, N.K. Soor, S.R. Street, N. Warnken, P.M. Mignanelli, M.C. Hardy, H.E. Evans, M.P. Taylor, Identifying heating rate dependent oxidation reactions on a nickel-based superalloy using synchrotron diffraction, Acta Materialia 181 (2019) 570-583.

[267] Y. Liu, Y. Wu, J. Wang, Y. Ning, Oxidation behavior and microstructure degeneration of cast Ni-based superalloy M951 at 900 °C, Applied Surface Science 479 (2019) 709-719.

[268] L. Klein, A. Zendegani, M. Palumbo, S.G. Fries, S. Virtanen, First approach for thermodynamic modelling of the high temperature oxidation behaviour of ternary γ′-strengthened Co–Al–W superalloys, Corrosion Science 89 (2014) 1-5.

[269] R.H. Bricknell, D.A. Woodford, Grain boundary embrittlement of the iron-base superalloy IN903A, Metallurgical Transactions A 12(9) (1981) 1673-1680.

[270] L. Volpe, M.G. Burke, F. Scenini, Understanding the role of Diffusion Induced Grain Boundary Migration on the preferential intergranular oxidation behaviour of Alloy 600 via advanced microstructural characterization, Acta Materialia 175 (2019) 238-249.

[271] R.W. Balluffi, Grain boundary diffusion mechanisms in metals, Metallurgical Transactions B 13(4) (1982) 527-553.

[272] L. Viskari, M. Hörnqvist, K.L. Moore, Y. Cao, K. Stiller, Intergranular crack tip oxidation in a Ni-base superalloy, Acta Materialia 61(10) (2013) 3630-3639.

[273] M.D. McMurtrey, G.S. Was, B. Cui, I. Robertson, L. Smith, D. Farkas, Strain localization at dislocation channel–grain boundary intersections in irradiated stainless steel, International Journal of Plasticity 56 (2014) 219-231.

[274] J.L.W. Carter, M.W. Kuper, M.D. Uchic, M.J. Mills, Characterization of localized deformation near grain boundaries of superalloy René-104 at elevated temperature, Materials Science and Engineering: A 605 (2014) 127-136.

[275] G. Martin, C.W. Sinclair, J.-H. Schmitt, Plastic strain heterogeneities in an Mg–1Zn–0.5Nd alloy, Scripta Materialia 68(9) (2013) 695-698.

[276] J.A. del Valle, A.C. Picasso, R. Romero, Work-hardening in Inconel X-750: study of stage II, Acta Materialia 46(6) (1998) 1981-1988.

[277] T. Hirata, K. Akiyama, H. Yamamoto, Sintering behavior of Cr2O3–Al2O3 ceramics, Journal of the European Ceramic Society 20(2) (2000) 195-199.

[278] A.A.N. Németh, D.J. Crudden, D.E.J. Armstrong, D.M. Collins, K. Li, A.J. Wilkinson, C.R.M. Grovenor, R.C. Reed, Environmentally-assisted grain boundary attack as a mechanism of embrittlement in a nickel-based superalloy, Acta Materialia 126 (2017) 361-371.

[279] H.S. Kitaguchi, M.P. Moody, H.Y. Li, H.E. Evans, M.C. Hardy, S. Lozano-Perez, An atom probe tomography study of the oxide–metal interface of an oxide intrusion ahead of a crack in a polycrystalline Ni-based superalloy, Scripta Materialia 97 (2015) 41-44.

[280] M.T. Lapington, D.J. Crudden, R.C. Reed, M.P. Moody, P.A.J. Bagot, Characterization of oxidation mechanisms in a family of polycrystalline chromia-forming nickel-base superalloys, Acta Materialia 206 (2021) 116626.

[281] A. Evangelou, K.A. Soady, S. Lockyer, N. Gao, P.A.S. Reed, Oxidation behaviour of single crystal nickel-based superalloys: intermediate temperature effects at 450–550°C, Materials Science and Technology 34(14) (2018) 1679-1692.

[282] T.M. Smith, R.R. Unocic, H. Deutchman, M.J. Mills, Creep deformation mechanism mapping in nickel base disk superalloys, Materials at High Temperatures 33(4-5) (2016) 372-383.

[283] J.M. Börgers, J. Kler, K. Ran, E. Larenz, T.E. Weirich, R. Dittmann, R.A. De Souza, Faster Diffusion of Oxygen Along Dislocations in (La,Sr)MnO3+δ Is a Space-Charge Phenomenon, Advanced Functional Materials 31(51) (2021) 2105647.

[284] M. Legros, G. Dehm, E. Arzt, T.J. Balk, Observation of Giant Diffusivity Along Dislocation Cores, Science 319(5870) (2008) 1646-1649.

[285] S. Senkader, P.R. Wilshaw, R.J. Falster, Oxygen-dislocation interactions in silicon at temperatures below 700 °C: Dislocation locking and oxygen diffusion, Journal of Applied Physics 89(9) (2001) 4803-4808.

[286] P.A. Sabnis, M. Mazière, S. Forest, N.K. Arakere, F. Ebrahimi, Effect of secondary orientation on notch-tip plasticity in superalloy single crystals, International Journal of Plasticity 28(1) (2012) 102-123.

[287] D. Zhang, J. He, J. Liang, Z. He, Surface Slip Deformation Characteristics of Nickel-Base Single Crystal Thin Plates With Film Cooling Holes, IEEE Access 8 (2020) 75145-75153.